Shape Analysis in Mammograms

Faraz Janan
Somerville College

Supervised By Professor Sir Michael Brady

Institute of Bio-Medical Engineering
University of Oxford, UK

Michaelmas Term 2013

ABSTRACT

The number of women diagnosed with the breast cancer continues to rise year on year. Breast cancer is now the most common type of cancer in the UK, with over 55000 cases reported last year. In most cases, mammography is the first step towards diagnosing breast cancer. However, it continues to have many practical limitations as compared to more sophisticated modalities such as MRI. The relatively low cost of mammography, together with the ever increasing risk of women contracting the disease, has led to many developed countries having a breast screening program. These routine breast screens are taken at different points in time and are called temporal mammograms. Currently, a radiologist tends to qualitatively assess temporal mammograms and look for any abnormalities or suspicious regions that might be of a concern. In this thesis, we develop an automatic shape analysis model that can detect and quantify such changes inside the breast. This will not only help in early diagnosis of the disease, which is key to survival, but will potentially aid prognosis and post treatment care.

The core to this thesis is the use of Circular Integral Invariants. We explore its multi-scale properties and use it for image smoothing to reduce image noise and enhance features for segmentation. We implement, modify and enhance a segmentation method which previously has been successfully used to acquire breast regions of interest.

We applied such Integral Invariants for shape description, to be used for shape matching as well as for subdividing shapes into sub-regions and quantifying the differences between two such shapes. We combine boundary information with the information from inside a shape, thus eccentrically transforming shapes before describing their structure. We develop a novel false positives reduction method based on Integral Invariants scale space.

A second aspect of the thesis is the evaluation of and emphasis on the use of breast density maps against the commonly used intensity maps or x-rays. We find density maps sufficient to use in clinical practice. The methods developed in this thesis aim to help clinicians in making diagnostic decision at the point of case. Our shape analysis model is easy to compute, fast and very general in nature that could be deployed in a wide range of applications, beyond mammography.

ACKNOWLEDGMENTS

This thesis would not have been possible without the inspiration, mentorship and direction of my supervisor, Professor Sir Michael Brady (Mike), who is not only a GREAT scientist but a super human being (I have seen it!). His motivation and advice has always greatly helped me on every step during the thesis and beyond.

I am very grateful to the Islamic Development Bank (IDB) for their generous scholarship to supporting my DPhil. I thank Professor John Fox for all his help in the admission process, writing scholarship proposals and finding my way through the initial stages of the DPhil.

I sincerely thank Tünde Szilágyi for giving me a head start on different ideas, introducing me to many nice people and helping me running some codes. I show gratitude to Dr. Osamah Khoja, Rehan (Bobby) Ali, Habib Baluwala, Manav Bhushan, Wehjunchi (Jim), and last but not the least, Syed Ahmar Shah, for their support and encouragement.

Finally, I am grateful to my wife *Sara* for helping me through my thesis, and my son *Kalandar* for bearing with me and keeping me 'alive' thorough some of very frustrating days. Best wishes to my daughter *Durkhanai*, who was born soon after my viva.

I thank all my family and extended family, both in the UK and in Pakistan, for their moral support, prayers and well wishes.

I dedicate this thesis to my mother, *'Amee'*, whose love, dedication and prayers have made me reach this far.

I also dedicate this to my school teacher, *Madam Munawar Gul*, who remains a constant source of inspiration for me.

To the *victims of cancer*, whose lives are shattered by the disease or are no longer with us.

TABLE OF CONTENTS

`

List of Publications

The work from thesis has appeared in [1]–[5].

Peer Reviews Conferences:

[1] F. Janan and M. Brady, “Region matching in the temporal study of mammograms using integral invariant scale-space,” in *Breast Imaging*, IWDM 2012 Springer, 2012, pp. 173–180.

[2] F. Janan and S. M. Brady, “Integral invariants for image enhancement,” in *Engineering in Medicine and Biology Society (EMBC), 2013 35th Annual International Conference of the IEEE*, 2013, pp. 4018–4021.

[3] F. Janan and M. Brady, “Shape matching by integral invariants on eccentricity transformed images,” in *Engineering in Medicine and Biology Society (EMBC), 2013 35th Annual International Conference of the IEEE*, 2013, pp. 5099–5102.

[4] F. Janan, M. Brady, C. Tromans, and R. Highnam, “Standard Attenuation Rate and Volpara(R) Volumetric Density Maps,” in *Second MICCAI International Workshop on Breast Image Analysis, BIA 2013, Nagoya, Japan*, 2013.

[5] F. Janan, M. Brady, and R. Highnam, “False Positive Reduction in CADe Using Diffusing Scale Space,”in *Breast Imaging.* IWDM 2014, Springer, pp. 597–605, 2014.

List of Journals:

[1] Faraz Janan, Sir Michael Brady: Shape Description and Matching Using Integral Invariants on Eccentricity Transformed Images. Accepted with subject to corrections at *International Journal of Computer Vision (IJCV)*

[2] Faraz Janan, Sir Michael Brady: Shape Localization, Quantification and Correspondence using Region Matching Algorithm (RMA). Accepted with subject to corrections at *The Journal of Biomedical Graphics and Computing*

Chapter 1

1. 1. INTRODUCTION

Signal and image processing, together with knowledge representation, when applied to medical images (e.g. mammography, ultrasound, CT, MRI, PET) is leading to many valuable clinical tools. The focus of this thesis is the development of a computer aided tool that aims to aid clinicians in making diagnostic and prognostic decisions in radiological contexts typified by mammography. Specifically, we develop a shape analysis model, which may be applied to clinical and research medical imaging modalities to detect incremental changes in shapes.

The aim of the work is to develop a shape analysis model for complex 2D shapes that could be eventually extended to 3D shapes, in order to match, correspond and quantify shape differences, and in particular, to study 'interesting' regions in mammograms. Figure 1.1 shows the shape analysis model implemented in this thesis.

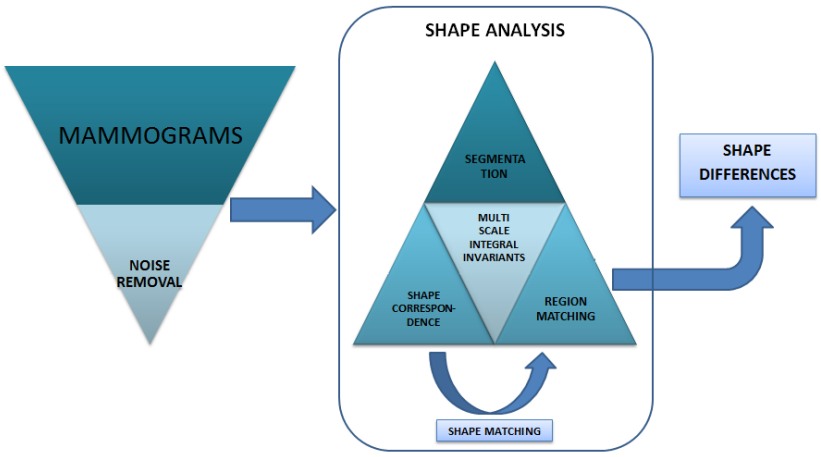

Figure 1.1: Overview of the temporal study of mammograms by the shape analysis model developed in this thesis

1. 2. Breast Cancer: A Fatal Syndrome

The increase in the number of breast cancer patients over the past few years is alarming. It has been reported that breast cancer is the second most diagnosed cancer in women, and was already the world most prevalent cancer by the year 2002 [6]. However, the mortality rate among women has decreased enormously with the development of more effective treatment techniques and early detection methodologies using computer aided diagnosis tools [7]–[9]. Breast cancer is far more common in women than in men. In the western world, approximately 11-12% of all women at some stage of their life are affected by breast cancer [6]. Conversely, breast cancer in men accounts for less than 1% of all breast cancer in the United States and less than 1% of all cancers in men. A woman's risk of breast cancer approximately doubles if she has a first-degree relative (mother, sister, or daughter) who has been diagnosed with the disease. About 20-30% of women diagnosed with breast cancer have a family history of breast cancer [10].

Based on the statistics from the World Health Organization (WHO), cancer accounted for 13% of all deaths in the world in 2004. Deaths caused by cancer are expected to increase in the future with an estimated 12 million people dying from cancer in 2030 [11]. [12]

1. 3. Imaging Modalities

Screening modalities can reduce the mortality rate and are helpful in early diagnosis and treatment of disease. There are a number of techniques that are used to detect and stage breast cancer. The common imaging technologies in routine use are x-ray mammograms and ultrasound (US); whereas as other imaging technologies that could be used, however are less common, are computed tomography digital synthesis (CT), Flurodeoxygulucose (FDG) positron emission tomography (PET), ultrasound, single-photon emission computed

tomography (SPECT) and magnetic resonance imaging (MRI). Magnetic resonance spectroscopy (MRS), optical computed tomography and (early or late) near infra-red image fluorescence may find clinical use in the near future. There are also machines that can provide PET-CT fusion images. The most extensively used imaging modalities are tray US, CT, PET zMRI [13]. Digital breast tomosynthesis is evolving rapidly as a second screening modality besides x-ray mammograms, to look for masked tumours and assess abnormality more clearly.

1. 4. Mammography

Though many different imaging modalities are used for the detection of breast cancer in clinical practice, mammography is currently the most common. A mammogram is a low-dose x-ray examination passed through the compressed breast to look for structures that are not normal. Nowadays, the results are fed directly into a computer for processing prior to being viewed by a radiologist. The two most common views are Medio-Lateral Oblique (MLO) and Cranio Caudal (CC).

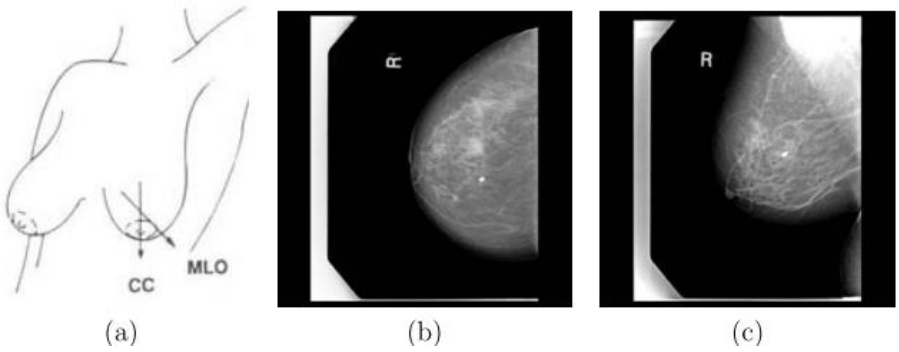

Figure 1.2: Different viewpoints of the same breast: (a) shows the direction of the two most used views, which produce images exemplified in (b) the Cranio-Caudal (CC) view, and (c) the Medio-Lateral Oblique (MLO) view. In the MLO view the pectoral muscle is prominent [14].

The MLO view, from shoulder to hip, contains the pectoral muscle in the upper right or left corner of mammogram as shown in the Figure 1.2. Mammograms may also contain additional information as seen in Figure 1.2, where R represents the right breast. Considered as images, mammograms vary hugely over the population, so radiologists find them complex to analyse. For this reason a number of reporting standards have been established, though the terms they use are qualitative in the sense that they are subject to the individual radiologist's perception. There are various categories to define breast density. The American College of Radiology (ACR) has established the Breast Imaging Reporting and Data (BI-RADS^{TM}) to guide the breast cancer diagnostic routine.

Mammograms are inspected to detect abnormalities in the breast. There are four main types of breast abnormalities,

1. Right and left breast asymmetry
2. Architectural distortion of breast tissues
3. Presence of a mass or cyst in the breast (benign or malignant)
4. Micro-calcifications

If a mass that is detected in the breast is a tumour then it can either be benign or malignant. Figure 1.3 presents some well-known features of breast tumours that define its shape.

1. 5.Analysing Mammograms Using Two or More Images

Because mammograms are such complex images and vary considerably over the population, it is common clinical practice in breast radiology to analyse two or more mammograms in order to detect abnormalities. While comparing two mammograms of the same patient, the breasts may vary in size and in the way they are imaged; but the internal structure is quite similar and

symmetric over large areas. This is done to detect asymmetry in the breast tissues by taking into consideration various features such as the size, shape and density of tissues. There are three commonly used comparisons that are of most interest to a radiologist:

1. Comparison of the right and left breasts (breast asymmetry)
2. Comparison of two different views of the same breast (i.e. MLO vs. CC view)
3. Comparison of the same views and of the same breast taken at different times (temporal study of mammograms)

All three comparisons are important, though initially we are most interested in the temporal study of mammograms, as it is not only vital for diagnosis and treatment but also for post-treatment care. It gives an intuitive idea of how a certain region in the breast may have evolved over time.

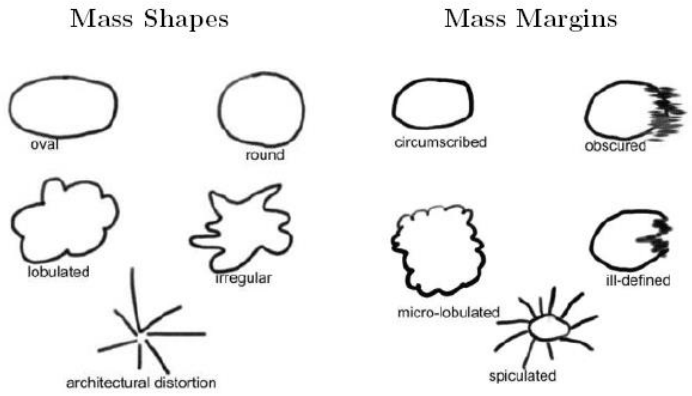

Figure 1.3: The above figure shows different shape and contours that a breast cyst or mass may have, and is used to discriminate between benign and malignant [15]

We address the temporal study of mammograms by employing the recently-introduced image analysis technique of Integral Invariants and by further exploiting its scale space for local

region matching in segmented masses. Figures 1.4 & 1.5 respectively show mammographic images and abnormal regions of the same breast taken at different times.

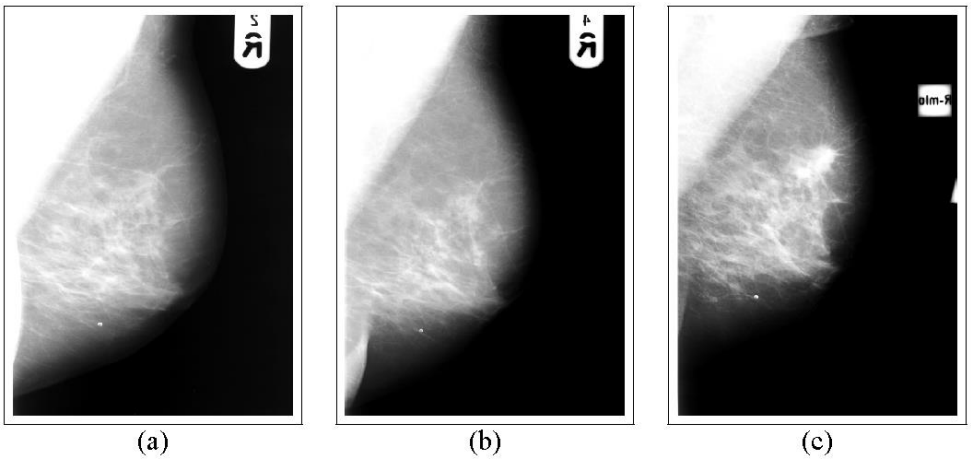

Figure 1.4: Temporal mammograms from various screening years: (a) 1992, (b) 1995 and (c) 2000.[16]

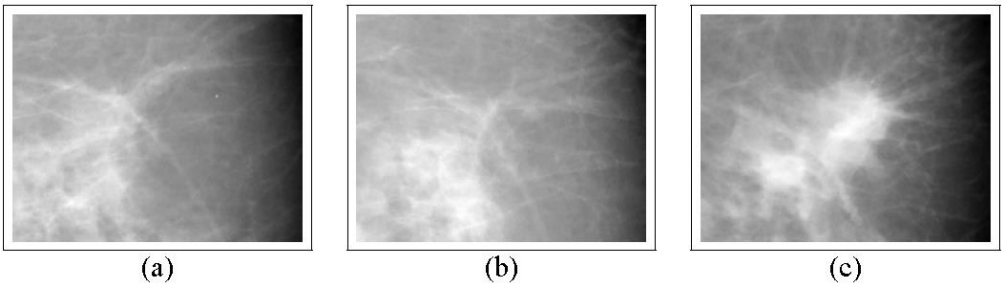

Figure 1.5: Tracking of an abnormal mammographic region in Figure 1.4 [16]

1. 6. Computer Aided Diagnosis

Over the past two decades, scientists and researchers have developed methods for Computer-aided detection (CAD) and classification techniques for the early detection of breast cancer based on mammography screening. In this area of research, the classification of breast masses into benign and malignant categories remains a challenging task. Therefore, there is a need to

develop and advance the existing computer-aided platforms that will provide a second opinion, as well as to manage the strategies for prevention, diagnosis and cure of breast cancer patients.

CAD systems are built on the basis of information engineering, mathematics, image processing, pattern recognition, machine learning and artificial intelligence. Systems that deal with imaging modalities such as mammograms, CT scans, MRIs etc. are designed for radiologists who use the output from analysis of medical images as a second opinion in detecting and making diagnostic decisions. Comprehensive surveys of CAD systems directed towards breast cancer are given in [15], [17]–[21].

Most CAD systems use image processing algorithms to detect abnormalities in mammograms such as calcifications, masses, and to support the temporal study of mammograms and architectural distortion. The use of CAD technologies by radiologists and pathologists is playing a key role in the early detection of breast cancer and helping to reduce the mortality rate among women [17].

1. 7. Breast Screening

Breast screening is routine in the UK: women between the ages of 50 to 70 are invited to undergo x-ray imaging every 2 years of the compressed breast (the age range is currently being extended from 47 to 73). The International Agency for Research on Cancer has shown that breast screening reduces the mortality rate from breast cancer by 35%. It has been estimated that each year the screening programme saves over 1400 lives in the UK. Out of 46000 cases diagnosed, about 12000 women die of breast cancer every year [22], [23].

The pool of mammograms acquired routinely creates a temporal series, which is extremely useful in detecting the development of abnormalities inside the breast. In this thesis, we have used temporal mammograms from routine screening and have applied our shape analysis model to establish correspondences between regions in them.

1. 8. Mammographic Segmentation

Mammograms are complex images with huge variations in their internal patterns including the size, heterogeneity, location and shape of dense tissue, volumetric density etc. As mammograms are two dimensional projections of a compressed three dimensional breast, the increasing intensity of a region in a mammogram is representative of the increased density of the region formed of higher intensities, and this may indicate the presence of a lesion. Therefore the algorithms we use and develop are based on iso-intensity contours.

There are three major challenges confronting the design of a good and practical segmentation algorithm.

1. Automation of the segmentation algorithm

2. Accuracy of the segmented regions

3. Reduced computational cost and time

Most state of the art algorithms such as level sets are computationally expensive, hence slow and may not suitable to implement in a real time system. The biggest problems with level sets in this application are: (a) the critical dependence on initialisation of the level set algorithm; and (b) leakage of regions of interest to the surroundings by most level set algorithms. These severely reduce all three of the requirements above. Most algorithms are semi-automatic and

require a seed point provided by a human for individual cases to segment the regions of interest. It might also be viewed as an advantage from the point of view that a radiologist can click a region to segment; nevertheless, it is quite manual to be used in practice where decisions are made very quickly in cancer multi-disciplinary meetings. This is counter to requirement 1 and severely limits the utility of such methods in clinical practice. The accuracy of the segmentation with respect to its margins is however an independent factor. Our considerations for a good segmentation algorithm are that it should be almost or absolutely automatic, fast to compute, can delineate the regions of interest and could be the basis of a real time CAD system with accuracy.

1. 9. Shape Analysis

Regions of interest in mammograms, typically masses, are very complex shapes. Masses usually have low contrast and therefore require enhancement. Detection quite often needs temporal analysis of mammograms, which is currently qualitative. Moreover, regions change over time as they grow, or shrink in response to therapy. This necessitates an accurate shape analysis model.

Image analysis aims to develop tools to interpret an image, for example a mammogram or an image of individual cell. A model has to be developed that can be used to extract the shapes of the regions of interest (ROI) from various imaging modalities applied with slight modifications. It should be able to compare images at a coarse level in order to match shapes, as well at a finer scale for matching regions in shapes. Such a system should be able to determine point-wise correspondences between two shapes, ideally with a computational cost that enables a real time system. It should provide a matching cost between two shapes.

Our shape analysis model works in following modules,

1. Segmentation of an image into salient regions
2. Point-wise correspondence of the segmented shapes
3. Development of a shape matching cost
4. Local region matching between two shapes

The choice of the noise removal filtering method depends upon the type of images and the specific application.

1. 10. Project Objectives

The objective of this project was the development and application of an image analysis model that extracts ROIs, then establishes correspondences and matching of rotated, reflected and articulated shapes from medical images at both global and local scales.

There are two well-known and widely used methods to infer diagnosis of cancer in a patient, namely mammography, ultrasound and biopsy, which are done by a radiologist and pathologist respectively. A CAD system that can be incorporated with a differential clinical decision support system could be of great help to clinicians. It could be used to feed data to a decision support engine that can generate a decision based upon the indications from CAD and an existing knowledge base.

We have developed a tool to detect ‘interesting’ breast regions and correspond them in temporal mammograms. Such a system should be able to enumerate new growths or occlusions in masses. Currently, temporal assessment is entirely qualitative and so depends on the individual radiologist. Our aim is to measure quantitatively temporal changes, either new

growth or occlusions of interesting tissues. For mammograms, such a system should be able to deal with breast asymmetry as well as identifying temporal changes in mammograms.

1. 11. Thesis Outline

This thesis studies segmentation, multi-scale shape description and shape correspondence, along with the usability of quantitative measures of breast density, such as Volpara® maps. Segmentation and shape analysis are central problems in the computer vision community and are extensively investigated fields. We have explored them for our research. From this study, Integral Invariants are used as shape descriptors to characterize shapes, which are then corresponded and matched in temporal mammograms. The outline of each chapter is as follows:

The background of breast cancer and the need of image analysis are presented in this chapter. Various breast abnormalities are defined; such as, shape of masses, computer aided diagnosis and the significance of the screening program are explained.

Chapter 2 advocates the use of breast density maps as compared to mammograms and emphasises the relationship between breast density and the risk of developing breast cancer. It gives a detailed literature review on a number of qualitative and quantitative methods to find breast density. It explains what are the limitations using x-ray mammograms. We have used Volpara® density maps alongside DICOM mammograms in this thesis, which is a breast density measure and is the visual representation of breast density.

A review of Integral Invariants, which is the shape description method we have used, is given in the Chapter 3 and explained in detail in Chapter 7. Integral Invariants are central to this thesis. We have also used them for image enhancement. An optimization method, called the

Fast Marching Algorithm (FMA) is explained in detail. The advantage of Integral Invariants over generally used curvature measures is emphasised.

Chapter 4 presents a topographic representation of mammograms, which effectively characterises important mammographic regions in a breast. It is a developed as a modification to an existing segmentation algorithm and has been applied successfully to detect masses in mammograms. This chapter provides a detailed critical evaluation of the segmentation algorithm used.

Chapter 5 explores multi-scale space Integral Invariants, and its various properties in accordance to Gaussian scale space. A novel and robust method based on multi-scale Integral Invariants is introduced to reduce the number of false positives in mammograms.

Integral Invariants are used for image enhancement in Chapter 6. They are compared to Gaussian smoothing and anisotropic diffusion to assess its usability as a noise suppression method.

Chapter 7 concerns shape matching and correspondence for both synthetic shapes and mammograms. A novel local Region Matching Algorithm (RMA) is presented that can find occlusions and articulations quantitatively. Furthermore, RMA is applied to segmented regions in mammograms.

Chapter 8 presents a novel approach of combining boundary information and the information from inside of a shape for matching and correspondence. It implements Eccentricity transforms alongside Integral Invariants leading to better performance in reducing

correspondence errors. The technique is shown to decrease mismatching in point-wise correspondences.

Chapter 9 evaluates the usability of Volpara® density maps and its robustness by comparing it to another quantitative breast density measure known as the Standard Attenuation Rate (SAR)[24]. Volpara® is based on the relative physics model whereas SAR is based on an absolute physics model. The chapter demonstrates a linear relationship between the two by comparing corresponding regions using a technique based on the super-pixel region segmentation method called Simple Linear Iterative Clustering (SLIC).

Chapter 10 concludes the impact of work described in this thesis and proposes a list of possible future work that can be realized by extending the current work.

Chapter 2

BREAST DENSITY ASSESSMENT

2. 1. Breast Density

X-ray mammograms are used in routine screening to detect abnormalities in the breast for an asymptomatic population of post-menopausal women, and to reflect the qualitative density of breast regions. However, the parenchymal study of x-rays is currently established on subjective assessment of mammograms, which leads to large inter- and intra-observer variability. The appearance of a mammogram, considered as an image, varies very considerably among women and depends upon the imaging parameters, tissue characteristics, and the response of different breast tissues to x-ray attenuation. Figure 2.1 show two mammograms of the same breast of a woman positioned very carefully, taken on the same date, by different radiographers. Here, the two radiographers chose slightly different but reasonable machine settings, such as the aperture setting, time of exposure, and the film speed. Despite the fact that these mammograms are taken on the same machine, the breast composition appears significantly different in the two images. The reason for the substantial difference in the intensity levels of the two images is that fibroglandular tissues have a higher attenuation of x-rays than fat. On the other hand, a tumour and benign conditions such as fibroadenomas have approximately the same attenuation as that of dense fibroglandular tissue. The imaging conditions that may make normal tissue appear dense, makes it difficult to detect abnormalities in a dense breast. This means that cancer detection in such cases may be delayed and makes prognosis very difficult. Women with high breast density are not only at

higher risk than their similar age peers, but detection of disease might be delayed because of dense appearance of breast parenchyma surrounding abnormality.

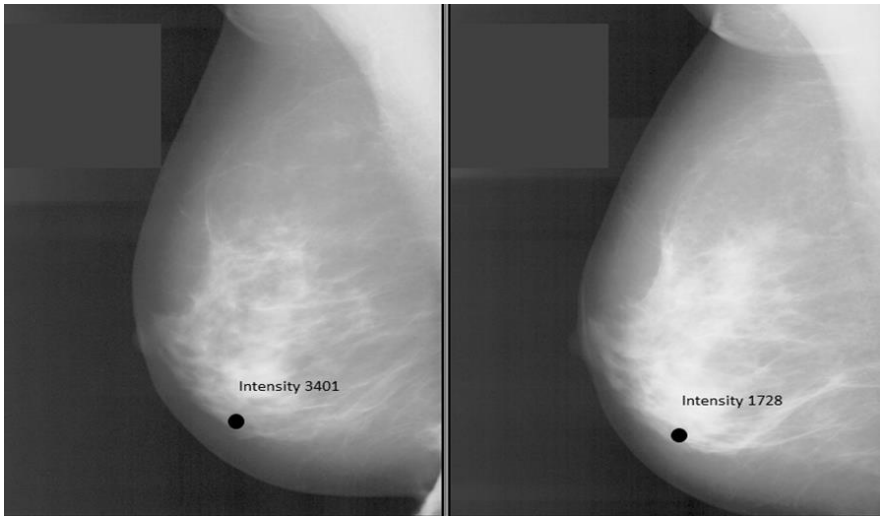

Figure 2.1: Difference in the appearance of mammograms of the same breast, taken on the same day, with slightly different imaging parameters. The point here is to show intensity values as well as tissue density of the two mammograms appears very different.

The need for reproducible breast density measurements (which, as we noted above, intensity based measures are not) is evident from the fact that its parenchymal patterns are subject to change over time due to a number of factors. The most obvious of these changes is the normal physiology of the breast that is caused by the premenopause and menopause. During menstrual periods cyclic changes in a mature breast causes increased cell proliferation of estrogen and the effect is boosted by progesterone. The volume of the breast increases due to enlargement of individual cells and cell proliferation. Lack of estrogen supply during the period of menstrual bleeding cause cell death, which changes the water content and volume inside breast. This results in the breast having varying density during different times of the year and generally over the course of age [25]. Therefore, a quantitative estimation of breast

density which is independent of imaging conditions is required, not only to assess the risk of developing cancer but also to help in the diagnosis and prognosis of the disease.

2. 2. Breast Density and Risk of Breast Cancer

The relationship between breast density and the risk of developing breast cancer was first investigated by Wolfe [26], [27]. Although Wolfe's quantitative assessment has remained popular, other methods were also developed that showed a positive association between breast density and developing of breast cancer [28]–[40].

However, researchers who followed Wolfe either did not confirm the relationship between breast density and the risk of developing breast cancer or for quite some time underestimated its importance. Some earlier studies cast doubt upon the usefulness of breast quantification [41]–[43]. This was supported by some cross-sectional studies [44] that showed a weak association or no association between breast cancer risk and Wolfe's criteria. The inconsistencies in the application of Wolfe's criteria added to this, which determined that the Wolfe's method is barely reproducible. On the other hand, investigators of case-control and cohort studies [45], [46] have found this association positive, however, not as high as reported by Wolfe.

Later, the analysis [47]–[49] of popular breast cancer risk assessment models [50], [51] determined that breast density is strongly associated with the risk of developing breast cancer. Breast density is currently considered to be the most important risk factor to be monitored, and is supported by the relationship between the biological basis of breast cancer and increased breast density [52]–[55]. As mammographic density characterizes the composition of breast as fat, epithelial tissue and stroma, and is associated with the risk of developing

histological abnormalities that can lead to breast cancer [37], [56]–[58] breast density by itself does not signify these abnormalities [59], [60].

Besides breast density, other high risk factors include age [61] and BRCA gene carrier status [62], [63] and adult birth weight and height [37], [64], [65]. BRCA status is currently considered to be prominent among all others, yet it is responsible for at most 5% of all breast cancers [62], [63], which suggests again that breast density is the most important risk factor.

2. 3. Breast Density Qualitative Assessment

The most popular breast density assessment models are Wolfe, BI-RADS and six category classification (SCC) methods, which are explained here. Other attempts included the categorization of a breast based on visual inspection of the breast tissue in a mammogram [31], [35], [66], [67]. Brisson et al [28] and Vanchon et.al [68] proposed nine and twenty tiers classification schemes respectively to quantitatively categorise breast.

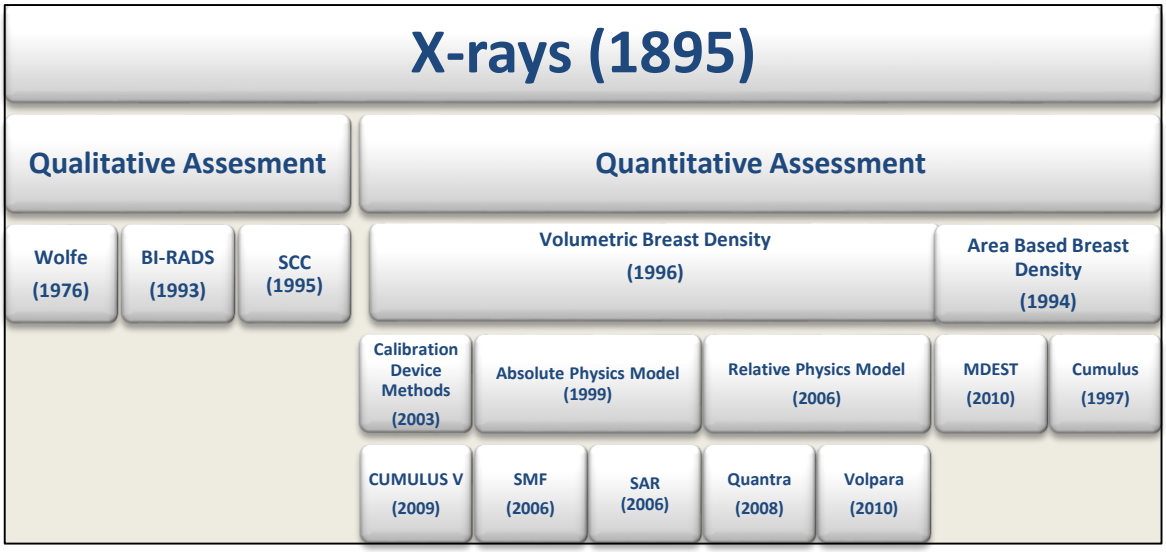

Figure 2.2: Popular breast density assessment methods. Refer to the text for abbreviations.

2. 3. 1. Wolfe's Classification Model

Wolfe studied the patterns of breast tissue observed in mammograms and their association with breast cancer. To assess the risk of developing breast cancer, he classified mammograms into four categories based on its composition in terms of fat, epithelial tissues, and prominent ducts. Fat is a radiologically transparent substance and appears dark in a mammogram. Epithelial tissues and prominent ducts appear bright since they are radiologically dense. The following are the four categories proposed by Wolfe:

N1: This is the lowest risk category in which a breast is almost entirely fat, radiologically lucent, with no prominent ducts and a few fibrous tissues. The breast appearance may vary with the subject's age but overall it will be an island of fat, with some dense tissues for younger women.

P1: This is a low risk category in which a breast is made of fat with a few predominant ducts making up to a quarter of the breast volume, typically visible in the sub-areoral area of upper-axillary anterior portion of the breast. Ducts are chord-like beaded structures extending to a heterogeneous region.

P2: This is a high risk category that involves a dense pattern of ducts in a nodular form that forms more than a quarter and up to half of the breast volume. The breast parenchymal cone appears very dense and the chords of ducts are found in most the breast.

DY: This is the highest risk parenchymal pattern and represents a very dense breast. The epithelial and connective tissues are very dense, comprising density greater than fat. The breast appears almost homogeneous because of its high density, so that prominent duct structures are very difficult to locate.

2. 3. 2. BI-RADS Classification Model

In 1993, the Breast Imaging Reporting and Data System (BI-RADS) was introduced to assess a mammogram and recommended risk categories as a way to regulate mammography reporting [69], [70]. BI-RADS was developed as an outcome of a collaborative effort by the American College of Radiology, National Cancer Institute, Centres for Disease Control and Prevention, Food and Drug Administration, the American Medical Association, the American College of Surgeons and the college of American Pathologists. Its aim was not to quantify breast density but to report the decline in the sensitivity of mammography with increasing breast density of a patient. It also comprises four classes:

BI-RADS – I: The breast is entirely fat (<25% dense)

BI-RADS – II: It has scattered fibroglandular densities (25-50% dense)

BI-RADS – III: The breast is heterogeneously dense (50-75% dense)

BI-RADS – IV: The breast tissue is extremely dense (>75% dense)

BI-RADS III and IV could result in obscuring a lesion on mammography. One of the major differences between BI-RADS and Wolfe's classifications is that in the former, the density percentage of breast parenchyma in each class is slightly greater than that in the latter, which consequently moves towards balancing the number of mammographic cases in P1 and P2. For example, a highly dense mammogram of class DY as per Wolf's classification may fit in BI-RADS III.

2. 3. 3. Six Category Classification

Six category classification (SCC) was introduced by Boyd et al [35], the inter-reader reliability estimation and interclass correlation was found high and with agreement with the visual assessment. SCC classification is subjective towards fractional density categories, that are: >10%, <10%, 10-25%, 25-50%, 50-75% and >75%.

2. 4. Breast Density Quantitative Assessment

The association between the breast parenchymal volumetric density by quantified estimation and the risk of developing cancer has been investigated in a few case controlled studies [71]–[77]. The Wolfe and BI-RADS classification models provide the basis for quantitative appraisal of the automatic breast density classification methods. These reporting standards are widely used, but are very subjective and a number of studies have shown that they are not repeatable. Various cohort studies exist in the literature that have attempted to quantify parenchymal breast density quantitatively [6, 8, 26-33]. However, all the presented methods have limitations. Boyd et al [35] presented a computer based interactive thresholding method that finds the percentage of segmented breast tissue relative to the segmented breast area. The method was semi-automatic and asks the user to enter an estimated threshold value to segment breast parenchyma. Petroudi et al [78] normalized the breast mammogram using Standard Mammographic Form (SMF) [79]–[81] and used the volume of adipose tissue in the breast for quantification. Texture representations of the breast have also been used for quantification. For example, Byng et at attempted to analyse the breast automatically using fractal dimension and skewness [82], [83]. Miller et al classified breast using texture information by applying Laws' texture features and granulometric techniques to discriminate between fatty and dense breast types. Bovis et al also used a texture feature based model using artificial neural

networks to categorise breast classes. Others used mathematical morphology [68], density segmentation using Kittler's method [84] and variance histogram discriminant analysis of segmented regions [85]. In other model studies, Van Gils et al [40], [86] investigated whether a reduction in breast density lowers the risk of breast cancer, whereas Karssemeijer [87] developed an automated determination of breast parenchymal patterns based on a distance transform, which is applied along with segmentation between breast tissue and skin line to study the relation.

Readily available software tools such as CUMULUS [47], [88] and MDEST [89], [90] are more objective, subject to the constraint of being semi-automated; and for this reason they have limited use in routine clinical practice. This is because such area based thresholding methods require additional decision time and are subject to inter-and-intra-observer variability along with the extensive training to use the software[48], [91].

2. 5. Breast Quantification Methods

Intrinsically, the amount of tissue in a breast occupies a volume and so is most reliably given using a 3D measure, unlike the projection of this volume to 2D as in a mammogram. Volumetric measures, such as SMF, Volpara®, and use of a calibration device, estimate a 3D measurement computed from a single mammogram. We review here a number of volumetric models, along with area based percent density technique CUMULUS, that quantitatively measure breast density.

2. 5. 1. CUMULUS

Byng et al proposed CUMULUS [83], [88] which is an interactive thresholding technique applied to assess radiologically dense tissue in mammograms using image histograms. The

technique was initially evaluated on mammograms of 30 women, both right and left CC projections, resulting in a total of 60 images for examination. Though, CUMULUS is not restricted to digitized mammograms and could be used on digital mammograms and FFDM.

Method:

For an 8 bit digitized spectrum of an image ranging from i_{min} to i_{max}, where the former is zero and the latter is 255 as provided by the digitizer, a grey value i_{edge} is selected which acts as a threshold to separate the image of the breast from the background. Most mammographic machines now provide 14 to 16 bit resolution. The pixels lying in the projection are filtered under the threshold i_{edge} by using an edge detection algorithm that traces the image from the chest wall to the nipple. For x_i pixels within the breast boundary, size of the projected area of the breast is the summation over the histogram:

$$A = \sum_{i=i_{edge}}^{i_{max}} x_i \qquad (3.1)$$

Radiographically dense tissues are denoted by selecting a second threshold i_{DY}, where pixels below i_{DY} are filtered out and the tissue density is calculated as the percentage density (PD) of entire projected area of the breast, A, consisting of dense pixels.

$$PD = \frac{\left(\sum_{i=i_{DY}}^{i_{max}} x_i\right)}{A*100} \qquad (3.2)$$

i_{edge} and i_{DY} have to be estimated for each image individually.

Results

Two experienced mammographic radiologists, a clinical scientist and a less-experienced research assistant viewed the images to select the thresholds and rate them in to SCC. The interclass correlation between the radiologist was R = 0.95, whereas a naive observer was able to make consistent classification with the other observer. Both non-radiologist observers did not classify the images as per SCC; however, a high degree of correlation with the radiologists for PD assessment. It was found that differences in mammographic technique could adversely affect the contrast of the dense and fatty tissue, and consequently lead to subjective classification.

Discussion

CUMULUS is a widely used density estimation technique and has been considered as the standard for measuring breast density. It has been shown to establish a strong correlation of breast density with the breast cancer risk [92]. However, like other area based approaches, the method is highly subjective and suffers from inter-and-intra observer variability, which is not reduced by training [91], [93] and is found to be at a disadvantage compared to other methods [71], [94]–[99].

The newer version of Cumulus made use of calibration device methods [73], [100]–[106], known as Cumulus V[104], which gives a 3-D volumetric estimate of a 2D mammogram.

2. 5. 2. Standard Mammographic Form (SMF)

SMF was developed by Highnam and Brady [79]–[81] to estimate breast density from film screen mammography, and was later improved to apply to digital mammograms. It is a

standardized, quantitative representation of the breast that estimates non-fat tissue and breast density. It has been recognised to have substantial potential to be valuable in large epidemiological studies which necessitates automated data analysis of large number of x-ray films, even where no calibration data is accessible.

Method

The central hypothesis of SMF is that the most of the tissue within the breast can be regarded either as fat or as "interesting", the name implying that adipose tissue is of no clinical interest for mammography. Note that it also assumes that microcalcifications occupy only a small region and so do not significantly affect the overall brightness or density of a region. Interesting tissue comprises fibroglandular, stromal and tumour. The primary energy equation of SMF models the number of x-ray photons imparted to the film screen in the area of the intensifying screen corresponding to a pixel *(x, y)*, defining the primary fluence to the detector while ignoring scatter [107], [108] is summarized mathematically as,

$$E^{imp}(x) = \emptyset(V_t, x)A_p t_s \int_0^{E_x} N_0^{rel}(V_t, \varepsilon)G(\varepsilon)exp^{-\mu_{lucite}(\varepsilon)h_{plate}}exp^{-h\mu(\varepsilon)}d\varepsilon \quad (3.3)$$

E_x is the maximum photon energy, $\emptyset$ denotes the x-ray photon flux, V_t is the tube voltage, A_p is the pixel, t_s is the exposure time, N_0^{rel} is the relative number of incident x-ray photons at the specific energy ε, G is the screen absorption rate, G is grid transmission, $h\mu(\varepsilon)$ is the linear attenuation coefficient the location x, h_{plate} is the thickness of Lucite breast compression plate, and μ_{lucite} is the linear attenuation coefficient of Lucite. If H(cm) is the compressed thickness of breast and the distance between the compression plates, that is either given in the

DICOM header or could be estimated [64], the breast composition for fat $h_{fat}(x)$ and 'interesting' tissue $h_{int}(x)$ is given by,

$$H = h_{fat}(x) + h_{int}(x),\ where\ h_{int}(x) \leq H, h_{fat}(x) \geq 0 \qquad (3.4)$$

Breast density and the density of interesting tissue h_{int}, can be found reasonably accurately given precise breast region segmentation. h_{int} is the height of the interesting tissue in z-dimension, which represent its density.

Results

In a study [79],SMF was run over 4028 digitized film-screen mammograms taken from 6 sites throughout Scotland over a period of 14 years, from (1988-2002), digitized at 100 μm with 8 bit precision, and with and without using known calibration data. The results show that running SMF both with and without calibration data (CD) determines a strong relationship with each other and with expert assessment. The results for without CD were graded 'excellent', that is 97.7%, whilst with CD it is 99.3% accuracy. Excellent indicates that less than "5% of the pixels in the internal region of the breast (away from the breast edge) had estimated *h* values that were physically impossible, that is either greater than *H* or less than 0". For the breast thickness H, comparison between recorded and estimated breast thickness values was performed for 3515 cases. The breast thickness values with CD agrees with the recorded thickness, on the other hand, for breast thickness without CD consistently underestimates the recorded value. No association was found between SCC and Wolfe grades to SMF volume estimated without CD; as SCC and Wolfe measures area of dense tissue and not absolute volume. However, a strong positive relationship was found for both with SMF%.

Discussion

The development of SMF later included calibration parameter compensation (CPC), which suggests default values for retrospective SMF. Given an approximate transfer function and estimation of H, CPC adjusts the transfer function to cross the h-axis (tissue height in surface plot) at the point determined by the ground truth and the breast volume would be sum of h values over the image. However, SMF tends to be susceptible to calibration data errors if errors are compensated for in the breast thickness. The correlation between SCC and Wolfe to SMF is found to be very strong. Another study [80] shows large differences between the estimates of SMF and SCC, which could not be reduced below 6% for 657 patients, despite improvements in SMF based upon breast thickness. This suggests that SMF might not have similar breast cancer risk capability as compared to SCC, and volumetric methods may perform better than area based methods. One of the limitations of SMF is that the $h_{int}(x)$ values are sensitive to inaccuracies in physics data and restricted availability of comprehensive and precise calibration data.

2. 5. 3. Standard Attenuation Rate (SAR)

SAR [24], [107]–[111] is a normalized measure of tissue radiodensity traversed by the primary beam incident on each pixel of a mammogram, enabling estimation of breast density and providing a basis for digital breast tomosynthesis. It calculates the x-ray spectrum incident upon breast, the energy exiting the breast, and subtracts the estimated scattered radiation, thus removing the effects of imaging conditions under which the images are acquired. Basically, SAR matches the primary attenuation of the breast to the reference material by scaling it. The

primary component of the pixel intensity is observed when SAR scaled reference material attenuation is traversed by an identical beam to that traversing the breast.

Method

The SAR is a so-called absolute physics model that consist of three parts, (i) an image formation model; (ii) a breast tissue attenuation model; and (iii) normalization. The SAR image formation model has five components [87], which provides "the transfer functions relating observed pixel intensity in an acquired image of an underlying tissue attenuation independent of the acquisition parameters" [88]. The five components are

1. A model of the x-ray tube that provides photon energy spectrum
2. A ray tracing algorithm that calculates the ray intersection points
3. A model of the image detector that converts raw pixel intensities in the DICOM into a measure of photon energy imparted to the detector pixel.
4. A model of breast tissue attenuation
5. A model of photon scattering within the breast that calculates the scatter signal incident on each pixel of the detector

The breast tissue attenuation model gives a measure of radiodensity, by establishing a scale to quantify breast tissue in a mammographic energy range based on their x-ray attenuation characteristics. Radiodensity is the relative transparency of the passage of x-ray photons through the tissue, when compared to some suitable reference material, which is a user defined parameter. The radiodensity SAR is obtained by,

$$E_{recorded} = \sum_{\varepsilon} D_{absorbed}^{(e^{-SAR_{\mu\, ref}(\varepsilon)\, H}\, I_{incident}(\varepsilon),\ \varepsilon)} \tag{3.5}$$

$E_{recorded}$ is the energy arising from the primary photon, $D_{absorbed}$ describing the detector absorption for a photon fluence of magnitude x; ε is the photon fluence incident on the upper surface of the breast from the x-ray tube; $\mu ref\ (\varepsilon)$ is the linear attenuation coefficient of the reference material; and *H* is the thickness of the compressed breast tissue traversed. The multiplicative factor $SAR_{x,\,y}$ at each pixel is,

$$SAR_{x,y} = m_{x,y} \ln\left(\frac{D^{-1}\left(I_{x,y}\right) - scat_{x,y}}{I_{incident,\ x,y}}\right) + C_{x,y}$$

$$= m_{x,y} \ln\left(\frac{E_{recorded,\ primary,\ x,y}}{I_{incident,\ x,y}}\right) + C_{x,y} \qquad (3.6)$$

Where $scat_{x,y}$ is the scatter fluence recorded by the detector; $m_{x,y}$ and $C_{x,y}$ depend on the spatial location (*x,y*); and D is detector calibration transfer function relating a recorded pixel intensity *i*, to the total photon energy absorbed by the pixel detector from which the pixel intensity resulted. The coefficients of the linear mapping from $\ln(primary_{x,y})$ to $SAR_{x,y}$ are calculated from a number of simulated images using the image formation model.

Results

To assess quantification of radiodensity using SAR, a hypothesis test was carried out [109] comparing the original mammograms and simulated images computed using image formation models of SAR. The method was applied to BIRADS 4 breast images of a 64 year old woman, taken on GE2000D digital mammography unit. The mammograms showed a cyst in the upper lateral quadrant, along with microcalcifications and invasive ductal carcinoma directly behind the nipple. It was shown that the method finds radiodensity of the cyst equal to 1.246 and that

of invasive carcinoma 2.27, thus clearly discriminating between the two, despite the extremely dense breast. Overall, the results were very promising and referred for further evaluation on a larger dataset.

Discussion

SAR is a method to compensate for the image acquisition conditions of an x-ray mammogram by constructing a model that is of imaging parameters and is based on the attenuation features of each tissue. A major problem with the SAR model is that it is highly dependent on the type of scanner used for imaging to estimate breast density and compensating imaging conditions.

2. 5. 4. Mammographic Density Estimation (MDEST)

MDEST is a computer aided breast density estimation technique [90], which automatically calculates breast boundary using a gradient based technique. It works on a user defined threshold to divide the breast in two classes, i.e., fatty and dense tissue. Breast density is then calculated by adding the pixels in the dense regions and dividing it by the total number of pixels in the whole breast.

A comparative study [89] was carried out on the premenopausal acromegalic patients and controls, to estimate the correlation between the disease duration, GH, and IGF1 levels. There were 60 patents and 30 controls in total. The results of the MDEST was compared to the observations made by two blind evaluation radiologist who were assessing the density on BIRADS standards. It was observed that patients showed significantly increase mammographic density as compared to controls; however, the agreement between MDEST and radiologists was termed excellent (k=0.63 and k=0.85). The major limitation of the method was its dependence upon the user defined threshold.

2. 5. 5. Volpara®

Volpara® is a so-called relative physics model and is a commercially available software product that has been recently selected for use in the European Union (EU) collaborative Adapting Breast Cancer Screening Strategy Using Personalised Risk Estimation (ASSURE) research project. It is fundamentally a combination of SMF and volumetric breast density estimation model given in [112] by Van Engeland et al. The latter method maps dense tissue by using a physical model of image acquisition based on the assumption that the breast is either composed of fat or parenchyma (dense tissue). The Volpara® model substantially reduces the dependence of breast quantification on imaging physics data. The fundamental assumption in this method is that the observed pixel image intensity in a mammogram has a linear relationship to the energy imparted to the x-ray detector.

Method

Volpara® finds the linear attenuation coefficients μ for fat and dense tissue at a specific filter, tube voltage and recorded breast thickness, area of the breast that is entirely fat P_{fat} and defines it as a reference intensity value to measure the thickness of dense tissue h_d at each pixel (x, y). The thickness of the dense tissue is given by

$$h_d\,(x,y) = \frac{\ln(\frac{P(x,y)}{P_{fat}})}{\mu_{fat} - \mu_{dense}} \qquad (3.7)$$

It uses phase congruency [113] and an approach to find the uncompressed breast edge [112] as well as relative breast edge [80], that helps to locate an accurate breast edge and calculate P_{fat}. The method is robust to errors in detector gain, multiplicative variations and exposure time as these parameters cancel out. To deal with different tissue types, the scatter removal

process works in a relative manner [80]. In the older version of the method, a fixed compression plate slant estimation is used that works for most imaging scanners that have parallel compression plates, however, in more recent versions it does not rely on the DICOM header and accommodates almost all non-parallel compression plate imaging systems.

The breast volume is the product of recorded breast thickness and breast area, whereas their ratio gives the breast density. The volume of the dense tissue is the summation of all $h_d\ (x, y)$ over the image.

Results

To demonstrate evaluation of absolute volumetric breast density and reproducibility of results [114], 5 image phantoms with different imaging combinations from the University of Toronto were used to validate breast density, along with conversions of 2,217 GE mammograms taken from Nijmegen, Oslo, and the University of Virginia for study. The error between the actual and estimated densities was less than 1.11%. Volpara® was assessed for clinical practice using different x-ray detectors, adding 20% noise in each image which usually do not exceed 10% in practice, and found the resulting estimates of breast density to be "remarkably accurate" [115]. As regards its evaluation against BI-RADS, it shows high correlation between the two. While comparing results from GE and Hologic scanners for 84 women, who were imaged over a period of one year on alternative scanners, the correlation was 0.91. Results from a clinical trial at the University of Utrecht Medical centre estimated MRI volumetric density of mammograms of 44 women, showed the correlation of 0.93 with the Volpara® results. In another study, 5000 women were imaged post-menopause to note changes in breast density over time and Volpara® results show the expected that reduction in

breast density with age. From the experiments on a population of 15000 women database obtained from the University of Toronto; the Volpara® study agrees with the Kopans' work [98] to estimate how many women at each age group should have which BI-RADS classification.

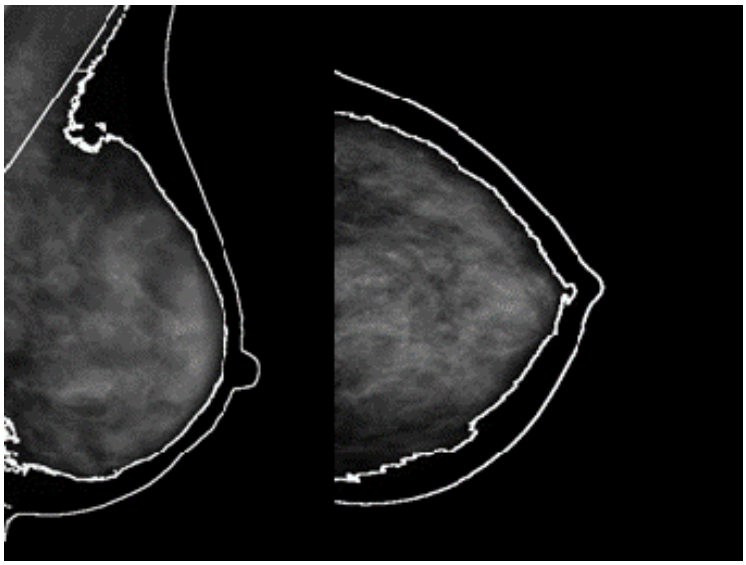

Figure 2.3: The breast edge in a dense breast found by Volpara® [114]

Discussion

Volpara® uses a relative physics model, which has now an established potential for a range of clinical work, including temporal comparison of mammograms. It works well for all commercially available x-ray scanners and the density measures are considered to be highly reliable.

2. 5. 6. Quantra

Quantra is a fully automatic system developed by Hologic Ltd. to generate density maps. It is FDA approved (2008) commercially available software, inspired from [99], it is considered to

be a rival of Volpara® . It calculates the total volume of the breast by accumulating the pixel wise estimates of the thickness of fibroglandular tissue in the breast. It compensates for the non-uniformly compressed regions inside the breast by considering the entire breast outline while calculating the total breast volume [98]. Quantra is marketed as the "future of breast density quantification in the digital age" [116], "with accurate and reproducible results by its expected correlation with lifestyle and demographic data" [117], [118]

Results

Digital mammograms from GE DS FFDM system, of 71 asymptotic women of age range 35-75 were obtained for a comparative study and were processed by Quantra and Cumulus (V4) [98]. The mean breast density obtained by two methods were compared using student's t-test to determine the relationship between the density measures from left and right breast. A correlation ($r = 0.79$, $p<0.001$) was found for Quantra volumetric density as compared to Cumulus percentage density, and the volumetric density estimate for the Quantra was lower than that of Cumulus i.e. 21.94% and 37.97% respectively.

From the results of linear and non-linear regression to observe the relationship between Quantra and Cumulus measures, a statistically significant association ($p<0.001$) was found, indicating a stronger second degree polynomial fit ($R2 = 0.70$). Figure 2.4 summarizes the results.

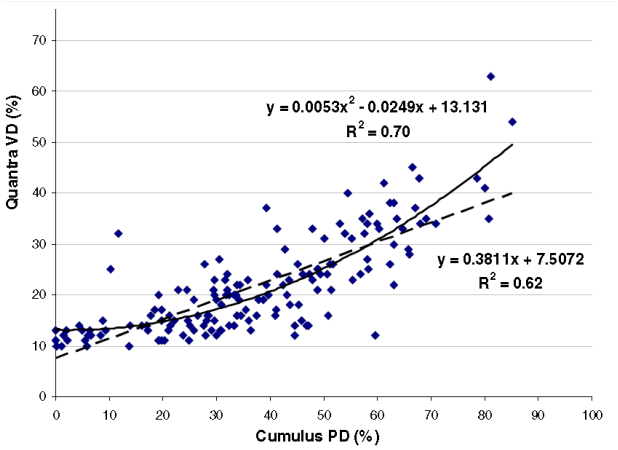

Figure 2.4: Linear and non-linear regression fits between the Quantra^{TM} volumetric (VD%) breast density measures and the Cumulus area-based percent density (PD%) [98]

In another study, correlation of age and HRT use with breast density was assessed by Quantra [99]. In total 683 women were invited to participate, out of which 320 (age 49-81, mean 59) were assessed for mammography. Mean density was 19.7%, while a decrease in the density with age was noted. There was a significant positive correlation (coefficient 0.07) found between HRT and breast density. To assess the accuracy of Quantra, it was compared to results generated by MRI based Fuzzy C-means technique for retrospectively analysed BI-RADS I and II population of 123 women with no breast cancer history [119]. Mixed correlation for the two measures was found, that were, total breast volume (R2 = 0.8909), fibroglandular tissue volume (R2 = 0.5015) and percent fibroglandular tissue (R2 = 0.3853). The agreement for total breast volume between the two methods was high as compared to other two findings, which may be because of the Quantra's method to estimate fat reference inside a breast. Refer to [120] for the first evaluation of breast radiological density assessment by Quantra software as compared to visual classification showing promising results and confirms previous reports [121], [122].

Discussion

Previous studies showed that Quantra outperformed the current area based breast density gold standard, Cumulus, by showing strong correlation between right and left breast indicating it can provide consistent measure of breast density. More recent studies suggests that Quantra does not correlate significantly with the risk [123].

2. 6. Conclusions

Here we studied literature on breast density assessment techniques, which indicates the importance of density maps to detect breast cancer, methods to overcome the intrinsic limitations of x-ray mammograms, and relation of breast cancer to breast density. From the literature presented above, we conclude that breast density maps help in establishing a risk profile of developing breast cancer. However, its sufficiency over mammograms in a clinical practice, especially from a computer aided diagnosis perspective, may be argued if,

i. We can get all the true positives detected that an x-ray mammogram can offer
ii. The boundaries of the regions of interest from density maps agree with the ground truth
iii. Gives a low number of false positives

Currently, there is no established standard to assess the number of false positives that x-ray mammograms produce, since most of the systems, including ours, are dependent on the user defined threshold, mammographic density of mammograms used, size of dataset and appearance of massed in it; nevertheless, a relative comparison is drawn in this thesis with a quantitative assessment in Chapter 6.

Chapter 3

SHAPE DESCRIPTION

3. 1. Introduction

The medical industry is highly dependent on human visual perception, either directly through the eyes of the clinician or as a result of using modern imaging modalities. Medical images contain two elements that clinicians look for: the shape and appearance of regions of interest (ROI). Shape analysis of anatomical structures in medical images is a highly demanding area in image processing and biomedical engineering. Shape is the primary source of information that informs any diagnostic process and encloses a texture within it. The objective of this thesis is to develop and apply a shape analysis system that can segment and detect incremental changes between shapes. A generic model is developed that is, we contend, capable of processing imaging modalities with application specific modifications.

A shape is considered to be a single closed contour that describes a solitary entity and that has a geometrical pattern [124], that is to say whatever is left over modulo some appropriate transformation group [125]–[131]. Either shape matching is performed by using the intrinsic statistical properties or by anatomical modelling and corresponding the boundary points to estimate a matching cost, which is a common practice in shape retrieval applications [132], [133]. Mathematically, shapes are described in the form of descriptors that are ideally invariant to affine transformations of scale, rotation, translation and sometimes reflection. Such descriptors are applied at several scales, in order to see various anatomical structures at varying levels of observation. We have used circular Integral Invariants to describe shapes.

This creates a scale space in which the Integral Invariants define features for the shape at different levels. Our application of shape analysis is focused on mammograms.

3. 2. Shape Description

Most medical imaging applications that aim to find abnormalities are based on assessing to what extent regions of interest (ROI) in images being compared are similar or different. ROIs can be represented as objects or shapes and, as such, require a mathematical representation to describe and process them: this is also known as shape encoding. Shape description depends upon the specific application. A detailed review of shape representation and description techniques along with their categorical classification is given in [130], [131]. Figure 3.1 gives a categorical list of methods for shape description.

3. 2. 1. Structural Description of Shapes

There are various contour based methods in the literature to describe the structures of shapes. Duci et al. [127] reported a novel approach to present closed planar contours that possess a linear signature embedded as a subset of harmonic functions of which the original contour is a zero level-set. However, it cannot be considered as a general shape analysis tool since it assumes that the two shapes are already registered. Sharon and Mumford [128] presented a similar study based on the assumption that a 2D shape is` a smooth and simple closed contour. They generate a series of conformal maps, starting from mapping the object to a unit circle in the complex plane, then from the boundary of the object to the exterior of the circle and the final boundary is the diffeomorphism from the unit circle to itself. They call this the finger print of the shape. B-Splines are widely used for shape representation and curve matching [134]–[139]. For example, Wang et al. used B-Splines for smoothing and construction of a curvature scale space (CSS) image. However, this method depends on the estimation of

control points which is generally difficult in complex occluded shapes. It deals with a whole curve as a single entity rather than resampled points on that curve and evaluates its accuracy based on affine transformations. Chain codes have also been used for contour based shape representation [140], [141], though they are not considered reliable for shape matching, mainly because they suffer from discretization errors with respect to rotation and scale. This can be overcome to a large extent by means of computation of multi-resolution structures at pixel levels [142]. Typically, in shape matching applications, curvature functions of the contour are used to encode the boundary of an object [143], [144]. This differential representation is considered to be one of the most prominent because it represents an object in a well investigated mathematical framework [145], [146]. The evaluation of curvature scale space as a shape descriptor for shape based image retrieval is given in [131]. One of the shortcomings of differential invariants is that they are based on derivatives which are sensitive to noise and small perturbations. In contrast to this, Manay et al. [147] used Integral Invariants to describe shapes with similar invariant properties as their differential counterparts. It is used for shape reconstruction [148] and has been found to be more robust to noise [147], [149], [150]. Sato and Cipolla [151], [152] showed that Integral Invariants are better than differential invariants for their lower noise sensitivity. They can deal with occlusions with suitable parameterization, and are clearly distinguishable at small scales. Most importantly, they guarantee a unique identification of shapes for correspondence. However, the theory of Integral Invariants has not been as thoroughly investigated as that of differential invariants. In particular, one of the challenges in shape description is the uniqueness of encoding or of shape signature. There must be a one-to-one correspondence between a shape and its signature. Recently, it has been proved that circular Integral Invariants give a unique representation for

each shape [153], as do conic Integral Invariants, though these have limited use [148]. Integral Invariants may be viewed as a structural approach since they represent a shape in terms of boundary primitives. An advantage of a structural invariant approach is the capability to handle occlusions and possibility of partial matching in shapes. These are of considerable importance in medical imaging.

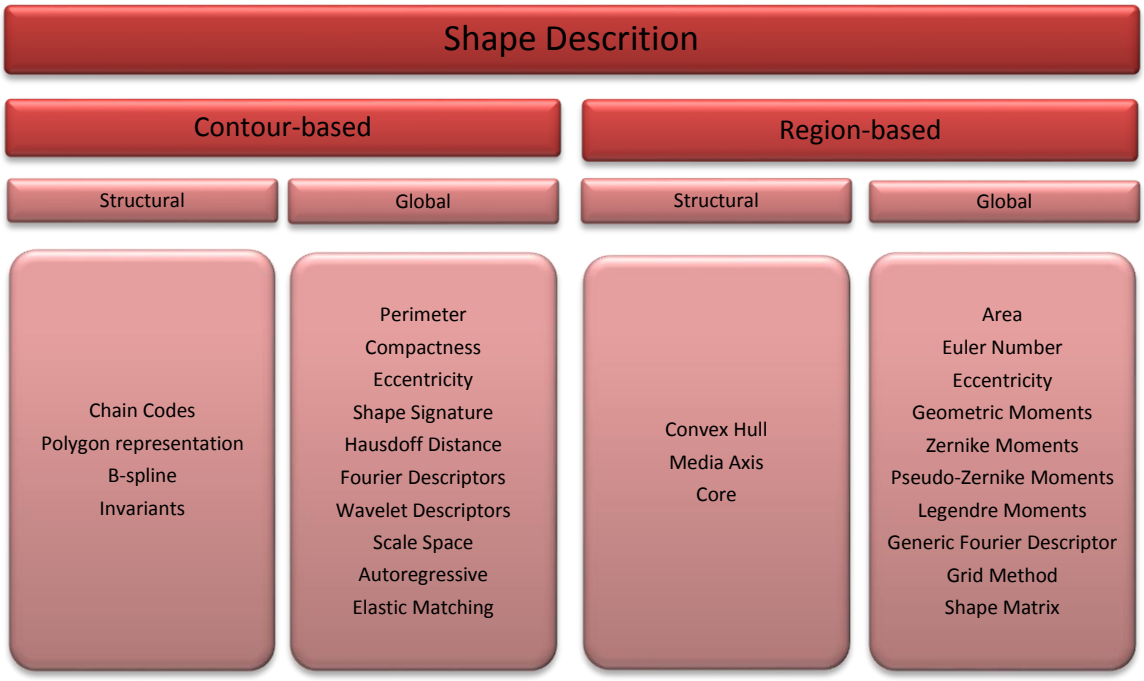

Figure 3.1: List of shape analysis method and their classification (mostly described in [130]).

3. 2. 2. Shape Invariants

Usually, invariants are properties that remain unchanged under an appropriate class of transformations (such as similarity transformations) as described in [154]. Transformations collectively form a group, such as the projective groups used widely in computer vision, because they can be composed and inverted. Such groups provide mathematical tools (group actions) for generating invariants that are applied to a range of applications [155]–[164] and

are considered to be the basis of invariant theory [131], [165]. Invariants are described by the number of features that define their order.

A broad review of different type of invariants used for shape description for the purposes of matching is given in [155]. The four most common type of invariants are:

(1) **Algebraic** invariants [154], [166]–[168] such as Eigenvalues, trace and determinant. Algebraic invariants additionally require correspondence of distinguished points to establish matching of two shapes.

(2) **Geometric** invariants [155], [169] such as distance transforms, measurement ratios, and invariants computed from a combination of coplanar points or planes [167], [168], [170]–[176]

(3) **Differential** invariants that are essentially invariant to Lie group actions, such as torsion, Gaussian measures and curvature [146], [160], [177]–[183]. Differential invariants do not require correspondence of image features; however, they are based on higher order derivatives that make them sensitive to noise.

(4) **Integral Invariants** such as semi-local affine [152], integral moments [184], circular [147] and conic invariants [185].

Note that many invariants are derived from pure geometric transformations; but this may not be appropriate for many real world problems, particularly those of most relevance to this thesis. Also, almost all invariants of types (1-3) are sensitive to boundary noise. However, Integral Invariants are comparatively robust to noise. Circular Integral Invariants are similar to the SUSAN feature detector [186] which has been used in a range applications [187]–[193] and are reproduced with various enhancements [193]–[196]. SUSAN extracts image features

by using a nonlinear circular mask that compares every pixel within that mask to the central pixel called the nucleus. Every pixel is assigned a feature value that is associated with the area of similar brightness called the USAN, and to the intensity of the nucleus, thus associating it with a local image region. It not only describes shapes and reduces noise but also performs segmentation by detecting edges and corners. One of the major limitations of SUSAN method for our application is that it assumes that the pixels which belong to a circular region are homogeneous (i.e. have relatively uniform brightness), which is not the case in mammograms, which are piecewise homogenous [196]. The SUSAN method results in poor localization for indistinct regions, which mammographic regions tend to be. One major issue with invariants when they are used for shape matching is that they have to be formulated as the intrinsically NP-complete problem [197] of finding the relationship between parts of shapes and of establishing a one-to-one correspondence for producing a matching cost. This reduces the problem to search for an acceptable rather than a definite solution given in a reasonable time. To deal with this problem and to partially reduce the computational cost, shape signatures have been proposed in various studies [147], [153], [166], [185], [198], [199]. However, it is difficult to conclude whether or not encoding shapes with signatures has improved results of matching than that produced by shape description using a direct invariant function.

3. 2. 3. Integral Invariants

Lawrence Zalcman [200] formulated and described Integral Invariants as *the subject that deals with determining properties of geometric objects from information concerning its sections by lower dimensional manifolds and integrals over those manifolds*. It is sometimes referred to as stereology or stereometry, and has been used in a wide range of applications,

most notably in x-ray tomography, where the aim is to determine using x-rays from various directions the size, extent, and the location of a tumour. Cramér & Wold [201] stated that circles and spheres are also geometrically natural sets that can be used as integral functions in the same way as lines and planes. In two dimensional spaces, circular and conic Integral Invariants are well-known in shape correspondence.

Fidler et al. [185] introduced Integral Invariant for inverse problems of geometry, initially for image retrieval. Let $\Omega \subset \mathbb{R}^2$ be a connected domain with a finite parameterisation; then the boundary of a shape can be parameterized by a continuous and injective curve $\gamma: S^1 \to \mathbb{R}^2$, where S^1 is the unit circle. The two dimensional Lebesgue measure is denoted by $\mathcal{L}^2$. A general definition of Integral Invariants from [185] is given below.

Let $f: \mathbb{R}_{\geq o} \times \mathbb{R}^2 \to \mathbb{R}$ such that for every $r \geq 0$ the function $f(r, x)$ is locally integrable. Furthermore, assume that for every compact set $k \subset \mathbb{R}^2$ and for $r_o \geq 0$

$$\lim_{r \to} \int_k |f(r, x) - f(r_o, x)| \, d\mathcal{L}^2(x) = 0 \tag{3.1}$$

Then define $I(\gamma): S^1 \to \mathbb{R}$ by

$$I(\gamma)(t) = \int_{R_{(\gamma(t)-\gamma^*)(\Omega-\gamma^*)}} f(\big||\gamma(t) - \gamma^*|\big|, x) \, d\mathcal{L}^2(x) \tag{3.2}$$

γ^* denotes the centre of mass or the barycentre for γ.

The function $I(\gamma)$ is called an Integral Invariants of the curve γ, and f is the kernel function of the invariant. To fix notation, we have selected the reference point as the barycentre γ^*that

guarantees that $I(\gamma)$ is invariant with respect to rigid motions. Two examples of Integral Invariants, namely circular and conic invariants, are illustrated in Figure 3.2.

The size of the integration kernel defines the level of localization in the shape description of a curve. As we increase the size of the aperture, there is less sensitivity to local perturbations.

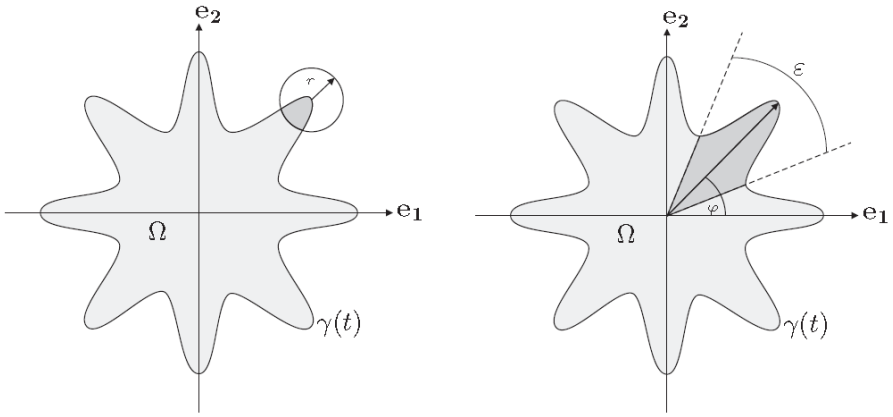

Figure 3.2: On the left circular Integral Invariants with radius r that integrates the intersection of the shape area inside the circle. On the right side, the cone or conic area integral where for each angle φ the area of intersection of conic region with the Integral Invariants size ε is calculated for each point on the curve [185].

3. 3. Circular Integral Invariants

Hong and Manay used circular Integral Invariants for shape matching. They are invariant under a group of transformations and suitable to be used when the shape is occluded. We are interested in local circular area Integral Invariants for their simplicity, robust shape description and properties of non-emergence and non-enhancement of extrema in feature space at varying scales. In various sections of this thesis circular Integral Invariants are used for noise suppression, shape matching, and region matching with multi-scale representation. Their use

closely resembles a Gaussian kernel in implementation; however, it differs substantially in its diffusion properties.

Hong [10] defines circular area Integral Invariants by considering a disc $B_r(p)$ of radius r applied to every point p of a closed contour C, the characteristic function is then given by,

$$\chi(B_r(p), C)\,(x) = \begin{cases} 1 \; if \; x\epsilon\{B_r(p) \cap \dot{C}\} \\ 0 \; otherwise \end{cases} \tag{3.3}$$

Where $\dot{C}$ is the interior of the curve C. The local integral area $I_r(C)$ of the curve C is given by the function $I_r(p)$ at every point $p \, \epsilon \, C$ with integral kernel χ as follows:

$$I_r(p) = \int_{\Omega} \chi(B_r(p), C)\,(x)dx \tag{3.4}$$

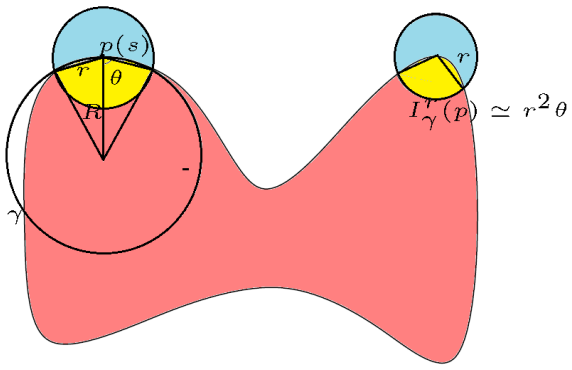

Figure 3.3: Area Integral Invariants defined in Eq-3.4

Where Ω is the domain of the curve *C*. Figure 3.3 provides an illustration of Integral Invariants as discussed in [147] and given Equation 3.4. The size of the integral kernel *r* can be varied to achieve a scale space without worrying about the amplification of noise, as in the case of differential invariants. As in fact, the results show that by increasing the range and scale of integration the kernel suppress noise and gives more robust results; however it

adversely affects the shape details. The value of the Integral Invariants for shape description is if the circle is centred not on a point along the curve but near to it, so that the circle overlaps the pink region. This enables us to relate our work to the SUSAN corner detection method, as discussed earlier.

It will be shown that Integral Invariants have strong expressive power to encode a shape and that it is closely related to representation using curvature functions. In fact, it is a weighted reciprocal of curvature. The maxima of Integral Invariants are the minima of curvature, but they have a far greater resistance to noise than the reciprocal. One of the major problems with Integral Invariants is scale selection. There is a certain ratio of the size of the shape and integration kernel that has to be maintained. The size of the kernel should be small enough to make explicit localized changes, yet large enough to read global position of shape regions in an image. As the size of the kernel is increased, its sensitivity to noise will decrease. Results show that compared to differential invariants the Integral Invariants are robust to noise and are effectual illustration of shapes for correspondence [150], [202]. Scale selection is particularly not a problem to our method alone, but it is more generally an issue fall in all scale space analysis applications, including ours.

3. 4. Relation of Integral Invariants with Curvature

As stated earlier, Integral Invariants are closely related to curvature for 2D planar shapes. Local curvature is invariant under rigid motions and has been used successfully for matching shapes [144]. A detailed mathematical comparison of projective curvature and Integral Invariants is given in [203] and with applications in [204]. Integral Invariants are considered to be better than differential invariants [151]. The representation of curves with curvature and its derivatives has been widely used, and with some encouraging results [144], [149], [182],

[203], [205]. However, the sensitivity of differential measures to small perturbations due to noise compromises its utility in shape correspondence and does not produce the desired results at increasing scale. The global behaviour of differential invariants reduces its robustness to noise. It is then necessary to smooth the results to suppress undesired residuals, however, at the cost of losing information content. Here we have used Integral Invariants to increase the image signal-to-noise (SNR). It is known that any order of differential invariants on a plane is a functions of curvature [206]. Intuitively, establishing a relation between Integral Invariants and curvature will enable the rich body of results on differential invariants to be drawn upon without worrying about computing higher order derivatives.

To illustrate the relation between Integral Invariants and curvature, Manay et al. [11] defines Integral Invariants I_D^r with $f = 1$ for a curve $C = \partial D, D \in \mathbb{R}^2$and at a point $p \epsilon C$, is given by:

$$A^r(p) = \int_{D \cap B_r^2} dx = \int_{B_r^2(p)} \chi_D(x) dx \qquad (3.5)$$

A^r is the area of the intersection $D \cap B_r^2$ of the interior of the curve C and the integration kernel $B_r^2(p)$. Then the relation between the curvature κ of C and the Integral Invariants of radius r at any point p is given by:

$$A^r = r^2 \arccos(\frac{1}{2} r\kappa) \qquad (3.6)$$

Changing r creates a notion of scale space of Integral Invariants. However, scale space is beyond the scope of this section and is discussed in detail later in Chapter 5. Circular Integral Invariants can also be obtained by the differentiation of area invariants as given in [12]. Figure

3.4 demonstrates the application of Integral Invariants to two example shapes. We will refer to circular Integral Invariants simply as Integral Invariants (II) in the rest of this thesis.

3. 5. Shape Description for Shape Matching and Correspondence

Shapes are usually matched by sequentially corresponding points on the boundaries of two shapes. This is done by identifying salient landmarks [207] using various shape descriptors, such as variational methods [208], phase information[160], [209], eccentricity [210], genetic algorithms [211] and curvature [143], [144], [205].

Shape matching depends on the type of descriptor used [126]. Transformation-based descriptors, such as Fourier components [212], which amplify certain features of a shape, usually suppress other important information such as local deformations, translation and rotation [210]. Shape matching that aims to find dense correspondences is particularly challenging in articulated shapes. Such correspondence techniques [160], [213]–[217] embed 2D or 3D shapes in a canonical domain that largely preserves geodesic distances [218]–[220], angles, and other important properties of the structure and lead to isometric deformations, such as bending [221], [222] and articulations. Other techniques involve feature analysis based on graph matching [223]–[226], which also combines the appearance of shapes. Laplace spectra [227], contour flexibility [228], shape skeletons [229], the rolling penetrate descriptor [230], and partial differential equations [231] have been explored in the past. Shape correspondence using histogram geometry for 2D shapes, which has also been extended to 3D, decomposes shapes into parts using topographic features and eventually registers them [227]. Recent evolutionary shape matching techniques, such as ant colony optimization (ACO) [232]–[234], bee colony optimization (BCO) [235]–[237] and artificial bee colony (ABC) [238] have enjoyed some limited popularity among the shape analysis community.

Comprehensive surveys of shape matching techniques with respect to correspondence can be found in [239]–[241].

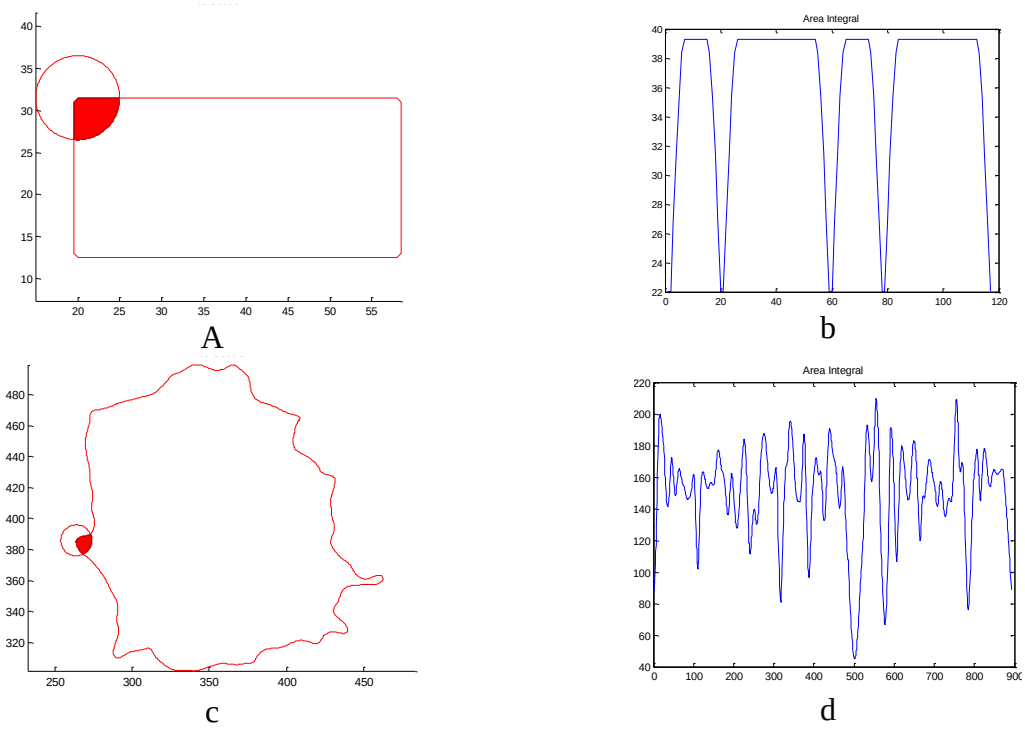

Figure 3.4: a) and c) are two examples of closed polygons with integration kernels imposed on them and highlighting the integration area in red, b) and d) are the corresponding Integral Invariants for the complete curves. c) is the outline of a segmented mass in mdb010 from the Mini-MIAS mammographic database. The II kernel moves all along the shape contour and by changing its size would create a scale space, which would be explained later in Chapter 5.

Sebastian [242] proposed a novel approach to curve correspondence based on alignment criteria with respect to a model curve. The method reduces the correspondence problem to finding an optimal path, or shortest distance, between every pair of points on those curves. The optimal correspondence problem was addressed using Dijkstra's algorithm [243], which solves the functional equation for the shortest path problem using dynamic programming. This

curve alignment method was applied to various shapes and performed well under a variety of transformations including: occlusions, articulations, affine transformations and deformations of shapes. The algorithm was tested on the retrieval of 1400 shapes belonging to 70 different categories each consisting of 20 shapes. Results were evaluated from the top 40 best matches. The percentage of correct correspondences was 78.17%, which was claimed at the time to be the best published retrieval rates when compared to curvature scale space [144], comparison using visual parts [244] and shape contexts [245] that give 75.44%, 76.45% and 76.51% respectively. However, one of the limitations of this approach is that it cannot deal with flipped shapes and, more seriously, it suffers from the initial alignment problem. Optimal alignment for each pair of shapes is found before and after flipping the shape and the one with the lowest cost is shortlisted. However, this multiplies the computational cost of the algorithm. Both the Manay [150] and Sebastian [242], [246] algorithms to find correspondences between shapes use Dynamic programming based on Dijkstra's algorithm. However, this algorithm suffers from sub-pixel accuracy and the city block distance problem in finding the shortest path to establish point-wise correspondences. To address this problem, we have used the Fast Marching Algorithm.

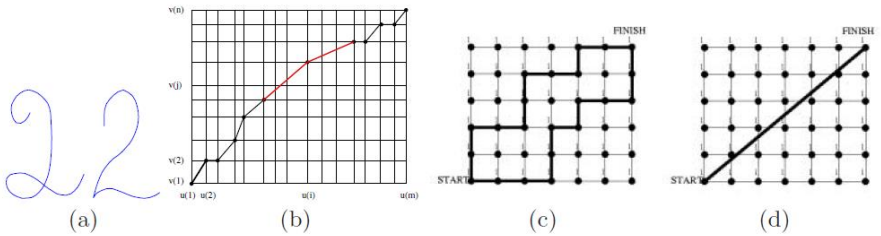

Figure 3.5: a) An example of a number *2* drawn in different ways and illustrating two curves that are to be put in correspondence. b) An example of the discrete alignment curve in (a)

given as a shortest path in a graph. c) Multiple "shortest" network paths, showing how Dynamic programming suffers from city block distance problem. d) The optimal diagonal path is the result of the Fast Marching Algorithm [247]

3. 6. Conclusions

Various shape descriptors are used in the literature for matching and corresponding shapes. Among them, differential and Integral Invariants dominate the pool for its robust performance. Since differential invariants are highly sensitive to small perturbations and boundary noise; we use Integral Invariants as our shape descriptor, which has been used in the past with promising results. Shape description is then fed to an optimizer to establish a point wise correspondence that deals it as an optimal path problem. The Fast Marching Algorithm does not suffer from sub-pixel accuracy while dealing with this issue and is selected for use in this thesis.

Chapter 4

TOPOGRAPHIC SEGMENTATION OF MAMMOGRAMS

4. 1. Introduction

Image segmentation is a well-established area in computer vision and image processing. From a mammography perspective, it is the process of detecting the whole breast or certain features within it, such as the breast, its boundary, any kind of abnormality, micro-calcifications, masses, and so on. Breast screening aims to identify Regions of Interest (RoI) that possess a certain level of abnormality and which may indicate breast cancer. There are a number of approaches presented in the literature that deal with the problem of segmentation in mammograms. After studying the strengths and weaknesses of most of these, we implemented a topographic representation of iso-contours; that is hierarchical grouping of contours.

It is generally accepted that the detection of masses is technically more difficult than that of finding micro-calcifications (for which there have been highly successful commercial systems). There are various reasons for this, including the confusion between dense breast parenchyma or the spiculated index of masses, or masses being obscured within normal breast tissue. The variety of morphologies of masses, including their shape, size and texture is huge. As a result, the number of features that could be used to detect and classify masses is enormous and this poses a huge challenge for optimal feature selection and computational cost.

In this chapter, we develop a variation to the topographic segmentation algorithm that has been reported in the literature and we use it to automatically extract regions of interest.

Experiments are carried out on mammograms from Mini-MIAS [248] and the University of South Florida (USF) [249], [250] mammographic database, as well on DICOM images made available by *mātakina technologies* NZ [114].

4. 2. Hierarchical Grouping of Iso-Contours

4. 2. 1. Iso -Intensity Contours

Iso-intensity contours, more precisely iso-photes, are closed curves of constant intensity that divide the image into regions on the basis of intensity levels and give a topographic representation of an image. Iso-contours have been used for image segmentation [251] by quantizing the intensity range into equal parts, yielding a topographic map of the mammogram. This enables one to detect the regions of interest. An image is considered to be a surface in which the intensity at each pixel represents height in three-dimensional space as presented in Figure 4.1. An ordered set of connected pixels at the same height (intensity) forms an iso-level contour.

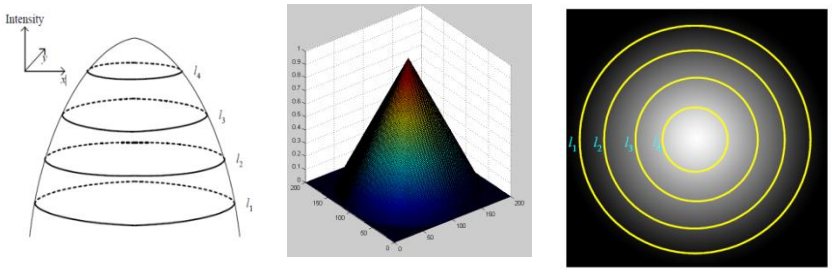

a b c

Figure 4.1: intensity slicing at various levels in a) [251], where b) shows a mesh of intensity diffusion. Iso-photes at various levels overlaid on intensity image in c)

Mudigonda et al. [252] presented an algorithm to perform segmentation of masses using hierarchical grouping of iso-intensity contours. They presented a parent-child relationship in a

family tree architecture: isolated salient regions are found to possess a dense pattern of contours surrounding them. A concentric group of contours, as seen in Figure 4.2 represent the diffusion of intensity in a dense pattern from the core of the object to the surrounding tissues.

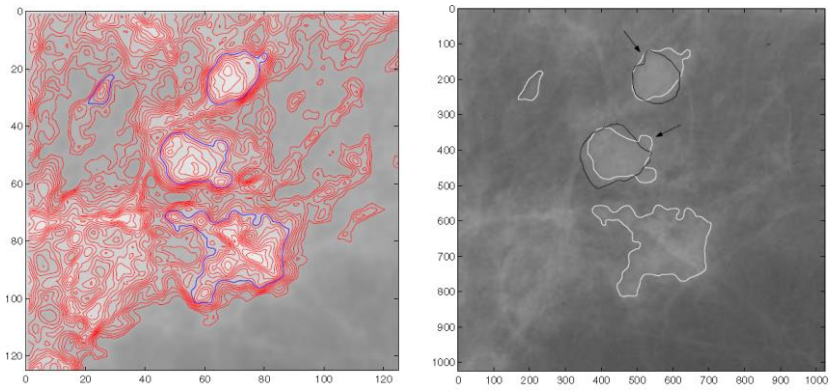

a B

Figure 4.2: In a) groups of iso-intensity contours (red) and the outermost contours in each group (blue) in low resolution image, whereas in b) the four shortlisted contours (white) and manually segmented masses (black). Segmentation results contain two false positives. (Courtesy of Mudigonda et. al. [252])

Regions with a higher family count, above a certain threshold, were selected as significant regions. A threshold of minimum family count was also used in order to discard regions which might prevent dense glandular structures from further analysis. The outermost contour for each selected region is assumed to be the boundary of a segmented region. In that study a set of 39 mammograms from the Mini-MIAS database [248] was used. Of these, in 29 cases (10 malignant and 19 benign) the regions segmented by the hierarchical grouping method agreed closely with the boundaries of masses identified manually by a radiologist. The segmentation of five cases in which there is a benign mass and one in which there is a malignant mass disagreed significantly from those delineated by the radiologist. Masses were merged with the

fatty background for the remaining 4 images that belong to the category of spiculated benign. Overall, the method worked reasonably well at segmenting low resolution malignant masses; but it had poor performance in segmenting benign masses.

One of the shortcomings of this method is that it could not deal with the mammograms correctly if the breast density profile was not established a priori. A dense fibro-glandular tissue will be selected as a concentric mass and an embedded tumour is hard to differentiate from its surroundings. A different threshold has to be selected every time a different density breast is to be segmented so the process remains heavily manual.

4. 2. 2. Inclusion Tree

Hong et al. [251] also implemented a topographic representation of iso-contour maps with a uniform distribution of contours across the intensity range. Hong's approach is similar to that developed by Mudigonda [252] as explained by Rangayyan in [21]. The object of interest has higher intensity values at the centre, and lower intensity values far from the centre. The levels of intensity for the thresholds are denoted by *l1*, *l2*, *l3* and *l4* and the quantisation represents a set of points on the image along the projection line shown in Figure 4.1a. The intensity quantisation with a three-dimensional image surface is equivalent to slicing the image surface with a series of horizontal planes of the same heights. This produces a set of two-dimensional contours on the image as shown in Figure 4.1c. Hong named the hierarchical tree of contours an *inclusion tree*. He examined the topological and geometric structure of the images using the inclusion tree and applied it to the same mammograms from the Mini-MIAS database. It is hard to compare the implementations since Hong does not provide a quantitative set of results in his thesis. However, in another study [202] he applied his segmentation algorithm to 400 images from the University of South Florida (USF) database and claimed to achieve 100%

accuracy in detecting masses with 3.8% false positives per image and 90% accuracy with 2.3 % respectively. Though the classification of images as benign or malignant is not known, the results of mass detection are very promising.

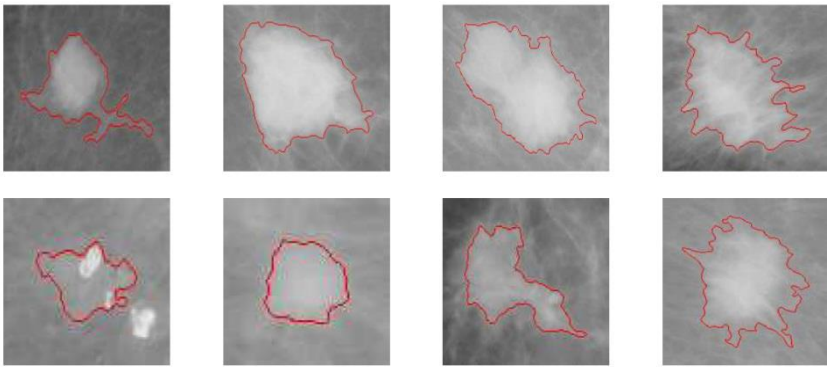

Figure 4.3: Some segmentation results from Hong's implementation of hierarchical grouping of iso-contours or inclusion tree applied on USF database

Hong claimed that his method is invariant to brightness and contrast and is robust in selecting salient regions in mammograms (see given references for further details).

4. 2. 3. A variation to Hong's Algorithm

In a variation to [251], which we will refer to as Hong's algorithm for convenience, we developed an effective way to describe regions of interest using iso-contours defined at non-uniform spacing in the intensity range so that it is skewed towards the intensities that comprise the regions of interest.

We modified Hong's method in order to evaluate its performance with respect to imaging conditions. Figure 4.4 shows that the algorithm is highly dependent upon the brightness, contrast and the dynamic range of an image, for the reason that it divides the existing intensity range into equal levels. Hence the mammograms should be pre-processed to attain a certain

level of normalization before applying any segmentation algorithm. Another point is that both [251], [252] compute and process numerous contours that are ultimately discarded while detecting breast masses. To reduce the computational cost, a mechanism is required to estimate and to filter out intensities that correspond to uninteresting regions, e.g. light fibro-glandular tissues, the breast boundary and solid annotations. The segmentation boundary of the mass in Figure 4.4d corresponds closely to the ground truth

4. 2. 4. Contrast Shedding & the Gamma Transformation

One disadvantage of dividing the intensity range into equal levels of iso-lines is that it also leads to forming contours in relatively brighter and homogeneous regions, where they may not be required. As our regions of interest are anticipated to be bright; the segmentation of transparent (dark) regions are of less importance. To address this issue and reduce the computational complexity even further we apply contrast shedding.

In this technique, the intensity levels that are not of interest are filtered out from the image in order to cluster contours around desired locations. The basic idea of this technique is inspired from the Watershed algorithm, as contrast is shed from an image to the level of preferred intensities. Figure 4.6 illustrates the contrast shedding technique applied on iso-intensity map, whereas Figure 4.7 illustrates its application to a mammogram. Alternatively, instead of taking intensities out of an image, the contrast of the image is weighted towards a desirable range of intensities. This results in a non-uniform distribution of contours by clustering them in the desired intensity range corresponding to the regions of interest. Let T be a certain transformation function such that,

$$g(x,y) = T[f(x,y)] \qquad (4.1)$$

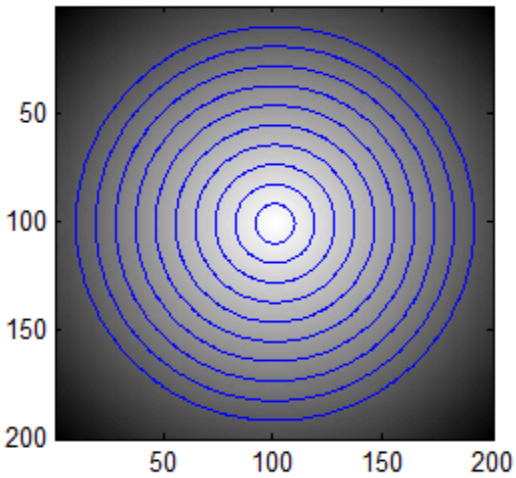

a. Iso-intensity map of an image with an intensity range from 0-255

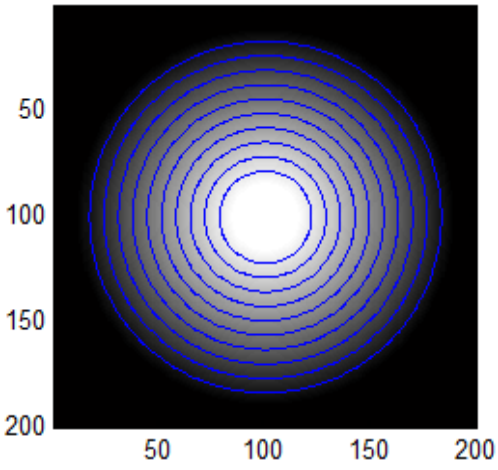

b. Iso-intensity map of an image with an intensity range from 25-235

c. Mass extracted for image with intensity range in a)

d. Mass extracted for image with intensity range in b)

Figure 4.4: As the effective intensity spectrum of the image changes, the allocation of contour to the grey-level values also changes and this affects the boundaries of the ROI as well as the contour hierarchy. Segmented mask overlaid on the original image.

If the neighbourhood size is 1x1 then the value of g at location (x, y) depends just upon the intensity of f at that point and T becomes an intensity transformation function. Consider the problem of mapping the intensity levels r_k to normalize intensity levels s_k as shown in Figure 4.5. This class of transformation is called Gamma transformation [253].

If the value of the Gamma transform is less than 1, the contrast stretch is weighted towards the higher output values. On the other hand, if Gamma is greater than 1 then the stretch is weighted towards the lower output values. A linear mapping is performed for Gamma equals to 1. This Gamma transformation is translated as to reduce the dynamic range of an image and skewing it towards the intensity of interest.

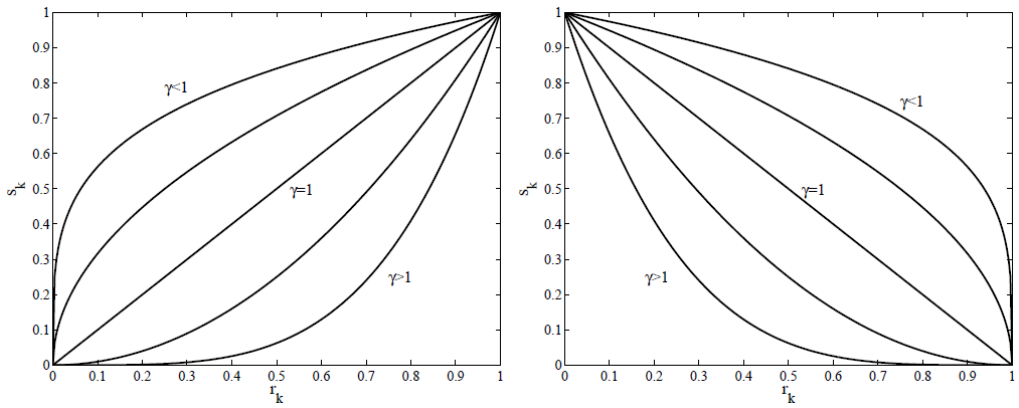

Figure 4.5: Behaviour of contrast mapping to varying Gamma [254]

Intensity map without Gamma transformation	Gamma=0.3, mapping weighted towards lower intensities	Gamma=1, mapping weighted towards higher intensities	Gamma=5, mapping weighted towards higher intensities	Gamma=10, mapping weighted towards very high intensities
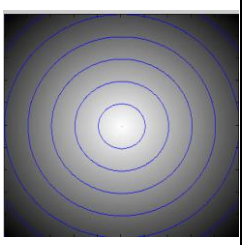 a	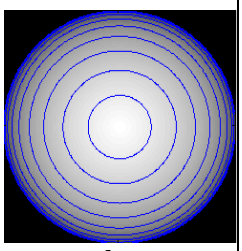 b	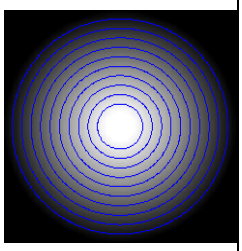 c	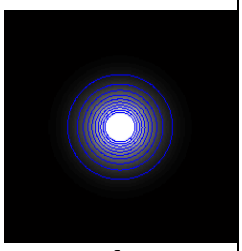 d	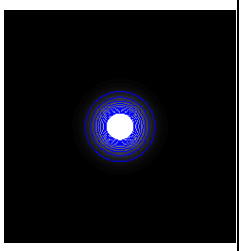 e

Figure 4.6: Effects of Gamma transformations on the iso-intensity map

Effects on original image for mapping of intensity range [0 255] and Gamma=10	Effects on original image for mapping of intensity range [153 242] and Gamma=10	Effects on original image for mapping of intensity range [178 242] and Gamma=10	Effects on original image for mapping of intensity range [216 242] and Gamma=10
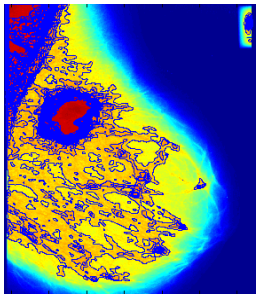	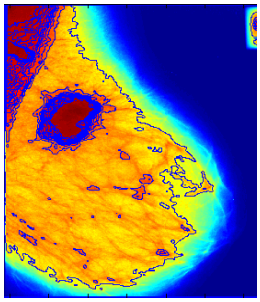	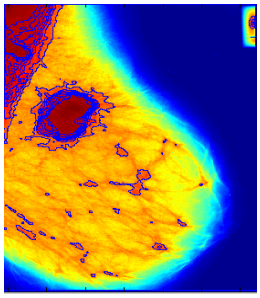	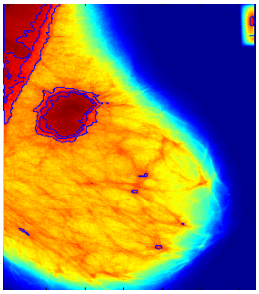
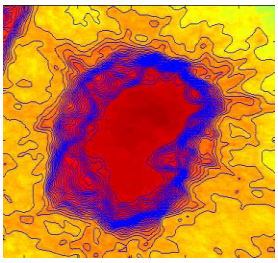	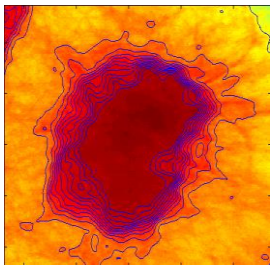	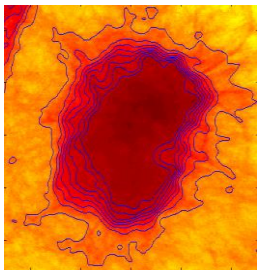	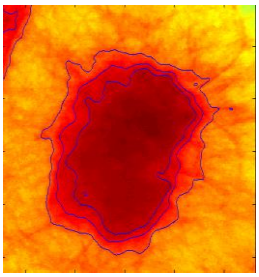

Figure 4.7: Effects of the Gamma transformation and contrast shedding on *mdb184*

The Gamma transformation may be viewed as a non-linear intensity thresholding technique; though more sophisticated methods based on brightness distribution or physics based model [80] could also be used.

As expected, the contrast shedding technique works reasonably well for segmenting well-defined and spiculated masses. An illustration of the method is given in Figures 4.8, 4.9 and 4.10, where a mass from the Mini-MIAS database has been segmented and its corresponding hierarchical tree plot is shown. The tree plot is threshold using the minimum nesting depth

(MND) criterion. The challenge in this method is to select the threshold for MND. If we reduce the threshold, it increases the number of false positives. On the other hand, a high MND count may result in missing out the ROI. Figure 4.11 shows various examples of mammograms from different categories segmented using this scheme. Therefore a threshold is set empirically with a trial and error strategy.

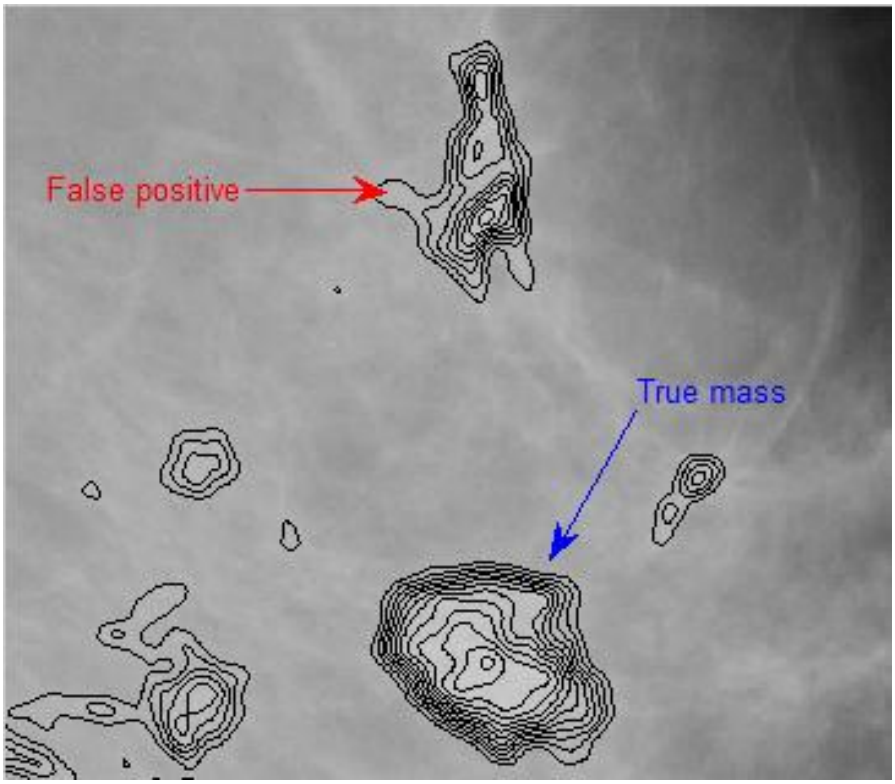

Figure 4.8: Iso-contour map of *mdb010* from the Mini-MIAS database depicting dense contours around a true mass and a false positive Salient regions detected automaticaly at the minimum nesting depth of $D \leq \frac{number\ of\ isolevels}{3}$

To detect both masses and the pectoral muscle, the effective dynamic range for contour formation has been reduced to [178 230]. This restriction may be removed to segment the breast boundary or other regions at lower intensity levels.

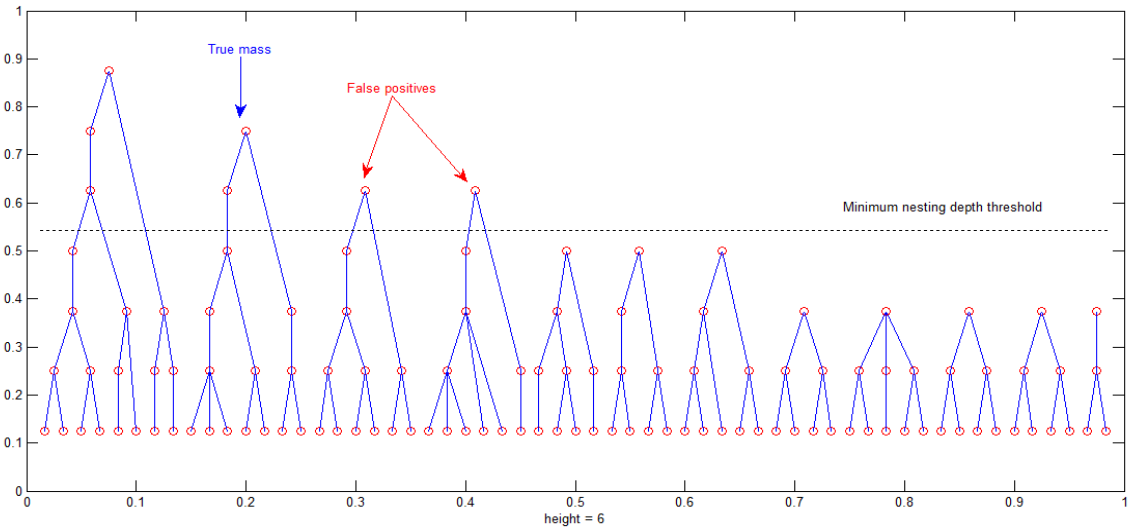

Figure 4.9: Tree plot of contours representing salient regions in *mdb010* given in Figure 4.8. Four regions are selected here; the left top represents the boundary of pectoral muscle.

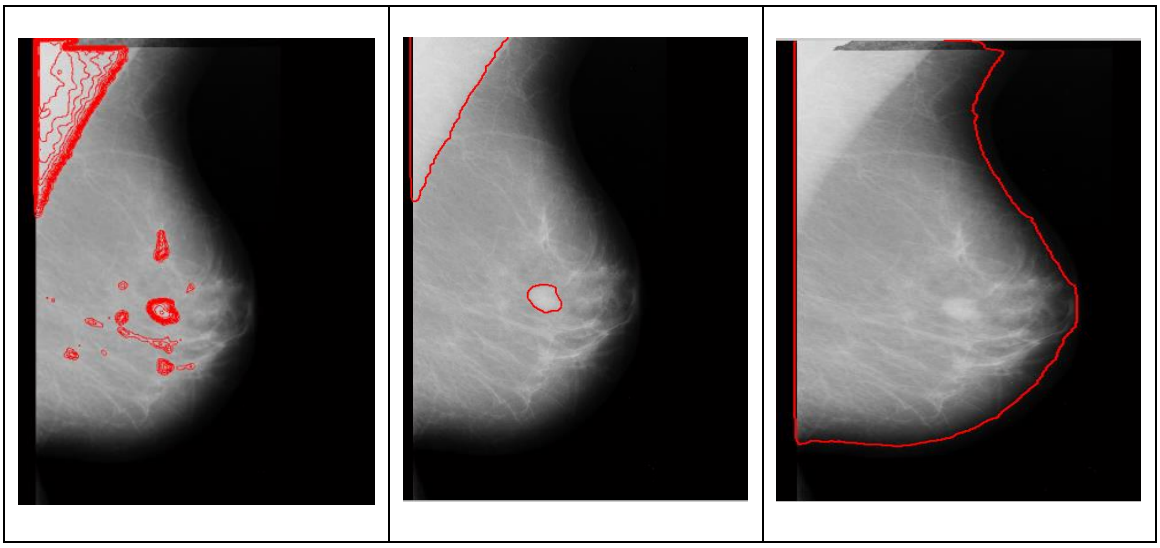

Figure 4.10: Pectoral muscle, suspected masses and the breast boundary have been segmented using the proposed method *mbd010* .

4. 3. Segmentation Examples from Mini-MIAS database

Type of abnormality	Fatty	Fatty - Glandular	Dense - Glandular
Well-defined /circumscribed masses	 *mdb005* – Benign	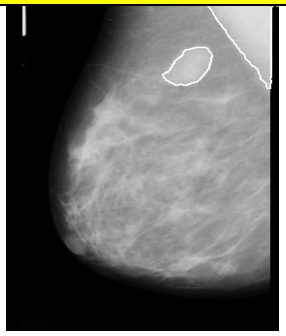 *mdb015* – Benign	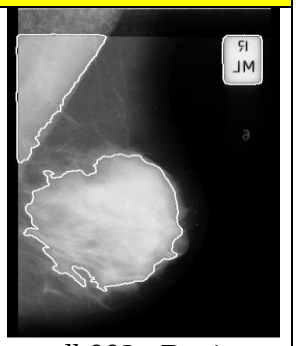 *mdb002* - Benign
	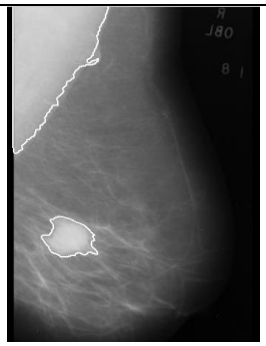 *mdb028* - Malignant	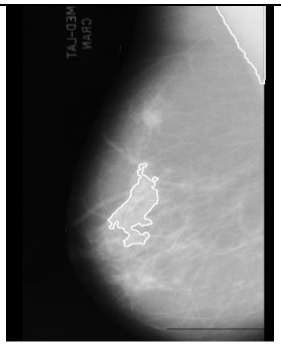 *mdb023* - Malignant	 *mdb001* - Benign
Spiculated masses	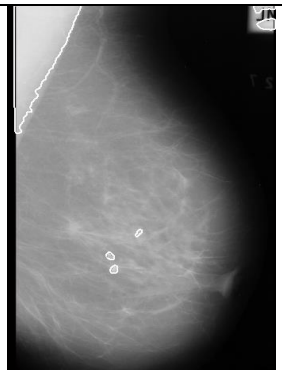 *mdb204* - Benign	 *mdb186* - Malignant	 *mdb179* – Malignant
	 *mdb184* - Malignant	 *mdb175* - Benign	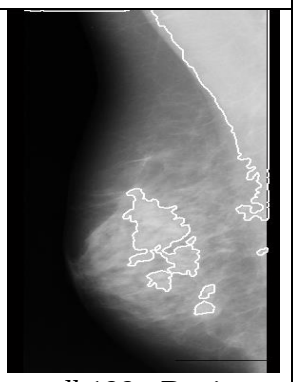 *mdb199* - Benign

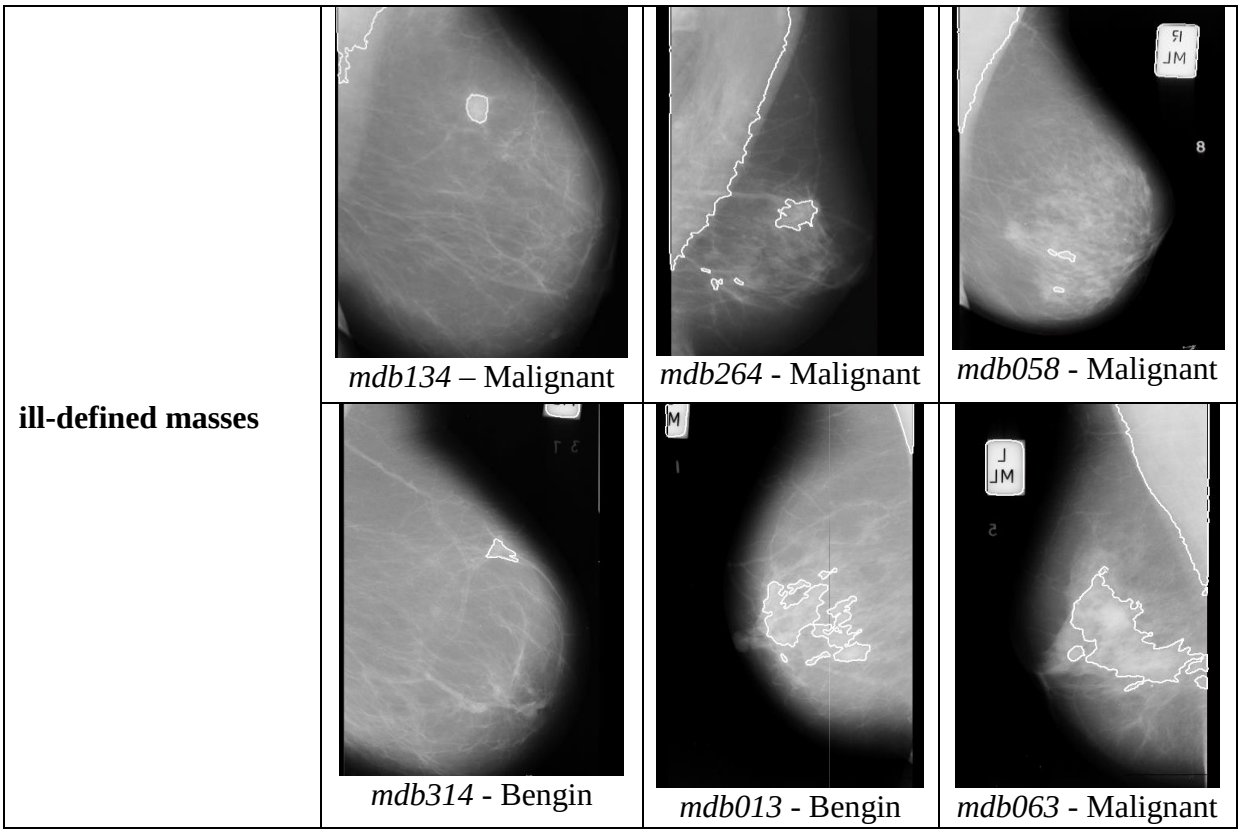

Figure 4.11: Segmentation results of masses and the pectoral muscle in mammograms from Mini-MIAS database

4. 4. Critical Evaluation of the Hierarchical Iso-level based Segmentation Algorithm

The modified segmentation method depends upon the intensity distribution and the dynamic range of the image, which is important in the case of mammograms (which are appearance images of dense subjects), and could be automated accordingly. It is based on iso-contours and is based around the topographic representation of an image, where a surface in which the intensity of each pixel represents height in a three-dimensional space. The spatial location for the formation of iso-contours on each image depends upon two major factors:

i) The dynamic range of the image; and

ii) The number of iso-contours.

Before evaluating Hong's algorithm, we give a skeletal description of it:

i) It draws a specified number of iso-contours on the intensity map of an image. An anisotropic noise removal filter is used to suppress noise and to retain smooth boundaries. This is explained below in the noise removal section.
ii) Those regions that have dense patterns of iso-contours surrounding them are considered to be salient.
iii) Note that iso-contours have an enclosure relationship, that is, contours formed at higher intensities will be enclosed by the contours formed at lower intensities. For pairs of such contours, the inner is assumed to be a child of the outer one, so all contours formed have a parent/child or sibling relation to each other. This relationship is made explicit in a representation.
iv) A minimum number of immediate nesting depth of a contour is required in order to identify a region as salient.

4. 4. 1. Assumption about the region boundaries

Our method assumes that a salient region (stroma, tissue, mass, ducts etc.) in a given mammographic image has a boundary, which is a line of connected pixels that possess a uniform constant intensity. This assumption may be valid for regions with strong high contrast background, for example the breast boundary, the pectoral muscle, or a bright mass in a fatty breast (BIRADS 1/II, which are the easy cases). However, for most of the "interesting regions" the boundary is obscured and it is difficult to differentiate it precisely from other tissues. In most cases, the "interesting" tissue in a mammogram has variable shading rather

than being uniform. This is also true for regions in temporal mammograms, which may result in significantly different boundaries and may result in the regions having unnecessary occlusions. This may also result in significantly dissimilar boundaries of the same breast region in different images. Note that this is a fundamental limitation, and hence the underlining assumption, of all contour based segmentation algorithms, including level sets.

4. 4. 2. Effective Intensity Range of an Image

The intensity histogram of an image defines the intensity distribution and the dynamic range of an image. It eventually determines the eccentric pattern and positioning of iso-contours around a region. For the underlying algorithm, it will affect the selection of the outermost contour. Though the histogram will reflect *n* levels of intensities and corresponding values for an *n*-bit image, this does not necessarily mean that a segmented shape in the darker and lighter images will have the same boundaries. This is illustrated in Figure 4.12, which depicts how the intrinsic range of intensities affects the locations where the contours are formed. Figure 4.4 shows boundary of a segmented mass in the same image with different intensity range.

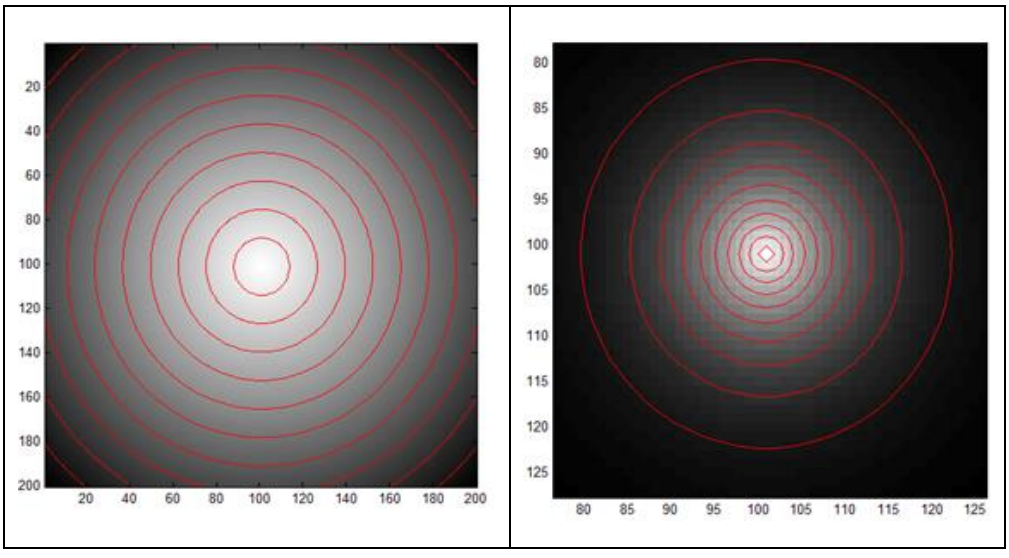

Figure 4.12: Iso intensity contour map

Though the number of iso-intensity levels is constant, the contour formation varies and ultimately will generate different boundaries. If those boundaries are to be used for shape comparison then this evidently makes the problem more difficult, if not intractable.

4. 4. 3. Issues with the Nesting depth

The Hong algorithm selects a salient region and its boundary based on the minimum nesting depth criteria as explained earlier. Higher MND works well for relatively straightforward mammograms such as fatty breasts. However, as we have seen, it is substantially more difficult in dense mammograms, which are the case of most interest. The selection of MND in Hong's algorithm is somewhat arbitrary and suffers from two major issues,

i) Depending upon the value of nesting depth, it may identify multiple base contours in a hierarchical order or enclosure relationship that fulfil the criteria, and this makes it more difficult to automatically identify the optimal boundary of an interesting region.

ii) For different MND thresholds, the algorithm may select, or entirely miss, different regions. In addition, the algorithm might fail to pick the boundary of a salient region if the immediate nesting order breaks due to noise, as nesting depth is based on immediate sequential count of contours. Figure 4.13 shows the effect of changing the value of nesting depth.

Keeping MND constant may lead to additional problems in some cases. For example, Figure 4.14 shows some examples of poor segmentation where the MND is kept constant for a temporal pairs of mammograms.

4. 4. 4. Over Smoothing and Under Smoothing

Smoothing a mammogram using a noise reduction scheme may help reduce the number of false positives and help define better boundaries. However, it may also miss a salient region if used extensively. Though we will have a closer look at Perona-Malik anisotropic diffusion filter (PM) in the next chapter, it is used here to serve this purpose. The optimal choice for the number of iterations to smooth a mammogram generally needs to vary from mammogram to mammogram. It is not completely arbitrary, however, as some empirical values for the number of iterations may work reasonably well on a range of mammograms. Nevertheless, there is no single value that works well for all mammograms. The difficult part is that results can only be evaluated qualitatively by looking at the results of segmentation following the smoothing.

It is difficult to conclude that the number of salient regions or base contours will increase or decrease by increasing or decreasing the number of iterations over a moderate range. However, in most cases, a value that is too small may result in over-segmentation and create the problems related to MND described above; too large a value may result in missing an important region or expanding the boundary of a salient region unrealistically. Figure 4.15 shows the effect of the noise removal filter on segmentation for various PM iterations on DICOM mammograms.

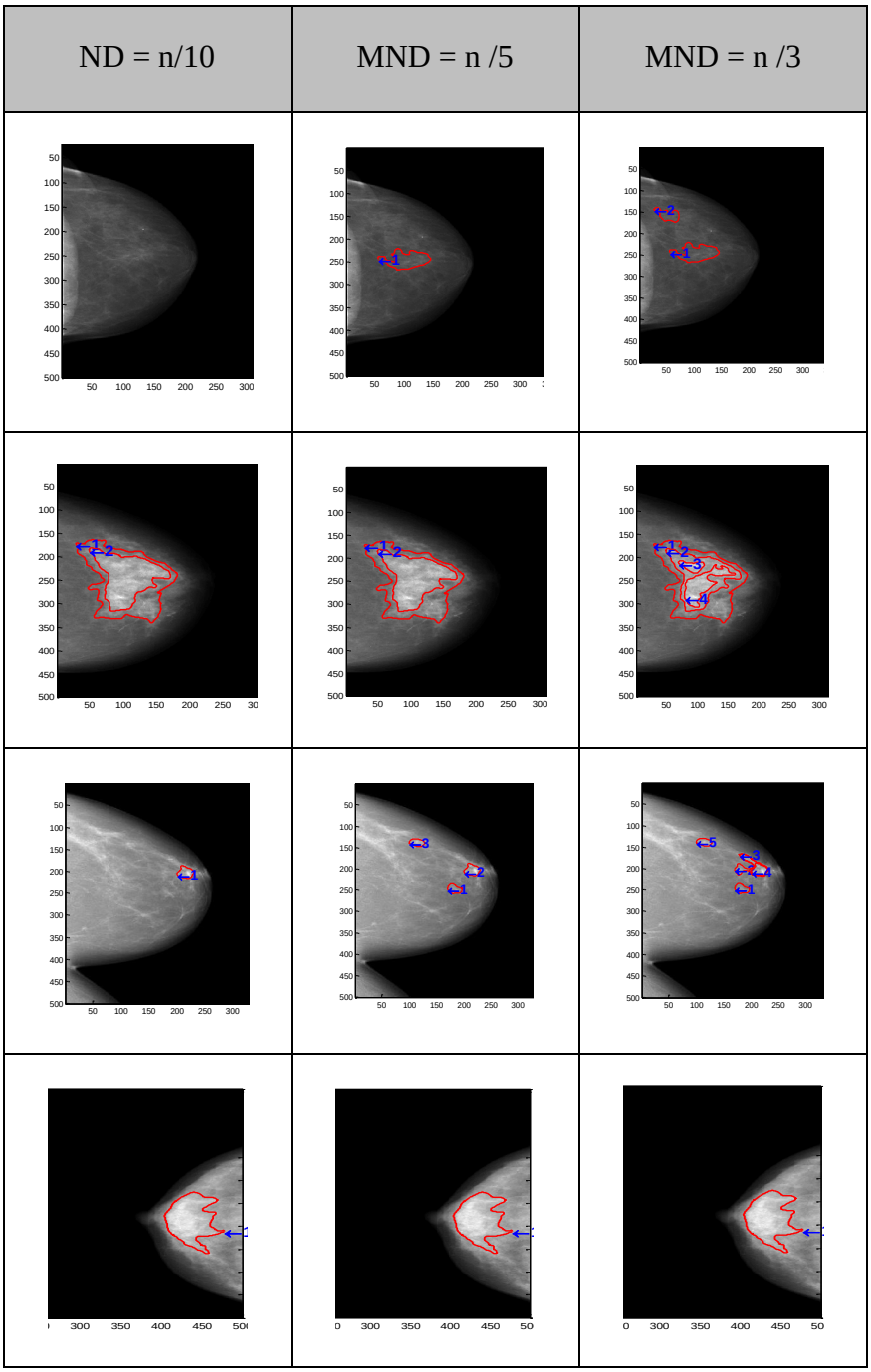

Figure 4.13: Selecting salient regions with variable MND. The resolution of iso-intensity levels is 100 and the mammograms are contrast adjusted before segmentation. *n* is the total number of iso-levels.

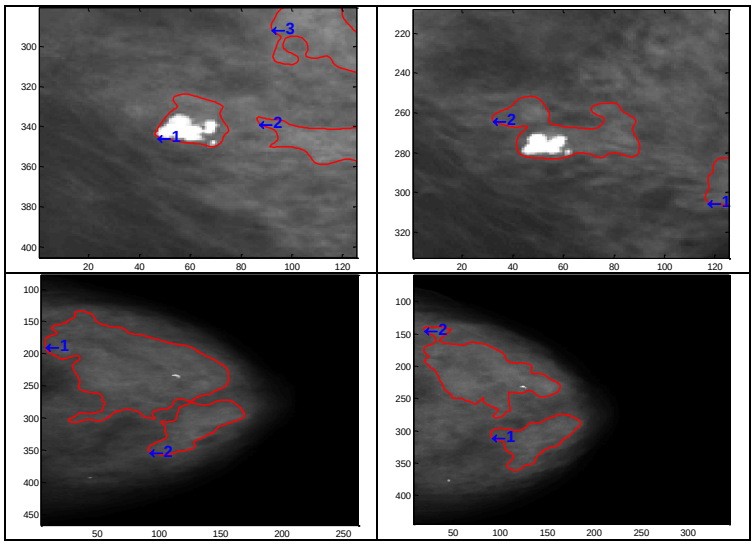

Figure 4.14: Examples of bad segmentation with constant nesting depth in temporal pairs

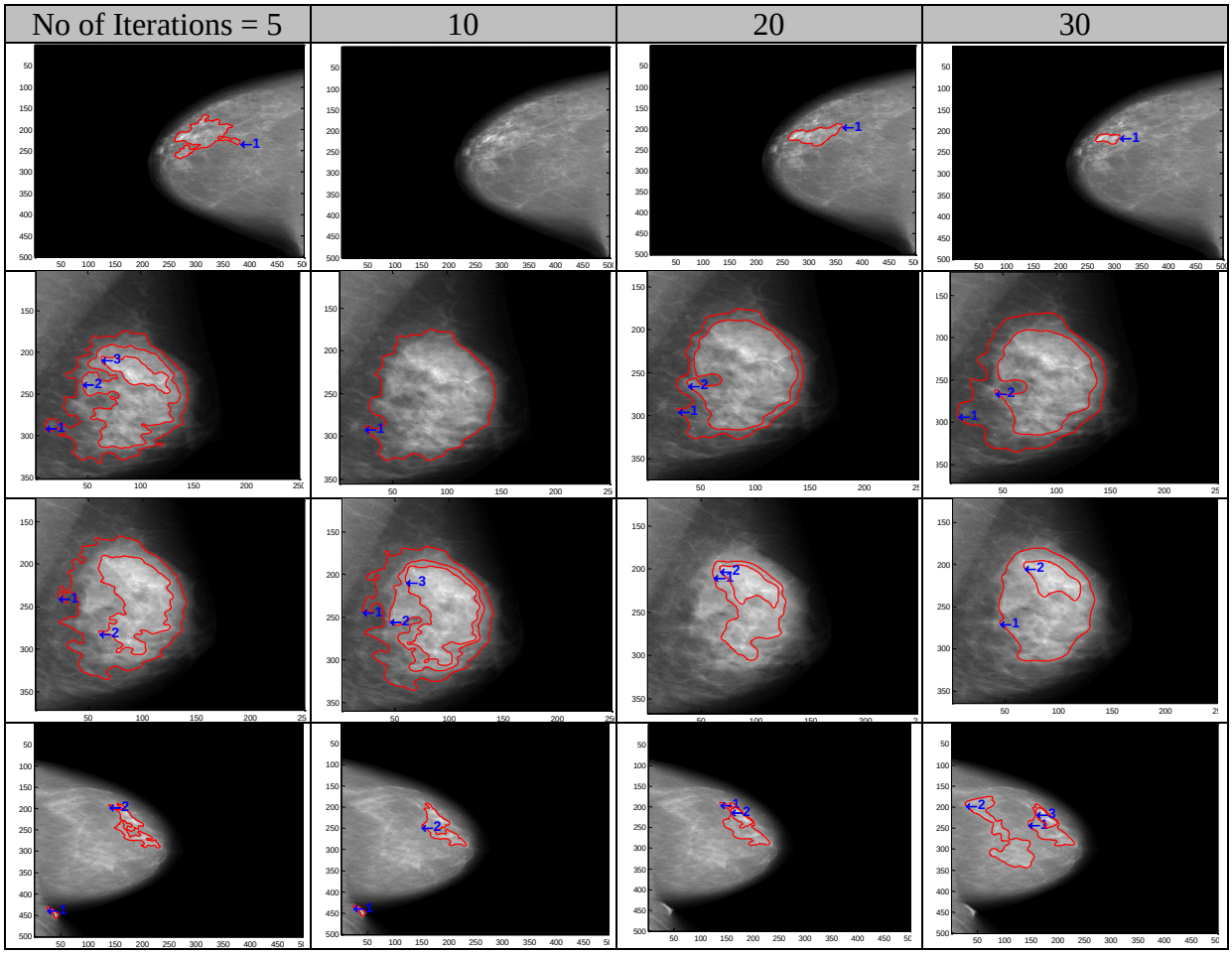

Figure 4.15: Effect of the number of anisotropic smoothing iterations on segmentation results

4. 4. 5. Pre-Processing Effects

One way to minimize the effect of brightness is to pre-process a mammogram. For this, we have applied a contrast shedding technique to reduce the effect of variability in intensity and contrast differences among temporal pairs. For example in Figure 4.16, nothing definite can be said about the effectiveness of normalization as per segmentation results. However, we decided to use it as given for example in Figure 4.17. Here we have used temporal pairs of mammograms to visually assess the selection of ROIs in different mammograms normalized to each other.

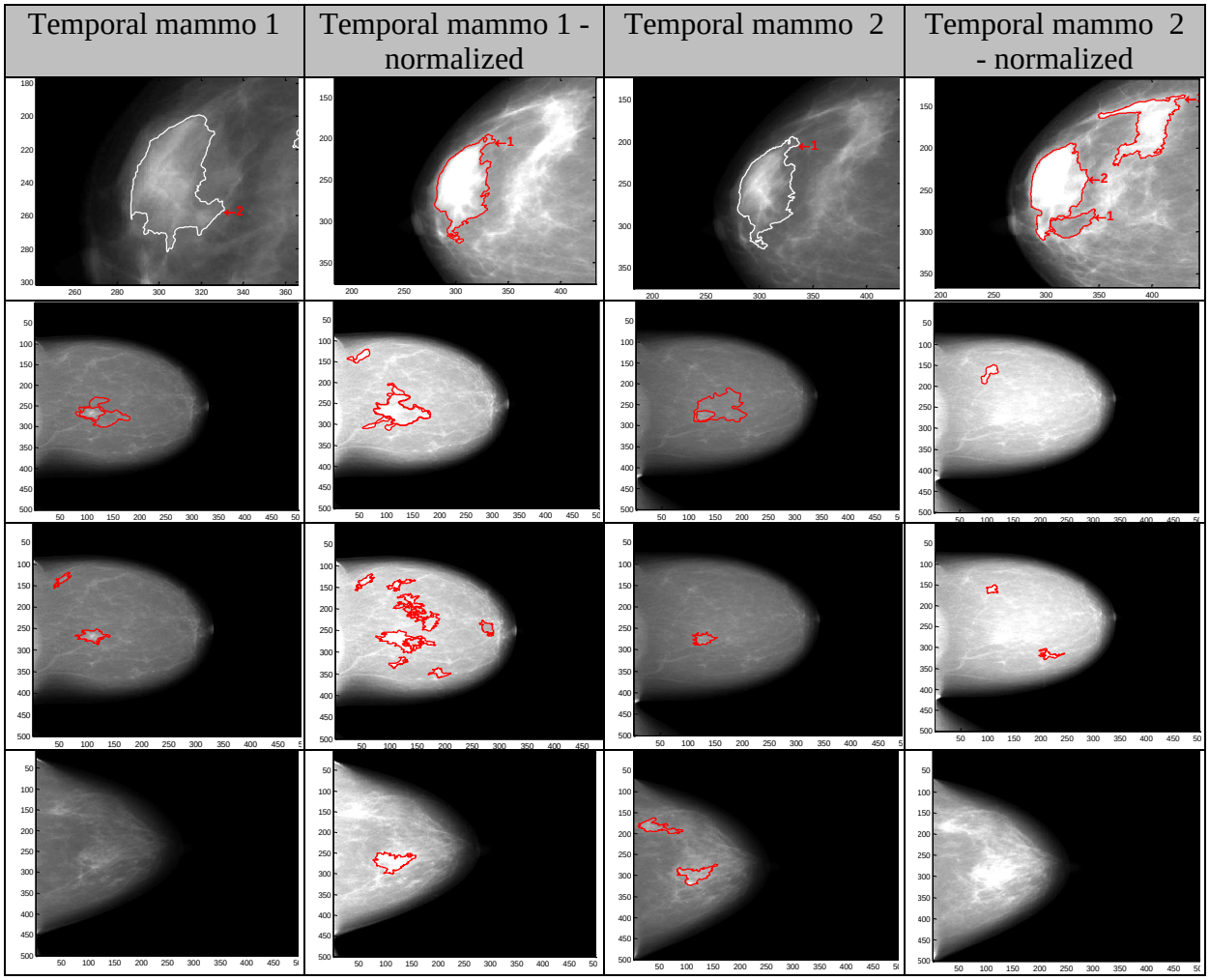

Figure 4.16: Examples of segmented mammograms with and without normalization

	Temporal mammo 1	Temporal mammo 2
Without normalization	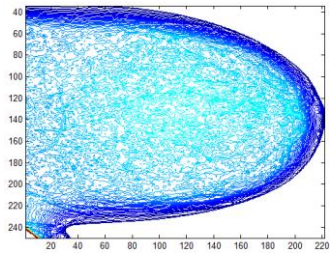	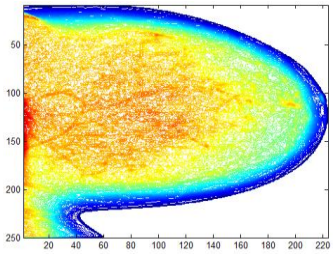
With normalization	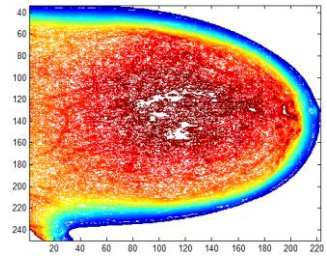	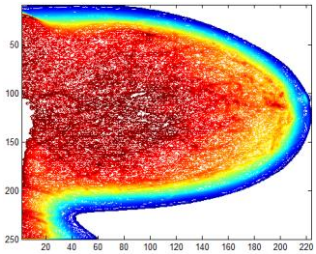

Figure 4.17: Example of normalization by contrast adjustment. Brightness of contours increases as the colour of contours goes from blue to red. The bright regions inside the breast near centre do not have any contour mapping.

4. 4. 6. Hybrid Method

Based on the above considerations, we have developed a hybrid segmentation algorithm, which combines the modified Hong's algorithm and Cerneaz's [255] area-based segmentation of mammograms. Pseudo-code for the algorithm is given below in Figure 4.18. Hong's algorithm is first used to delineate salient regions by keeping the nesting depth criterion low.

Cerneaz's Segmentation Method

Cerneaz's algorithm helps to define the boundary of a segmented region by looking into the ratio of the areas of the parent and child regions. If the area of the two nested regions is less than a certain threshold, which is chosen empirically using trial and error strategy then it is

assumed that they represent a single entity whose effective boundary is the one with the greatest nesting depth. This will select regions in a nested pattern. It gives a choice of outermost boundary, from which an optimum can be selected. One of the limitation of the Cerneaz method is, though it can deal favourably well with curvilinear structures, it finds hard to segment dense breast with almost uniform intensities.

Examples of this new segmentation algorithm along with the following variation to the noise removal method are given at the end of this chapter. Figure 4.18 shows a flow diagram of our modified version of the iso-intensity based hierarchical segmentation method. Results from the USF database are presented in Figure 4.19 along with the ground truth.

The hybrid method offers an extra check for the regions that are surrounded by a number (usually two) base contours passed through the MND criteria of Hong's method and it is difficult to decide which of the selected contour represent the actual boundary. It does not affect the shape of the selected contour since the contours are formed by Hong's method.

4. 4. 7. Discussion on Relevant Segmentation Methods

We have applied a contour based segmentation method to mammograms that depends upon the formation of iso-contours on an image surface. Contour based segmentation methods are primarily used to segment masses or other suspicious regions, rather than microcalcifications. Nevertheless, there is very low consistency in the way contour based segmentation methods for masses are compared to each other; they have been mainly tested upon the Mini-MIAS and DDSM database. While MIAS provides digitized mammograms with a bias towards circular and large masses, which makes it less reliable to conclude a hypothesis, DDSM contains 2500 studies in dozens of categories with distinctly different statistical features picked arbitrarily

by authors. Keeping in mind the above limitations in which mammographic segmentation methods are tested, it is hard for us to compare our method objectively to prior literature. .

In relation to our approach, some of the methods for finding suspicious regions are listed here. Zhang et al [256] applied a contour based method on DDSM database, which segments lesions and further classifies them into benign or malignant. The method has an offline pre-marking and contrast stretching step, which makes it manually intensive. The method was found to be computationally very expensive, depending upon a number of texture, shape and gradient features, with a feature reduction step using artificial neural networks (ANN). Cascio [257] applied a contour based method to 3762 mammograms belonging to MAGIC-5 collaboration (Medical Applications on a Grid Infrastructure Connection). It used an ROI hunter algorithm, having feature extraction and classification using ANN as the core of the method. The overall results were quite impressive with 2.8 false positives per image at a sensitivity of 82%. A comparative study was performed by Singh and Al-Mansoori [258] to compare contour based region growing segmentation approaches to gradient based method. The method aimed to segment the texture of cancerous masses. A total of 30 randomly select mammograms from the USF database where first histogram equalized using fuzzy enhancement techniques, followed by segmentation. The study showed that the region growing technique gives a fewer number of regions for analysis while maintaining true positives. Muralidhar [259] implemented the Snakules segmentation method into an evidence-based active contour model to apply on mammograms from DDSM database. The method used shape features for automatic classification of spiculated masses to differentiate lesions from non-lesions using k-means clustering. An AUC score of 0.79 ± 0.5 was achieved, showing good potential for further work. Other non-contour based methods include local

thresholding [260], [261], image difference [262], watershed and wavelets [263], [264], pseudo segmentation [92], [265], graph based segmentation techniques [209], [266], [267], Markov Random Fields [268] and others.

Despite that some of the methods mentioned above show promising early results, our aim to segment ROIs is not in order to classify regions into benign or malignant. Instead the goal is to obtain regions and/or shapes, which are suspicious and may develop into an abnormality over a period of time. A computationally efficient, robust and fast method which can segment the complete tomographic structure of the breast (before any post-processing) without any a priori knowledge and good accuracy is desirable for our study. With these considerations in mind, Hong's approach [202], [251], originally i inspired from Madagonda [19], [21], [252], along with the method of Cerneaz [255] as an additional check, fits well for our requirement.

4. 5. Conclusions

Despite the shortcomings mentioned above, we elected to use this segmentation algorithm. The first reason is that it is computationally very efficient and feasible for a real time system. It segments the complete internal topography of the breast in a structured way that can be used for corresponding mammograms. Shape is defined on iso-levels that give a notion of pattern and texture change in a limited sense. This is important because image segmentation using a single mammographic view relies on the fact that pixels inside a mass have tissue compositions that are different from pixels in other parts of the breast. It is hard to explain this difference in terms of x-ray attenuation. Despite its simplicity, the segmentation results are very accurate, as shown in Figure 4.19.

As for this method, brightness at any point in a mammogram is inversely proportional to the number of x-ray photons present at that point during the exposure of the film. Therefore, the brightness in a mammogram is proportional to the density of tissues. This property of x-ray imaging naturally leads to consideration of an image as a surface where intensity represents height. The complex structure of the breast gives way to a wide range of intensities to reflect heterogeneous information and hence iso-contours are perhaps one of the most competitive techniques to analyse those independent anatomical structures.

The most important reason for using the topographic method is that it will be more meaningful on density maps that we will use in this thesis, where the boundaries of a region will be formed on iso-density rather than iso-intensity pixels. Hence, we can assume that the boundary of an interested region is at a uniform attenuation, forming a relatively well-defined border from the background.

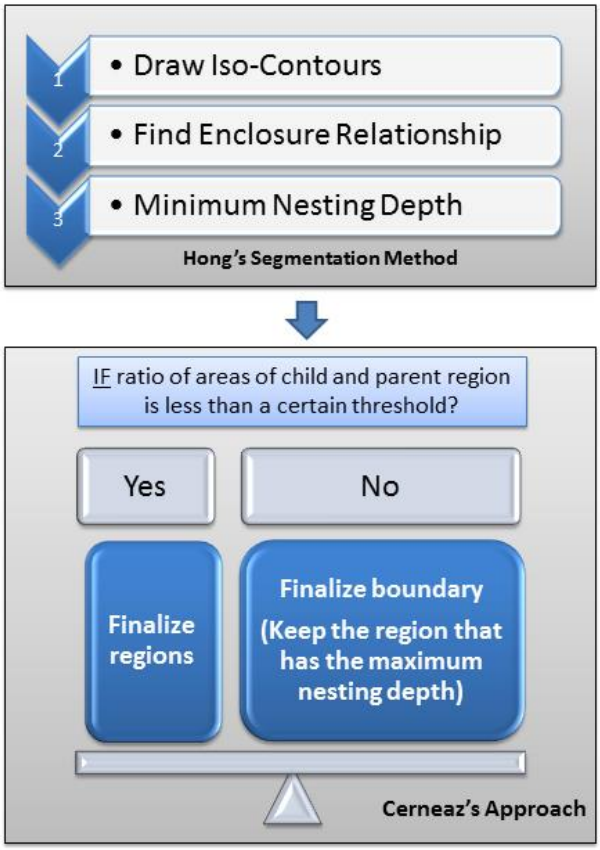

Figure 4.18: The overall segmentation process

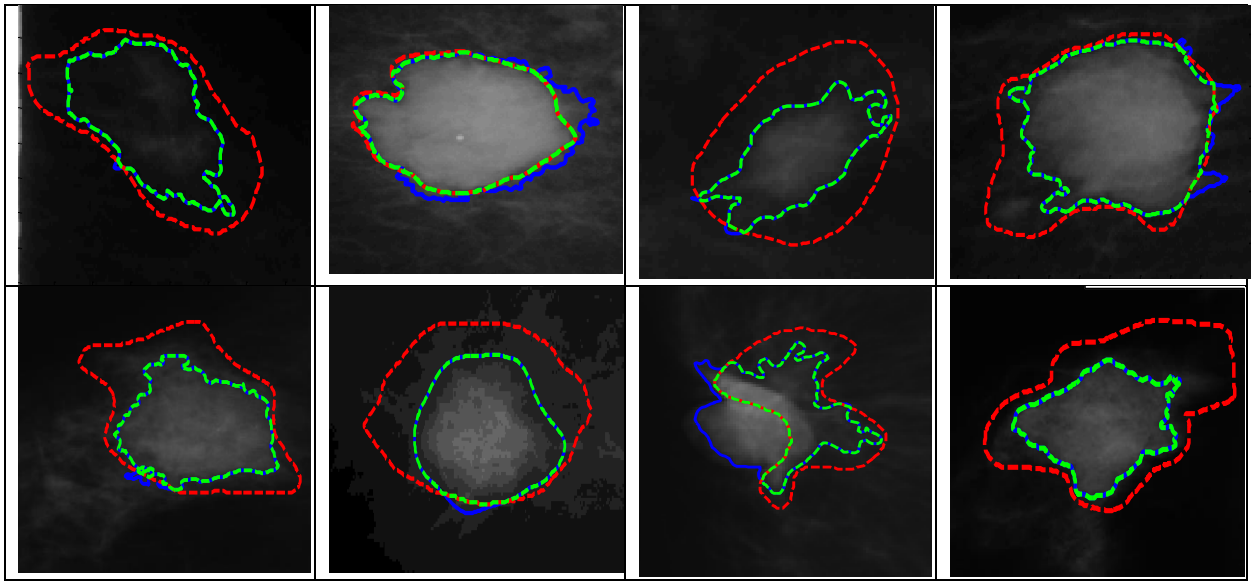

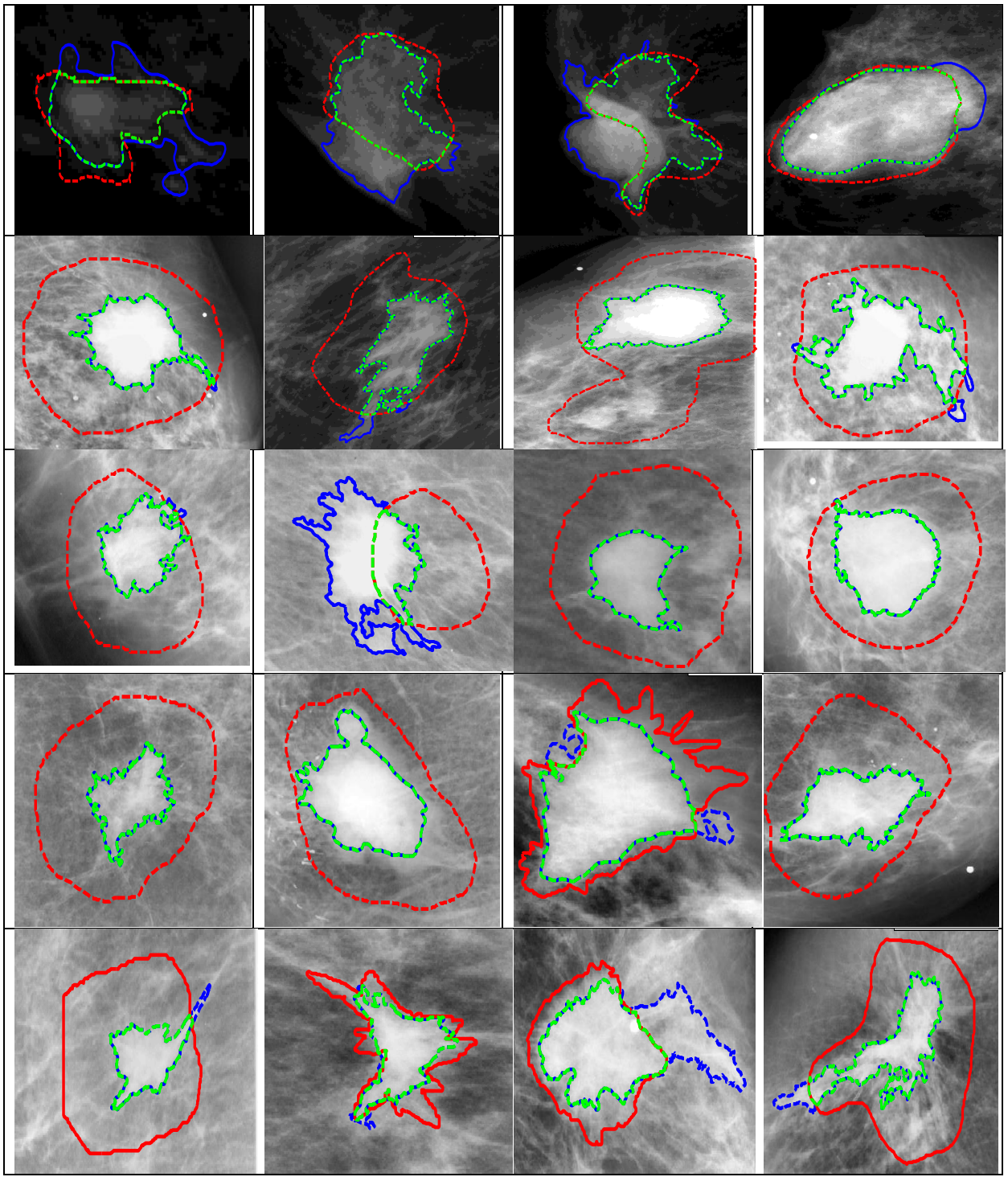

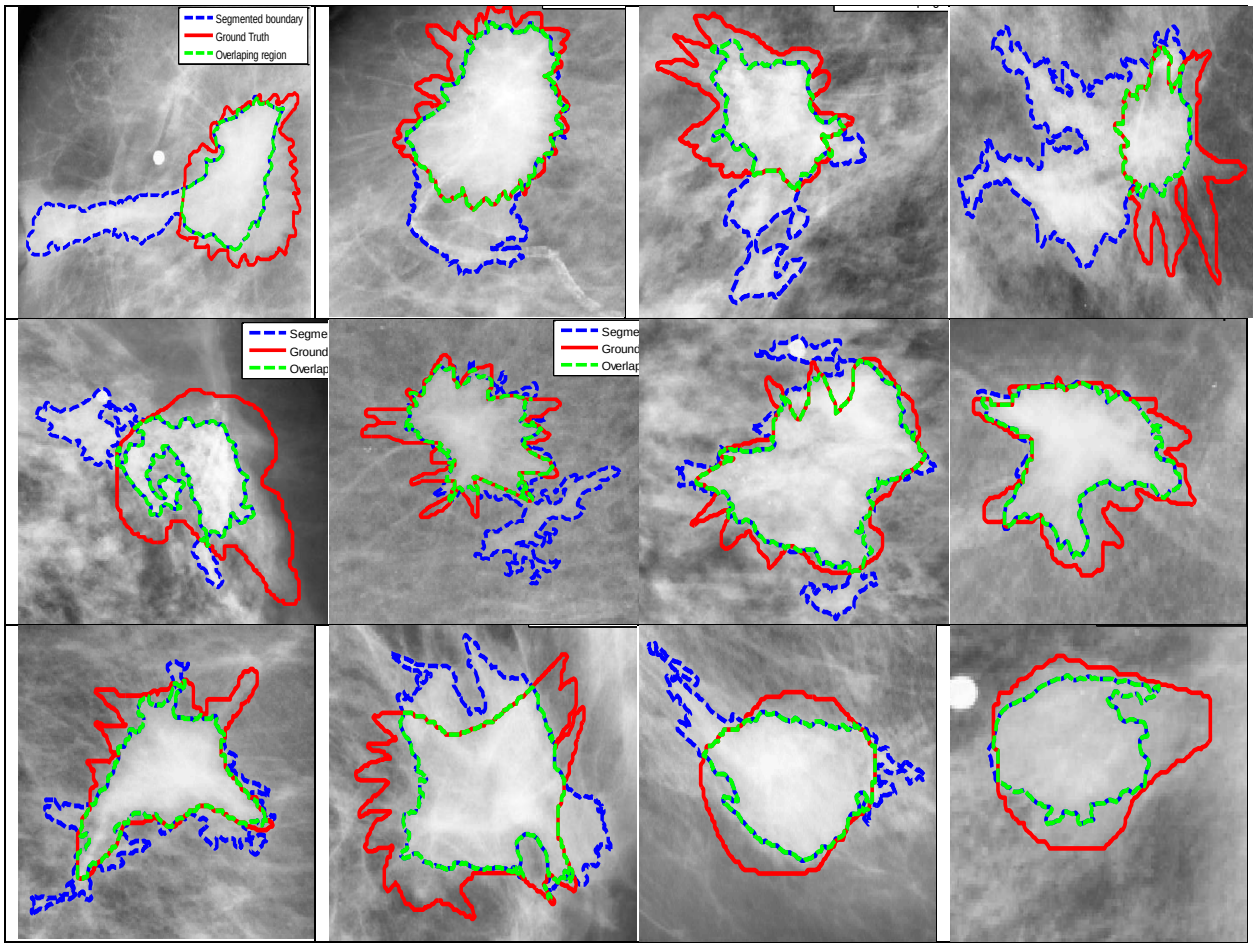

Figure 4.19: Segmentation results of mammograms from USF database. Red lines represents "ground truth", which are rough indications by a radiologist of the location of a mass, whereas blue and green dotted lines show the segmented boundaries and overlapping region respectively

Chapter 5

INTEGRAL INVARIANT SCALE SPACE

5. 1. Introduction

To date, Integral Invariants have been used exclusively for shape description. In this chapter we explore the properties of Integral Invariant scale space and have used it to reduce the number of false positives in mammographic segmentation. Using this technique may eliminate the use of a separate false reduction method while describing shapes at multiple scales.

Objects in the real world are perceived at a variety of scales. For instant, looking at a house, one may notice the design of its bricks, windows, house as a whole or its relevance to the scenery. In all those cases our focus depends upon what we are looking for, in other words we are scaling our view, restraining or expending our limits of understanding and vision according to our objective. Fixing the bounds of the scales taken into account creates a scale space, where the inner limit or fine scale contains the smallest details i.e. leaves on the tree, window panes, or the style of bricks on the wall, while the outer limit or coarse scale can be used for judgments about the whole house, tree or scenery. This is called scale selection [269], [270]. The observations that we make using our eyes, any physical device that resembles a retina, mathematical analysis, or a camera (we may call it the front end) may not involve any memory or prior knowledge, anything specific, or any sort of nonlinearities. Such an observation may be called uncommitted. That is a scale space that has an uncommitted front end may be called a linear scale space.

In this Chapter and in the next, we introduce Integral Invariant as an image enhancement filter, and have shown that it creates a causal scale space, if we understand that term in a slightly relaxed fashion. Here, we explore the scale space properties of Integral Invariants. However, before discussing the properties of Integral Invariant scale space, it is important to establish the terminology, for which we use Gaussian scale space as an example.

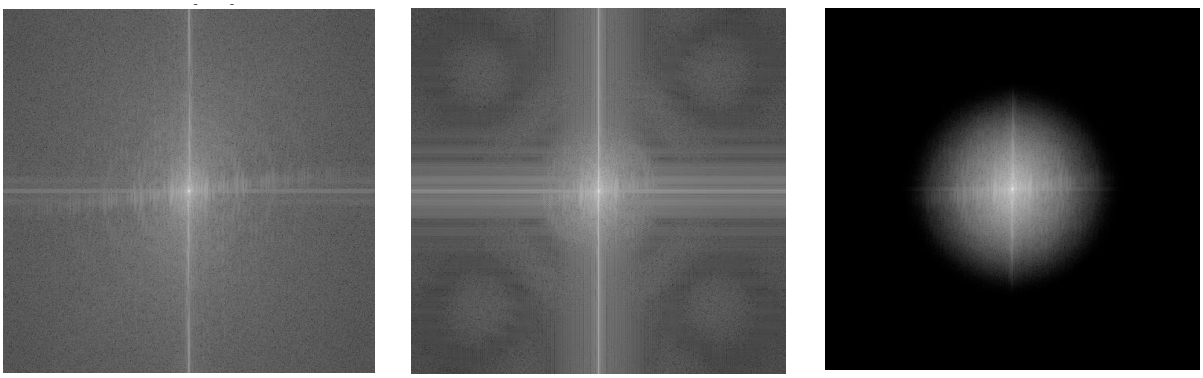

a B c

Figure 5.1: a. Fourier transform of an image, b. Integral invariant diffused version of (a), c. Gaussian diffused version of (a). Gaussian diffusion takes away the high frequency content more aggressively than Integral Invariants .

To achieve a scale space, we need to probe the image with some operator that we may call a kernel, aperture, or filter. The size of this aperture determines the scale of observation and is a free parameter. If this kernel is a square and applied to an image, then we may have a resulting blocky effect where new details such as edges or corners may appear which were not there previously. This leads to an increase in the detail in the image rather than decreasing it as shown in Figure 5.2 b. Alternatively, we can use a Gaussian blur [192], [271]–[275] as in Figure 5.2.c, where an image has been blurred by convolving it with a Gaussian filter and information content is reduced by increasing scale.

The Gaussian kernel is considered to be the unique choice for an uncommitted front end in essence for its mathematical formulation for knowing nothing without any prior commitment. The following are the key properties of a Gaussian kernel as described by Romeny, [272], [276], [277]

1. Linearity
2. Spatial shift invariance
3. Isotropy
4. Scale invariance

a b c

Figure 5.2: a) is an MRI of head that is convolved with a squared aperture shown in (b) and with a Gaussian filter in (c). [272]

A Gaussian kernel has the property of self-similarity, that is, the observation through an aperture blurs the image and increases the inner scale. Moreover, if we repeat the same observation again, blurring for a second time, the inner scale is increased with the same aperture. Concatenation of two smaller rescalings is equivalent to rescaling with a single large scale parameter.

The blurring of an image or increasing the inner scale of an observation of a signal to a coarse or outer scale can also be assumed to be a diffusion process of intensity, where the intensity is regarded as the energy or strength of a signal. This was noticed by Witkin [278], [279] and re-formulated by Koenderink [280], who showed that the linear scale space equation is actually a linear diffusion equation where the Gaussian is a Green's function of the diffusion equation. If the standard deviation of the Gaussian kernel is uniform for all data i.e. data blurs in all directions uniformly then the process is isotropic and when it is equal at every point the process is called homogeneous.

All partial derivatives of the Gaussian kernel are solutions of the diffusion equation, and together with the zeroth order Gaussian, they form a complete family of scaled differential operators. The process of diffusion can be analysed in multiple ways [213], [270], [272], [273], [276], [277], [280]–[294], including [272] as following:

1. Causality [280], [290] finer scales shape and directly reflect upon what will happen at the coarser scales.
2. One dimensional signals do not form new extrema by increasing scale [292]
3. Maximum principle [295], [296]: "at any increase of the inner scale (blurring) the maximal luminance at the coarser scale is always lower than the maximum intensity at the finer scale, the minimum is always larger;"
4. As the scale increases, the information content is reduced in a linear diffusion process, which is basically log of the signal's entropy. [297]
5. "According to the physics of the diffusion process (see many textbooks in physics, e.g. [298], the decrease of the luminance with time (or scale, which is here equivalent) is

equal to the divergence of a flow, i.e. equal to the divergence of the luminance gradient".

5. 2. Causality

For an action to be called a smoothing operation it must ensure that no new details or extrema emerge by increasing the scale of observation equivalently by increasing the size of the aperture or kernel. Koenderink not only extended scale space theory to higher dimensions; but he also formalized causality as a necessary condition for a smoothing process. He combined causality with the notion of isotropy and homogeneity, which means that all spatial positions and all scales must be treated in a similar manner. From this basis, he showed that the scale space representation must satisfy the diffusion equation. The causality requirement means that level surfaces in scale-space must point with their concave side towards finer scales or decreasing scales giving rise to a sign condition on the curvature of level surface. [273], [292]

For a one dimensional signal, the level surface becomes a level curve condition and follows the idea of non-creation of new zero-crossings at a higher level of observation scale. According to the causality principle, what happens at the outer scale or an extremum at a coarse scale can always be traced back to finer scales. Similar results are given by Yuille and Poggio[293], Babaud[278] and Hummel [295].

It is possible that a smoothing process applied over a limited and bounded set of scales may decrease the number of maxima; however, this is not always necessary. It is confirmed that by increasing scale the information content in a signal will decrease. Lindeberg characterized those kernels which guarantee not to produce new extrema by increasing scale for a signal that goes through the process under convolution. A kernel $h \in L_1$ is termed a scale-space kernel if

it possesses the property that for any input signal $f_{in} \in L_1$ the number of extrema or zero crossings in the convolved signal is $f_{out} = h * f_{in}$ is always less than or equal to the number of local extrema in the original signal: [292]

Scale Space kernel:

$$\text{extrema}\,(f_{out}) \;\leq\; \text{extrema}\,(f_{in})\;\forall f_{in} \in L_1 \qquad (5.1)$$

Such kernels are positive and uni-modal both in time and frequency domain.

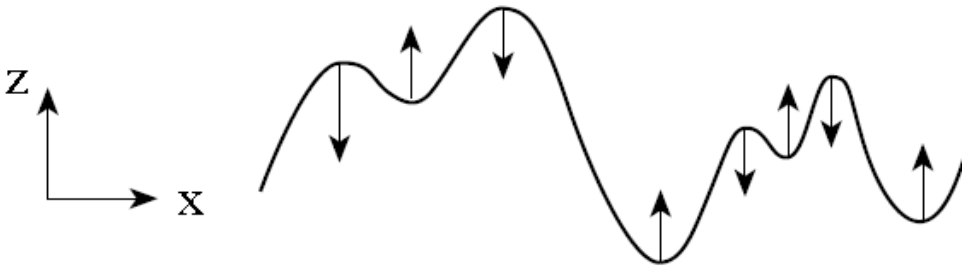

Figure 5.3: The non-enhancement principle of local extrema means that the grey-level value of a local maximum must not increase with scale and that the grey-level of a local minimum must not decrease [291].

5. 2. 1. Maximum Principle

For the non-increasing of a local extremum, as per Lindeberg's reformulation of Koenderink's causality requirement [292] [291]: if for some scale level S_0 a point x_0 is a non-degenerate local maximum for the scale space representation at the level (regarding as function of the space coordinates only) then its value must not increase when the scale parameter increases. Analogously, if a point is a non-degenerate local minimum then its value must not decrease when the scale parameter increases.

This property will be automatically fulfilled if the scale space formulations are based on scale invariance and follow a complementary requirement of scale space kernels to form a semi-group.

5. 3. Integral Invariant Scale Space

A multi scale representation of Integral Invariants is required to reduce noise by suppressing high-frequency variations in lower-resolution versions of the signal and by converting global image features into local image features. This also helps us to estimate salient regions in shapes or images by helping us to follow coarse-to-fine scale features.

Integral Invariants form a relaxed causal scale space where the non-creation of extrema or non-enhancement and the maximum principle is followed for most scales; however, it is not satisfied in a strict sense at very high and unrealistic scales.

According to Koenderink's causality requirement, as re-formulated by Lindeberg, the value of a maximum must not increase with increasing scale. From Figure 5.6 and Figure 5.7, we can see that unlike Gaussian scale space, at some scales peaks at the lower scales are exceeded by the Integral Invariant signatures at the higher scales. However, no new peaks are seen and the causality requirement remains valid.

It can be seen that the Integral Invariant scale space follows the causality property, as the extrema of the convex planes face upwards and maintain convexity despite increasing scale. Furthermore, it also follows the principle of non-emergence of extrema; the number of extrema in an outer (coarser, higher) scale is less than or equal to the number of extrema at a finer scale. The concept is somewhat similar to, but stricter than monogenic and Poisson scale space, where it follows 'relaxed causality', as shown in Figure 5.4.

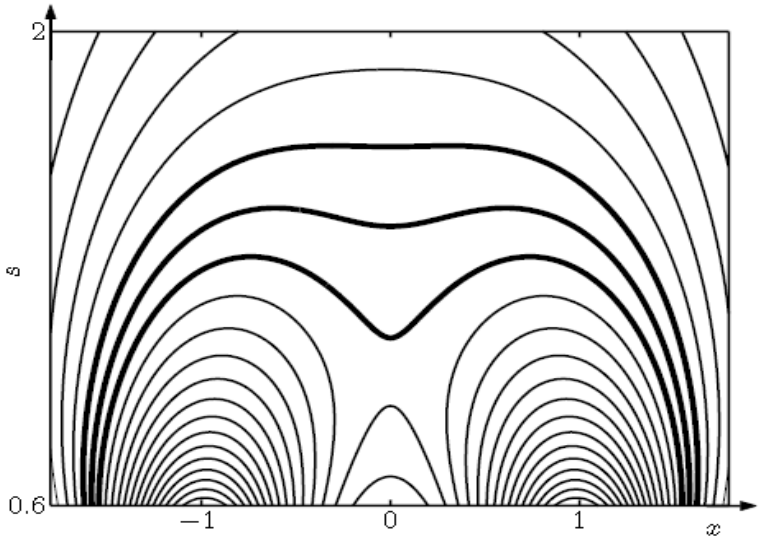

Figure 5.4: 1-D poison scale space that does not fulfil the non-enhancement principle.

(Monogenic-poison [299])

5. 4. Observations

The following observations may be drawn from analysis of Integral Invariant (II) scale space:

1. Generating integral invariant scale space is a **linear operation**. Scale space generation through Integral Invariants implies convolution.

$$L(\vec{x}, \Lambda) = L_0 \otimes I(\vec{x}, \Lambda), \text{ Where, } L \otimes I = \int_{-\infty}^{\infty} L(k) I(x - k)\, dk \quad (5.2)$$

in which Λ is the size of the integration kernel and $\otimes$ denotes convolution.

2. the II scale space representation is **scale variant** and the concatenation of two smoothing kernels

$(\Lambda_1) and\ I(\Lambda_2)$ is not equivalent to smothing with $I(\Lambda_3)$, for the effective scale parameter $\Lambda_3 = \Lambda_1 + \Lambda_2$.

3. It also implies in a subsequent formal treatment that the convex side in an extremum of a contour should be directed towards the higher scales and can be interpreted as non-enhancement of local extrema. Integral invariant scale space does not follow this **non-enhancement principle** in a strict sense; nonetheless, it is causal by definition and satisfies a **relaxed causality**.
4. The main point of causality is to avoid creation of unwanted spurious structures, such as corners or edges, as a result of the filtering process. Such spurious structures can only become visible if they are strong enough to supersede noise and reach the next quantization level. For integral invariants, the enhancement of extrema at higher scales does supersede previous peaks for a few scales; it does not have the capacity to appear at a finer scale level. However, new peaks are not created.
5. Since the integration kernel is a circular disc it has the same length to the centre from all sides and diffuses identically in all directions. It follows that the process of generating scale space is **Isotropic**.
6. Due to its consistent sum of product nature at every point in the data, the amount of diffusion is equal at every point in the data space and the evolution process is **homogeneous**.
7. It is **memory-less** and every new scale is computed **without any prior knowledge** or dependence on the previous scale observations. It does not depend on a specific model, hence can be termed **linear scale space**.

8. At each scale, diffusion at any one point is independent of observation through an aperture at the previous point in the same scale. Evolution of scale space by integral invariants is also spatially or **shift invariant**; as there is no preferred location for smoothing in the data or image. The aperture is scanned over any possible location in the data and the result will be linear and finite.
9. The total number of extrema before diffusion is greater than the total number of extrema after diffusion by an integral invariant. Thus we can say that it is a **positive kernel** and is **uni-modal** both in the time and frequency domain. See [269], [272], [277], [285] for further explanation of kernel types.
10. As regards scale selection in any specific application, a criterion may be established by selecting a salient point in the scale space which is strongly causal over a range of scales and is de-generative. The term de-generative means that a peak will not increase by increasing scale if it is local maxima, and conversely, local minima will not decrease by increasing scale. Scale spaces based on these properties are based on the formulation of scale invariance and are considered to be semi groups. Integral invariant does not fulfil these properties in strict sense neither is it scale invariant.

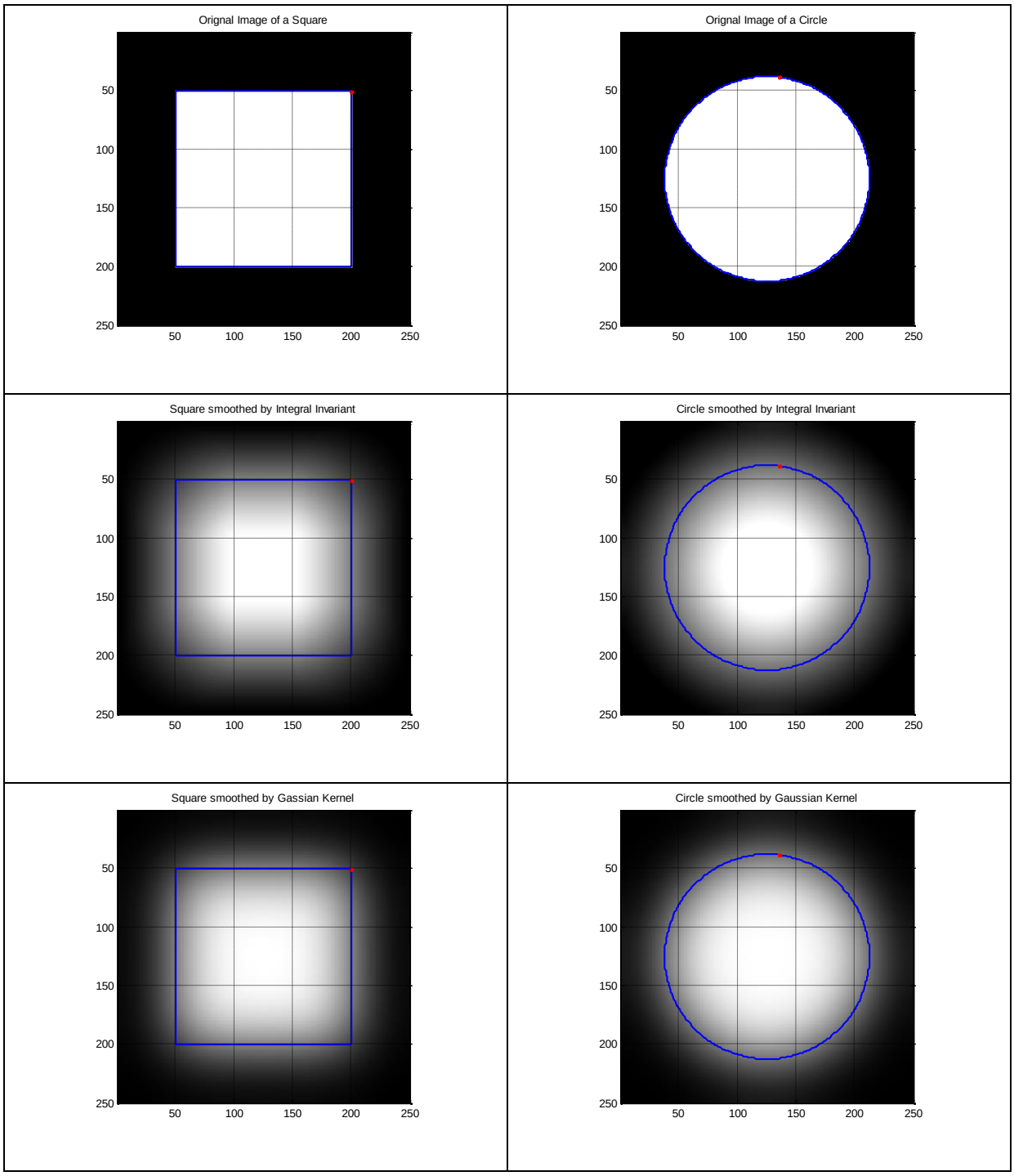

11. **Figure 5.5:** A visual illustration of a square and circle that are smoothed via circular Integral Invariants in the second row and Gaussian kernel in the third row.

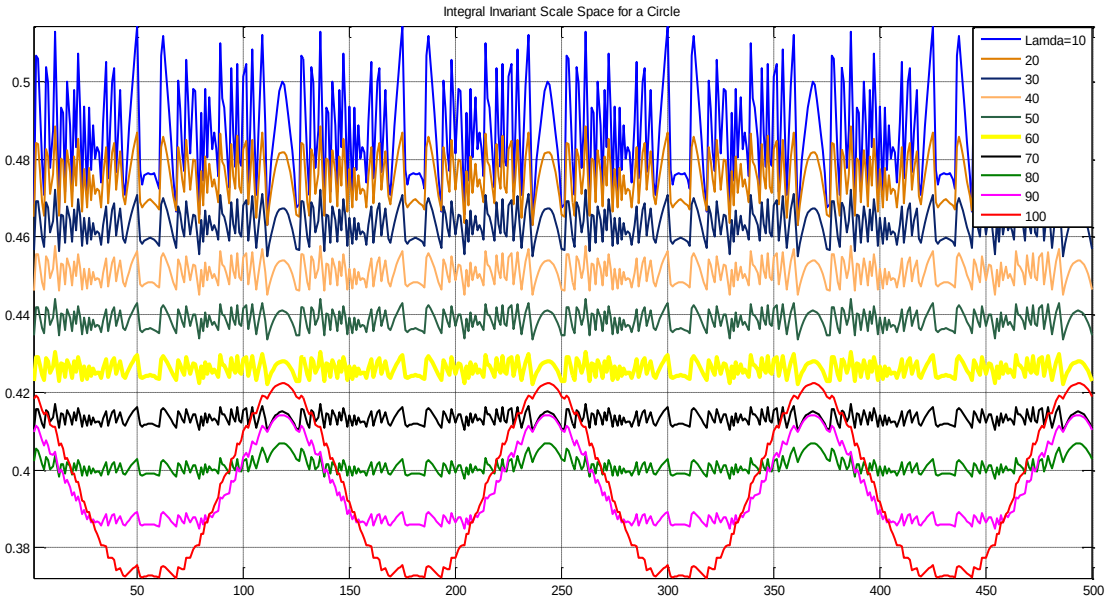

Figure 5.6: Integral invariant scale space of a circle with variable Lamda (kernel) sizes

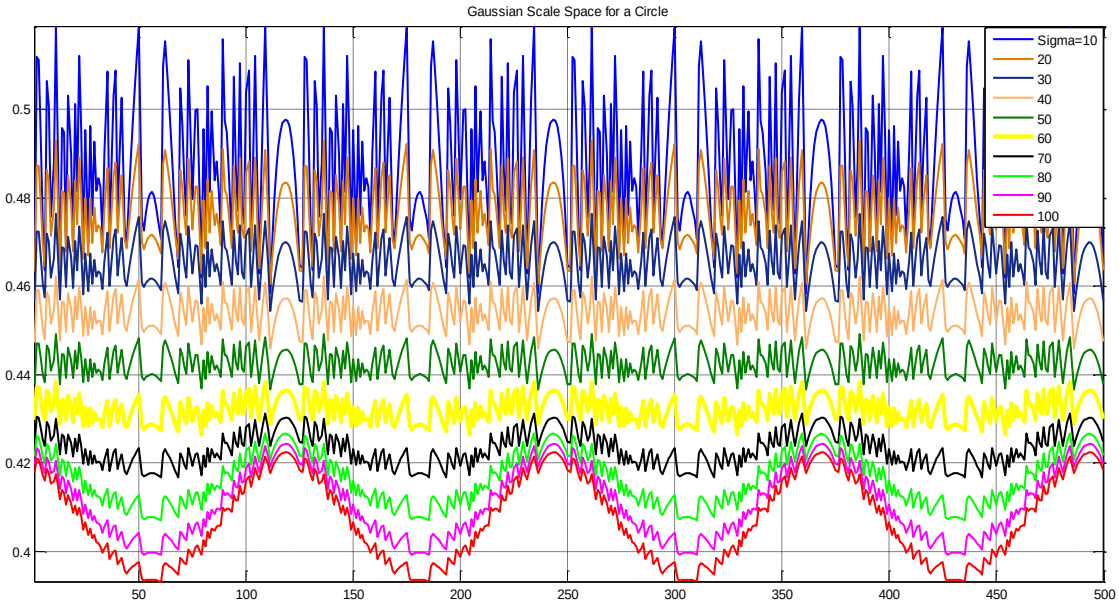

Figure 5.7: Gaussian scale space of a circle with variable Sigma (kernel) sizes

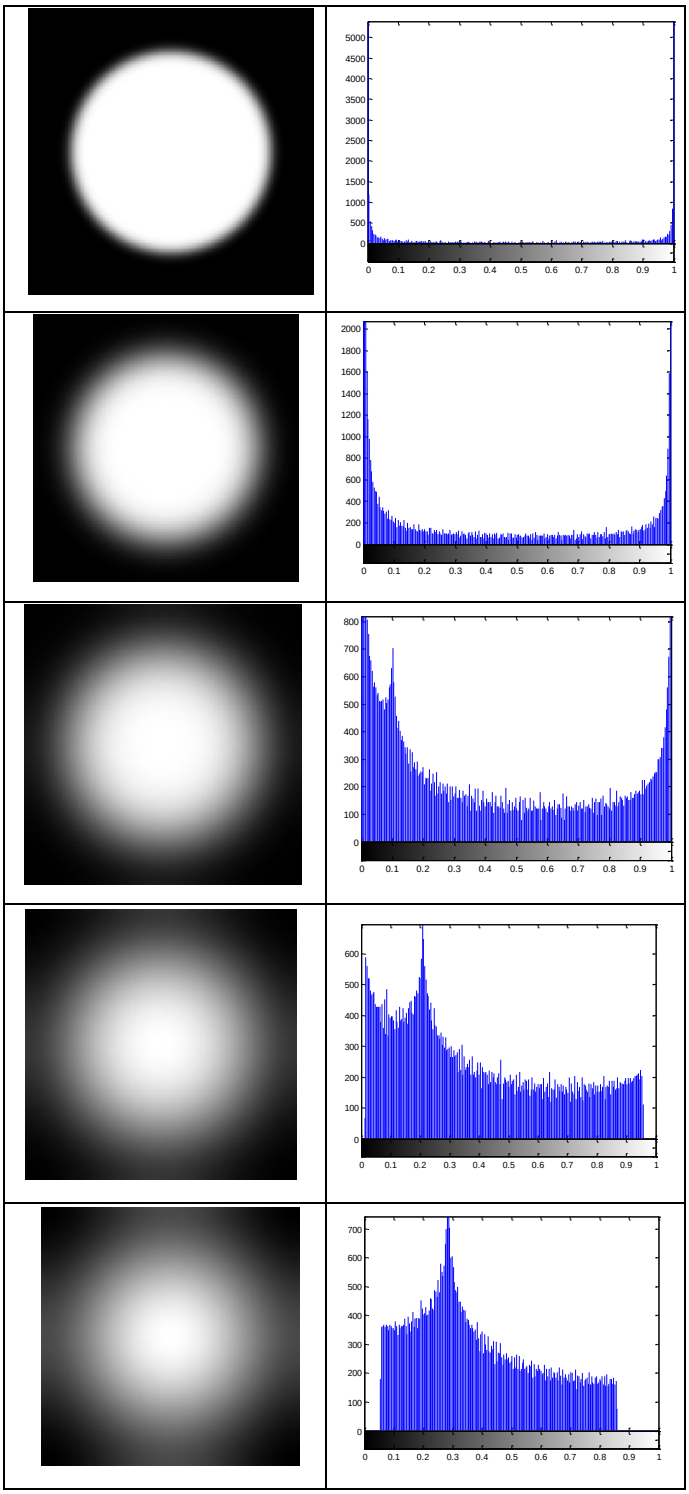

Figure 5.8: Diffusion of intensities at increasing scales for an image of 256x256 pixels. The size of diffusion kernel is 10, 30, 50, 70 and 90 pixels from top to bottom in that order.

12. Unlike Gaussian scale space, II scale space does not follow the cascaded property. This states that if an observation reaches a certain inner scale in a single step from input data by applying a bigger kernel, it should be same as by applying a sequence of smaller apertures to reach the same scale. Integral invariant scale space is **not self-similar**.
13. It is not presently clear if Integral Invariant fulfils the requirements to be called a semi-group kernel [269]; the observations above indicate it may not be. For Integral Invariants to be a semi-group, may not need to have an identity element but should have a single associated binary operation i.e. Moniod. It requires a more careful study to conclude this behaviour and is not covered in this thesis. A possible asymptotic behaviour of the kernel is not studied here. At unrealistically higher scales, it violates the non-enhancement of extrema principle and will give birth to new extrema by reverting convex to concave curves and vice versa.

5. 5. False Positive Reduction

False positive reduction methods in mammography are highly dependent upon the parameterization of thresholds that defines what is interesting and what is not. It is also dependent upon the density of mammograms used, quality of mammograms, imaging parameters and they appearance of regions of interest. Therefore, there is no gold standard to compare false positives in mammograms; nevertheless, see [16], [300]–[305].

Here, we have applied Integral Invariants scale space to reduce the number of false positives in mammograms [1]. As the integral invariants retain causality at increasing scales for salient regions in 2D shapes; they also retain causality when applied to a surface, which is a 3D embedding of a 2D image. An x-ray image is an example of such an embedding in which ‘interesting regions’ appear brighter (and denser) than normal breast tissue and form causal

peaks. These peaks maintain causality in response to integral invariant diffusion. This may be seen in Figure 5.9, where a mass retains its profile over a number of integral invariant diffusion scales. Here, we show that this could be applied to the scale space of segmented regions in order to evaluate their saliency, and consequently to reduce the number of false positives in mammograms. Here we have aimed it by developing a method to grade or rank salient regions in mammograms. Most of the mass segmentation algorithms segments three types of regions inside a breast, which are: 1) a masses 2) fibro-glandular tissues or stroma and 3) regions of light intensity and homogeneous texture surrounded by higher intensity and heterogeneous textures. The number of false positives could be reduced by extensive noise removal; linear/non-linear filtering, however, this drastically affects the true positive results and its boundaries. We have devised a mechanism to restrict the selection of fibro-glandular tissues and lighter homogeneous regions. Simulations are performed on synthetic images and density & intensity mammograms.

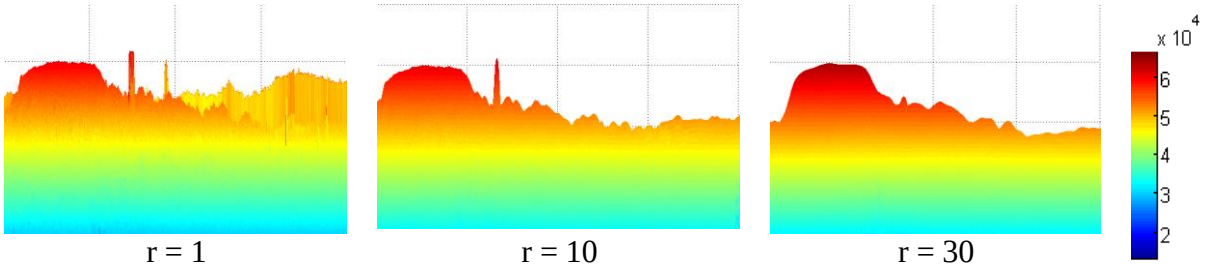

Figure 5.9: Integral Invariants diffusion at various scales of a mass surface in a mammogram taken from USF database. 'r' is the size of integral invariant difussion kernel. A mass from the MIAS database, shown as a wide peak, survives over all given scales.

Suppose that a certain region R_i has an intensity profile C_i^k extracted across it at k scales, such that:

$$C_i^k(p) \in R_i \quad where \;\; i = 1,..,n; \;\; r = 1,..,k$$

$$p = II(x,y) \in \Omega_i \,, \qquad (5.3)$$

Here II is the integral invariant function at the pixel (x, y) in a diffused domain Ω_i of a region R_i . We define the cost function T to determine the saliency of the region R_i by

$$T_i = \left(\sum_{r=2}^{k-i} \left(\frac{C_i^r(p) - C_i^{r-1}(p)}{length\ of\ C_i}\right)\right) \qquad (5.4)$$

However, we contend that the saliency of region should also depend upon the overall density of the breast. For example, a dense region of a certain volumetric density that is certainly salient in a fatty breast may not be regarded as salient or suspicious inside a very dense breast. With this in mind, we modify the cost function as follows:

$$T_i = \left(\sum_{p=1}^{l} \left(\frac{C_i^1(p) - C_i^k(p)}{length\ of\ C_i^1}\right)\right) * \frac{\bar{D}_i}{D_B} \qquad (5.5)$$

Where, $\bar{D}_i$ is the average density of the region R_i and D_B is the overall volumetric density of a breast. For SAR, this will be the ratio of corresponding attenuations, while for intensity images it is the ratio of average intensity in the region versus the maximum intensity inside the breast. The other point is that the range of values at the y-axis for a mass is larger (almost double) than that of the fibroglandular tissue or local lower intensity homogeneous regions. This means that a mass will have a relatively higher peak than that of the 'non-interesting' regions. This is one of the reasons to include the difference between the peaks of maximum and minimum intensity scale space, as illustrated in Figure 5.10. The equation evolves as,

$$T_i = \left(\sum_{p=1}^{l} \left(\frac{C_i^1(p) - C_i^k(p)}{length\ of\ C_i^1}\right)\right) * \frac{\bar{D}_i}{D_B} * \left(D\,{}_i^1 - D\,{}_i^k\right) \qquad (5.6)$$

$$where\ D\,{}_i^r = \text{abs}(\ \max\ (C_i^r) - \min(C_i^r)\ );\ r = 1, .., k \qquad (5.7)$$

A threshold is to be set for T, to exclude in the set of regions that are not of interest and possess a higher cost. In these experiments, T is empirically set to compare against T_i and will affect the selection of regions if changed. Based on the score of each region, they can be ranked for likelihood to be a mass. T is negative for the low intensity locally homogeneous regions, which have a dense pattern of iso-contours surrounding it. All contours that yield a negative T are discarded. These observations are used to reduce the number of false positives, while not affecting the true positive results.

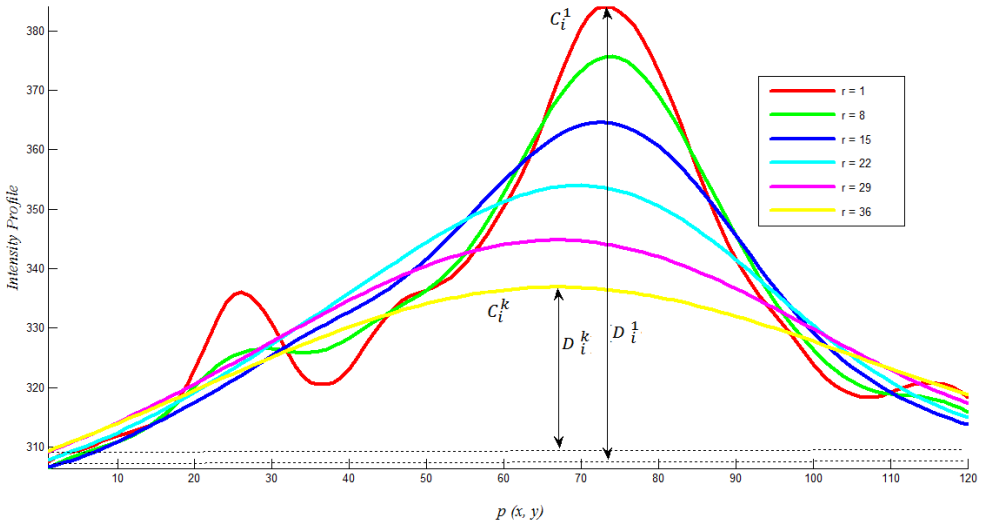

Figure 5.10: Intensity profile scale space of a certain region. This is a profile of a false positive region shown in Fig 5.11.

The intensity profile itself is extracted using Fast Marching Algorithm and the gradient descent, as illustrated in Figure 5.11. Some examples of regions from Volpara® density maps dissected for scale space extraction is given in the Figure 5.12. To understand how the method works, we simulated a surface which has peaks and dips of various amplitudes, as shown in the Figure 5.13.

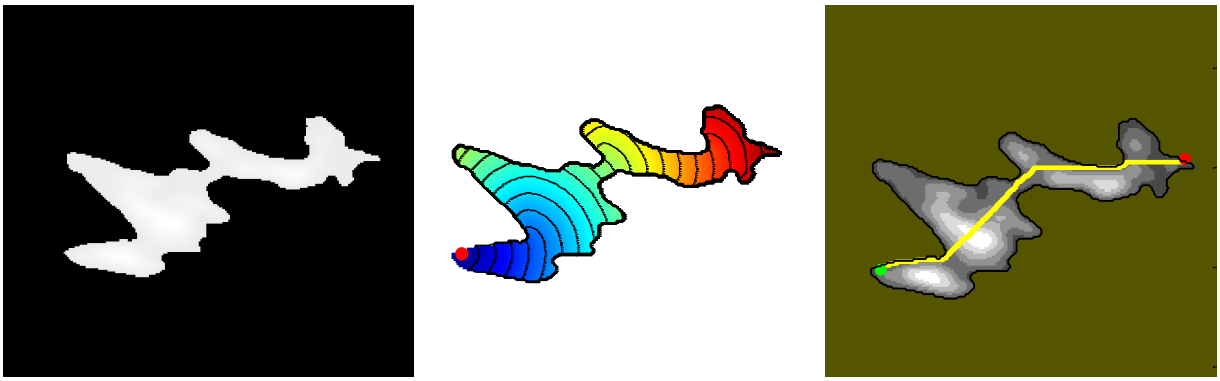

A mammographic region | Distance map using FMA | Disected path using Gradient descent

Figure 5.11: Dissection of a mammographic region to extract intensity profile. The path is labelled as yellow, approaching from green to red spot.

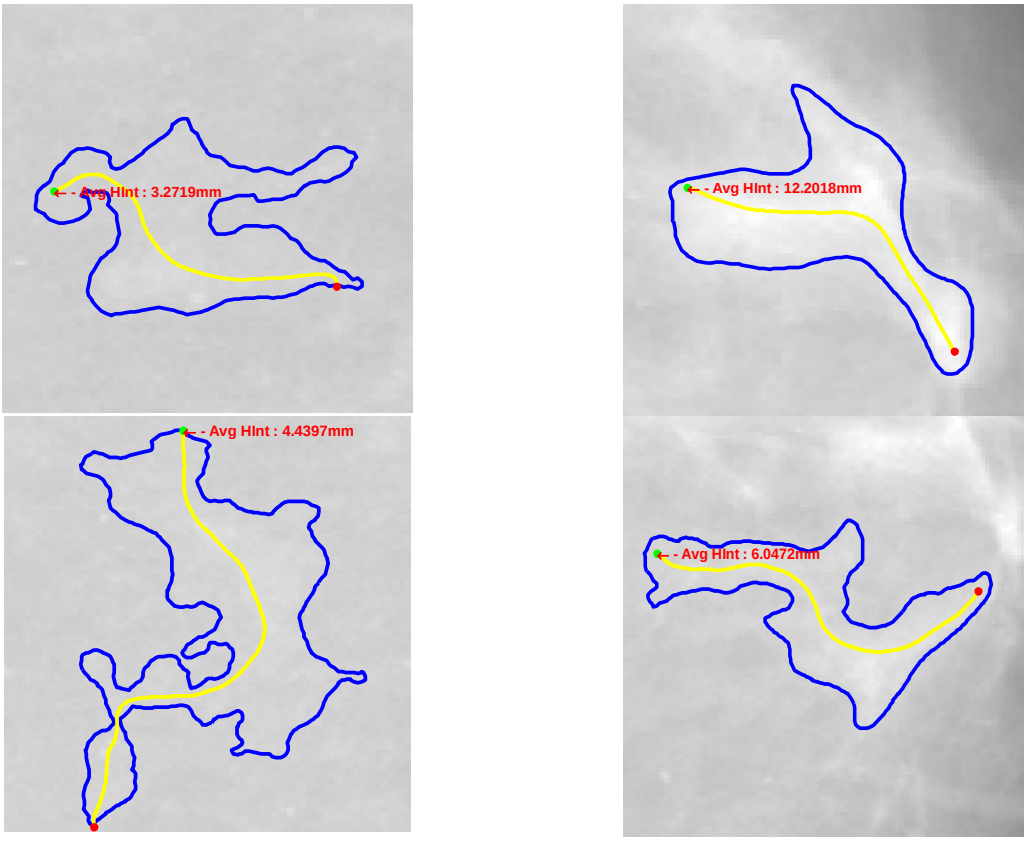

Figure 5.12: Geodesic path obtained by the Fast Marching Algorithm following density of regions inside breast regions

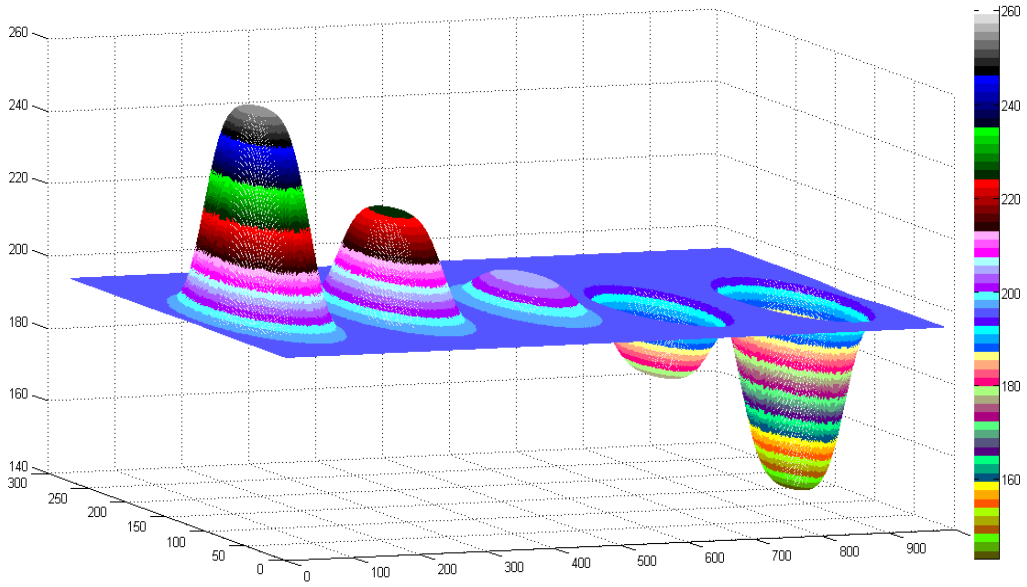

Figure 5.13: A simulation surface in a false colour model

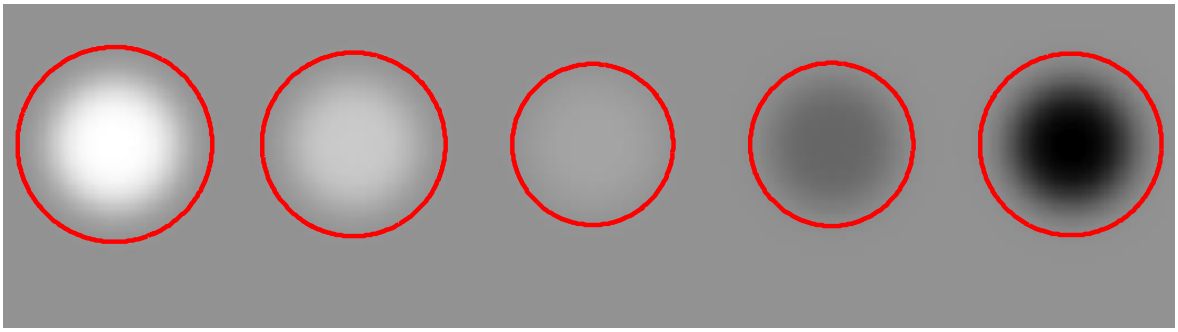

Figure 5.14: Segmentation of the surface given in Figure 5.13.

Figure 5.15: Final results from false positives reduction method.

It can be seen in Figure 5.15 that both less bright and all dark regions are eliminated by this process. Based on the *T* values, the method can grade regions based on the probability that it is of interest. This grading and selection of very bright to less bright regions is dependent on

the threshold, which is user defined and is application specific. In particular, a very different range of thresholds will be used for intensity mammograms and for SAR images. However, darker regions will generate a negative value of T and will be automatically discarded. Figure 5.17 shows segmentation of another synthetic image, which has a variable texture in its regions, whereas as its profile is given in Figure 5.16. False positive reduction method has not only reduced the number of uninteresting regions but also graded the remains with a certain user defined confidence level, as shown in Figure 5.18. Before we apply the method to density maps, it is applied to mammograms from the USF database. Figure 5.16 shows the intensity profile scale space of surface in Figure 5.13.

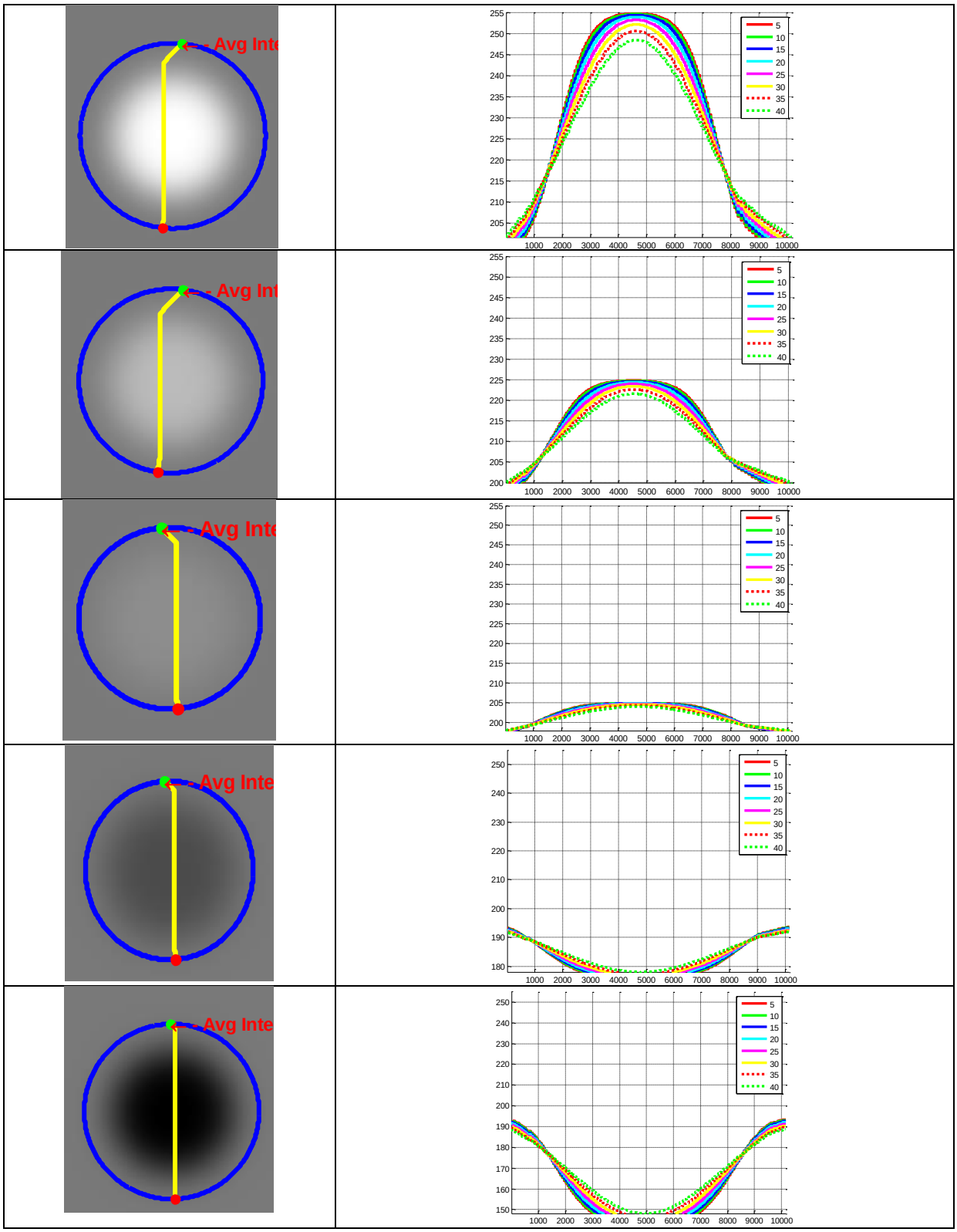

Figure 5.16: Scale Space of Segmented regions

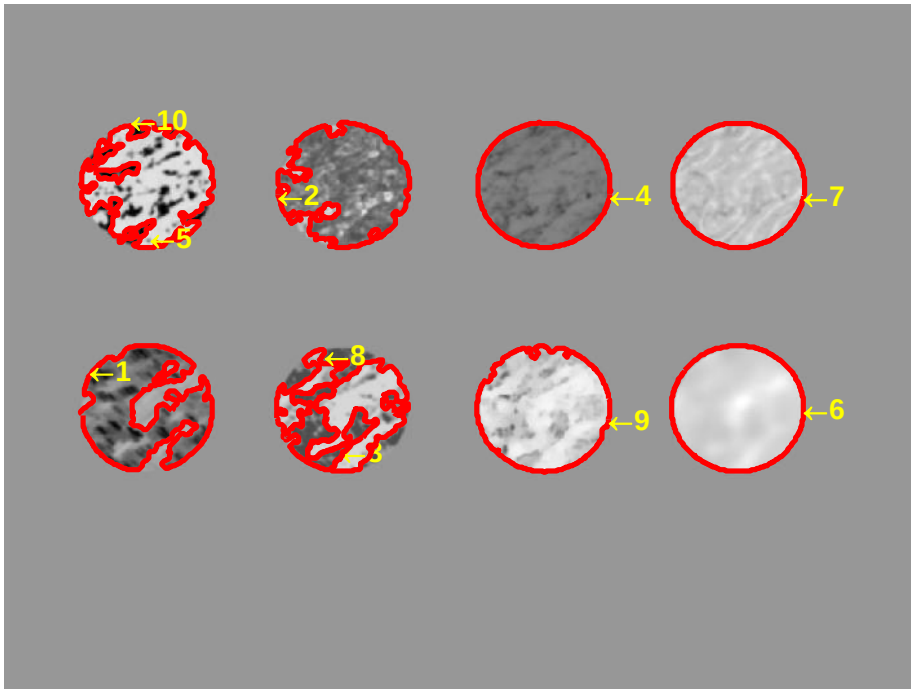

Figure 5.17: Segmentation of a synthetic image with texture

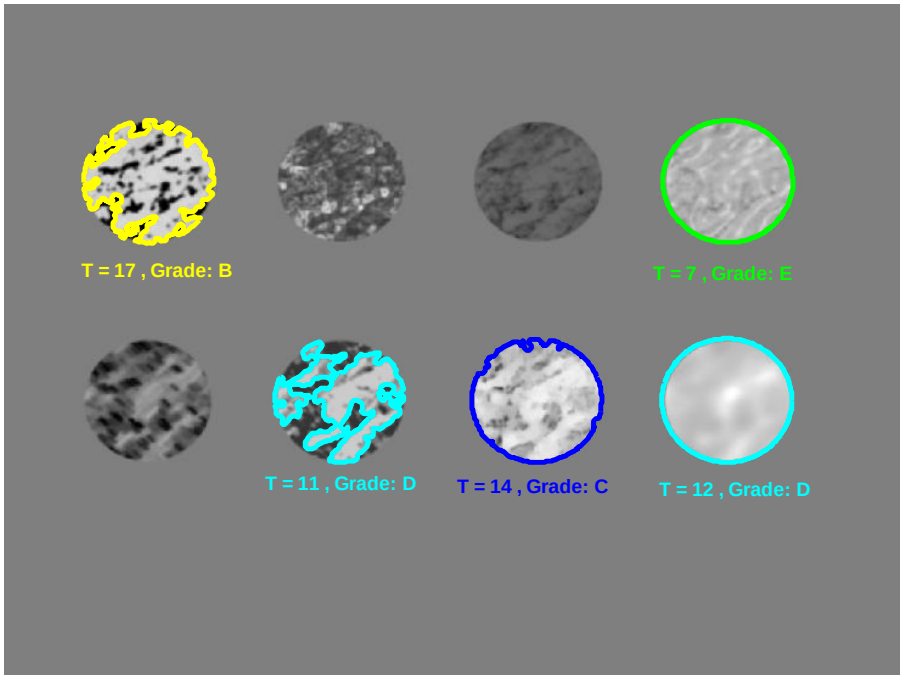

Figure 5.18: Outcomes of false positives reduction method applied on Figure 5.17

. Figure 5.19 shows a mammogram from the USF database, segmented into a number of regions and the corresponding ground truth. It can be noted that a large number of false positives are segmented along the region of interest.

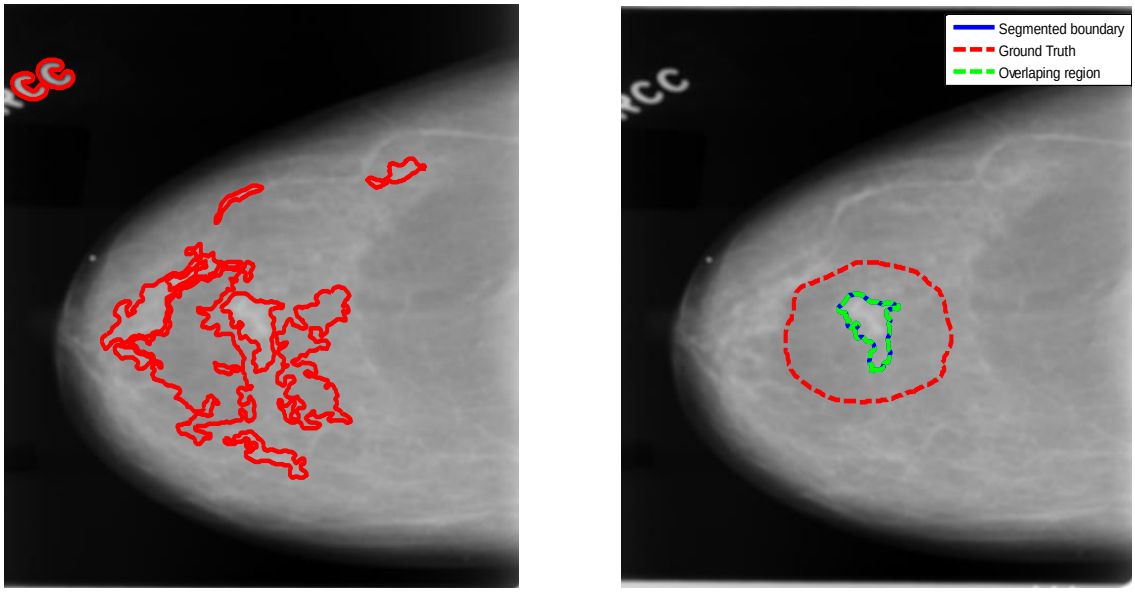

Figure 5.19: A segmented mammogram on the left, whereas the ground truth and the segmented boundary of ROI on the right.

. The scale space of certain regions is given in the Figure 5.20. Other examples are given in Figure 5.21, with very promising results.

We have applied the method to density maps generated by Volpara. We find a significant decrease in the number of false positives. Figure 5.22 shows a pair of segmented temporal mammograms with overall volumetric densities respectively of 54mm^3 and 52mm^3 for Figure 5.22(a) and 5.22(b) respectively. The grading of T is given in Table 5.1, which is estimated empirically for this example. At this stage, we do not know if there are any abnormalities in mammograms, and the goal of applying false positive algorithm is to retain regions, (a) which are dense; (b) and survive over causal scales of integral invariants diffusion. Both these factors

are considered in order to assess the saliency. A higher grade of T value means larger probability that the region is suspicious (and so is listed for further analysis). The outcome of the false positive reduction method for this example is given in Figure 5.23. Note that both temporal mammograms are processed independently. Examples of density mammograms processed by this method are given in the appendix 1. It is not known whether or not those mammograms contain abnormalities.

Grade	A	B	C	D	E
T Value	1.2	1	0.8	0.6	0.4

Table 5.1: Grading of mammographic regions in density maps based on T values, which are set empirically based on the observation. However, a better estimate may be used by consulting a radiologist and classify regions based on their likelihood to be a mass.

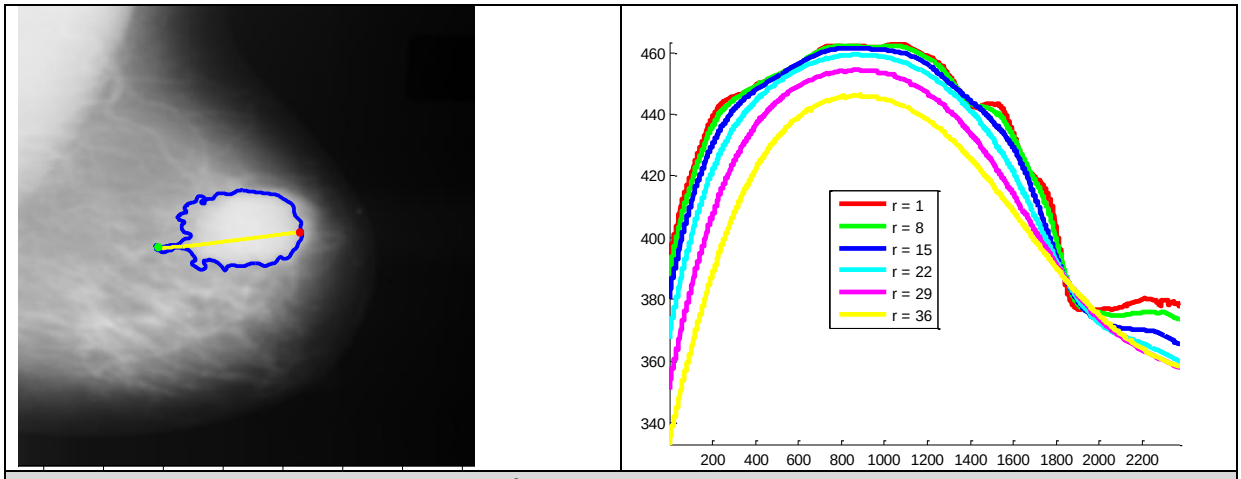

A cancerous mass

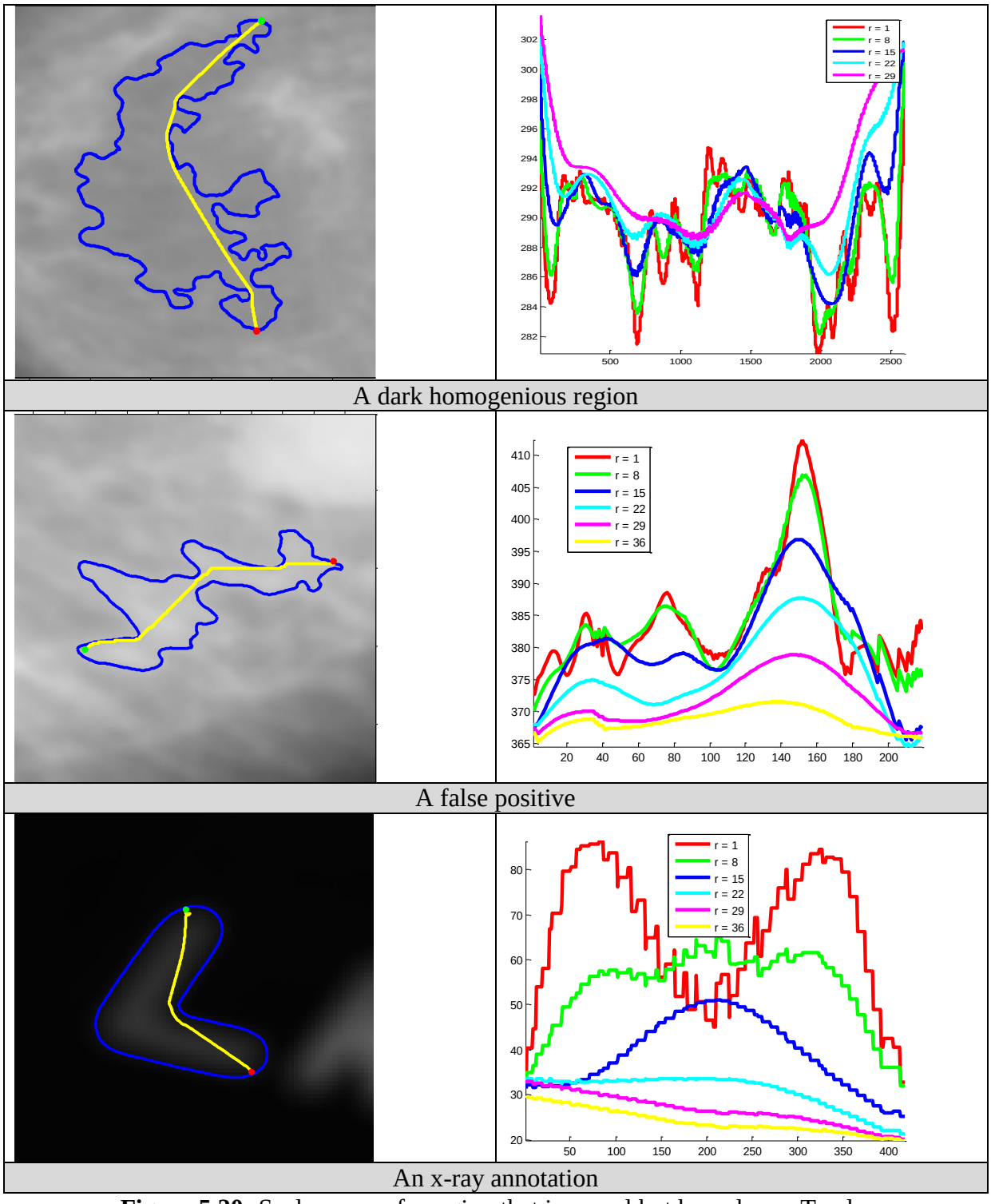

Figure 5.20: Scale space of a region that is causal but has a lower T value

5. 6. Conclusions

We observed the properties of Integral Invariants scale space and used this scale space to reduce the number of false positives in mammograms. The causality principle here is used throughout the thesis for shape analysis, matching and correspondence. The false positive reduction technique has been applied to the University of South Florida database, with promising results. The density mammograms used here are not known for any abnormalities, though the numbers of segmented regions are reduced and the retaining dense regions are graded accordingly.

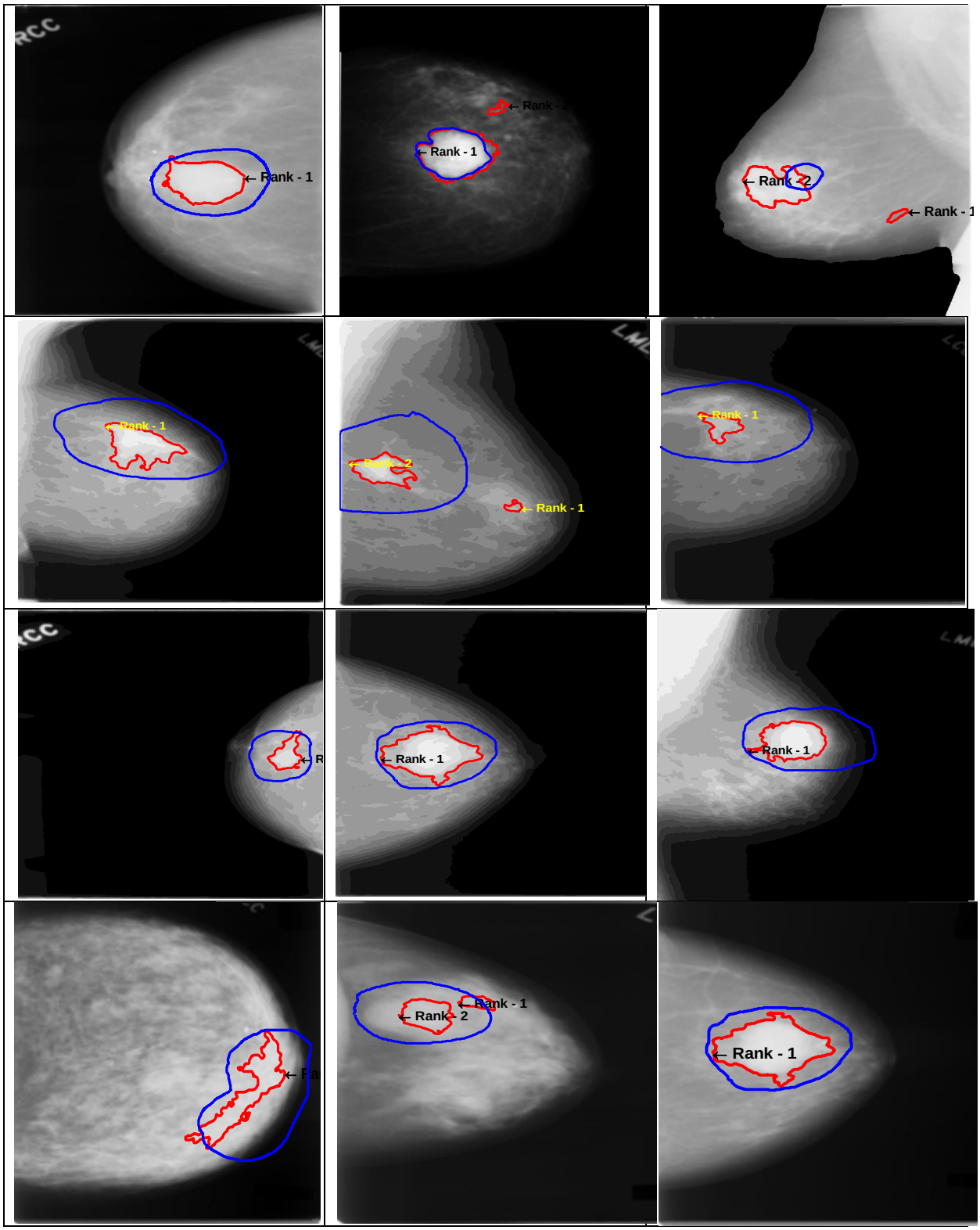

Figure 5.21: Examples of segmented mammograms using the illustrated method with reduced false positives. Rank 1 and 2 defines grades of segmented regions, i.e. their likelihood to be a mass. Rank shows the likely hood or the preference of a certain region to be considered as a suspicious region. A higher ranker represent a greater score of T in a single image.

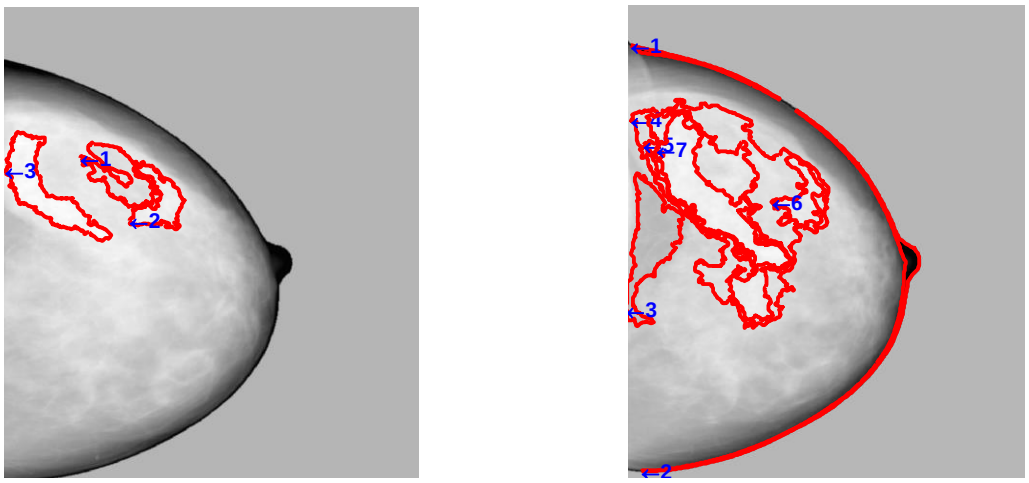

(a) (b)

Figure 5.22: A segmented pair of temporal Volpara® density maps

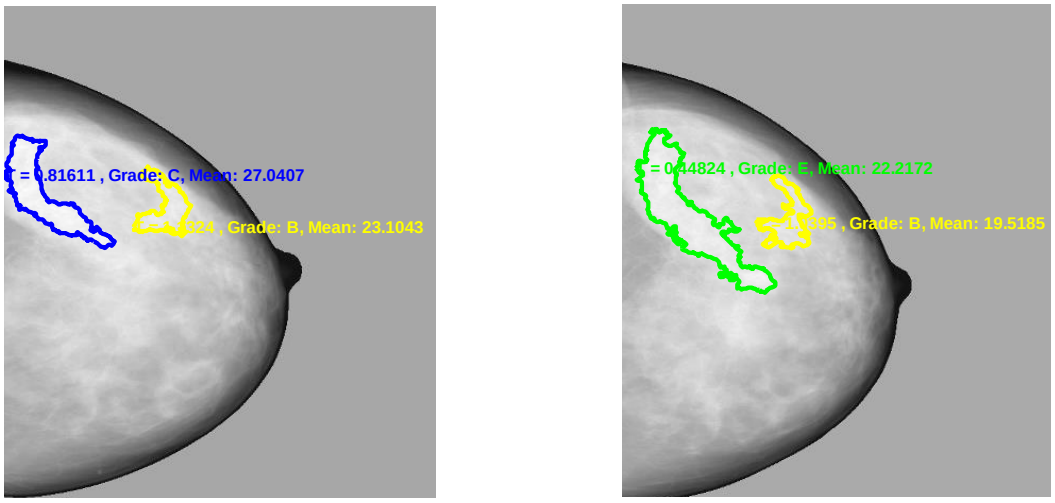

(a) (b)

Figure 5.23: Outcomes of false positive reduction method applied to the temporal density mammograms shown in Figure 5.22

Chapter 6

INTEGRAL INVARIANTS FOR IMAGE ENHANCEMENT

6. 1. Introduction

Before attempting to segment masses, it is crucial to remove image noise. The choice of noise removal methods and the amount of allowable noise in an image is application specific. Noise can cause significant problems while extracting the boundaries of regions in mammograms. It can result in contours that are jagged or discontinuous; moreover noise can generate contours at insignificant levels of intensity variations inside an image. For these reasons it is important to smooth an image so that unimportant details are suppressed, whereas edge information is retained.

Typically, in image analysis applications, a Gaussian filter is used to suppress noise by diffusing the intensity content of an image. The problem with a Gaussian filter is that the diffusion process is isotropic and homogeneous. This means that it does not have a preferred location or direction and, in particular, it blurs image locations that are significant intensity changes (e.g. edges). Applying a Gaussian essentially amounts to a low pass filtering of the image, essentially assuming that the high frequency component of the image is of little or no consequence. This is clearly not true at edges, and, in the case of mammography, the high frequency content - microcalcifications, curvilinear (ductal) structures, and spicules of masses are of major clinical significance. The challenge, therefore, is to remove noise so as to enhance the image for human or machine analysis while not suppressing clinically important high frequency content. One way to approach this is to use anisotropic diffusion, such as the Perona Malik noise removal filter. Anisotropic diffusion is an iterative process and becomes

computationally very expensive if the number of iterations are too high. Here we explore the use of Integral Invariants as a smoothing kernel, which will eliminate the use of a separate noise removal filter in a shape analysis application. In the previous chapter, we studied the scale space properties of Integral Invariants, which have been applied linearly in all directions in an image. In this chapter, we applied them for image smoothing and compare the results to anisotropic diffusion (Perona Malik as a case study) and Gaussian diffusion.

6. 2. Perona-Malik Anisotropic Diffusion Filter

The Perona-Malik (PM) filter aims to reduce noise in an image while preserving important information such as edges and corners. In practice, PM works similar to the process of creating a scale space, where an image is convolved with a family of convolution kernels that increase in width to form a scale space. However, PM is non-linear and spatially variant in its application over an image. It computes a filter shape that is elongated and has an orientation that is adapted for each point in the image (at each scale). It smooths a region within its bounds that are significant edges or lines of a certain strength, and not across the bounds.

It diffuses the gradients under a given threshold value with a low contrast and enhances the opposite with a high contrast. A regularised Perona-Malik filter is used to constrain the amplification of edges degraded due to noise. It is insensitive to structures smaller than size of the Gaussian kernel that is convolved with the original filter. An anisotropic diffusion tensor is used to prevent smoothing across edges and enhances smoothing along them; this property is the reason that the Perona-Malik filter is called anisotropic or directional. Figure 6.1 and Figure 6.2 shows the effect of noise removal by the Perona-Malik anisotropic diffusion filter. For detailed information about the PM see [282].

It may be observed from the Figure 6.2 that the number of contours following diffusion is much less than that of the contour map in original image. Reduction in the number of contours after noise removal process depends on the amount of noise present in an image, the strength of the margins of an ROI to be segmented, and various other factors. It will reduce the computational cost of processing unimportant details by dealing with fewer contours.

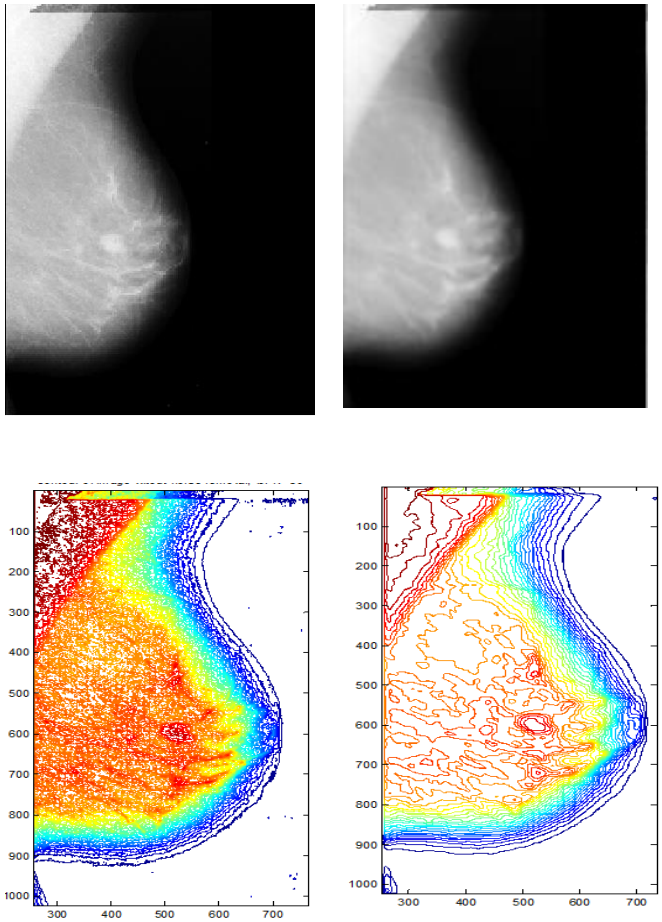

Figure 6.1: First row: on the left, *mdb010* without smoothing by Perona-Malik diffusion filter and on the right mammogram after 30 smoothing iterations. The number of contours mapped are reduced as a result of smoothing.

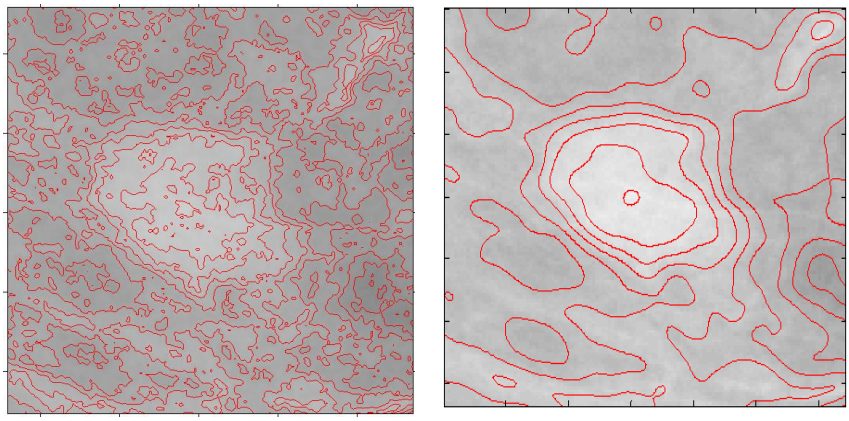

Figure 6.2: On the left, contour mapping of a suspected mass in Figure 6. 1 before removing noise; plot of contours after removing noise is shown on the right

The diffusion process smooths the contours giving it a more focused look. Intense smoothing may reduce the noise considerably and reduce the number of contours; nonetheless, it can affect the shape of contours by over smoothing them by diminishing the spicules, as can be seen in Figure 6.3, which is important for breast masses. PM is an inhomogeneous process which reduces diffusivity at those locations which are likely to be edges. The likelihood is measured by $|\nabla u|^2$.

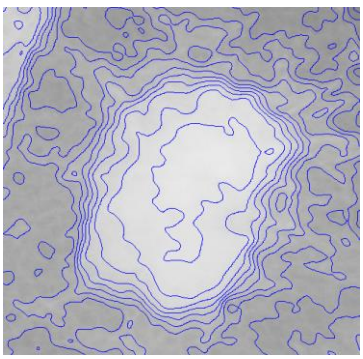

ROI after 10 Perona-Malik Iterations

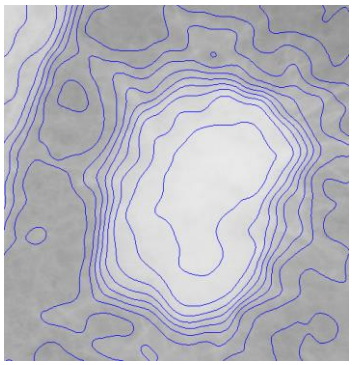

ROI after 50 Perona-Malik Iterations

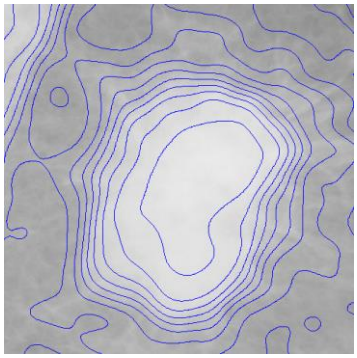

ROI after 100 Perona-Malik Iterations

Figure 6.3: Behaviour of contours after various anisotropic smoothing iterations

The diffusing equation is given by,

$$\partial_t u = div(g(|\nabla u|^2)\nabla \mathrm{u}), \text{ Such that, } \quad g(s^2) = \frac{1}{1+ s^2/\lambda^2} \ (\lambda > 0)$$

Here u is the density of the diffusion kernel, λ controls the sensitivity to the edges and $g(s^2)$ denotes the diffusion coefficient and control the rate of diffusion.

6. 3. Integral Invariant vs Perona-Malik Noise Suppression

A question arises if noise reduction/smoothing using an Integral Invariants kernel is sufficient to avoid a separate noise removal filter. To investigate that question, we compared the performance of Integral Invariant (II) smoothing to Perona-Malik anisotropic diffusion for noise suppression and the deterioration of structures in images. To this point in our thesis, we have used PM as a noise removal filter; however, further we will use Integral Invariants both as a shape descriptor for the segmented regions in mammograms, as well as an image enhancement filter to supress noise.

Integral Invariants can operate at different scales by changing the radius whereas the action of Perona-Malik (PM) usually tunes upon the number of iterations over which it is applied at a fixed scale. Here we attempt to compare the performance of PM and II at analogous scales, though the comparison of scale in II to that in PM is not straightforward, as we discuss in the next subsection.

6. 3. 1. Finding Comparable Scales

Before we relate the performance of the two methods, it is important to select approximately corresponding scales for Perona-Malik and Integral Invariants. The radius of integral invariants and the number of iterations for the Perona-Malik are independent of each other and

are parameters of two quite different methods and are not easy to compare. The amount of diffusion or conduction in anisotropic Perona-Malik is less than that of isotropic methods so there is diffusion within the regions and not across edges. Perona-Malik is anisotropic; however, it may result in substantial blurring if the conduction coefficient for diffusion across the edges is insufficiently high, in which case it will have an isotropic effect on the image. If the conduction coefficient is too low then the filter may fail to effectively recover the signal from noise. Scales are found in conditions where both Perona-Malik and Integral Invariant diffuse intensities similarly. The conduction coefficient k for Perona-Malik controls the amount of diffusion. If we can find a value of k for which Perona-Malik gives similar diffusion of an image to that of Integral Invariant, then we can find comparable scales in terms of the Integral Invariant kernel size and the number of iterations for Perona-Malik. At this stage it is enough to estimate it empirically.

This is done by examining the signal to noise ratio (SNR) of the resulting images after diffusion. The more images are diffused, the more information is lost and the less the SNR will be. Higher diffusion is achieved by increasing the radius r of Integral Invariant or the number of iterations n in Perona-Malik. However, the latter depends not only on n, k has been found to be important to control the amount of diffusion.

The images here do not possess any noise. For the purpose of establishing correspondence between the scales; the conduction coefficient ‘k for Perona-Malik is fixed at 450 and is found empirically for the purpose of finding roughly corresponding scales. The reason for using such a high value of k is that with a certain number of iterations it almost matches the amount of diffusion of the Integral Invariant while giving a more or less isotropic effect. Once we have

found the corresponding scales, then we can use a more typical value for k, which is suitable for mammographic images.

We have compared the SNR of a noiseless image after applying both diffusion methods. Then we optimize k and r to result in a close match of resulting SNR. The process is carried out until the error is minimized. The results are presented in Table 6.1 and the SNR for corresponding scales is given in Figure 6.4. First, comparable scales are found at equal levels of diffusion by using SNR as a matric, then the two methods are compared in standard conditions using these scales.

r - Integral Invariant radius in pixels	1	2	3	4	5	6	7	8	9
n - Perona-Malik iterations	1	3	6	9	15	22	29	38	47

Table 6.1: Corresponding scales of Integral Invariant and Perona-Malik at *keppa (k)* equal to 450. The radius of integral invariant is outward from the centre of the mask.

Consider for example two cases: r = 3 & n = 6; and r = 9 & n = 47. We follow the profile of intensity diffusion in a series of 'star' shapes given in the phantom image. We choose to follow the star shape at this point because it resembles a spiculated mass. Figure 6.6 presents the diffusion of intensity on the line shown in Figure 6.4 across the star shaped objects. Similarly, the intensity profile for all the scales given in the table were found to confirm that the Integral Invariant and Perona-Malik scales correspond to each other.

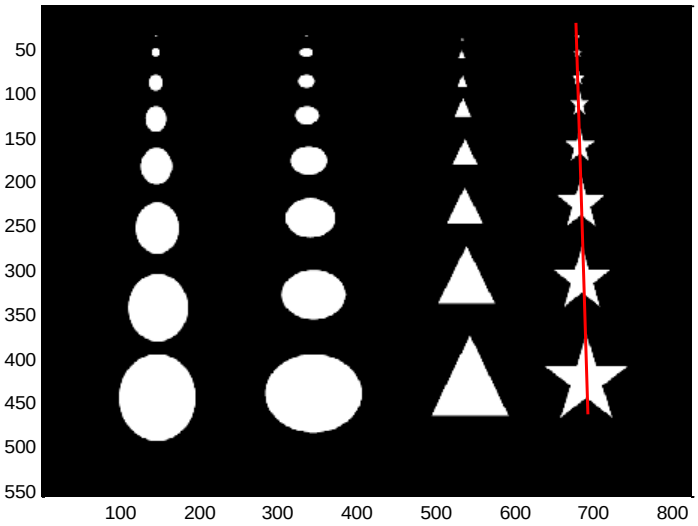

Figure 6.4: The red line across the *star* shape is the intensity profile followed in Figure 6.6

We note that the SNR depends upon the amount of diffusion in a noisy image. Secondly, in the given conditions the amount of diffusion for Perona-Malik and Integral Invariant is roughly the same. Hence we may say that the scales correspond to each other.

It has to be noted that as we increase the scale of integral invariants, the diffusion becomes more pronounced and smaller objects start disappearing as their intensity profile is flattened. As we can also see in that Figure 6.6, the shapes range from large to small as we go from left to right. Following the causality principles, no new peaks or objects emerge as a result of diffusion.

From the figure 6.6, and object in question as explained above, one end of the shape is a convex top of star which falls on itself after diffusion, the other end in concave bottom, which expands downward. Thus it shifts the intensity pattern from right to left and makes it asymmetric to the original figure. This does not happen when we dissect vertically through a rectangular shape.

As these scales approximately correspond to each other in their results we use them in the

remainder of the chapter. Our goal here is not to achieve identical results after diffusion but to evaluate the performance of Perona-Malik and Integral Invariant under standard conditions.

6. 4. Performance Comparison of Perona-Malik and Integral Invariant without Noise

The value of *k* is usually set between 10–100 depending upon the nature of the image and amount of noise. We have found that *k* equals 30 is usually sufficiently high to deal with a high resolution mammogram. A higher value of *k* preserves edges to a much lesser extent.

For the coefficient of conduction, the deterioration of image features by the Perona-Malik is less than that of the Integral Invariant. This is because the diffused image, after applying Perona-Malik, has preserved the edge information more effectively than that of Integral Invariant. Figure 6.8 shows the effect of deterioration of small objects in the Integral Invariant diffusion as compared to Perona-Malik. We can see that though the SNR at the lower scales are quite different; the intensity profile is very similar for bigger objects. As stated before, isotropic diffusion leads to more deterioration of smaller objects.

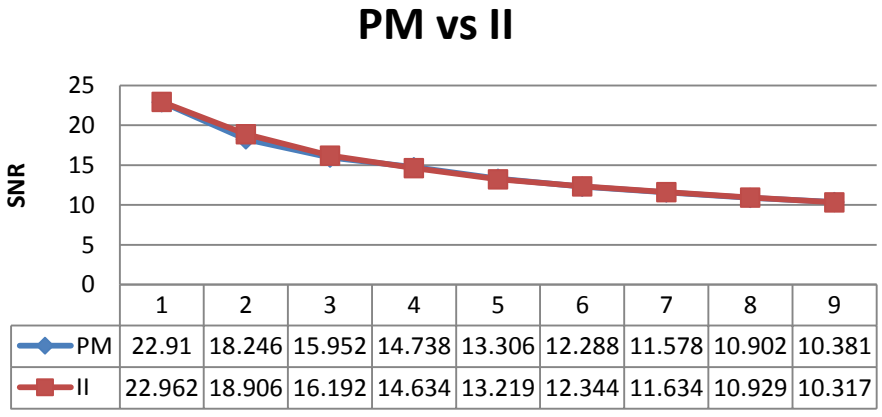

	1	2	3	4	5	6	7	8	9
PM	22.91	18.246	15.952	14.738	13.306	12.288	11.578	10.902	10.381
II	22.962	18.906	16.192	14.634	13.219	12.344	11.634	10.929	10.317

Figure 6.5: Comparison of SNR of the noiseless phantom image given in Figure 6.4 when applied Perona-Malik and Integral Invariant *at k* = 450 for all scales in Table 6.1. It shows that the scale corresponds to each other in the given conditions, as confirmed in the Figure 6.6.

Since the Integral Invariant suppresses noise more, the signal-to-noise ratio (SNR) for it will be always less than that of an anisotropic method at corresponding scales, as shown in Figure 6.7. Therefore, we do not rely on SNR to compare the performance of two.

A star shape is used here not only because it has a spiculated shape, which a malignant mass more likely has, but also because the two end of this shape i.e. concave and convex, behaves differently to the process of diffusion. The convex end falls upon itself and is deteriorated quickly whereas the concave end expands between the two arms of the star.

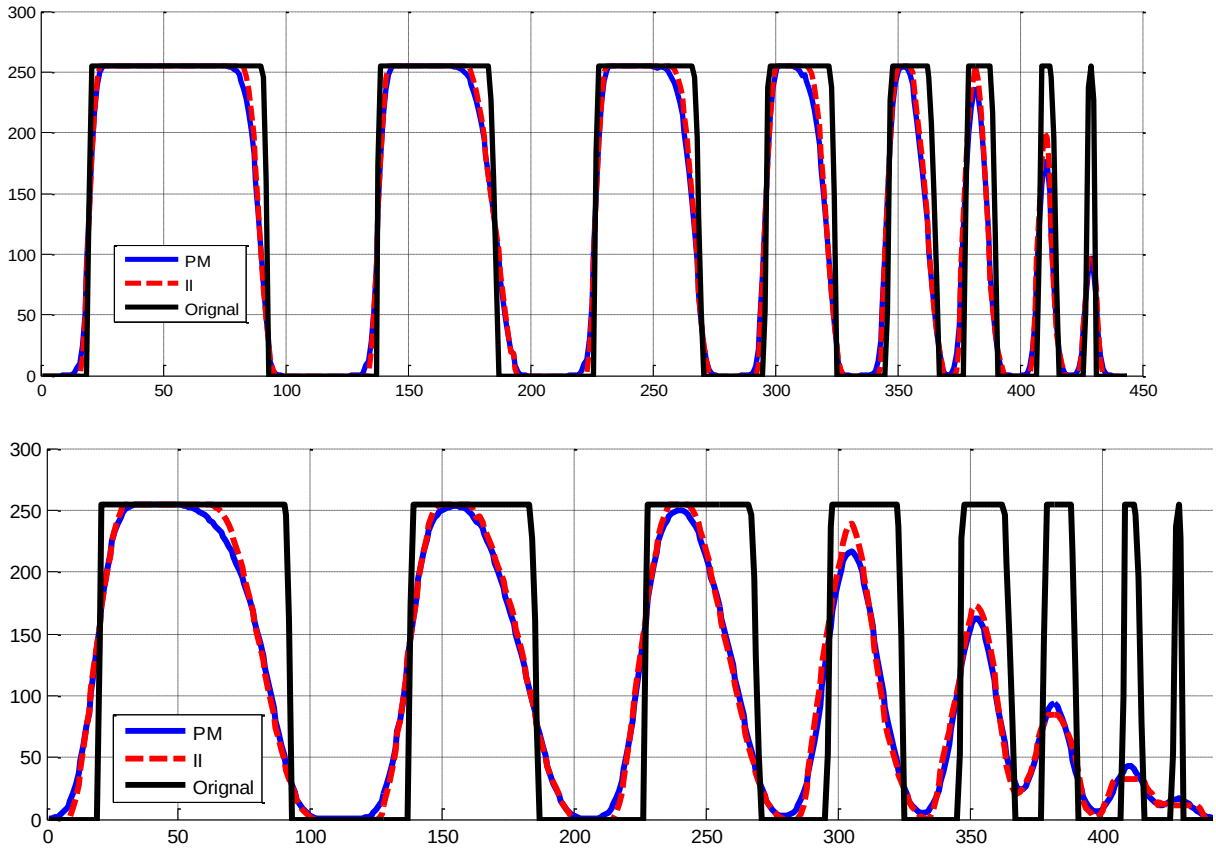

Figure 6.6: Intensity profile for Integral Invariant (upper) and Perona-Malik diffusion (lower). This is done at corresponding scales r = 3 and n = 6 in the top row and r = 9 and n = 47 in the bottom row of a star shape series in Figure 6.4. *Original* represents the intensity profile when the image is not diffused.

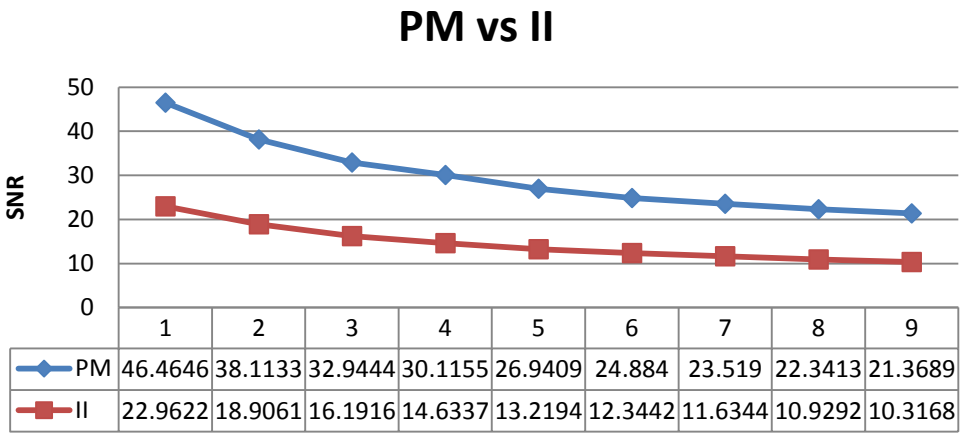

	1	2	3	4	5	6	7	8	9
PM	46.4646	38.1133	32.9444	30.1155	26.9409	24.884	23.519	22.3413	21.3689
II	22.9622	18.9061	16.1916	14.6337	13.2194	12.3442	11.6344	10.9292	10.3168

Figure 6.7: SNR of Perona-Malik and Integral Invariant at scales in Table 6.1 under standard conditions i.e. *keepa = 30*

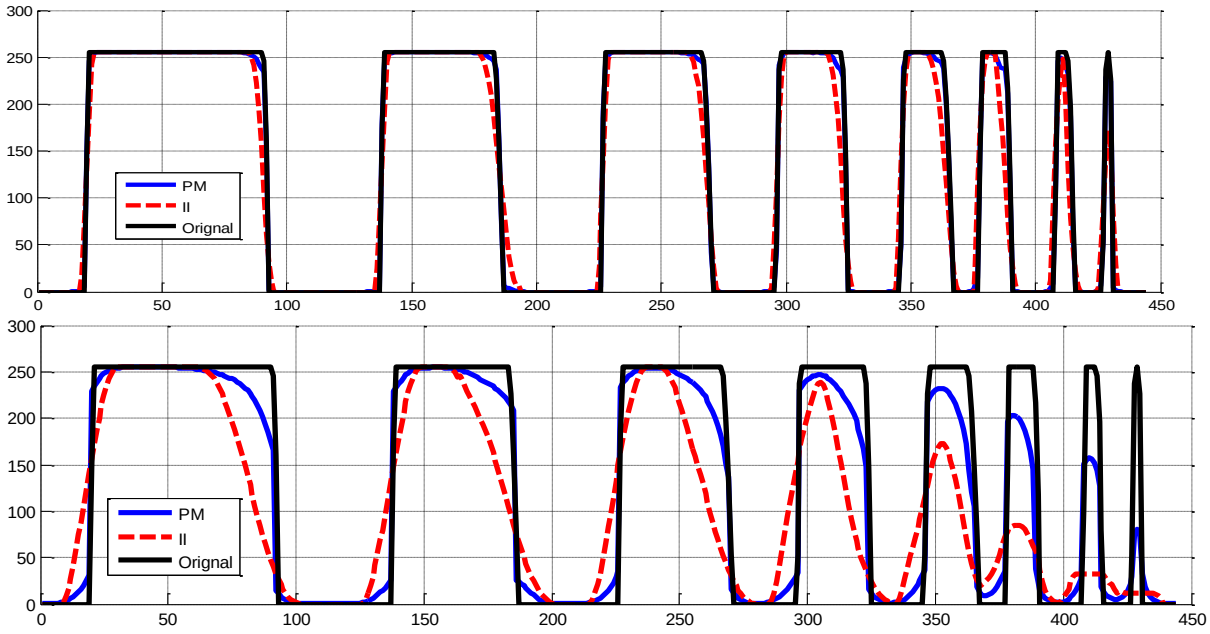

Figure 6.8: Intensity profile of line followed in the noiseless image in Figure 6.4 for Integral Invariant and Perona-Malik at *k* = 30. Top row show the intensity profile from the diffused phantom at r = 2, n=6. The second row shows intensity profile at the highest scale, r =9 and n = 47.

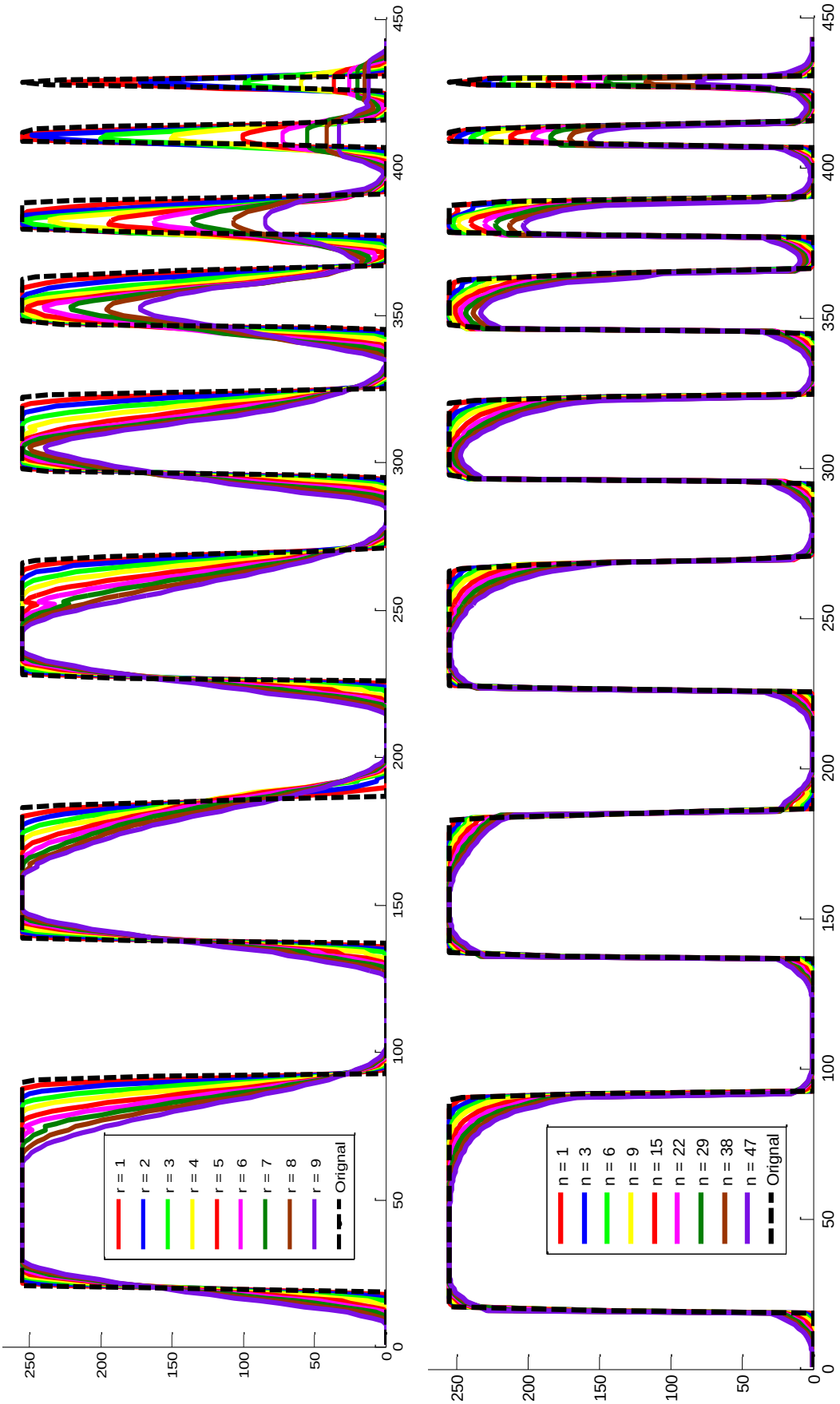

Figure 6.9: In the top row, we have intensity profile scale space of Integral Invariant applied on the star shape series. Whereas in the bottom we have the corresponding Perona-Malik scales space.

The noise suppression scheme affects the formation of contours around the ROI as discussed previously. Figure 6.9 illustrates this. The grey scale representation of the diffused phantom shows the blurring of the image. However, if we look at this using the HSV colouring model, we observe that the borders of objects in Integral Invariant diffusion has widened. This is also evident from the contour representation, where the Integral Invariant diffused image has a denser pattern of contours surrounding objects. Figure 6.10 compares the diffusion results of Integral Invariant and Perona-Malik. The shape edges are compromised in the case of Integral Invariant diffusion. However, the objects have attracted a denser pattern of contours surrounding them as depicted in the contour model, which is precisely what we need for the segmentation algorithm we use.

6. 5. Performance Comparison of Perona-Malik and Integral Invariant without Noise

To this point we have assumed that the image has no noise. We now apply various noise models and compare the output of both methods.

6. 5. 1. Example 1: Multiplicative Uniform Noise Model

Uniform noise models are usually used to simulate real-world imaging systems. It is hard for a linear averaging system to approximate the mean of a uniform distribution. Perona-Malik is a non-linear noise removal filter and should be efficient in dealing with such a noise model. On the other hand, Integral Invariants is a linear smoothing operation; however, it is more aggressive for its isotropic nature.

We observe that for multiplicative uniform noise, Integral Invariant performs better at the corresponding scales in smoothing the noise especially in the background, as shown in Figure

6.11, where the Perona-Malik diffused image has high and sharp peaks in the signal area that represent background regions even for a high number of iterations. On the other hand, in the Integral Invariant smoothed image the background is almost uniformly clear as its signal is very smooth for all scales except when the radius of Integral Invariant is just a single pixel.

Now keeping in mind the above examples, let us analyse the behaviour of Integral Invariant and Perona-Malik diffusion on scales relevant to mammograms. For this purpose, the radius of the integral invariant kernel $r = 3$ and the number of iterations for Perona-Malik is $n = 30$, where $k = 30$. A denser set of concentric contours are formed around ROIs that undergo Integral Invariant diffusion. In the examples above, it is observed that Integral Invariant enhances the borders of high contrast objects by expanding them, thus attracting more contours to surround them, as illustrated in Figure 6.15.

Figure 6.10 illustrates the contour model surrounding shapes in the phantom. The contours formed as a result of noise in the Integral Invariant processed image have irregular spiculated shapes with no nested contours. Whereas in the case of Perona-Malik, those contours are smooth and may contain nested contours.

We have applied the method to mammograms, for example, the one with a mass shown in Figure 6.17. The contour model of the mammogram smoothed by Integral Invariants has more dense contours surrounding the mass and so appears darker in the false color map. This facilitates the automatic detection and segmentation of the mass.

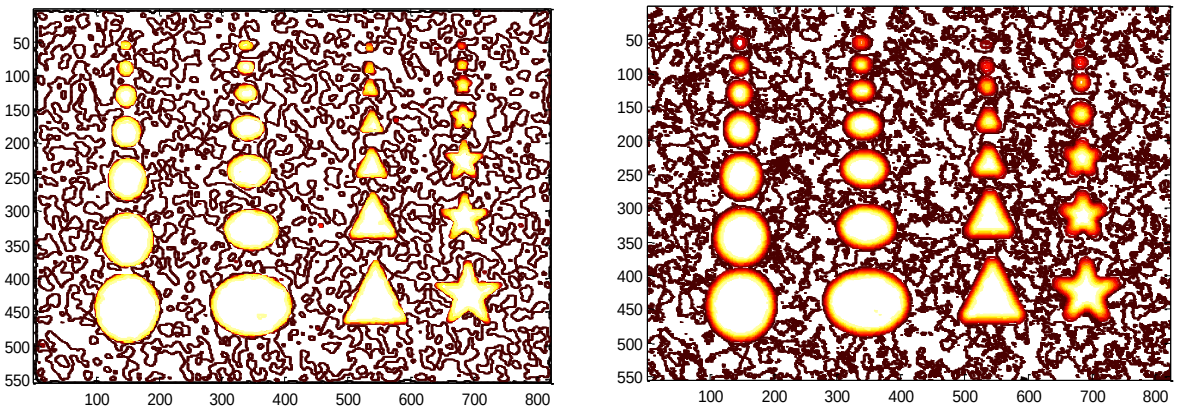

Contour model after Perona-Malik diffusion

Contour model after Integral Invariant diffusion

Figure 6.10: Diffused images and their corresponding contour maps

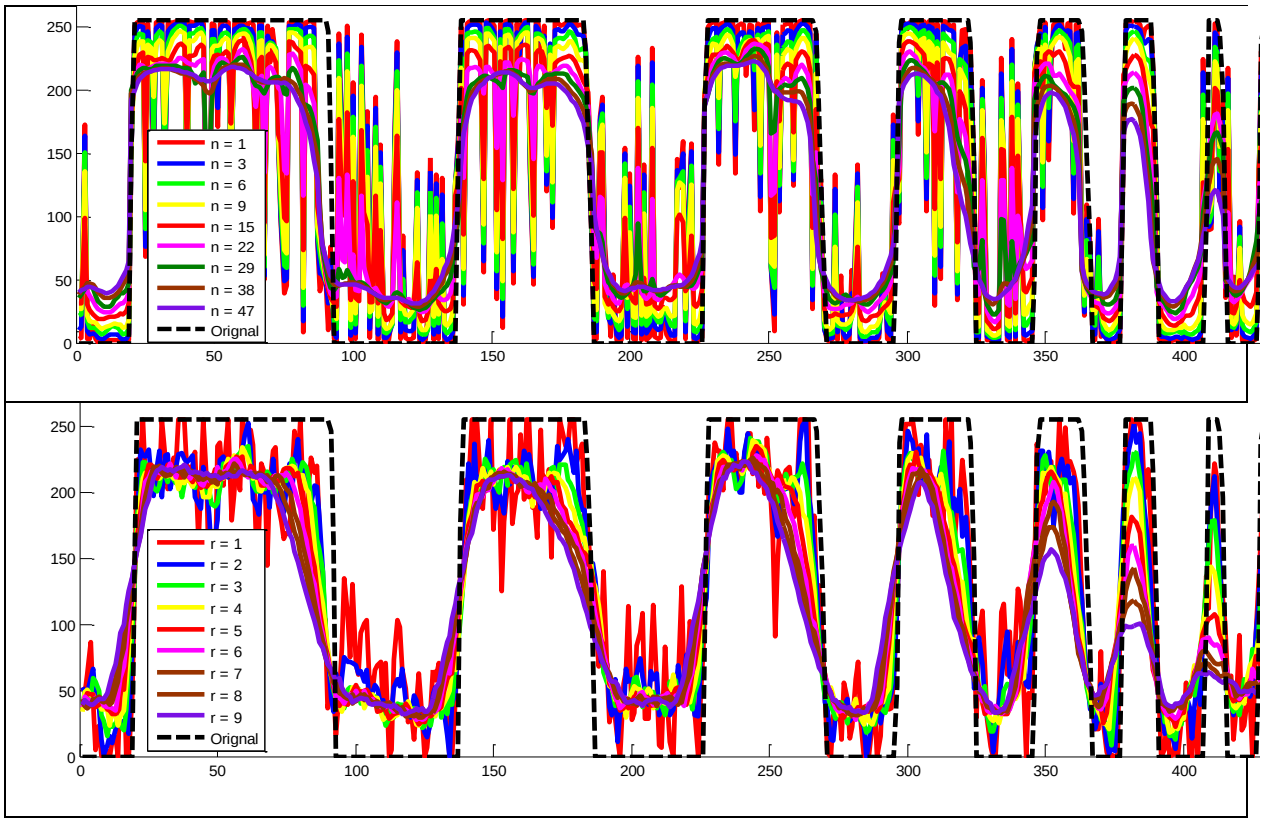

Figure 6.11: Upper row: intensity profile scale space of Perona-Malik applied on the star shape series. Lower row: the corresponding Integral Invariant scales space smoothing.

6. 5. 2. Example 2: Salt and Pepper Noise Model

Salt and pepper noise is added to the phantom image and the two techniques are applied on it. Integral Invariant can diffuse noise to get a uniform background with a much smaller scale than Perona-Malik. Concentric nesting of contours around the remnants of noise speckles can be seen in the background of Perona-Malik diffused image.

Figure 6.12 shows the results after diffusion and contour segmentation of the phantom image. It only confirms our previous observations, as integral invariants have thickened the border of the objects, helping segmentation. Figure 6.13 shows that Integral Invariants have more effectively faded the speckles in the background as compared to Perona-Malik.

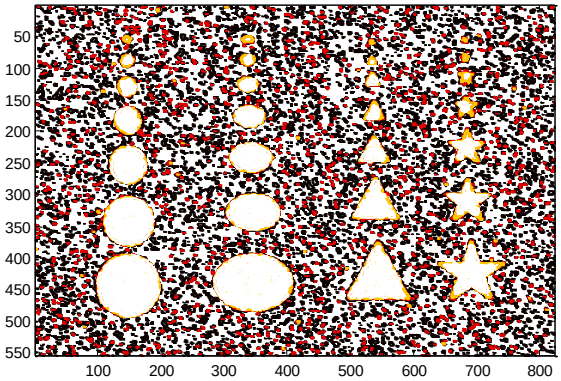

Contour model of Perona-Malik diffused image

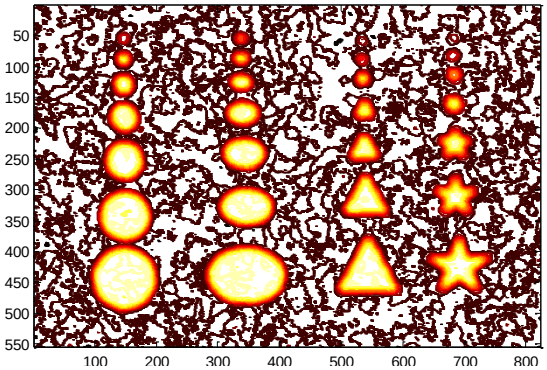

Contour model of Integral Invariant diffused image

Figure 6.12: A detailed example of Integral Invariant vs Perona-Malik diffusion for suppressing salt and pepper noise.

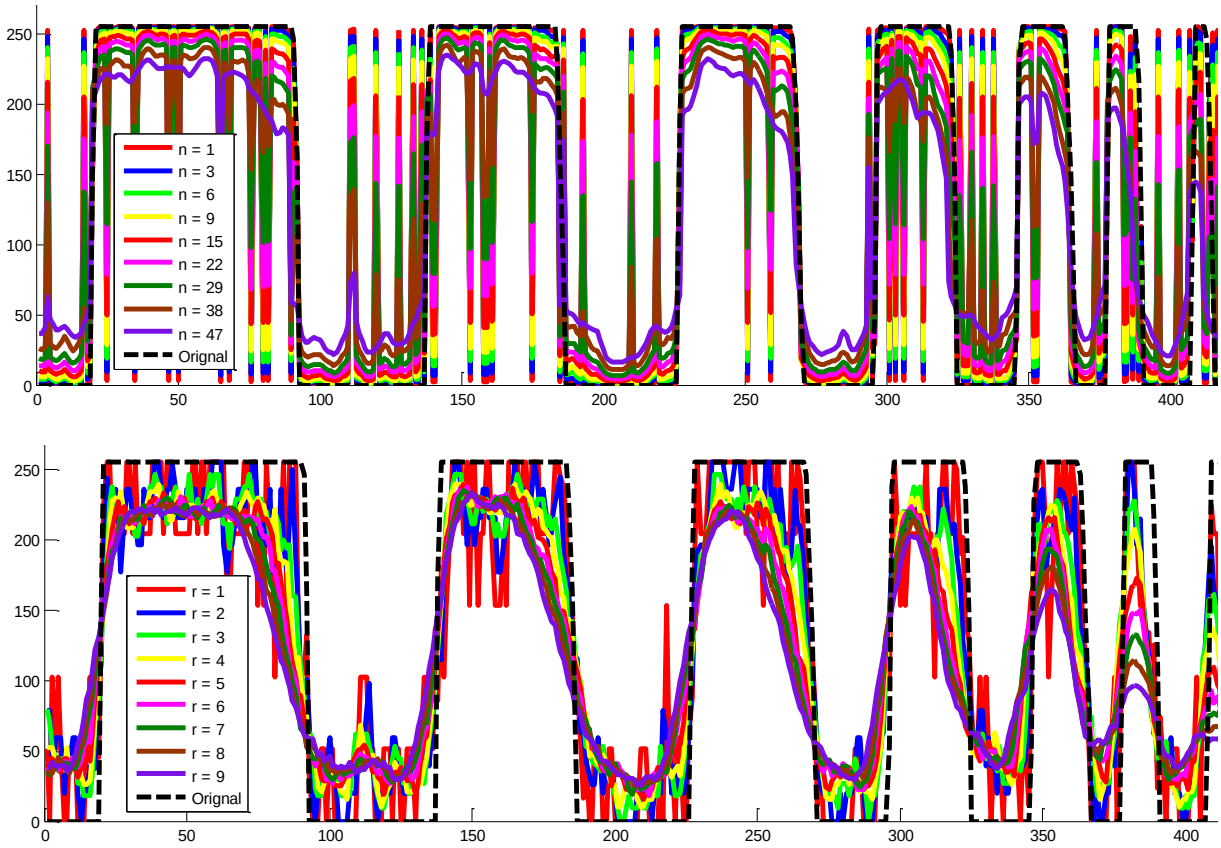

Figure 6.13: In the top row, intensity profile scale space of Integral Invariant applied on the star shape series. In the bottom is the corresponding Perona-Malik scales space. The original intensity profile of the shape is given in the black dotted line.

6. 5. 3. Example 3: White Gaussian Noise Model

Finally, we have applied the White Gaussian Noise model to the phantom image. Integral Invariants, as previously, reduce the noise more effectively than the Perona-Malik, as shown in the Figure 6.14.

We emphasise that in all the observations discussed for the various noise profiles here, Perona-Malik is less deteriorative to the shape borders and stays closer to the original intensity profile, taken from the phantom image.

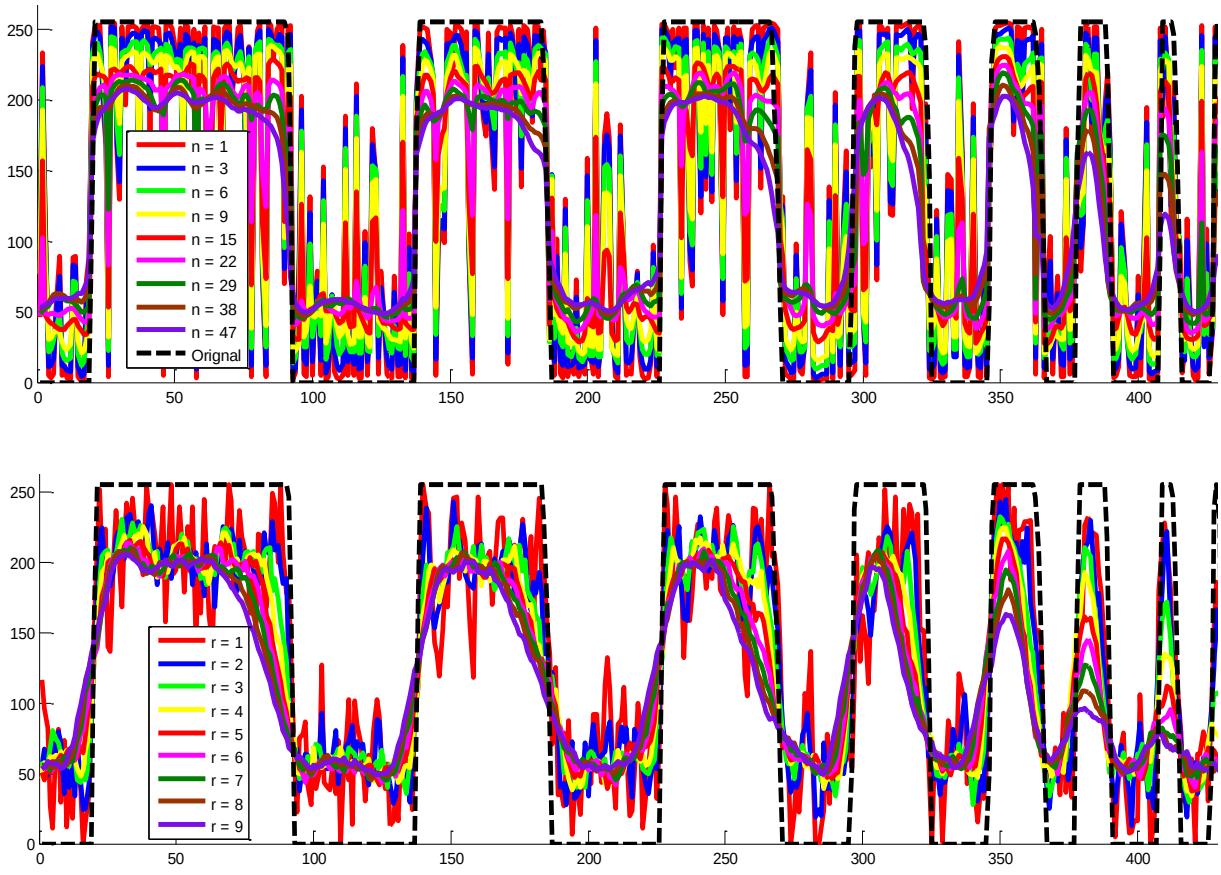

Figure 6.14: In the top row, intensity profile scale space of Integral Invariant applied on the star shape series. Whereas in the bottom is the corresponding Perona-Malik scales space suppressing White Gaussian noise.

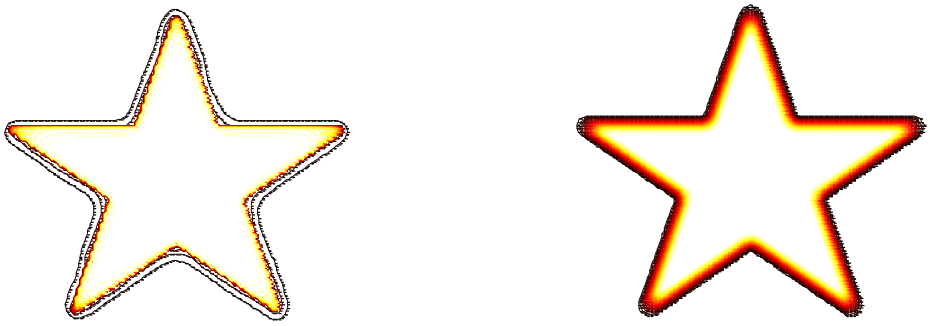

Contour map of a star diffused with Perona-Malik

Contour map of a start diffused with Integral Invariant

Figure 6.15: Contour maps of Integral Invariant & Perona-Malik at the scales used previously for mammograms.

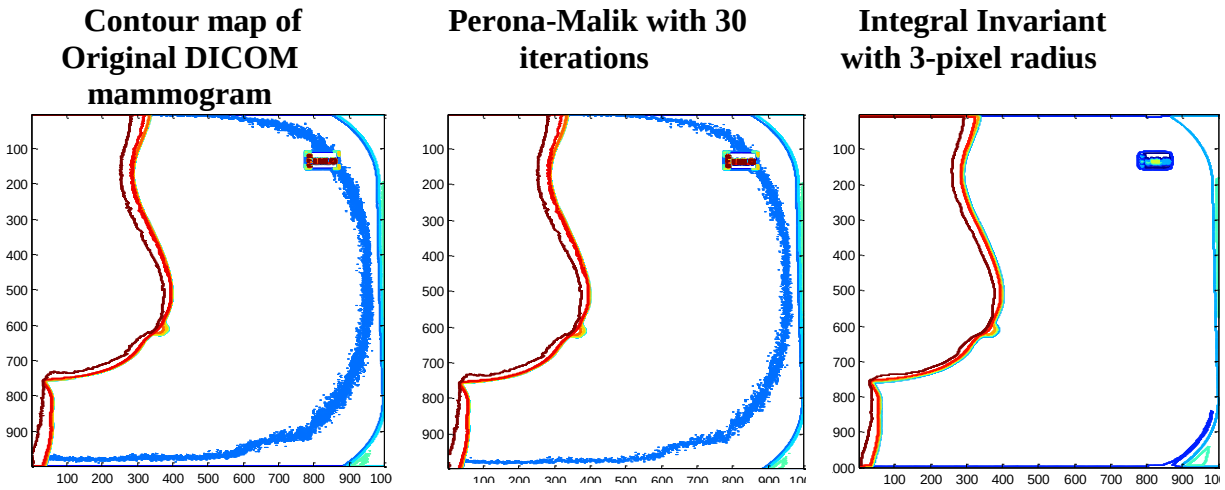

Figure 6.16: Intensity profile of Integral Invariant and Perona-Malik diffused images. A dust noise cloud layer shown in blue is present in the original image on the left. Perona-Malik reduces noise, however, does not completely remove it, as shown in the middle row. Integral invariants (on the right) remove the noisy layer completely while keeping the breast boundary unharmed.

In Figure 6.16, a mammogram is smoothed to remove noise. The original mammogram contains a layer of dusty noise (shown in blue), shown in (a) at the right end of the image that surrounds the mammogram concavely. In (b) PM is shown to have reduced this artefact. In (c), II has eliminated the noisy layer completely while the breast boundary is retained. Similarly, it enhances the region of interest for segmentation shown in Figure 6.17.

We observe that PM clusters high intensities at the borders of the image and induces an unwanted artefact that may give rise to new image structures. This may be problematic in applications where image borders contain important information. II does not induce such artefacts, as shown in Figure 6.18.

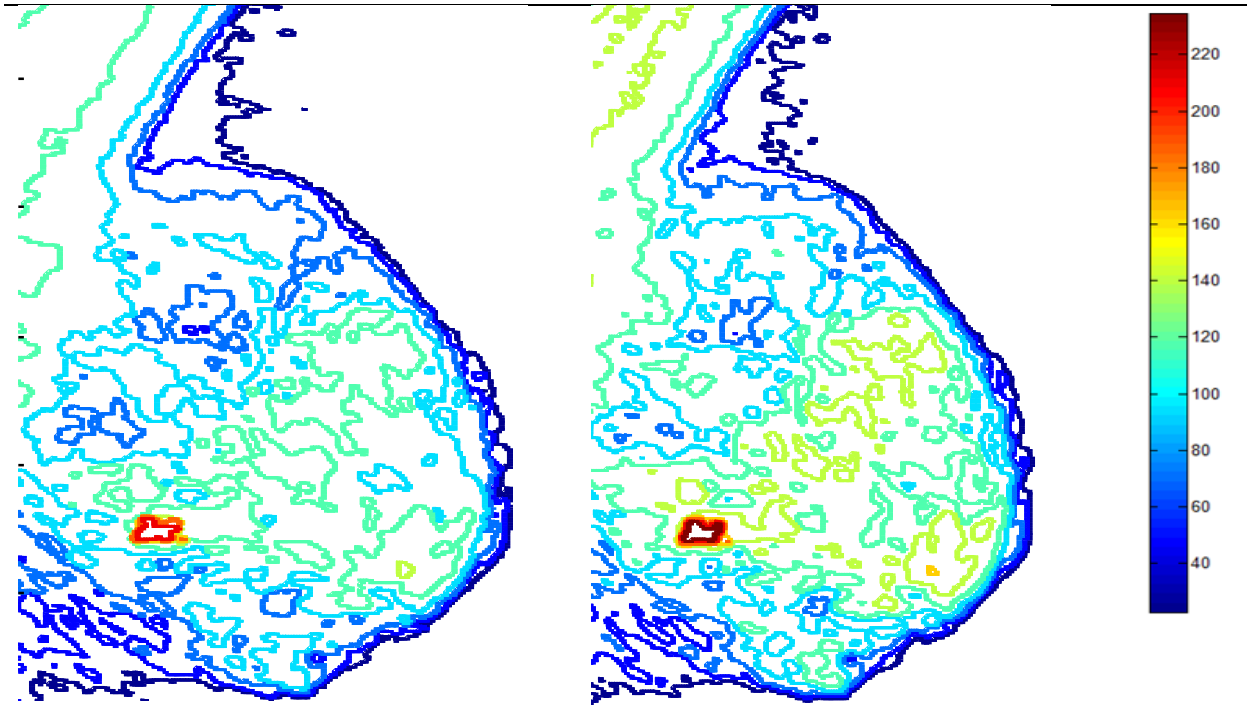

Figure 6.17: Contour model of an enhanced mammogram by Perona-Malik (left) and Integral Invariant (right). Integral Invariant has enhanced the region of interest.

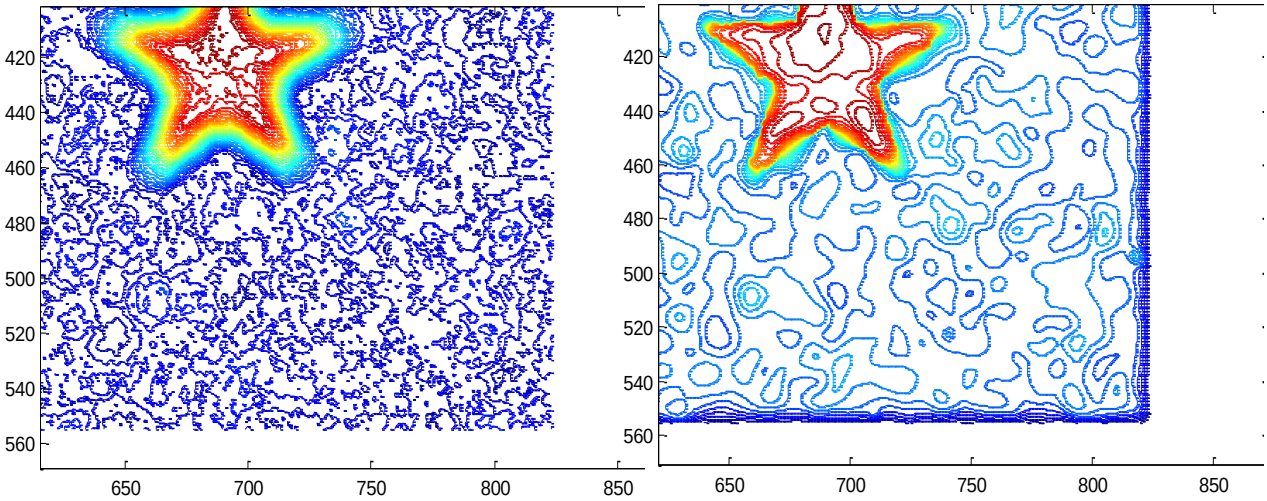

Figure 6.18: Contour models show the effects of II (left) and PM (right) on image boundary

6. 5. 4. Discussion of Perona-Malik and Integral Invariant Comparison for Noise Removal

These experiments address why we get denser patterns of iso-contours around regions of interest compared to Perona-Malik. Integral Invariant enhances the borders of salient regions by widening them. In fact, this is the key to multi-scale segmentation.

Integral Invariant can remove small spots more efficiently than Perona-Malik and giving overall cleaner regions. For a reasonable range of scales, Integral Invariant makes dark regions darker and the bright regions brighter while recovering image from noise. Another important point that we have observed is that Perona-Malik diffusion clusters intensities at the borders of an image.

Finally we conclude contour based topographic segmentation algorithms depends upon the width of ROI boundaries, and Integral Invariant performs better than Perona-Malik in this regard. Integral Invariant reduces noise more effectively than Perona-Malik at a substantially lower computational cost.

6. 6. Assessment of Integral Invariant for Noise Removal in a Segmentation Application

Image smoothing is known to reduce the number of false positives and negatives in image segmentation applications. For this reason, we have compared the segmentation results of speckle reducing anisotropic diffusion (SRAD) [281], Perona-Malik [282] and total variation denoising and Sobolev method (TV) [306], [307] to Integral Invariant.

The purpose of these experiments is not to evaluate the accuracy of segmentation in terms of the region's boundary. Rather, it is to find if the "interesting regions" are segmented and described as salient after diffusion. The mammograms used here are highly suspected of abnormalities and suspicious regions are delineated.

Segmentation is carried out after applying the noise removal filters and the results with respect to false positives are summarized in Figure 6.20. A total of 14 lesions were suspected as a ground truth in 10 temporal pairs of mammograms. It is observed that integral invariant and Perona-Malik perform equally well in reducing the number of false positives, where the former performs best in detecting true positives. For one mammogram, the lesion has not been detected by any method. Overall, Integral invariant and Perona-Malik perform equally well in terms of segmentation results.

The advantage that integral invariant smoothing has over Perona-Malik is the computational time. Integral invariant comes out to be the fastest method to reduce noise among the pool. Figure 6.19 illustrated the computer time taken by each method in this study. The number of iterations for Perona-Malik and SRAD is 20, whereas the aperture of integral invariant kernel is 5. However, this could not be viewed as the core strength of the Integral Invariant over Perona-Malik, rather an advantage of using it, because the former is isotropic and the latter is anisotropic with far greater complexity and less deterioration to shapes.

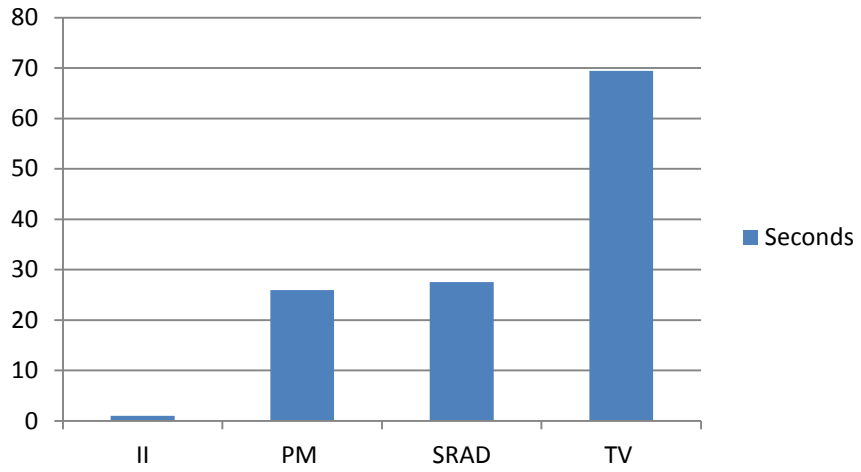

Figure 6.19: Comparison of the computational time for various noise removal methods used to smooth a mammogram.

Besides masses, as far as the effect of Integral Invariant on the detection of small structures that might be salient is concerned, the above segmentation method with Integral Invariant smoothing has been applied to find the calcifications in density mammograms, with encouraging results as shown in Figure 6.24. The reason for including these results here is to observe if Integral Invariant can preserve small structures that might be significant in mammograms.

Figure 6.20 gives a detailed false positive reduction result for each noise removal method applied here on both intensity and density images. We have used two modalities here: by intensity we mean DICOM x-ray mammograms, whereas, the density images are Volpara maps of the corresponding x-rays provided to us by Matakina International. The graphs show that density images give significantly fewer false positives than the intensity images over all methods for the complete set of 10 mammograms. Even for SRAD, the results before and after smoothing are almost the same for intensity images. This shows the sufficiency of density maps over intensity mammograms in a computer aided diagnosis perspective.

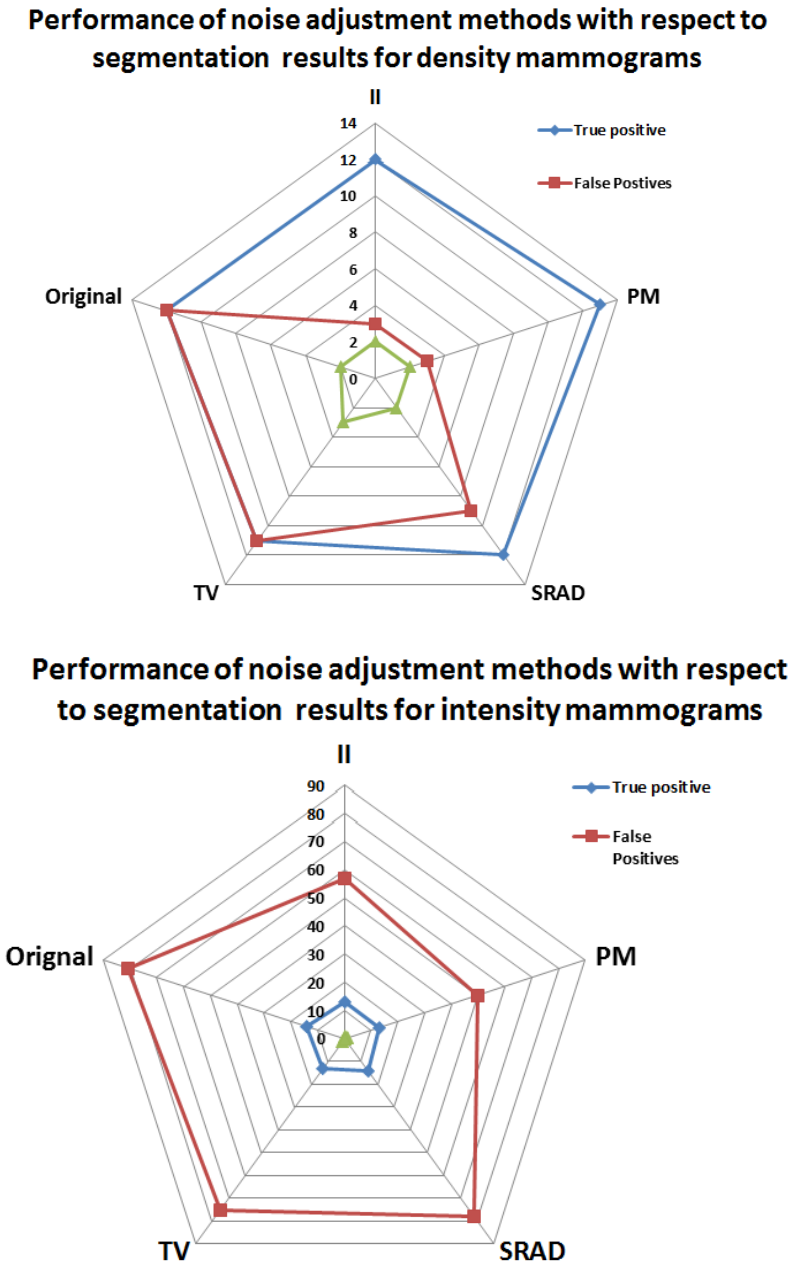

Figure 6.20: Comparison of noise intensity and density mammographic segmentation results over various noise adjustment methods. The results compare the number of accumulative true positives, false positives and false negatives over all 10 mammograms. Integral Invariant and Perona-Malik gives the lowest number of false positives and false negatives, and performs well for finding true positives. Overall, density maps giver lower number of false positives than intensity images. Original refers to unsmooth mammograms.

Secondly, integral invariants perform comparable to Perona-Malik anisotropic diffusion in detecting true positives and reducing false positives. Some results of topographic segmentation after integral invariant image enhancement are given in Figure 6.21.

Detailed false positive results are given in the Figure 6.21, which translates Figure 6.24 for each individual image smoothing method used here. It can be seen that density maps out-perform intensity maps while reducing the number of false positives. Overall, Integral Invariants and Perona Malik performs equally well, with a slight edge to the latter.

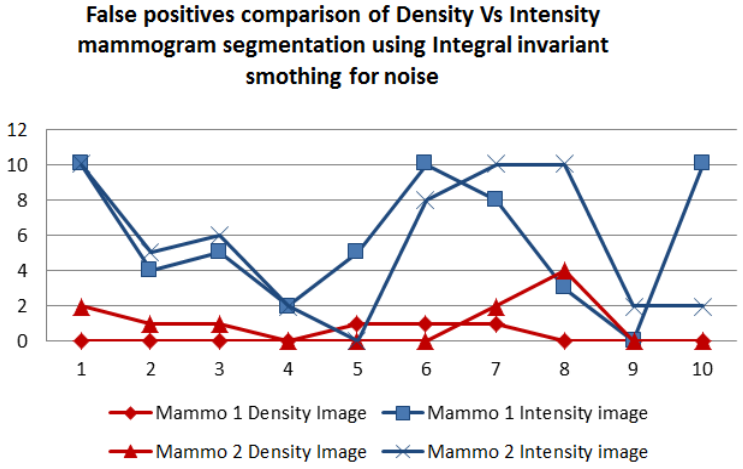

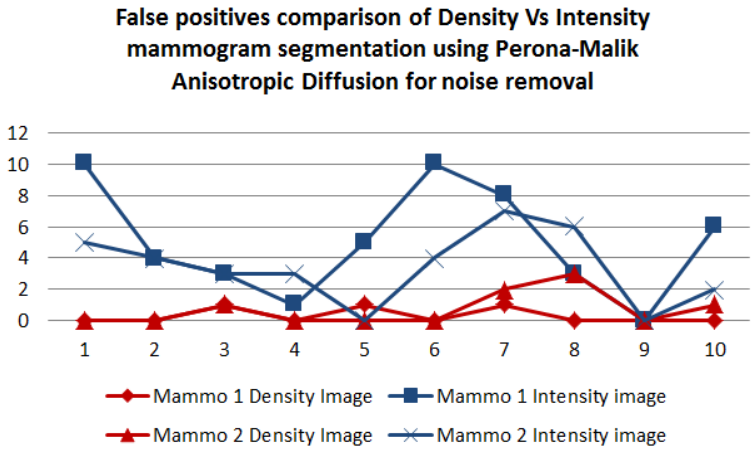

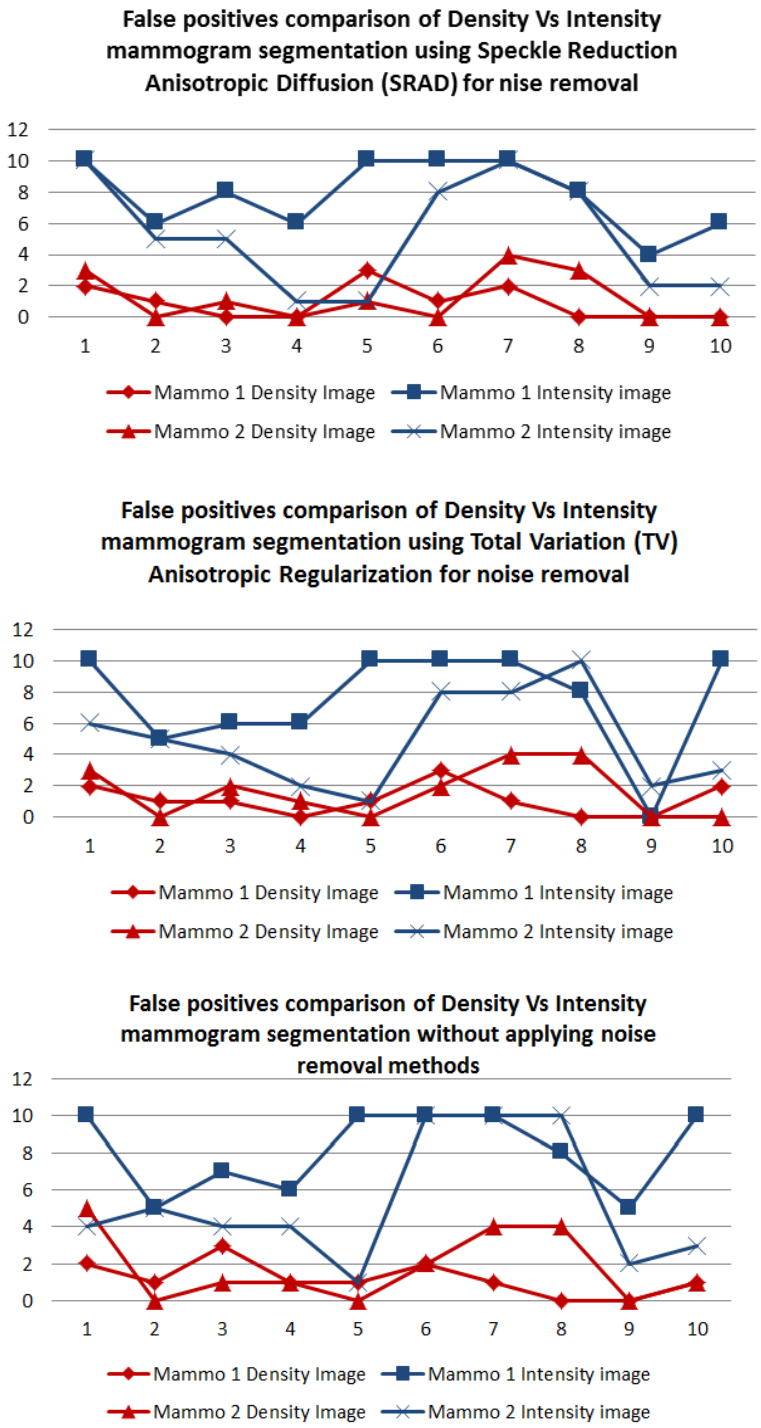

Figure 6.21: Comparison of false positives of density and intensity mammogram segmentation using various noise removal modes. On x-axis are the number of mammographic pairs, whereas the y-axis shows the number of false positives.

We have assessed the suitability of integral invariant as a method to reduce noise in mammograms and reduce the number of false positives while not affecting the true positives. Integral invariant smoothing performs almost similar to the Perona-Malik with a clear edge of lower computational time and complexity. Mammograms with small segmented regions after passing them through Integral Invariant diffusion is given in Figure 6.24, which are accurate with respect to verification in temporal pairs. False positives are supressed and supposed regions of interest are retained.

6. 7. Shape Deterioration in Integral Invariants vs Gaussian Diffusion

This section analyses the effect of the Integral Invariant on deterioration of shapes used as a noise removal filter and compares it with Gaussian diffusion. Previously we compared Integral Invariant with Perona-Malik anisotropic diffusion and found that the Integral Invariant is better for the class of segmentation algorithm that we are using. However, we found Integral Invariant to be more aggressive to deterioration of shape. Now we attempt to observe shape deterioration of objects or shapes by applying Integral Invariant diffusion and compare it to Gaussian diffusion (GD).

6. 7. 1. Object Deterioration

Object deterioration in an image as a result of intensity diffusion depends upon the ratio of size of the object to the size of diffusion kernel and the shape of an object, which we focus upon. The former could be estimated empirically by fixing an appropriate ratio. Here, we study how Integral Invariant and GD deteriorate shapes with variable specula and curvature.

There are two ways to approach shape analysis at multiple scales. We know that Integral Invariant and GD can be used as shape descriptors to describe the boundary of a shape. For a set of scales of different kernel sizes applied to a shape we will get a set of boundaries as a

result of diffusion that we refer to as scale space. We can either note the resultant intensities at the original shape boundaries as a result of diffusion flow or we can analyse shape with new boundaries. For our convenience in the above two cases, we will call them **intensity scale space** (ISS) and **boundary scale space** (BSS) as they refer to the deterioration of objects in-terms of intensity and its resulting diffused boundary, respectively. In the case of BSS, we have the outer boundary of diffusion that will actually expand the shape area and the inner boundary that will show the deterioration and may lead to diminishing the structure. Both these boundaries are important; however, at this point we are interested in the inner boundary of a diffused shape. We have used small scales that are suitable for the type of images and objects we are dealing with. As stated previously, Integral Invariant is causal for a limited set of scales and will not only deteriorate but will add new information to the current image if applied with unrealistically large scales.

It illustrates the behaviour of the deterioration of shapes for Integral Invariant and compares it to Gaussian diffusion (GD).

Mammographic regions that are of interest are curvilinear structures, and benign and malignant masses. The arrow shape at the end simulates a curvilinear structure in Figure 6.23. In both the examples, Integral Invariants diffusion maintains the inner boundary better than by the Gaussian diffusion.

Radius	Integral invariant diffusion	Gaussian diffusion
r = 3	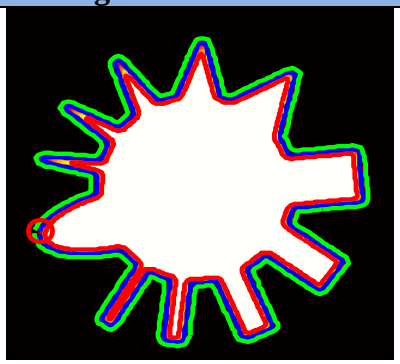	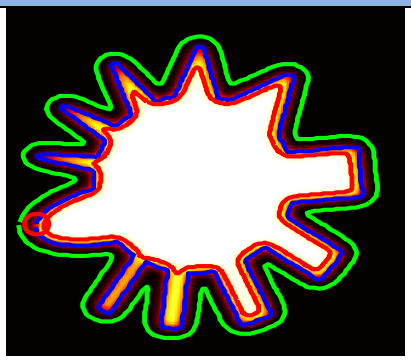
r = 9	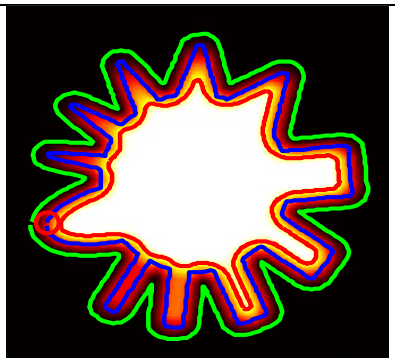	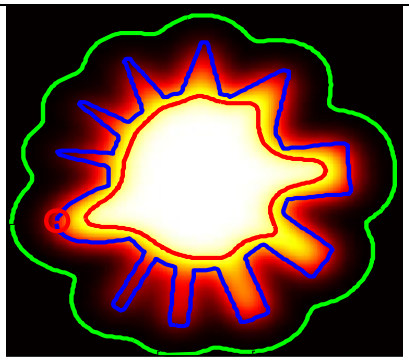

Figure 6.22: A closer look of deterioration of a spiculated shape. The first two rows show the diffusion of the image at the scales r = 3 and r = 9.

Integral invariant diffusion **Gaussian diffusion**

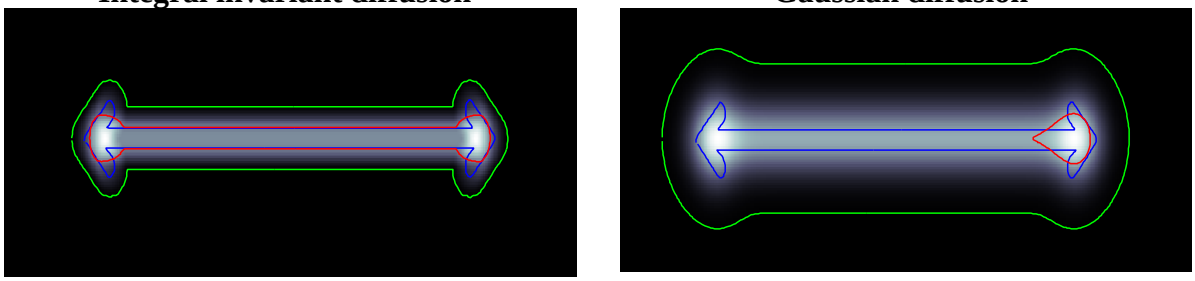

Figure 6.23: This shows the deterioration of a shape for Integral Invariant and Gaussian diffusion. The blue line is the original boundary, whereas the red and green lines are the inner and outer boundaries of the diffused shape respectively.

6. 7. 2. Discussion on Comparison of Integral Invariant and Gaussian Smoothing

Deterioration of objects in an image depends both upon the size with comparison to the diffusion kernel and upon its shape. From the above experiments, we conclude following:

1. Integral Invariant performs better than GD for slow deterioration of objects. Thin objects are approximately high/band pass, while diffusion is low pass filtering process. Integral Invariant retains high frequency content better than GD.
2. Besides area, the rate of deterioration also depends upon the shape of an object. A triangle will deteriorate faster than a rectangle or an oval with an equal area. Hence we can say that *high curvature is more vulnerable to deterioration in an intensity diffusion process*.
3. An object diffuses intensities both inwards and outwards from its boundary. It is observed that the outer boundary achieves homogeneity in curvature quicker than the inner boundary.

6. 8. Conclusions

We have introduced Integral Invariants as a smoothing kernel for noise suppression and feature enhancement in a contour based segmentation application. We explored its scale space properties and analysed its behaviour to image enhancement. It has its intrinsic limitation for being isotropic; however, it performs comparably to Perona-Malik anisotropic filtering. We found it less deteriorative to the boundary scale space, retaining boundaries effectively at higher scales as compared to Gaussian diffusion. Nevertheless, it is not fully causal and scale invariant as a Gaussian scale space.

The core strength and the reason of using Integral Invariant diffusion in this thesis is

that since it can enhance images for the type of segmentation method we use and reduce noise effectively, it is also widely known for describing shapes in a shape matching and correspondence application. Therefore, having used this, there is no need to use a separate noise removal and image enhancement filter in a shape matching application; which eventually reduces the computational cost. Secondly, II is very fast for being isotropic filter, such as a Gaussian filter; nevertheless, it is less deteriorative to shape boundaries, particularly spicula and small curvilinear structures (as shown in examples) and is nearly as effective as PM in supressing noise. Unlike PM, it does not result in intensity clustering artefacts at the image borders and deals well with salt-and-pepper noise. Overall, it is a strong all-round technique for image processing applications, particularly with shape analysis.

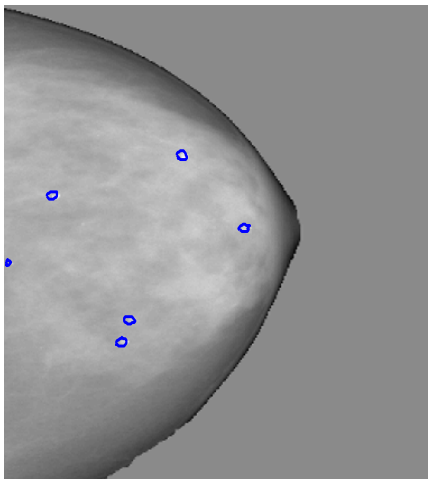

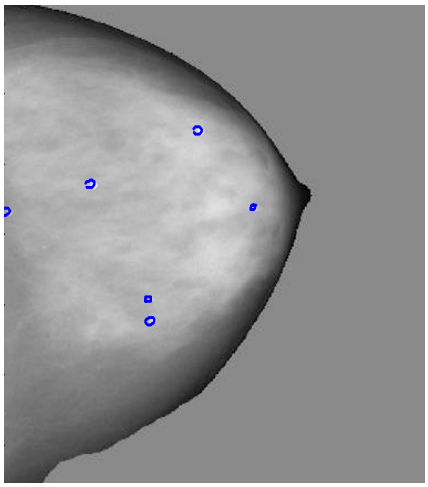

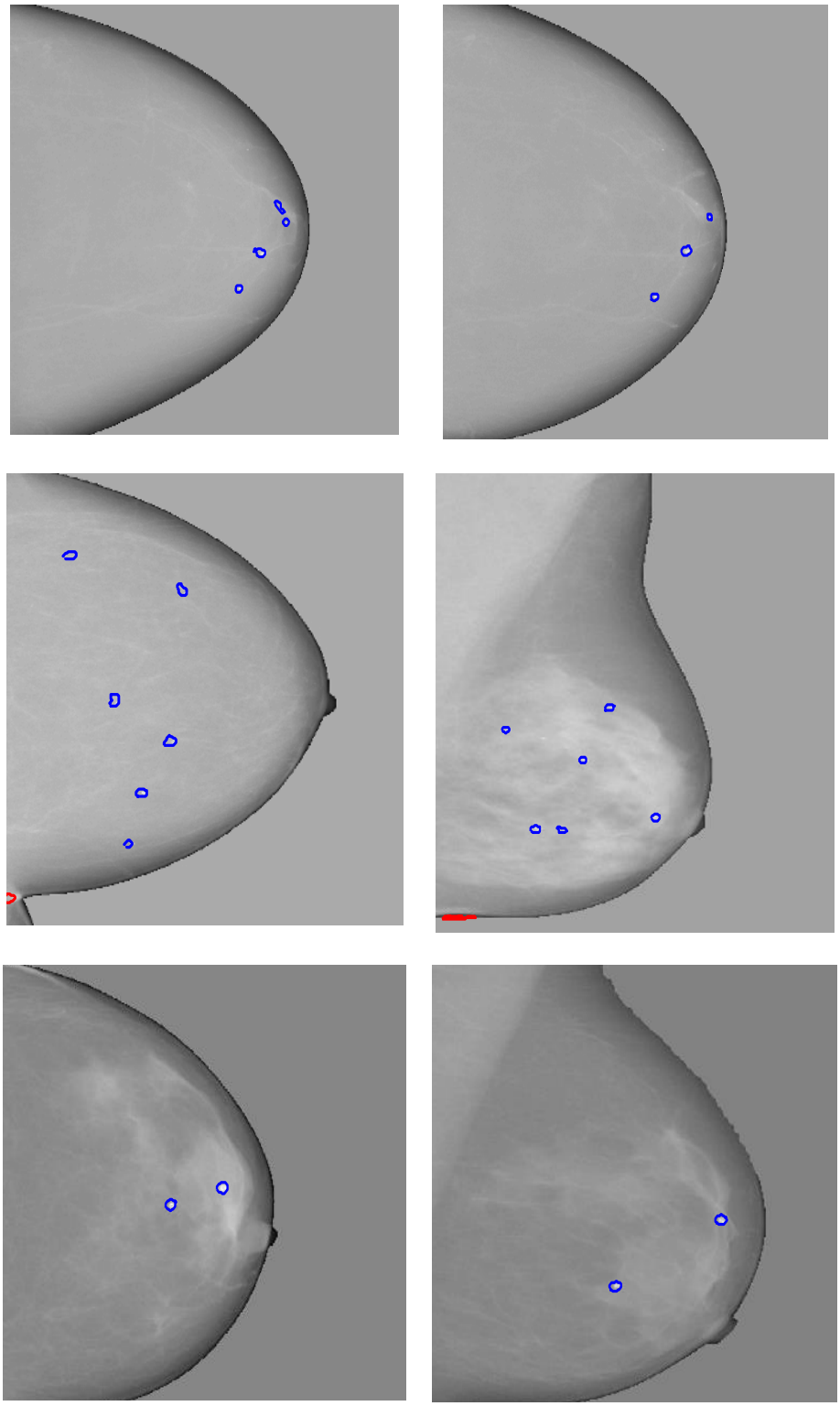

Figure 6.24: Automatic Segmentation of Integral Invariants enhanced temporal pairs of mammogram density maps created by Volpara®

`

Chapter 7

SHAPE MATCHING AND CORRESPONDENCE

7. 1. Introduction

Geometric invariant functions are generally used to describe the shapes that result from images taken under various transformation such as affine, similarity, Euclidean or a range of projection types. We are particularly interested in describing and comparing two planar contours with no self-intersections in a two dimensional space. Shape descriptors can be used to find point-wise correspondences typically in terms of extremizing a shape distance or matching cost between the two shapes. Our main interest is in descriptors that define edges, corners, peaks and ridges. As we have described earlier in Chapter 3, the sensitivity of differential measures to small perturbations due to noise limit their use in shape matching does not produce the desired results at increasing scale.

If we consider images of two similar objects or of the same object taken at different times, angles, and from varying distances, we expect to find changes in the extracted shapes. Of course, using projective invariants can cope with many such changes. However, the shape variations may be in the form of missing data, with complete or partial articulations, and in many practical applications, particularly in medicine and biology, such changes are significant. For example, in oncology, such changes may indicate regions of new growth. Past efforts to compare two shapes have typically involved image registration techniques, for example [125], [126]. However, most such approaches depend upon a 'shape space' and require training data before we can do actual comparisons [129]. Most published algorithms that are based either on rigid or non-rigid registration to compare images

typically yield a dense warp map, establishing correspondences for all pixels in the shapes. Typically, they focus on shape matching rather than localizing matching to regions. Indeed, there appears to have been little or no research aimed at identifying and quantifying new growths and partial occlusions in comparing two planar shapes regardless of scale, spatial variations and orientation.

The first step to comparing two shapes is to align them by identifying key points. The alignment of curves and matching of shapes is discussed in [127] based on local curvature information, and often produces good results. Nevertheless, curvature, being a second derivative is intrinsically susceptible to noise. Our algorithm imposes a metric based on circular Integral Invariants [128] on a shape, which in combination with a scale space analysis [130], enables us to obtain descriptive information and key points, then divides the shape into a number of regions based on those key points. Integral Invariants are used for shape matching in [128]. In that work, computationally expensive dynamic programing and Fast Marching Algorithms are used to match shapes and to establish point-wise correspondences between them. These studies neither detect nor quantify changes in shapes.

In this Chapter, we develop a shape analysis framework that can match shapes and divide them into regions using Integral Invariants scale space to find, in a quantitative manner, partial or complete occlusions and new growth in cancerous nuclei.

7. 2. Shape Correspondence

Establishing a point-wise shape correspondence is tackled as an optimization problem. One of the well-known and extensively used techniques is dynamic programming based on Dijkstra's algorithm. Sethian [308] imposes a unilateral metric on the rectangular graph with all edges having a unit weight. The graph can be represented as a city block problem,

directing several paths that can be eligible for a shortest path from bottom left to the top right corner, instead of a straight line on the diagonal. Thus the length of the true path will never be portrayed correctly even by interpolating the discrete graph for subsampling refinement. The path can be very far from optimal if the grid resolution is very high. If dynamic programming can be enhanced to achieve sub-pixel matching of curves then the technique can be restricted to a very precise cost function. The Fast Marching Algorithm, introduced by J. Sethian [308], [309] fulfils this requirement. Frenkel [247] describes this as each point in the graph represents a match $w = (u(t), v(s))$ as a node that is linked to the predecessor node $(u(t_p), v(s_p))$ of w, where $u(t)$ is a curve parameterized by t and $v(s)$ is the second curve parameterized by s. Then an edge that connects two matches corresponds to the cost of deforming the segment $[u(t_p), u(t)]$ in a way that it coincides with the segment $[v(s_p), v(s)]$. Finding a match with the lowest cost reduces to finding the shortest path from the start node $[v(1), u(1)]$ to the end node $[v(n), u(m)]$. Figure 7.1 illustrates the idea.

We propose a method RMA (Region Matching Algorithm) for local, region-based matching of planar shapes, especially as those shapes change over time. This is a problem that is fundamental to medical imaging, specifically determining new loci of growth in tumours. The method is based on the non-emergence and non-enhancement of maxima, as well as the causality principle, of Integral Invariants scale space. The main idea of the Region Matching Algorithm (RMA) is to sub-divide a shape into a number of "salient" regions and then compare all such regions for local similarity in order to quantitatively identify new growths or partial/complete occlusions. To illustrate the method, the approach is first applied to the 2D planar shapes from the Kimia database [242]. RMA is shift and rotation invariant and gives local region matching for optimal shape correspondence. It also yields a (generally unique) initial alignment of two shapes, which often forms the basis for establishing point-wise correspondences of the shapes. The algorithm is

computationally efficient. It eliminates the need for registration to identify salient differences in shapes and is fully automatic.

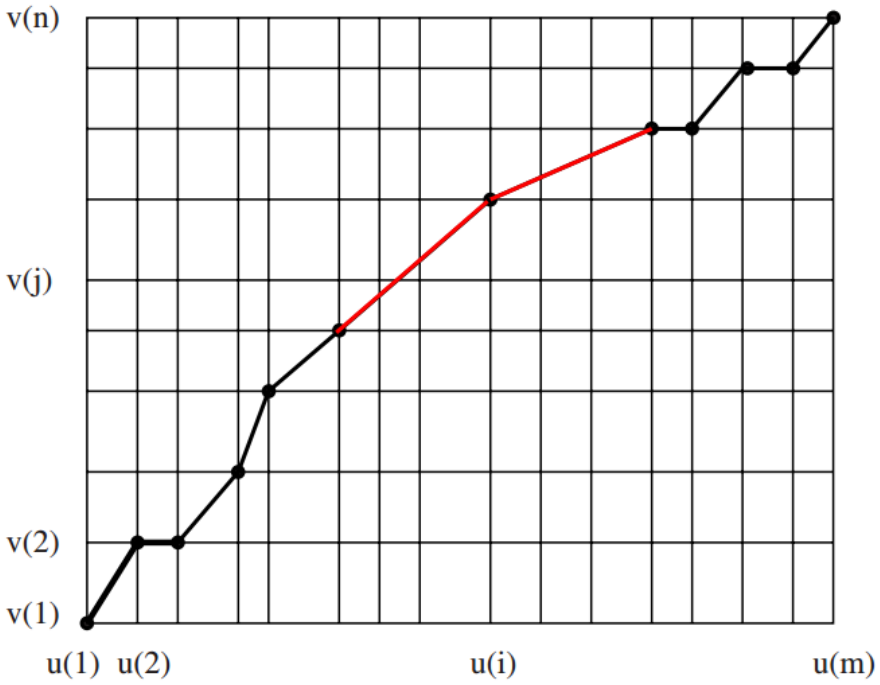

Figure 7.1: Curve matching using Fast Marching Algorithm (FMA). The red line shows relabeling or stretching of the curve for lowest cost. This ability differentiates FMA from other methods such as the Djikstra algorithm, which is, FMA can achieve subpixel accuracy at very efficient cost.

Figure 7.1 is an illustration of the above mentioned idea and shows how FMA is different from Dijkstra's method, which suffers from the city block problem. The red line shows how FMA can deal with sub-pixel accuracy while traversing through the nodes of un-uniformly spaced distance map.

The scale space is obtained by varying the size of the kernel in the Integral Invariants, and can align the two shapes before supplementary correspondences are established. First, an initial alignment is established by finding key points by picking causal peaks at the coarsest scales. Subsequently, shapes are divided into regions and then regions between

two shapes are compared for similarity to establish regional correspondences. Regions that exceed a certain matching cost threshold or do not find any match against any regions in the comparator shape are notified quantitatively as a new growth or a complete occlusion. Note that partial occlusions give relative values. Before going into further detail, we explain here the Fast Marching Algorithm.

7. 3. Fast Marching Algorithm

The Fast Marching Algorithm is a numerical algorithm that computes a viscosity solution of the Eikonal equation. Assume a two dimensional real domain Ω where $\Omega \subset \mathbb{R}^2$ and a set of source points X_o and for each point $x \in \Omega$ measures its distance from X_o to $T(x)$then solving the Eikonal equation, [246], [307], [310]|.

$$\|\nabla_\Omega T(x,y)\| = 1, \quad T(X_o) = 0 \qquad (7.1)$$

If Ω is imagined to be a uniformly distributed forest and at time T = 0 it catches fire at at least one point, which defines its initialisation. Once the fire is set at the initial point, it burns the trees at that point moves on and will never visit this point again. T(x) is the time at which the fire reaches point x in the forest, the fire front may take a new direction with new adjacent and far points. Hence there are points that are burnt, points next to the fire and points far from fire yet to be explored, this process continues until all points are reached and explored. This process continues until all points are reached and explored. This simulation is the core idea behind the Fast Marching Algorithm. The output of a Fast Marching Algorithm is a distance map starting from the initial point to the final point, exploring all points in the map. In our case, as the curves are parameterized to equal lengths of *l*, the resultant distance map will be a square matrix from (0,0) to (*l, l*) of size *l x l*.

Figure 7.5 illustrates the difference between the Djikstra algorithm and Fast Marching Algorithm. The following stepwise explanation is adopted from a tutorial.[311]

7. 3. 1. Initialization

1. Set T(X0) = 0 and mark the points from X0 as Black.
2. Set the rest of the points T(Ω\X0) = ∞ and mark them X0 as Green.

7. 3. 2. Iteration

1. Green points adjacent to Black points become Red.
2. Red points are updated, i.e. their T is estimated from the arrival times of the neighbouring Black points.
3. The Red point with the smallest T becomes Black.
4. The process reiterates until all points are black.

The idea is explained in the Figure 7.2. Note that a point is updated only by adjacent points (4-neighbor adjacency) with smaller value of T, and we demand that the new T value is larger than that of the updating points. A Black point has a T value smaller than that of all non-Black points. Therefore, once a point becomes Black, it need no longer be updated. This can also be thought of in terms of updating an upper and a lower bound until they (almost) meet. The maximum number of point updates is the number of neighbours on the grid, which is O(N).

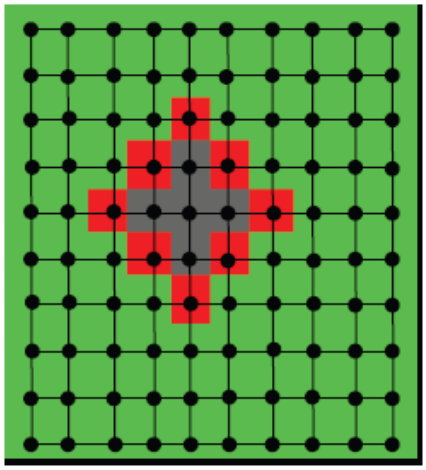

Figure 7.2: Illustration of fast marching grid, black pixels are explored, red are viewed as a fire front while green are far pixels and yet to be explored [311]

The Fast Marching Algorithm is computationally more efficient than previous attempts to solve the Eikonal equation [312], [313], including: the fast sweeping algorithm [314]–[316], and dynamic programing [133], [317]–[319]. FMA has been applied to many applications including active contours [320] and shape from shading [321]. Frenkel and Basri [247] used the FMA to solve the Eikonal equation to align handwriting shapes. It implements curvature information to match closed curves, morphs one curve into another, and can find the average curve for a group. Experiments were carried out on 110 shapes and the results were promising through 13 experiments performed on the complete database. The behaviour of open shapes with arms and teeth (numbers and alphabets) led to interesting conclusions about the relationship of curvature to shape correspondence. However, the method failed to quantify the difference between two shapes other than matching cost. In this chapter, we develop a framework that can match, and then quantify, real shape differences.

7. 4. Shape Matching using Fast Marching Algorithm and Integral Invariants

The following steps establish pointwise correspondences between Shape 1 and Shape 2.

1. Parameterize Shapes 1 to Shape 2 to have *n* points.
2. Select a set of *k* scales to calculate Integral Invariants shape signatures.
3. Apply Integral Invariants to Shape 1 and Shape 2; this results in *k* signatures for each shape.
4. The Integral Invariants difference for comparing points P1 and P2 in Shape 1 and Shape 2 is computed at all given *k* scales, which form a difference vector. Then the largest singular value, which is the obtained by singular value decomposition of *1*x*k* difference vector, is considered to be the largest feature difference between

points P1 and P2. This process is continued until the largest singular value feature difference is found for every point in Shape 1 against every point in Shape 2

5. This yields an *n*x*n* feature matrix, such that at each point in that matrix contains the largest feature difference for two comparing points in Shape 1 and Shape 2 at all given scales.
6. The Fast Marching Algorithm is applied on the *n*x*n* feature matrix, which creates a distance map.
7. The geodesic distance along the diagonal of the distance map is found using the gradient descent method. This indicates the lowest cost matching while mapping points on two shapes.
8. The geodesic path maps points of Shape 1 to points on Shape 2 and establish a point wise correspondence between the two shapes.

The singular value for the difference vector, that contains the Integral Invariants difference for a proposed correspondent at all scales, gives the distance of that point from the origin in the feature space. For a three dimensional feature vector x, the singular value decomposition (svd) is,

$$x = [x_1\ x_2\ x_3];\ svd(x) = norm\ (x) = \sqrt{x_1^2 + x_2^2 + x_3^2}$$

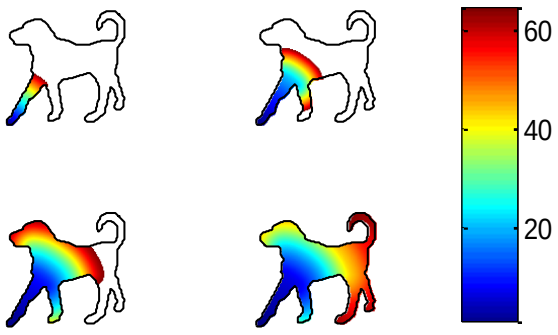

Figure 7.3: Illustration of Fast Marching Algorithm exploring an animal shape. Colours show distances as we move away from the initial point.

The norm of a matrix is its largest svd value; however, for a one dimensional matrix it is a single value. The cost matrix is the arrangement of svd values of the difference vectors of II of two shapes, for each point of one shape against every point of the other shape.

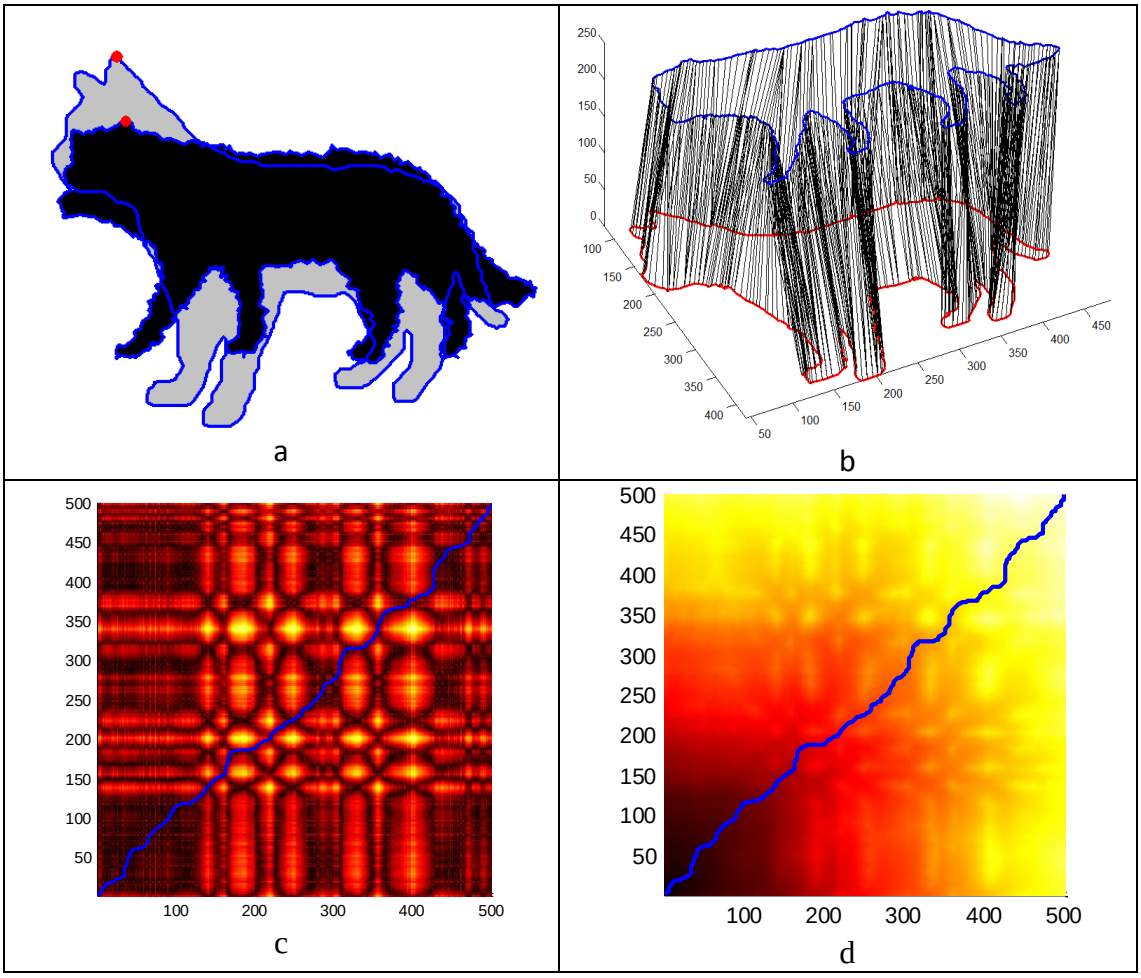

Figure 7.4: Another example of shape comparison between shapes in a) where b) present a point wise correspondence between all points as parameterized. c) is the difference or similarity matrix for Integral Invariants of two curves. d) is the distance matrix calculated by the Fast Marching Algorithm that contains distances from initial point at lower left corner of the image to the final point at the top right corner. The shortest path or the cost for reaching final point in c &d is overlaid in blue. Here, c) is a feature map, which is then processed using FMA to generate a distance map as seen in d). Geodesic distance is overlaid for illustration on the both, which is originally calculated by applying Gradient decent on d).

It is to be noted that the optimal paths or minimum cost overlaid in Figure 7.c & d are attained by finding the minimal cost in the geodesic mapping algorithm. This computation takes the distance matrix calculated by the Fast Marching Algorithm and then extracts the minimum path from it. The geodesic path does not itself find distances but only records the length of each possible path. Once the geodesic distance map D(x) to a starting point is computed, the geodesic curve between any point x_1 and x_0 extracted through gradient descent, [307].

The gradient of the distance map is computed using centred differences then normalized to obtain unit speed geodesic curve parameterized by arc length. The geodesic is then calculated numerically using a discretised gradient descent that defines a discrete curve.

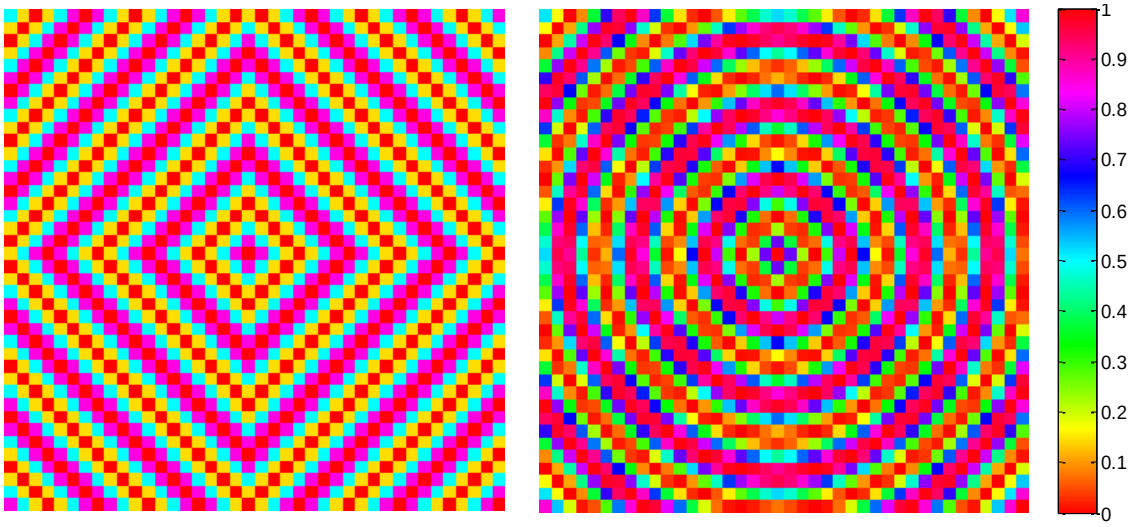

Figure 7.5: Example of Geodesic distance maps using a cosine modulation by, Djikstra algorithm on the left and fast marching method on the right hand side.

The length of the geodesic path and its values are affected by the range of scales used for shape correspondence. Application of multiple scales describe shapes in a way that makes a pool of features, bounded from fine to coarse as the scale progresses from low to high.

7. 5. Issues in Shape Correspondence

Some of the key issues in Shape Correspondence are:

7.5.1 Initial alignment of the two shapes

7.5.2 Scale selection i.e. the size of the disc or integration kernel for generating Integral Invariants shape signature.

7.5.3 Maintaining the speed of point-wise matching despite occlusions and articulations

7. 5. 1. Initial alignment of two shapes

A shape is a closed planar contour that can have any point designated as a starting point. However in shape correspondence problems, the starting points of the two shapes should match. Point-wise correspondence using Integral Invariants and FMA can be established even if two shapes are unaligned to a certain extent. However, if the shapes are highly out of alignment relative to each other, or one or both contain major occlusions, then a correct correspondence is difficult to achieve. This is precisely the problem we have addressed. The shape signature is divided into regions based on causal peaks of Integral invariant scale space and the starting points of the best matching regions in two shapes are designated as the points of initial alignment.

Figure 7.6 illustrates a shape correspondence of two hands, with and without initial alignment. From Figure 7.6 (e) and (f), the geodesic path for initially aligned hands is quite short (straight) in diagonal, showing a closer match.

7. 5. 2. Scale Selection

A range of Integral Invariants scales are used to obtain the feature space given in Figure 7.6 and consequently to maximize the difference between two shapes. Larger scales are good for locating and differentiating larger regions whereas smaller scales are essential to distinguish fine details. Scale space reflects the saliency of regions that maintain causal

peaks at all given scales. Shapes are divided into regions based upon peaks of the coarsest scale. Finding a suitable single coarse scale to correspond shapes with significantly large size ratios is cumbersome. Let r_{max} be the maximum scale indicator, then comparing shapes (S_1, S_2) for correspondence where the area of shape to Integral Invariants ratio (SIR) is fixed, r_{max} is,

$$r_{max} = \lceil \text{mean}(r_{S_{1max}}, r_{S_{2max}}) \rceil, \qquad (7.2)$$

$$\text{Where } r_{S_{imax}} = \sqrt{\frac{Area\ of\ S_i}{SIR * \pi}}\ ,\ i = [1, 2] \qquad (7.3)$$

Though to a large extent, the scale selection depends upon the size of the shape, we have observed experimentally that it also depends upon the variability in the shape boundary. To date, we have not found a generalized relationship between the two and consider it application dependent. This will form part of our future work.

7. 5. 3. Speed of Matching

Speed of matching means that an occlusion in one part of the shape should not affect point-wise correspondences in other regions and the speed of matching should remain smooth. We found that the FMA has an advantage over the commonly used Dijkstra's algorithm to match all regions independently and not sequentially, as shown in example in the Figure 7.7. In this example, the occluded leg of the red shape is matched with the complete leg of the blue shape and has not affected the correspondence process in other regions as shown in the graph. Example of geodesic maps overlaid over a distance map for shapes in Figure 7.7, obtained by Fast Marching Algorithm are given in Figure 7.8 and Figure 7.9. The twist in the path near the bottom is due to high cost of matching, and reflects a mismatch because of occlusion shown in Figure 7.8. A 3D representation of this distance map is given in the Figure 7.9.

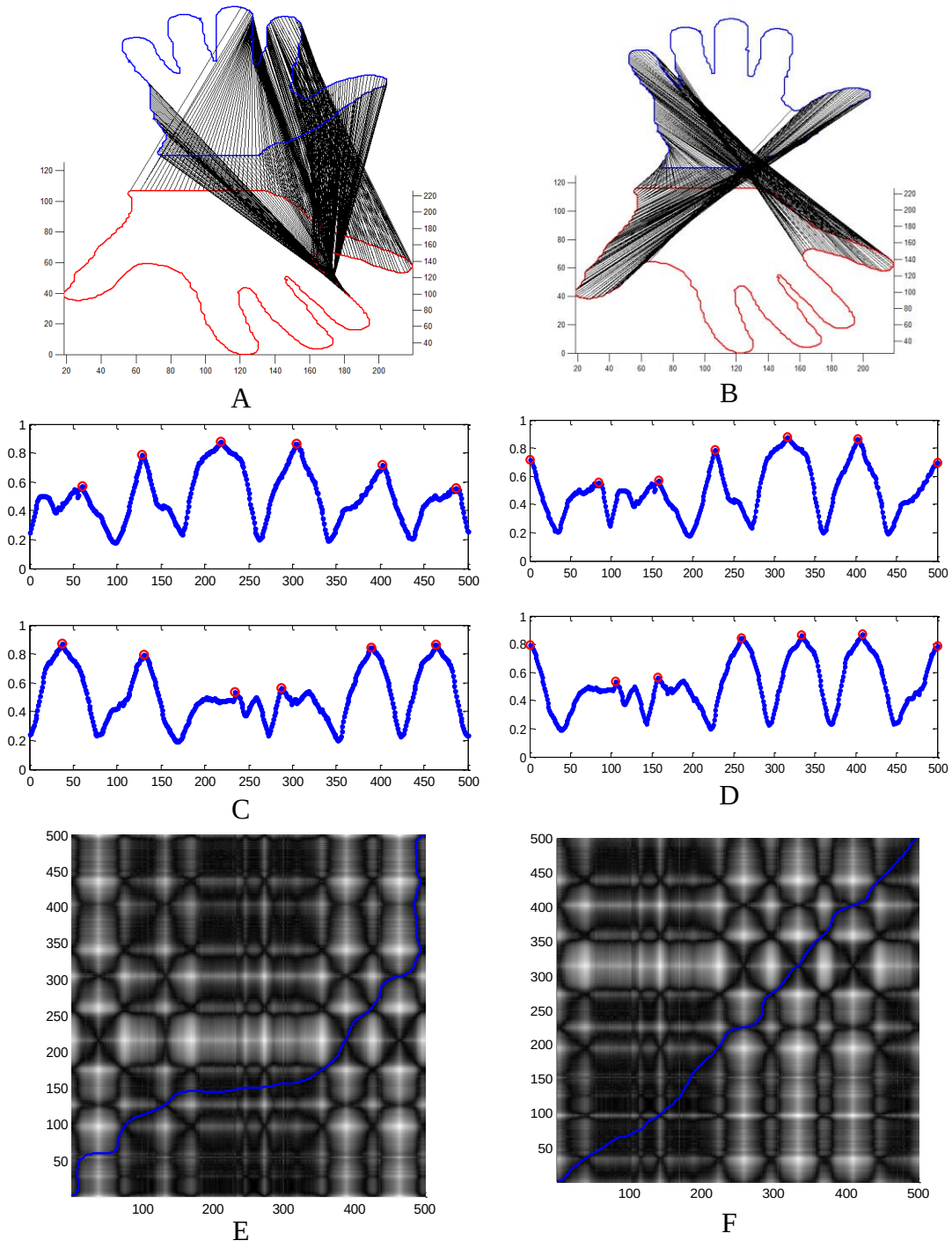

Figure 7.6: Shape correspondence example of two hand shapes that are out of phase to each other. Shapes are wrongly corresponded without an initial alignment in the first column, while correctly corresponded in the second column after initial alignment. The second row compares the shape signature at the coarsest scale for both shapes, whereas, the third row contains the shortest path superimposed on the feature space and compares the point-wise correspondence results, which is better for (f).

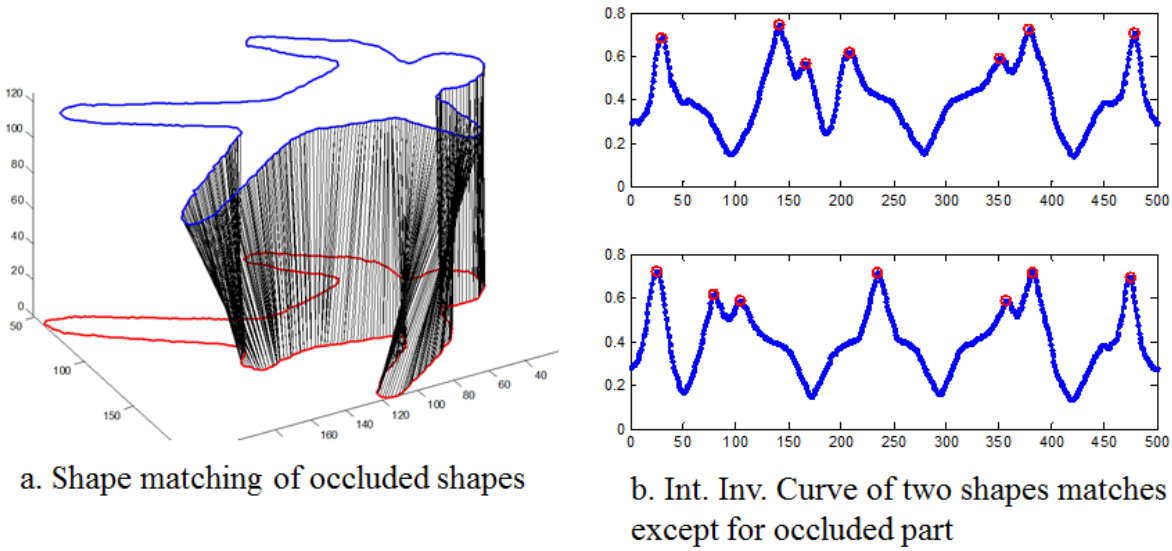

a. Shape matching of occluded shapes

b. Int. Inv. Curve of two shapes matches except for occluded part

Figure 7.7: Speed of matching for an occluded limb shown in (a). The corresponding shape signatures are given in (b)

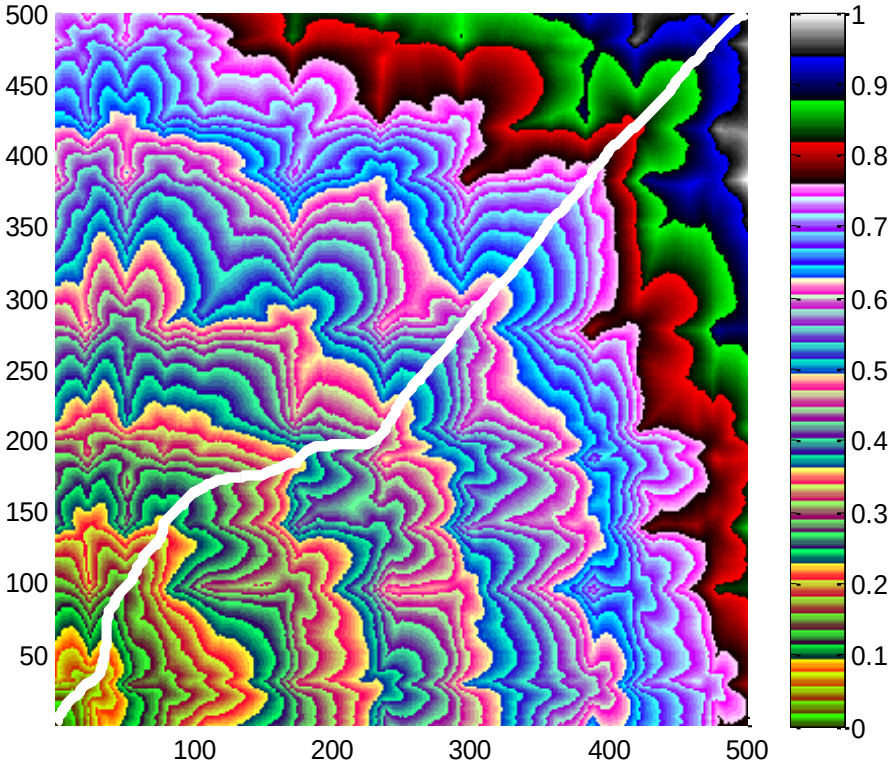

Figure 7.8: Geodesic distance map calculated by the Fast Marching Algorithm for shapes corresponded in Figure 7.7, along with the shortest path superimposed as a white line, that follows the lowest values or matching cost.

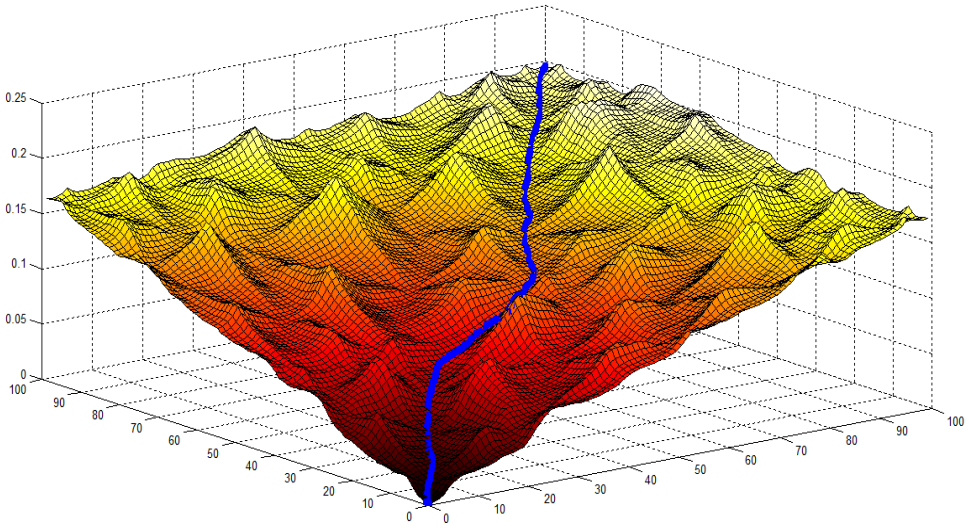

Figure 7.9: Distance map created by FMA, where Geodesic path is being calculated using gradient descent, shown as a blue line passing across the diagonal.

7. 6. Shape Distance

For the given parameterized curves $C_1\ (k)$ = [x_1(k), y_1(k)] and $C_2\ (k)$ = [x_2(k), y_2(k)] at arc length k ϵ [$0,\ l$], with the similarity matrix Ḍ (C_1, C_2) and geodesic map G of length n, the shape distance can be defined as minimal sum of the individual differences between the curve point pairs at the parameterized length. Due to the same parameterization of both curves, the scale factor between the two shapes may be suppressed and, consequently, two exact shapes with exponentially different sizes or scales can be identified without any distinction. However, this may be useful in some applications where only the geometry of the shapes is important rather than their scale. In our case, the sizes and eventually the areas of the shapes is important. The shape distance as a scalar that quantifies similarity of two shapes for a lower value is then given by,

$$\mathcal{L}(C_1(s), C_2(t)) = \mathrm{T(k)} + \left|1 - \frac{\min(s,t)}{\max(s,t)}\right| \ where\ s \in (1,m), t \in (1,n) \qquad (7.4)$$

$$\mathrm{T(k)} = \min_{c} \int_o^l \dot{D}\,(C_1, C_2)dk \qquad \mathrm{k} \epsilon\ [0, \mathrm{l}] \qquad (7.5)$$

Figure 7.10 and Figure 7.11 show examples of matching cost calculated for a family of quadrupeds and fish using the proposed method. Strong intra group similarity and intergroup dissimilarity is observed in the example. Furthermore, shape matching is performed for 54 shapes of 6 different families of shapes from the Kimia database with added white Gaussian noise (signal to noise ratio = 0.01) and the results are presented in Appendix A (will be compiled later).

7. 7. Region Matching Algorithm

After matching shapes globally, we apply a Region Matching Algorithm to find local differences between shapes. As noted above, the central idea underlying our method is the use of circular Integral Invariants, from which we exploit the associated scale space.

Recall from Chapter 5, Integral invariants reduce the information content by diffusion. We have used to divide shape into regions, using a multi scale causal description in developing RMA. Though RMA does not require initial alignment for region matching, it can be used to find points of initial alignment in applications that are used to establish a point-wise correspondence of shapes. Currently, regions are picked simply on the basis of least sum of squared differences and variation between two regions can be presented in number of pixels and percentage difference.

The coarsest scale of the Integral Invariants is determined automatically by taking the mean value of the shape-to-integration kernel ratio (SIR) of the two shapes. Let r_{max} be the maximum scale indicator (this equates to the radius of the circular Integral Invariants disc at the maximum scale). Then comparing shapes (S_1, S_2) for region matching where the area of shape to Integral Invariants ratio (SIR) can be adjusted depending upon the size and variability of shape.

	0.29	0.49	2.41	1.81	2.66	3.34	4.07	4.41	4.10	3.59
	0.49	0.24	2.16	2.03	2.28	3.67	4.15	4.24	3.95	3.91
	1.98	1.88	0.00	1.10	2.11	3.42	3.70	4.08	3.82	4.05
	1.96	1.72	0.91	0.35	2.51	3.26	3.98	4.00	3.93	3.81
	2.82	2.40	2.24	2.64	0.31	3.91	4.11	4.88	4.42	5.00
	3.71	3.65	3.17	3.24	3.85	0.17	0.88	2.61	1.97	1.90
	3.82	3.81	3.87	3.66	3.84	0.90	0.52	1.97	1.77	1.60
	4.30	4.01	4.10	3.62	4.93	2.47	1.38	0.39	1.98	2.74
	3.67	3.47	3.78	3.58	4.45	1.53	1.90	2.15	0.79	0.99
	3.98	4.11	4.38	3.48	4.63	1.85	1.32	2.05	1.25	0.61

Figure 7.10: Two families of shapes are matched in the presence of noise for shape correspondence using FMA and are presented with the matching cost.

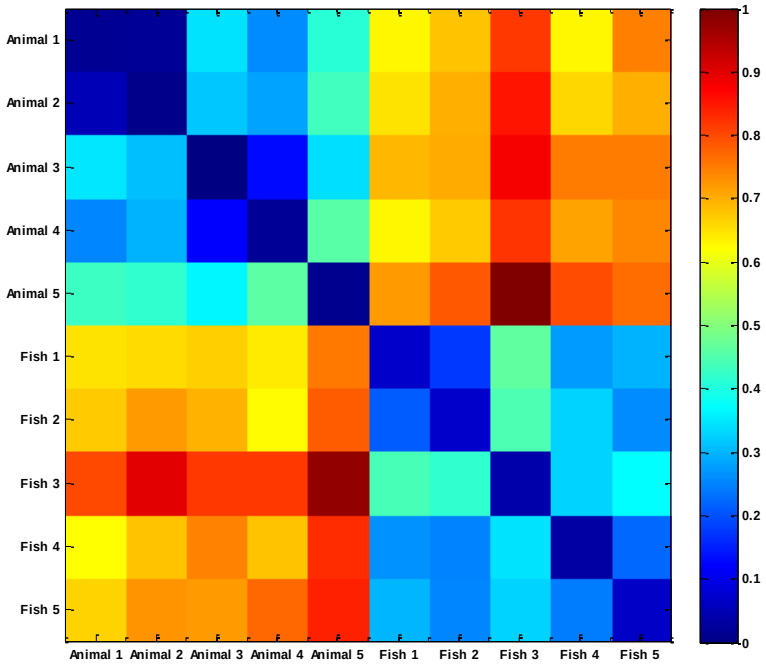

Figure 7.11: The matching cost is colour coded. It can be seen that strong matching is observed (shown in blue) along the diagonal.

If the two shapes being compared are not expected to differ substantially, then the normalized difference of centroids of regions can also be added as an additional feature for finding similarity. The areas of regions might be useful in applications where most of the regions in corresponding shapes are likely to be the very similar in size. Other factors such as texture and gradient measures as well as additional shape features can be used with the existing shape descriptor to meet the needs of specific application.

7. 7. 1. Application of RMA on Synthetic Shapes

We have applied RMA to a range of shapes, in particular to the variable and occluded shapes from the Kimia database, and assessed its performance for within group similarity. The accuracy of region matching is evaluated manually as a ground truth. Experiments were carried out on 146 dissimilar shapes from four similar object groups of the Kimia database. Region matching for each pair of shapes was assigned a score from 1-6, whereas the accuracy of new growth and occluded regions was assessed qualitatively and assigned a grade from 1-4. The results are summarized in Table-7.1.

Criteria	**“bunny” /Rabbits**	**“dude” /Man**	**“fgen” /Alien**	**“kk” /Kite**	**“hand”**
Initial Alignment	91.7	100	91.67	77.78	55.56
Detection of new growth	98.05	None	90	91.38	53.34
Regional Correspondence	98.33	100	86.11	91.61	78.05

Table 7.1: RMA applied to variable and occluded shapes from Kimia database. Note that matching asymmetry is considered as an error here (keeping mammograms in mind), though in machine vision applications it may accept and which will improve results.

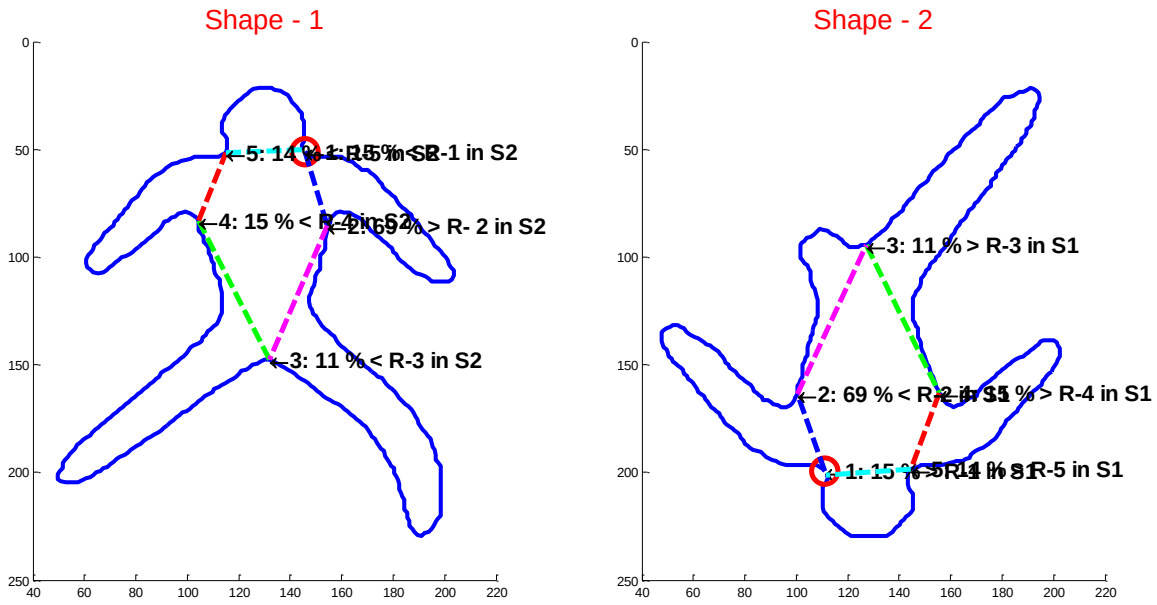

Figure 7.12: RMA applied to two shapes of 'dude' category from Kimia database for local region matching. Regions are identified accurately in this example while quantifying regional change in each part.

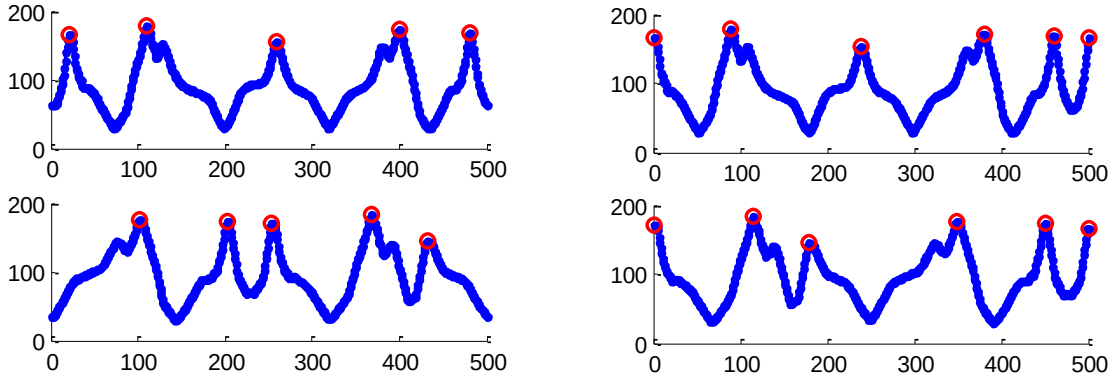

Figure 7.13: Integral invariant signature at the coarse scale with causal peaks of two shapes in Figure 7.12, for shape-1 on the top and shape-2 in the bottom row. On the left, signatures are without initial alignment and on the right; its after intital alignment. Causal peaks at the coarset scale are highlighted in red. The x-axis of the graphs is the paramterirization of shapes, which are sampled to equal lengths, whearas the y-axis show the number of pixels overlaping with II kernal.

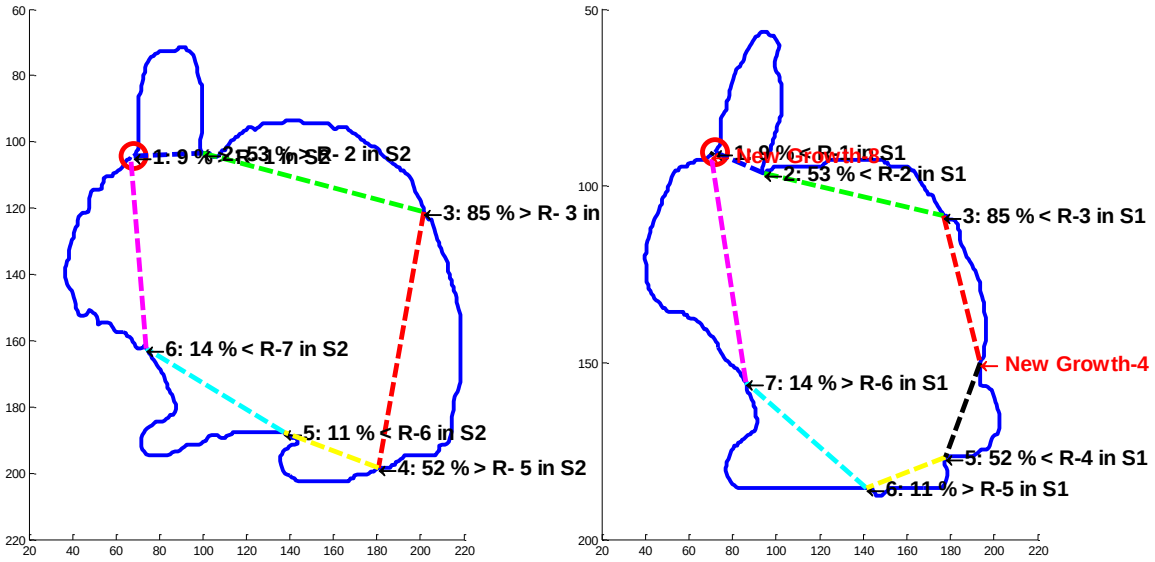

Figure 7.14: RMA applied to two shapes of 'bunny' category from Kimia database for local region matching. Shape on the right is been identified with a new growth in comparison with the shape on the left.

As an example, RMA is applied to a pair of shapes in Figure 7.12, whereas Figure 7.13 shows its Integral Invariants signature at the coarsest scale. It also represents the effectives of RMA for initial alignment of two shapes. It finds the best region with the minimum matching cost and designates its starting point as a point of initial alignment. Another example is given in Figure 7.14 where a new growth has been identified (which corresponds, in fact, to the rabbit's tail). Other examples are given in Figure 7.15. The accuracy of initial alignment for shapes with locally distinct geometry is supposed to be very high and is evident from Table 7.1.

Finally, we note that the relatively poor results of RMA on hand shapes stems from the fact that the inner left, right and centre fingers of each hand have very similar structures. Similarly, the symmetry of kite shapes is also a misleading factor in identifying regions correctly. In machine vision applications matching asymmetry is generally accepted and may not be counted as an error, which will improve results dramatically. Incorporating

translational and reflectional symmetries into our framework, while enabling the detection of new growths and occlusions, is the subject of current work. More results are given in Appendix II.

7. 7. 2. Application of RMA to Temporal Study of Mammograms

In this section, we apply RMA to a temporal pair of mammograms. Recall from Chapter 1 that we are initially most interested in the temporal study of mammograms, since it is not only important for the detection of cancers but is also used increasingly for post-treatment care. It provides a quantitative measure of how a certain region in the breast may have evolved over time. Temporal images are used by the radiologist to reduce the number of false positives and correspondingly suspicious lesions over time and to detect possible masses. However, changes in breast density, positioning, and the growth and development of lesions, together with the intrinsically projective nature of mammography, mean that establishing temporal correspondences remains a challenging task. Efforts have previously been made to compare two shapes regionally, for example registration techniques [239], [245]. Algorithms that use rigid or non-rigid registration to compare images typically yield a dense warp map, establishing correspondences for all pixels in the mammograms. However, in most studies this phenomenon is dependent on the 'shape space' that requires a set of training data before we can do actual comparisons [322]. However, the appearance of a mammogram can change markedly with small changes in compression, imaging parameters and any adjustment in the positioning of the breast prior to compression. For example, such small changes can change the textural properties of stromal tissue. Fortunately, most such changes are clinically irrelevant. Rather, correspondences are only relevant for *regions of interest*, typically locally dense regions that may (or happily, may not) be lesions. (We accept that this does not extend completely to architectural

distortions; but they are a separate problem that requires a measure of a symmetry). This section addresses the temporal comparison of mammograms by employing Integral Invariants, in particular exploiting its scale space, for local (sub-) region matching in segmented masses. The temporal mammograms in this study are first segmented, and then the resulting regions are matched by performing shape matching. The best matching shapes are then divided into local /sub -regions and RMA is applied for local region matching.

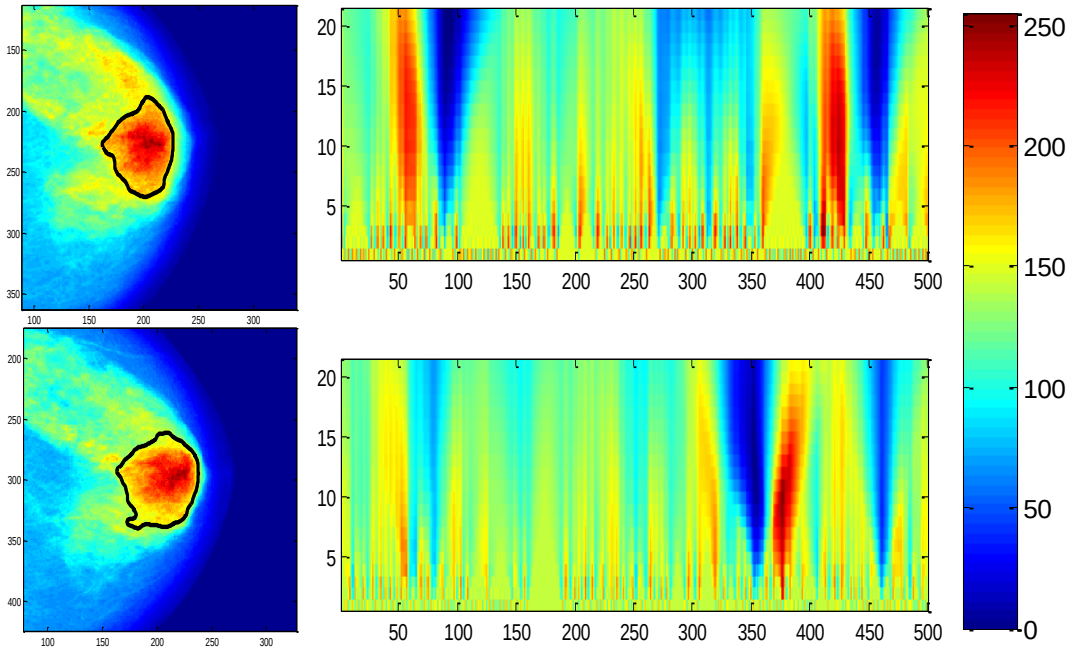

Figure 7.15: Segmented regions from temporal mammograms on the left while their corresponding II scale spaces are given on the right hand side. The units on the x-axis show the parameterization of the region curves, which are brought to equal lengths.

The temporal mammograms that are used in this study were made available to us by Mātakina Technologies. We begin by applying a variation of the hierarchical algorithm based on iso-contours as discussed in the earlier chapters [251]. The reason for using this algorithm here is that it is computationally very efficient, and indeed it can be the basis of a real time system, even without resorting to a GPU implementation. The algorithm

segments the complete internal topography of the breast in a structured way that can subsequently be used to establish correspondences between mammograms. The algorithm has worked well of mammograms processed in this case study.

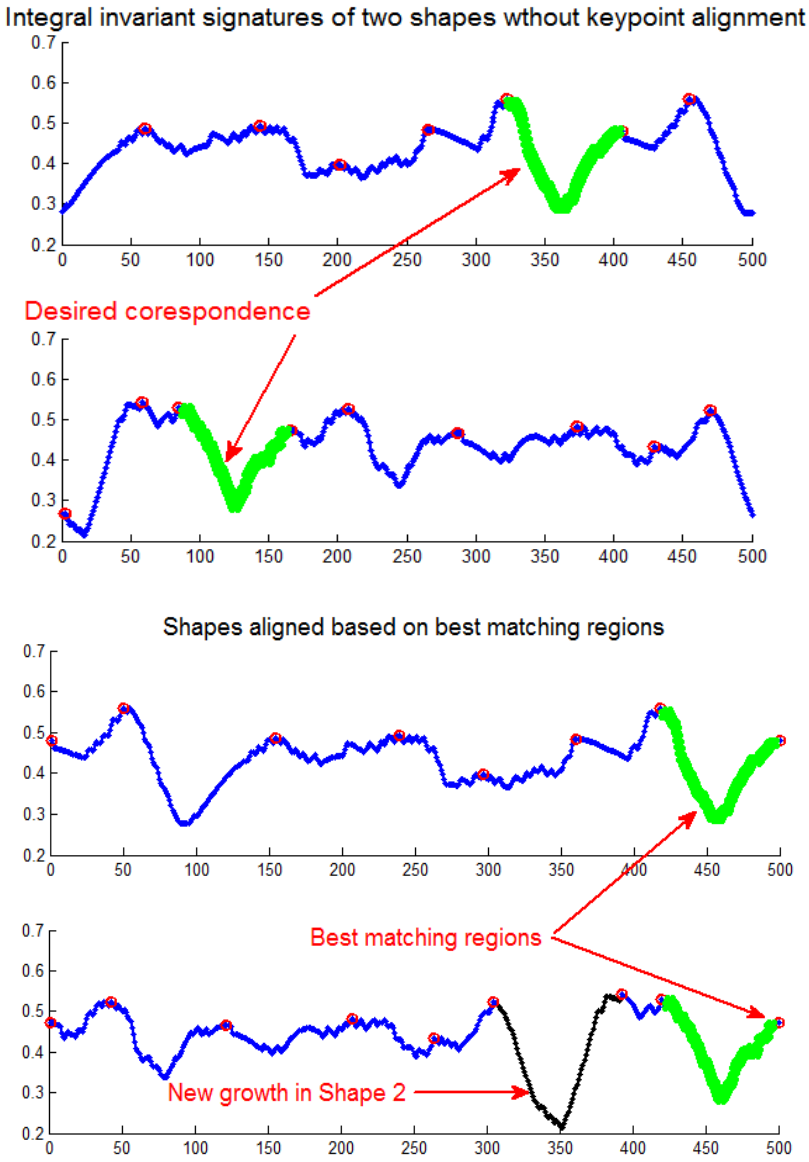

Figure 7.16: Above is the scale space signature of two corresponding shapes in Figure 7.15 at the coarsest scale. On the left, the signatures are unaligned whereas on the right side they are aligned using *RMA*. Here, the x-axis show the parameterization of the boundary of two shapes to equal lengths whereas the y-axis show the normalized II values for each point on the boundary curve.

An example of alignment for a segmentation of nested regions is shown in Figure 7.16. RMA matches regions in shapes irrespective of their sequence. However, in this particular case the accuracy of matching is obvious by comparing Integral Invariants signature of both mammograms after initial key-point alignment.

Shape correspondence using RMA has been applied to the regions segmented in this way illustrated in Figure 7.15. The mammograms are de-noised Integral Invariant diffusion. The lesions from pairs of temporal mammograms are put into regional correspondences. In some cases the algorithm identifies the segments (and associated sub-regions) that correspond to new growth, while at the same time calculating the percentage change in other sub-regions. It may be noted that the number of regions in both shapes may not be equal. Some obvious mismatches can also be seen where the regional differences are substantial or the non-corresponding regions are very similar. The correspondence of regions does not currently depend upon the texture or gradient information enclosed in them. Figure 7.17 shows the region matching results of the mass in Figure 7.15. Other detailed examples for pairs of temporal mammograms are given in Figure 7.18.

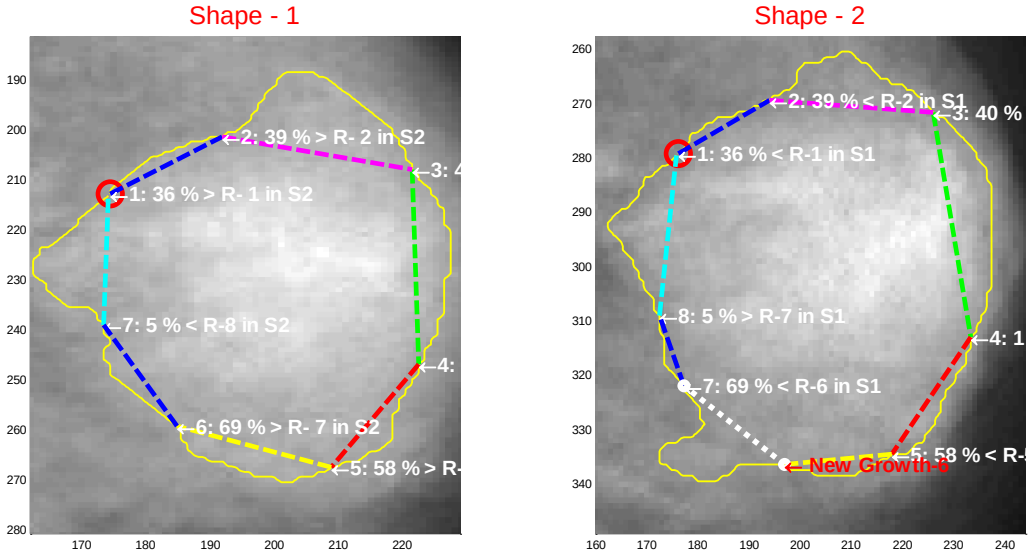

Figure 7.17: Region matching of the mass shown in Figure 7.15

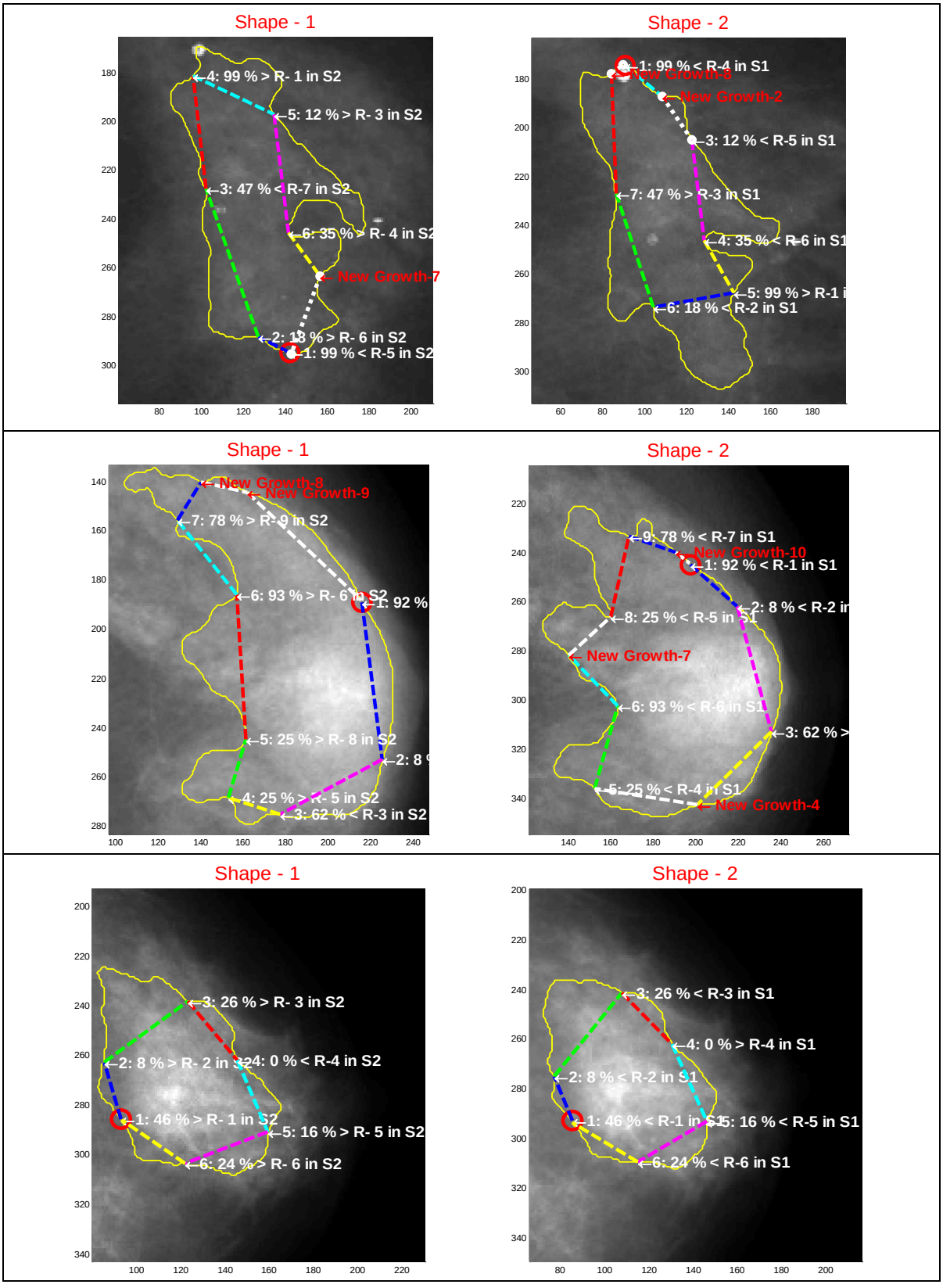
Shape - 1
4: 99 % > R- 1 in S2
5: 12 % > R- 3 in S2
3: 47 % < R-7 in S2
6: 35 % > R- 4 in S2
New Growth-7
2: 18 % > R- 6 in S2
1: 99 % < R-5 in S2
Shape - 2
1: 99 % < R-4 in S1
New Growth-8
New Growth-2
3: 12 % < R-5 in S1
7: 47 % > R-3 in S1
4: 35 % < R-6 in S1
5: 99 % > R-1 i
6: 18 % < R-2 in S1
Shape - 1
New Growth-8
New Growth-9
7: 78 % > R-9 in S2
6: 93 % > R- 6 in S2
1: 92 %
5: 25 % > R- 8 in S2
2: 8 %
4: 25 % > R- 5 in S2
3: 62 % < R-3 in S2
Shape - 2
9: 78 % < R-7 in S1
New Growth-10
1: 92 % < R-1 in S1
2: 8 % < R-2 in
8: 25 % < R-5 in S1
New Growth-7
6: 93 % < R-6 in S1
3: 62 % >
5: 25 % < R-4 in S1
New Growth-4
Shape - 1
3: 26 % > R- 3 in S2
2: 8 % > R- 2 in S2
4: 0 % < R-4 in S2
1: 46 % > R- 1 in S2
5: 16 % > R- 5 in S2
6: 24 % > R- 6 in S2
Shape - 2
3: 26 % < R-3 in S1
4: 0 % > R-4 in S1
2: 8 % < R-2 in S1
1: 46 % < R-1 in S1
5: 16 % < R-5 in S1
6: 24 % < R-6 in S1

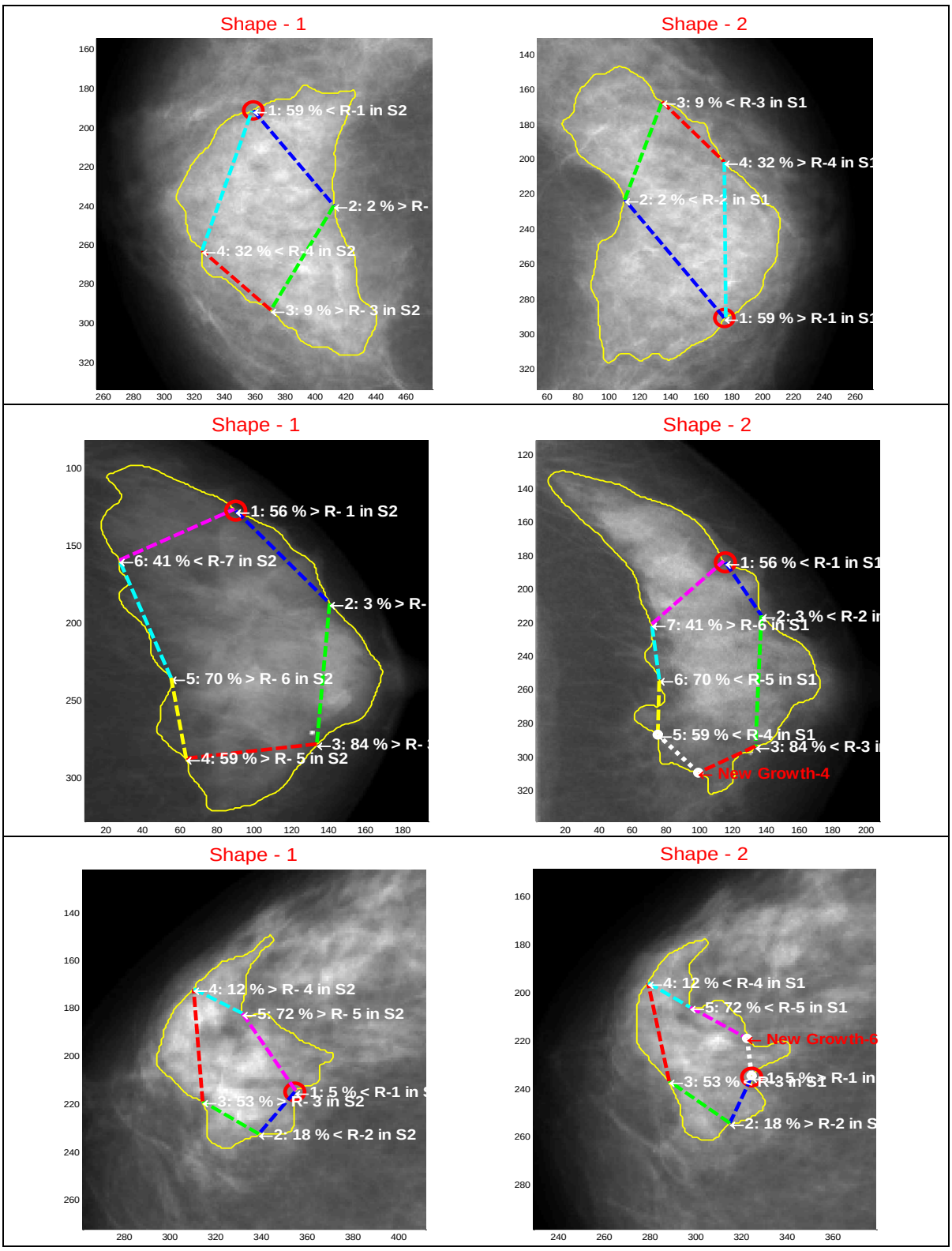
Shape - 1
1: 59 % < R-1 in S2
2: 2 % > R-
4: 32 % < R-4 in S2
3: 9 % > R- 3 in S2
Shape - 2
3: 9 % < R-3 in S1
4: 32 % > R-4 in S1
2: 2 % < R-2 in S1
1: 59 % > R-1 in S1
Shape - 1
1: 56 % > R- 1 in S2
6: 41 % < R-7 in S2
2: 3 % > R-
5: 70 % > R- 6 in S2
3: 84 % > R-
4: 59 % > R- 5 in S2
Shape - 2
1: 56 % < R-1 in S1
2: 3 % < R-2 in
7: 41 % > R-6 in S1
6: 70 % < R-5 in S1
5: 59 % < R-4 in S1
3: 84 % < R-3 i
New Growth-4
Shape - 1
4: 12 % > R- 4 in S2
5: 72 % > R- 5 in S2
1: 5 % < R-1 in
3: 53 % < R- 3 in S2
2: 18 % < R-2 in S2
Shape - 2
4: 12 % < R-4 in S1
5: 72 % < R-5 in S1
New Growth-6
3: 53 % < R-3 in S1
2: 18 % > R-2 in S

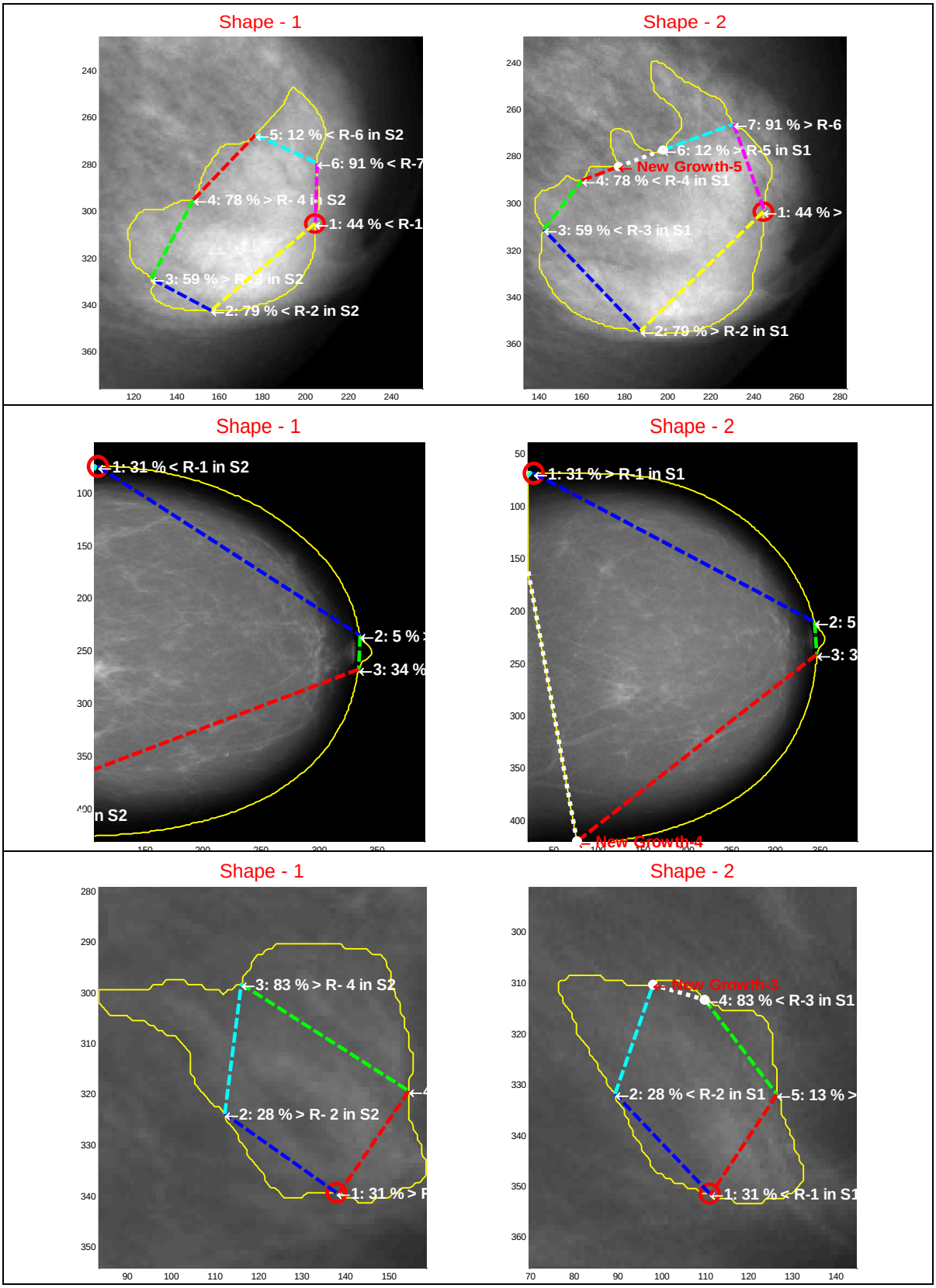
Shape - 1
Shape - 2
5: 12 % < R-6 in S2
6: 91 % < R-7
4: 78 % > R- 4 in S2
1: 44 % < R-1
3: 59 % > R-3 in S2
2: 79 % < R-2 in S2
7: 91 % > R-6
6: 12 % > R-5 in S1
New Growth-5
4: 78 % < R-4 in S1
1: 44 % >
3: 59 % < R-3 in S1
2: 79 % > R-2 in S1
Shape - 1
Shape - 2
1: 31 % < R-1 in S2
2: 5 %
3: 34 %
n S2
1: 31 % > R-1 in S1
2: 5
3: 3
New Growth-4
Shape - 1
Shape - 2
3: 83 % > R- 4 in S2
2: 28 % > R- 2 in S2
1: 31 % > R
New Growth-3
4: 83 % < R-3 in S1
2: 28 % < R-2 in S1
5: 13 % >
1: 31 % < R-1 in S1

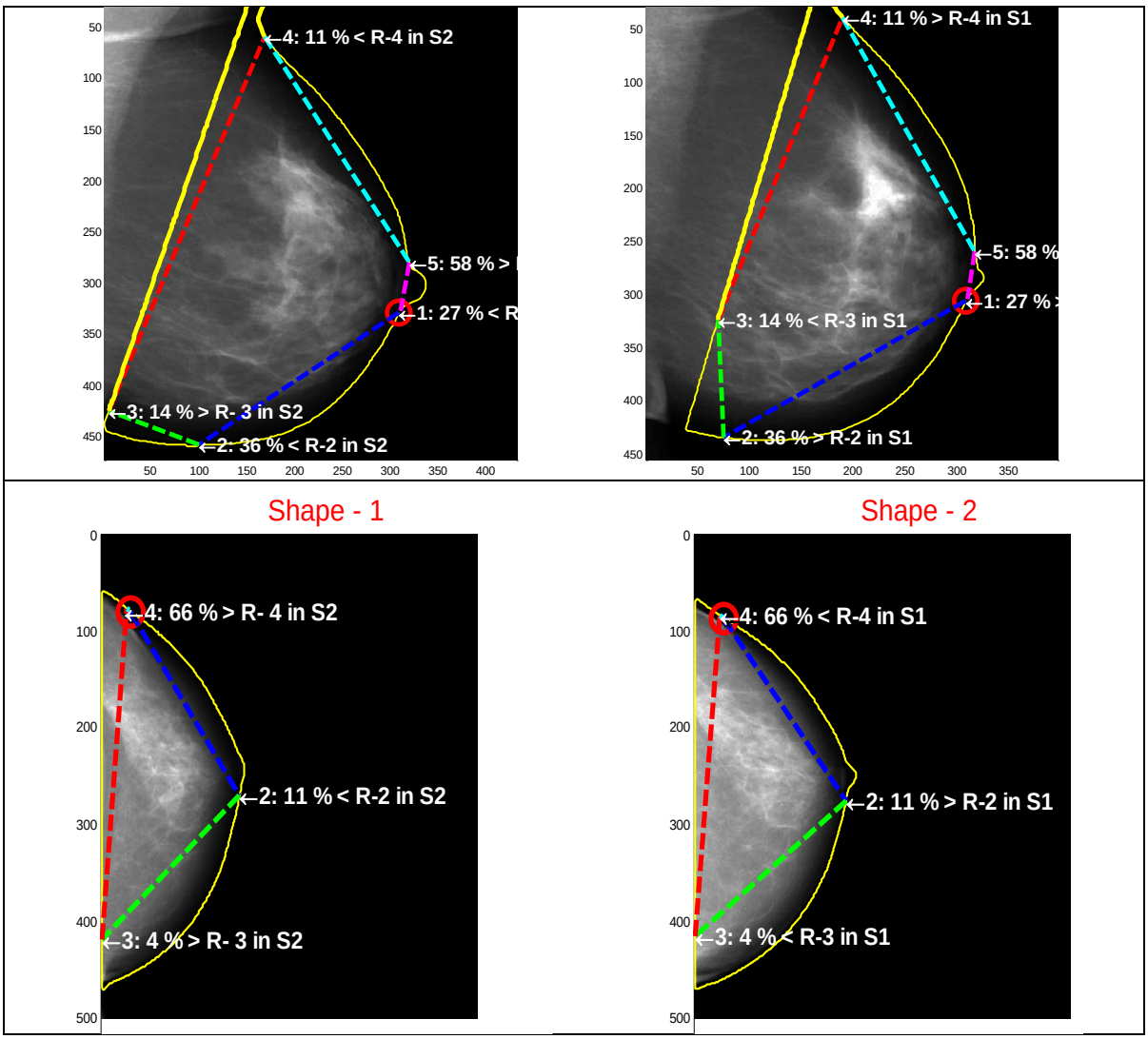

Figure 7.18: Region matching of corresponding contours on the temporal mammograms. The red circles in the shapes identify points of initial alignment. Regions are color-coded and show both good and bad examples of regional correspondences. The quantification is on area based measurements and are relative to corresponded regional differences.

7. 8. Conclusions

This chapter implements shape matching using the Fast Marching Algorithm and introduces a novel local Region Matching Algorithm (RMA) using Integral Invariants scale space. Shape matching and correspondence algorithms usually match and establish point-wise correspondences between two shapes and may even handle partial occlusion. However, they typically do not quantify partial occlusions nor identify complete

occlusions or new growth. It is important to measure regional differences quantitatively within each shape and establish correspondences based upon region matching. For masses, it is vital to analyse their growth and notice the emergence or disappearance of any region. This can be helpful in detecting new growths and identifying their orientation. Following region of interest segmentation, we have introduced a method of local shape correspondence and region matching using Integral Invariants scale space. Integral Invariants are calculated for segmented shapes from mammograms at all scales. The algorithm identifies causal peaks of this scale space as key points and breaks the shape into sub-regions based upon them. The best matching region is selected as a point of initial alignment and regions are corresponded based on a similarity measure. RMA gives encouraging results in detecting tumour growths and its aggressiveness with respect to shape.

`

Chapter 8

SHAPE MATCHING BY INTEGRAL INVARIANTS AND ECCENTRICITY TRANSFORM

8. 1. Introduction

As we saw in the previous Chapter, shape transformations, computed both with Integral Invariants and geodesic distance, yield signatures that are invariant to isometric deformations, such as bending and articulations. Though Integral Invariants were used to describe the shape boundary, they provide no information about *where* a particular feature on the boundary lies with regard to overall shape structure, which is important. On the other hand, eccentricity transforms can be used to match shapes by signatures of geodesic distance histograms based on information from inside the shape; but they ignore the boundary information. In this Chapter, we describe a method that combines both the boundary signature of a shape obtained from Integral Invariants and structural information from the eccentricity transform to yield improved results**.** The continuous eccentricity transform is used to find descriptors of shape based on geodesic distance maps. Such descriptors then yield histograms in the form of shape signatures. The signatures obtained by the eccentricity transform are considered to be invariant under rigid motion and isometric transformation of shape.

8. 2. Eccentricity Transform as an Inside Shape Descriptor

Compared to curvature measures [141], [144], [149], [178], [182], [203], [206], [242], eccentricity transforms (Ecc) are robust to noise [323]. Ecc finds the geodesic distance for each point within a shape, to every other point on the boundary. Figure 8.1 illustrates the geodesic distance inside a shape as compared to Euclidean one. It then assigns to each point a distance to the point farthest away from it. Instead of assigning the maximum

distance, the mean, median or minimum distance may also be used as shown in Figure 8.6. The geodesic distances for this purpose are calculated using the Fast Marching Algorithm (FMA). The Ecc shape matching algorithm, matches histograms obtained from Ecc transformed images. Such a geodesic distance histogram does not explicitly contain boundary information, including information such as curvature. They do not appear to have been used previously for establishing point-wise shape.

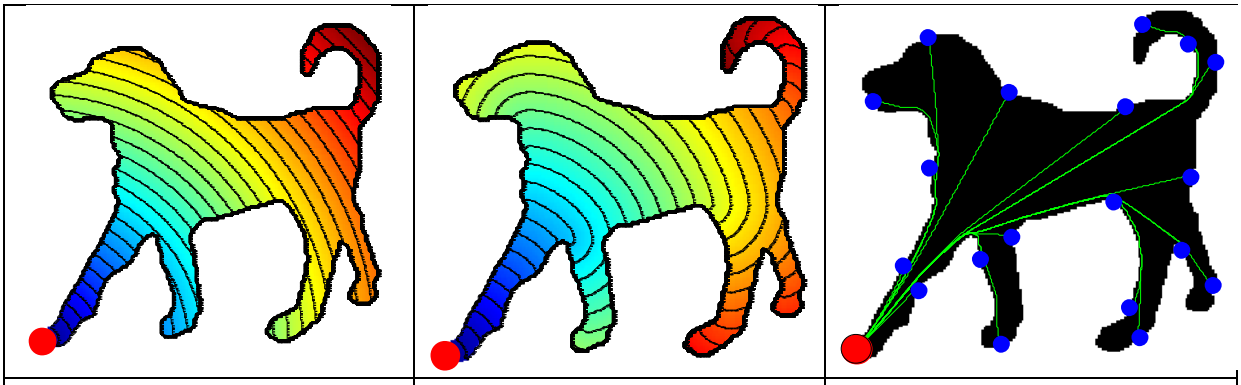

Euclidean distance shown in level contours inside the shape from the red dot in the bottom-left end of the shape	Geodesic counterpart of the shape on the left, attained using the Fast Marching Algorithm (FMA)	Illistration of geodesic paths to various points on the boundary, traced inside the shape

Figure 8.1: A Euclidean and geodesic space representation. Figures on the left and the middle are colour coded with distances, increasing from blue to red in the standard 'jet' false colour map.

8. 3. Limitation of Integral Invariant

As we have seen in previous chapters, Integral Invariants are shape descriptors that are preferred to curvature for their robustness to noise, and have been used effectively for shape matching applications and for dividing shapes into further regions to quantify occlusion and new growth. However, a fundamental limitation of Integral Invariants is that they relate only to the boundary and do not take into account the information from inside the shape. As a result, two similar geometric features on a shape boundary, at very different geometrical locations will produce the same shape signature. This may result in

false matches in point-wise shape correspondences. Our aim in this Chapter is to combine the two ideas, tuning Integral Invariants boundary signatures based on the eccentric information about locations within a shape. Figure 8.2 shows a shape with two pointed peaks, which have similar features, though in different locations. In the eccentricity transformed version of shape; it is immediately apparent that the two peaks now contain different values in the false colour model, and shown in Figure 8.3 using shape signatures.

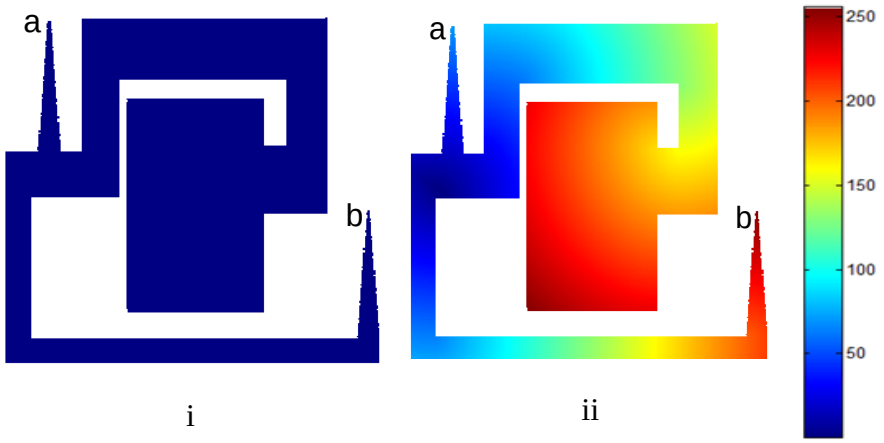

Figure 8.2: A shape (i), with eccentricity (Ecc) transformation in (ii)

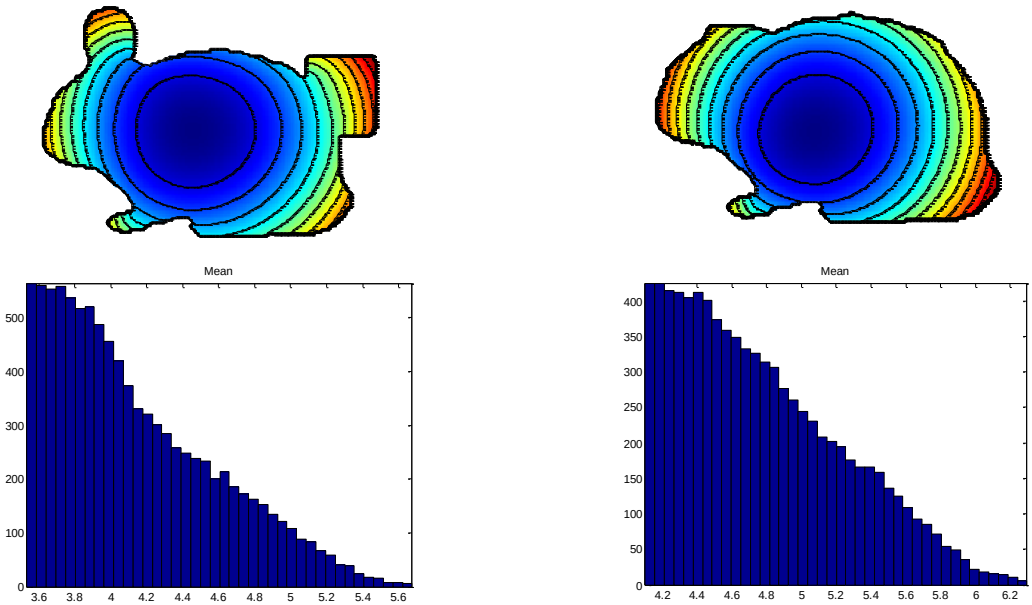

Figure 8.3: Shape histogram signatures of two shapes from Kimia database. The eccentricity transform fails to describe the difference in a meaningful way between the two shapes.

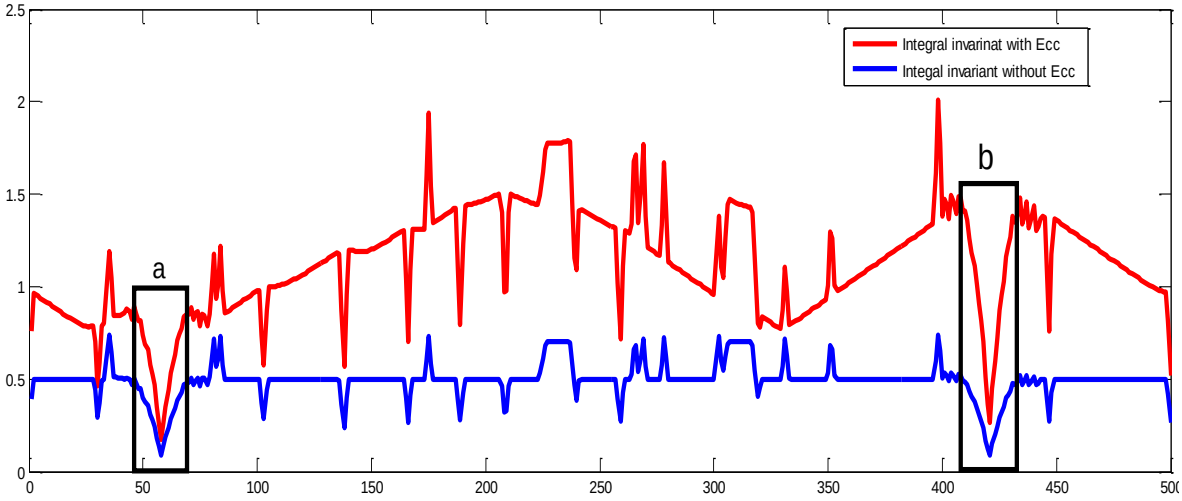

Figure 8.4: Normalized II signature (blue) of the original shape in Figure 8.2. The II invariant signature of the Ecc version (II-on-Ecc - red). The portions *a* and *b*, show how two similar features may be tuned based on their locality using proposed method.

Figure 8.4 explains our approach. The integral invariant shape signature, shown in blue, cannot differentiate between points ‘a’ and ‘b ’, giving no clue about the location of these points inside a shape. By location we mean intend spatially invariant and based on the structure of the shape. The eccentricity transform gives a distinct meaning

In a typical shape correspondence application, this will help in establishing correct correspondences. Figure 8.3 illustrates this limitation. Figure8.5 shows two shapes, *S1* and *S2*, with a pair of corresponding points, where *a1* corresponds to *a2* and *b1* corresponds to *b2*. Both shapes are processed and corresponded as shown. Eccentricity transforms are used for shape matching and retrieval applications, however, they fail to identify difference between two shapes.

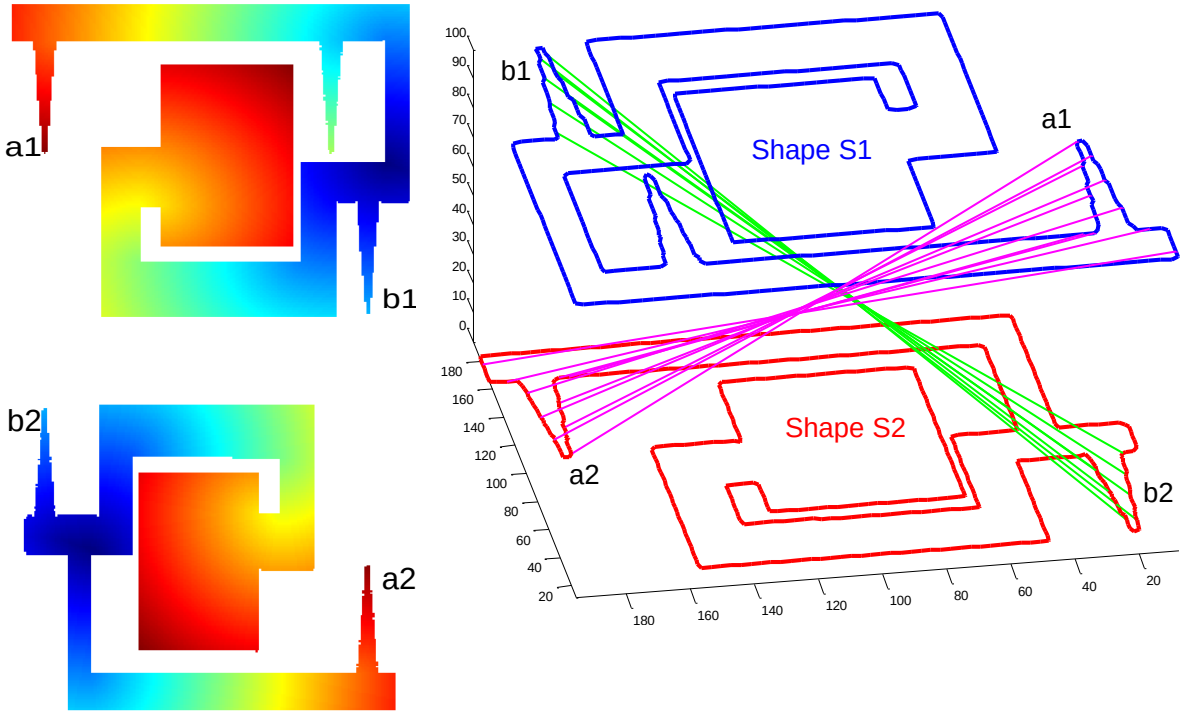

Figure 8.5: Two Ecc transformed shapes (left) and its correct correspondence (right) using II and Fast Marching Algorithm. II without Ecc will incorrectly match points *b1* to *a2* and *a1* to *b2*.

8. 4. Eccentricity Transforms Implementation

Ion [210], [323], [324] defines the eccentricity transform by considering a shape $S \subset \mathbb{R}^2$ with a smooth boundary ∂S, where S may be an image f_s of $n * m$ pixels, such that,

$$f_s(x) = \begin{cases} 1 \; for \; x \in S \\ 0 \; otherwise \end{cases}$$

The geodesic distance $d_s(x, y)$, between any two points x and y on the shape S is given by,

$$d_s(x,y) \stackrel{\text{def}}{=} \min_{\gamma \in p(x,y)} L(\gamma) \quad , \; where \; L(\gamma) \stackrel{\text{def}}{=} \int_0^1 |\gamma'(t)| dt \qquad (8.1)$$

Where, $p(x, y)$ is the set of paths $\gamma(t)$ from x to y, such that

$$\gamma(t)\begin{cases}0\ for\ t = x\\1\ for\ t = y\end{cases}$$

Inside the shape, and for any starting point x_0, the distance function $U(x) \stackrel{\text{def}}{=} d(x_0, x)$ can be computed by the finding solution to the Eikonal equation,

$$\forall x \in S,\ \|\nabla U(x)\| = 1, and\ U(0) = 0 \qquad (8.2)$$

The Fast Marching Algorithm is used to solve the above Eikonal equation to find the minimum path between $x_0\ and\ x$.

The eccentricity transform (Ecc) of S to each point $p \in S$ is the shortest geodesic distance to the point on S, farthest away from it. In the feature set of the shape, where the distance for each point inside the shape is calculated to every point in the boundary, thus forming $I_n \times I_m \times n$ feature space, where $I_n \times I_m$ are the image dimensions and n is the parameterization of the boundary curve ∂S.

$$Ecc_S(x) \stackrel{\text{def}}{=} \max_{y \in S}\ d_s(x, y) = \max_{y \in \partial S}\ d_s(x, y) \quad (8.3)$$

The original paper [210] on Ecc shape matching calculates a histogram to calculate the shape signature, without giving boundary correspondences. We have used Integral Invariants to perform shape matching and establish boundary correspondence.

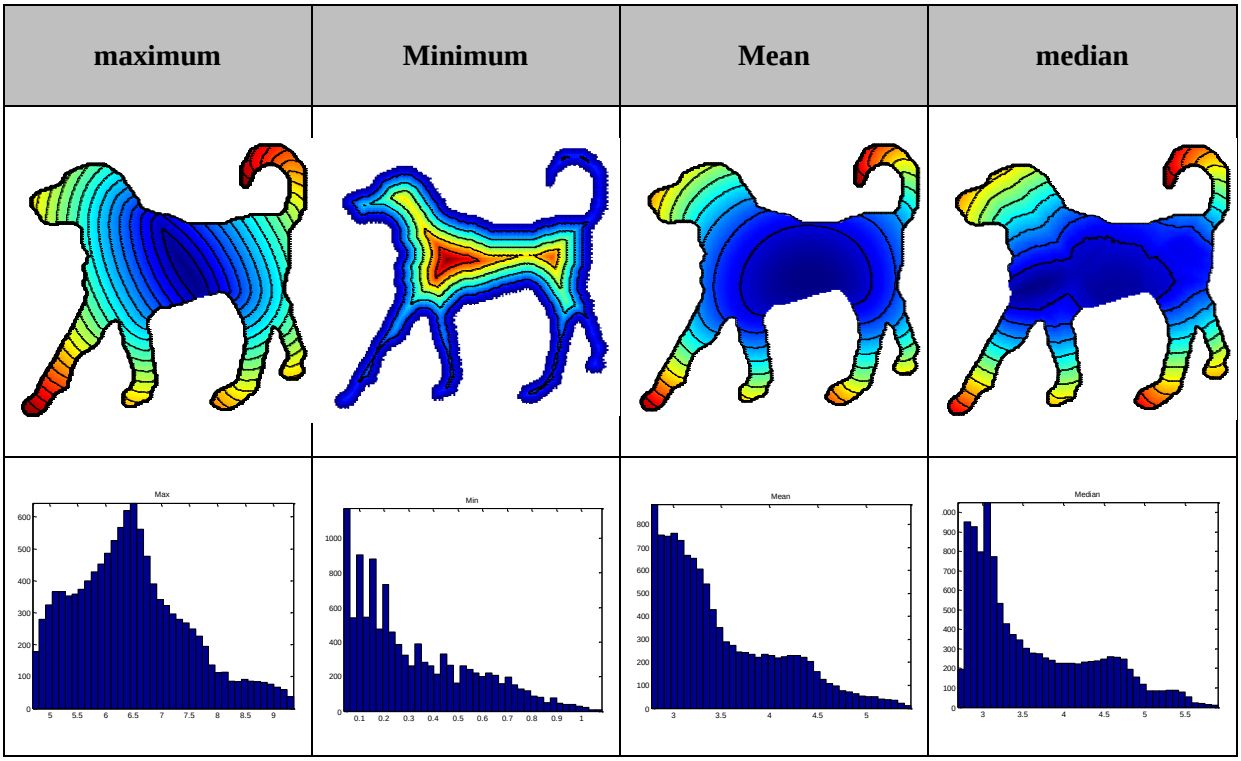

Figure 8.6: Eccentricity transformed shapes and their corresponding histograms underneath each shape. The top column shows what type of distance is taken into account from the feature space while finding shape transformations.

Figure 8.7 shows the feature set, where a geodesic distance of each point on the boundary to every point inside the shape is found. Hence we have a feature array for each point inside the shape with a size of 1xn, where n is the total number of samples on the boundary. The image size in this example is 200x200 and n = 500. The eccentricity transform shape signature is computed from this feature space, depending upon the type of distance used (i.e mean, maximum etc. as shown in Figure 8.6). Examples of shapes and their eccentricity transforms are given in Appendix III.

8. 5. Integral Invariants on Eccentricity Transformed Shapes

Once an Ecc image is acquired, a multi-scale approach is used for Integral Invariants (II) shape correspondence. The kernel size r is varied to span a range of apertures. As a result, Integral Invariants analysis creates a scale space where for every two points $x \in S1$

and $y \in S2$, the sum of squared difference of Integral Invariants is computed, and this forms a feature vector V_S. The largest singular value of V_S is considered to be the maximum distance between x and y. In this way a similarity/distance matrix $D(S_1, S_2)$ is obtained, which contains the Integral Invariants difference for each point between two shapes. For shape correspondence, the Fast Marching Algorithm is applied to the similarity/distance matrix to find a distance map $\widehat{D}(S_1, S_2)$, and then the shortest geodesic path $G(S_1, S_2)$ from $D(0,0)$ to $D(n, n)$ is calculated using gradient descent algorithm, where n is the parameterization of both boundary curves ∂S_1 and ∂S_2. An example of a similarity matrix is shown in Figure 8.10, with the geodesic map superimposed. The procedure is explained in the previous chapters.

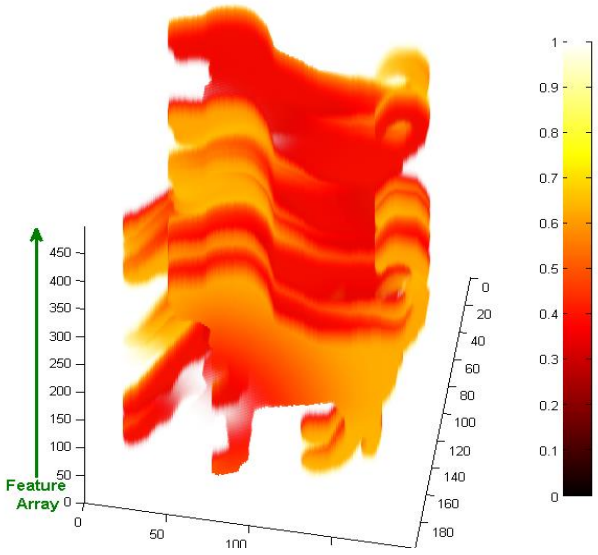

Figure 8.7: Feature set of all the geodesic distances inside the shape to every point on the boundary. The farthest point, or the maximum distance, is calculated along the direction of the feature array. The first two dimensions are the size of the image, the third is the number of feature points on the shape, whereas each point inside each shape describes a distance, normalized and presented in the false colour map with a colour bar on the right hand side of the figure.

The matching cost between two shapes is given by,

$$C(S_1, S_2) \stackrel{\text{def}}{=} \int_{D(S_1,S_2)} G\left(S_1(t), S_2(t)\right)dt \qquad (8.4)$$

8. 6. Results

The algorithm has been applied to 36 shapes from Kimia database - 4 shapes each from 9 shape categories. As the method is quite generally applicable, a broader evaluation may be carried out to evaluate precision of this method for a specific application. Though this algorithm is aimed at finding corresponding regions of interest in temporal mammogram, we have used Kimia database as it is considered a standard to assess shape matching algorithms. All pairs of shapes are compared and a matching cost is calculated for II, Ecc and II-on-Ecc matching. II-on-Ecc gives the *strongest intra group matching*. Figure 8.8 summarizes the result of matching. Dark blocks along the diagonal reflect low cost of matching within a specific shape group, which means higher similarity. Figure 8.11 shows the shape retrieval results for this method.

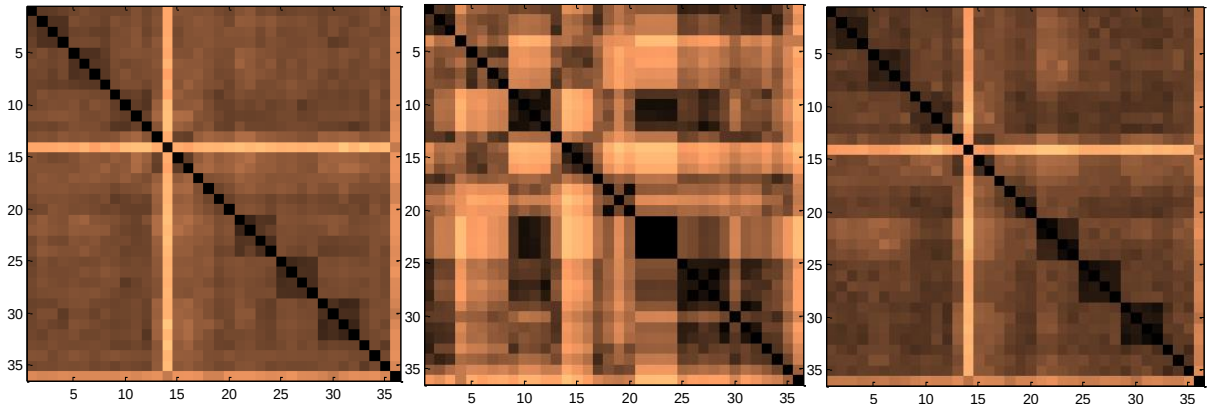

II Ecc II-on-Ecc

Figure 8.8: Shape matching results of methods mentioned above. Dark pixels reflect a low matching cost and higher shape similarity, which is greater for II-on-Ecc. Refer to 8.11 for shape retrieval details.

This following charts show the shape retrieval using Integral invariants, eccentricity transforms and Integral Invariants on eccentricity transform shapes. The X and Y axis of the chart consists of shapes, which are indexed consecutively from 1-36 in 9 different shape groups from Kimia database. Each box represents a shape on x-axis, and its height (range) on the y axis represent top 4 matches among all 36 shapes. The red bar in each box shows the median shape value of retrieved matches. Categories of Rabbits, Aliens, Tools, Men and Kite have perfect group retrieval results for II-on-Ecc method. Overall, using eccentricity transform prior to Integral Invariants show incremental improvements in results. However, this is neither the core strength nor the purpose of developing this method. The method is focused on reducing the correspondence error, for which it shows considerable promise.

8. 7. Application to Mammograms

We applied Integral Invariants on eccentricity transform to mammograms. The aim is to find changes in the region of interest, over time or in different views of the same mammogram. Figure 8.10 shows a pair of Craniocaudal (CC) and Mediolateral oblique (MLO) breast density maps created by Volpara® [10]. Both mammograms were automatically segmented using a hierarchical segmentation method (topographic approach) based on iso-contours. As a result, a number of regions were segmented and were matched using the method described above. Two regions, suspected of being abnormalities are shown in Figure 8.10. It may be noticed that II-on-Ecc performs better than II alone; the difference is clearly seen in Figure 8.11, where the geodesic path for II-on-Ecc shows a more regularized matching and consequently yield a lower matching cost for a closer match. Few more examples of this method applied to mammograms are given in Figure 8.12.

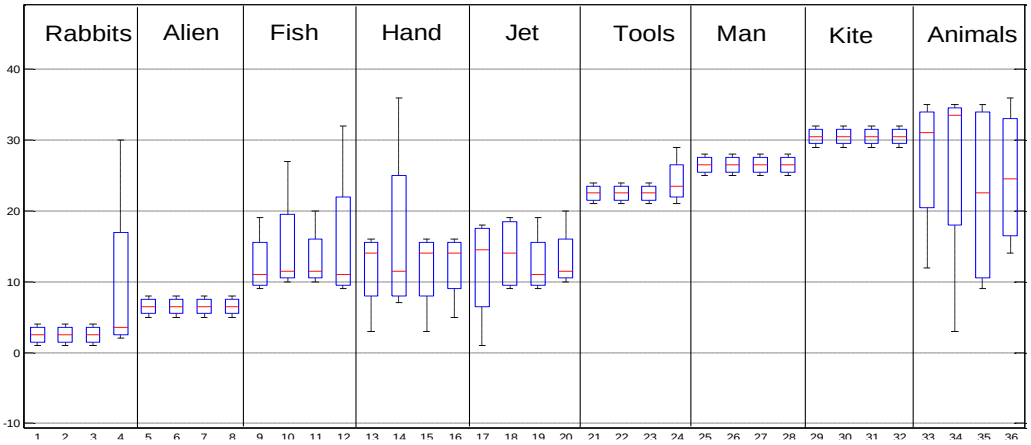

(a) Integral Invariant shape retrieval with noise

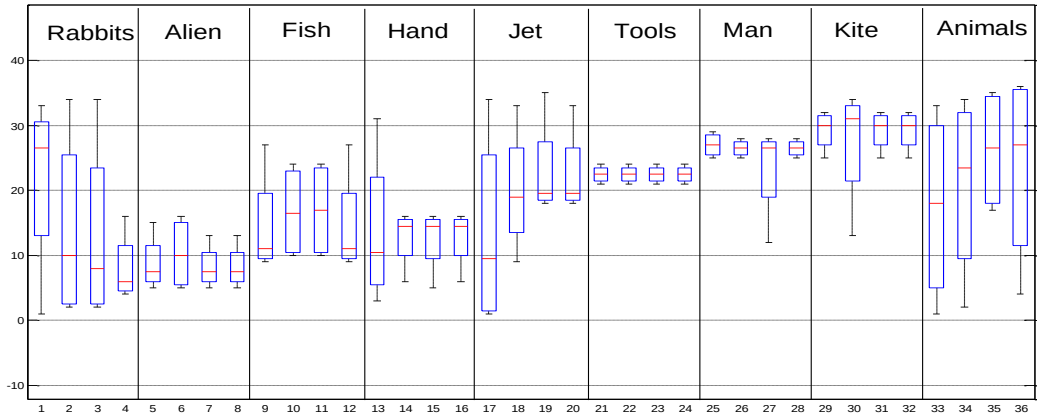

(b) Eccentricity transform shape retrieval with noise

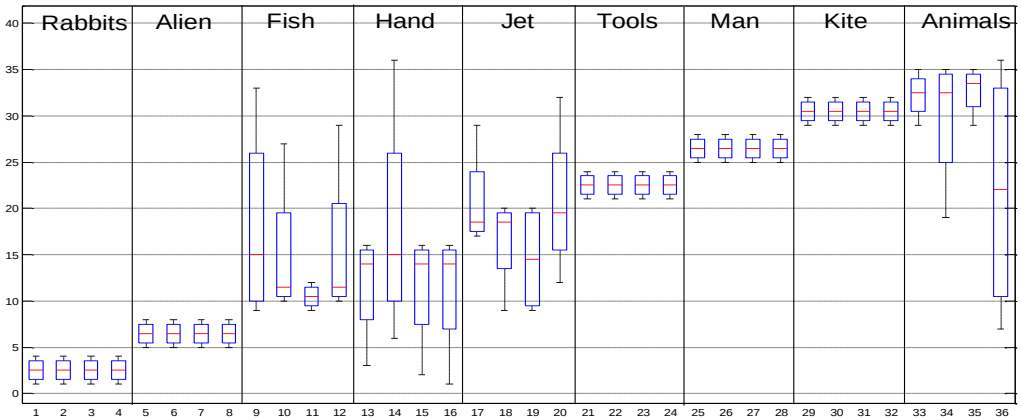

(c) Integral Invariants on eccentricity transform shape retrieval with noise

Figure 8.9: Shape retrieval results using mentioned methods

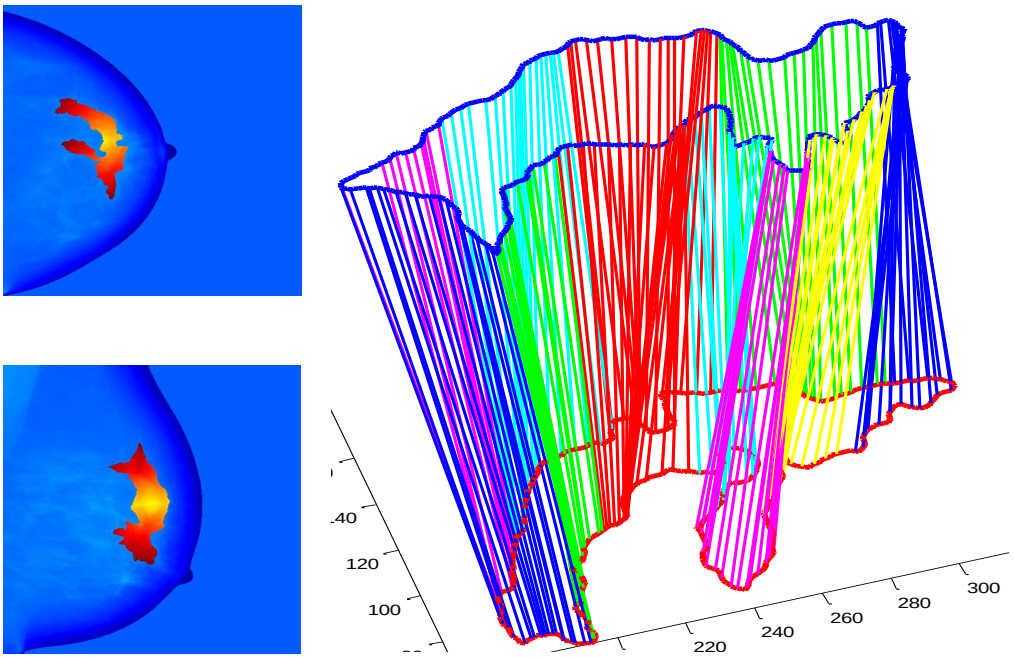

Figure 8.10: Segmented pair of CC and MLO views of breast density maps, obtained by Volpara® , and matched and corresponded using our proposed method.

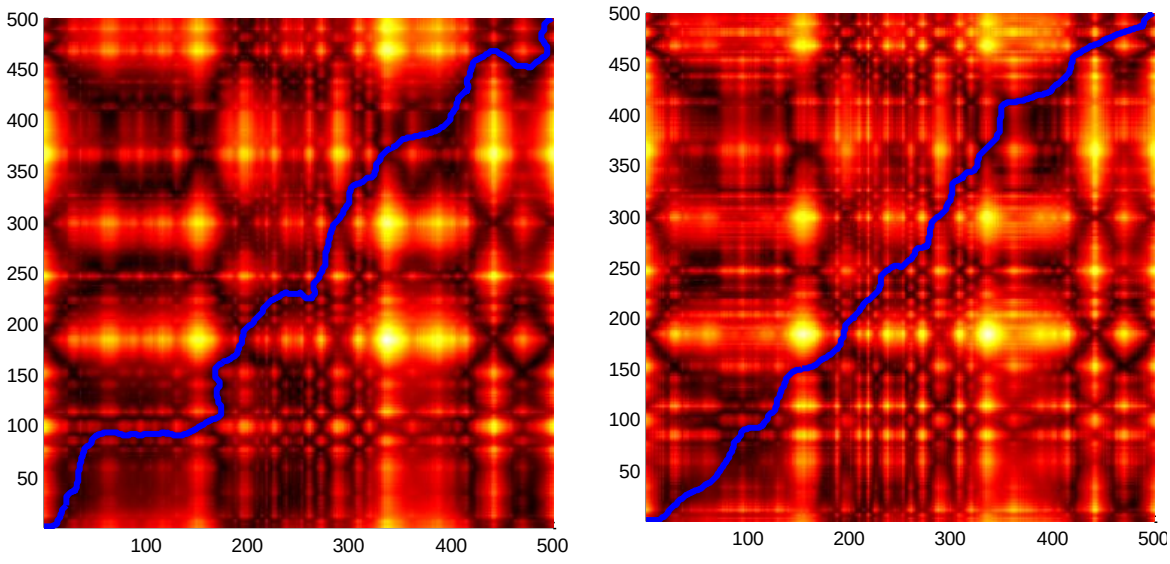

II II-on-Ecc

Figure 8.11: Geodesic path drawn over similarity matrix, which shows point-wise correspondence between regions in Figure 8.9. No results for Ecc given here, as it cannot establish point-wise correspondence of shapes.

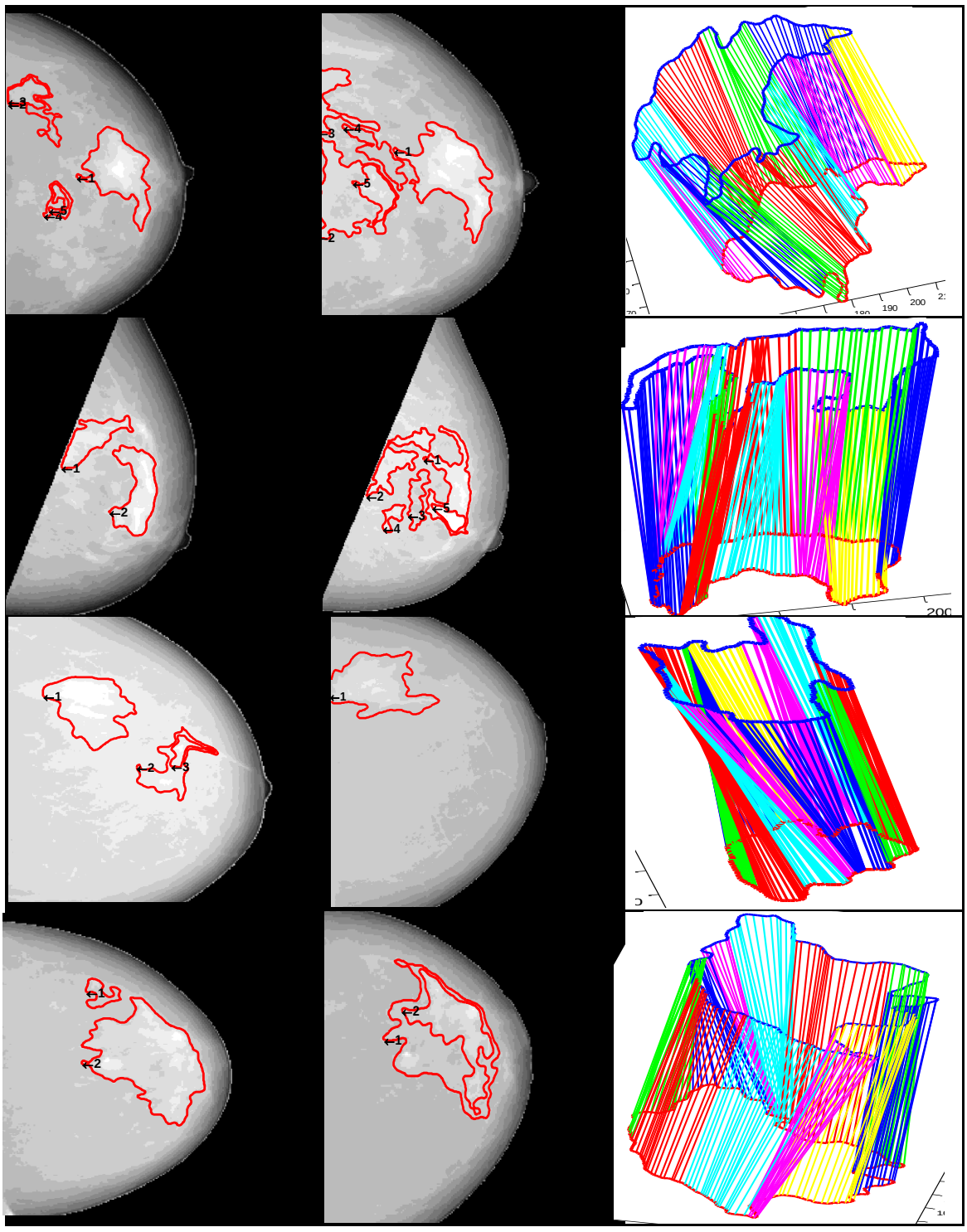

Figure 8.12: A few more examples of segmented, temporal mammograms, where regions are matched and corresponded against each other using the proposed method.

8. 8. Conclusions

We have combined structural and boundary information in a shape matching application, applied to regional correspondence in temporal mammograms. Integral invariants and eccentricity transform are invariant to isometric deformations, such as bending and articulations. However, the integral invariants is a contour based local descriptor, which relates to the boundary of the shape and do not take into account inside the shape. On the other hand, Ecc is a global region based descriptor that maps the structural anatomy of a shape, however, does not explicitly contain the boundary information, including curvature. We describe a method that combines both techniques by tuning the integral invariant boundary signature based on the eccentric information about regions within the shape.

Experimental results here reflect upon the correct matching, which is a qualitative improvement compared to integral invariant results; however, the main aim of this method is to reduce the correspondence error while matching two shapes. Shape matching algorithms usually stuck in local minima while establishing point-wise correspondences. This method first stretches regional differences within each shape, thus elaborate dissimilarities before comparing them, which reduces the probability of false correspondence. This feature is the fundamental strength of our approach.

We have applied our method to shapes from various groups of Kimia database and have compared the results to those obtained by integral invariants and eccentricity transforms when applied separately. There is an overall improvement in results for both inter and intra group shape matching. The fast marching algorithm was applied to establish a point-wise correspondence between shapes and to calculate a matching cost. The results are encouraging and indicate scope for further improvement.

`

Chapter 9

REPRODUCEBILITY OF MAMMOGRAPHIC DENSITY MAPS

9. 1. Introduction

X-ray mammograms are used routinely in screening to detect abnormalities in the breast for an asymptomatic population of post-menopausal women, and to assess the qualitative density of breast regions. However, the study of mammograms currently relies on subjective assessment, which leads to large inter- and intra-observer variability. The appearance of a mammogram, considered as an image, varies very considerably among women and depends upon the imaging parameters, tissue characteristics, and the response of different breast tissues to x-ray attenuation. The need for reproducible breast measurements is evident from the fact that parenchymal patterns are subject to change over time, for a number of reasons. Therefore, quantitative estimation of breast density which is independent of imaging conditions is required, not only to assess the risk of developing cancer but also to help in diagnosis and prognosis of the disease.

In this chapter, we investigate the reproducibility of mammographic density maps and we compare two volumetric density estimation techniques for a mammographic screening population: Standard Attenuation Rate (SAR) [111] and Volpara®®, commercial software provided to us by Matakina Ltd. Our primary goal is to evaluate consistency in volumetric measures by investigating the nature of their relationship, and to this end we show a strong linear association between their outputs. The results further reinforce the use of volumetric measures to assess risk of breast cancer with respect to mammographic density in clinical

practice. Please refer to Chapter 2 for a detailed review of breast density measurement methods.

We have used Volpara® density maps, along with the intensity mammograms, throughout our thesis. In this chapter we have evaluated the robustness of Volpara® density maps by comparing it to another accurate density model, the Standard Attenuation Rate (SAR). SAR is an absolute physics model, unlike Volpara® which is based on relative physics. It does not rely on the information from the image but evaluates tissue density as a measure of observed x-ray attenuation with the help of carefully quantified breast tissue phantoms. We have found a linear relationship between the two and have seen that both the modalities have a close tissue to background ratio for bright regions, indicating the finds of Volpara® to be accurate.

9. 2. Methods

Digital Mammographic images of seven women aged 45-71 were processed using both the SAR and Volpara® systems. The mammograms were taken at the Elizabeth Wende Breast Centre in Rochester, New York with a General Electric DS FFDM scanner, during routine screening and were made available by Matakina Ltd. The images were acquired between 2010 and 2011 with standard x-ray dose and tube voltage. At least two of the mammograms were suspected to contain abnormalities. Processing of the images to produce the SAR maps was kindly done by Dr. Chris Tromans. SAR and Volpara®(V 1.4.3) generated density maps, though they have substantially different resolutions covering slightly different regions. The Standard attenuation rate and Volpara® were explained in detail in Chapter 3.

9. 2. 1. Simple Linear Iterative Clustering (SLIC)

To compare the two techniques, a direct pixel-by-pixel comparison cannot be applied because of the high variability in density values of neighbouring pixels, particularly in the bright regions; making it difficult to estimate a tissue value from a single pixel (see Figure 9.1).

The reason to use a different segmentation method to assess the reproducibility of density maps, other than already developed, is that topographic segmentation of isocontours do not give piecewise homogeneous segments of mammographic regions, instead contours at the same iso-levels. Since we are comparing regions of various densities and radiodensity regions, it is important that we compare clusters with similar pixel properties and SLIC is an answer to this.

An average tissue value could be estimated from averaging or isotropic diffusion. However, this may give misleading results by averaging pixels across non-homogeneous regions. The hierarchical iso-contour based algorithm (Hong's algorithm) we have used so far does not necessarily look for feature based homogeneous regions. Instead, it forms contours at the connected pixels lying at the same iso-level irrespective of the enclosed region. It is highly dependent upon the nesting depth of eccentric contours, is sensitive to noise, and to the number of iso-levels that is set initially.

To address this issue, we have applied Simple Linear Iterative Clustering (SLIC) [325], [326] to decompose the image into visually homogeneous regions. This is based on a spatially localized version of k-means clustering where each pixel is associated with a feature vector and k-means clustering is then run on those vectors. The image is first divided into a grid of a certain region size and the centre of each grid tile is used to initialize a corresponding k-means. Finally, the k-means centres and clusters are refined by

using the Lloyd algorithm [327]. The standard Lloyd algorithm assigns pixels to the closest clusters and iteratively updates their centres. After k-means has converged, SLIC eliminates any connected region whose area is less than a minimum region size. This is done by greedily merging regions to neighbouring ones.

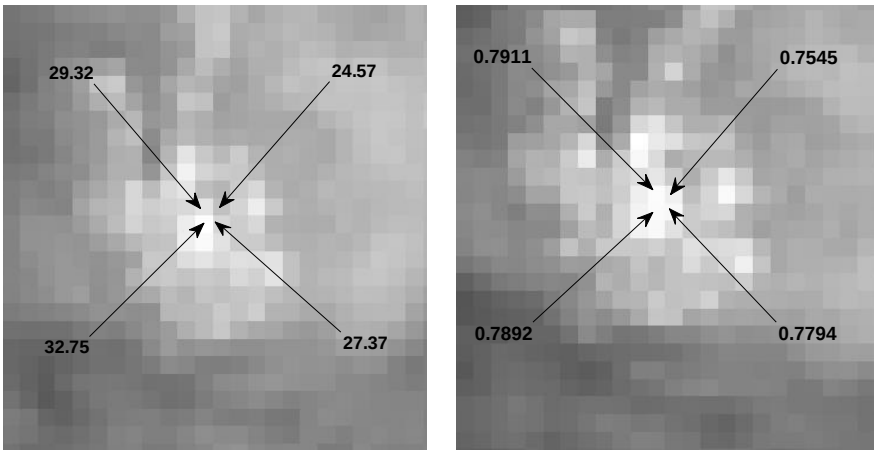

Figure 9.1: Variation in neighbouring pixel densities in units as: in Volpara® mm (left) and in SAR x-ray attenuation measure (right)

Figure 9.1 shows significant variation in the values between the neighbouring pixels of both breast density measures and forms the basis of regional segmentation for the analysis given in this chapter, as compared to pixel based approach.

SLIC starts by dividing the image domain into a regular grid with M×N tiles, where

$$M = \left\lceil \frac{W}{S} \right\rceil \ , \ N = \left\lceil \frac{H}{S} \right\rceil$$

W is the width, H the height, and S is the size of the image. Each region is called a super-pixel, which is a k-means cluster with a grid center$(x_{i,}, y_j)$, where,

$$x_{i,} = \text{round}\left(i * \frac{W}{S}\right), \qquad y_j = \text{round}\left(j * \frac{H}{S}\right)$$

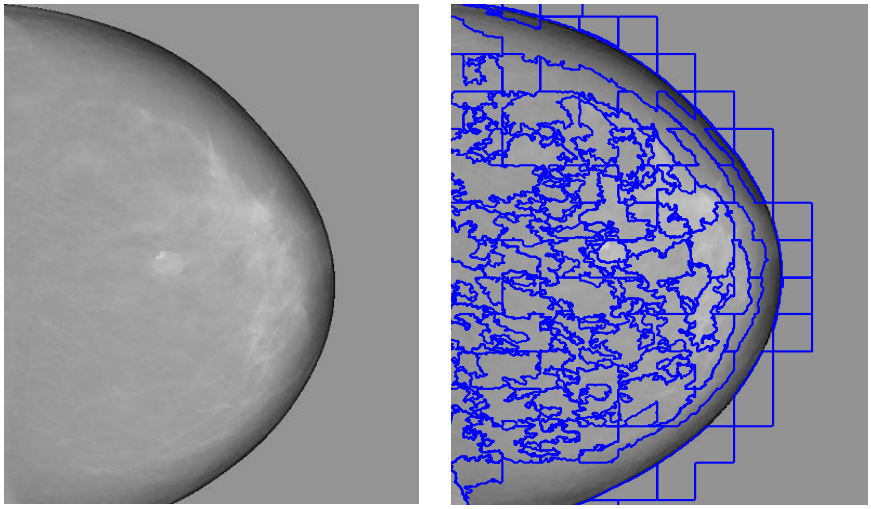

Figure 9.2: A Volpara®image (Left), SLIC segmentation overlaid (Right).

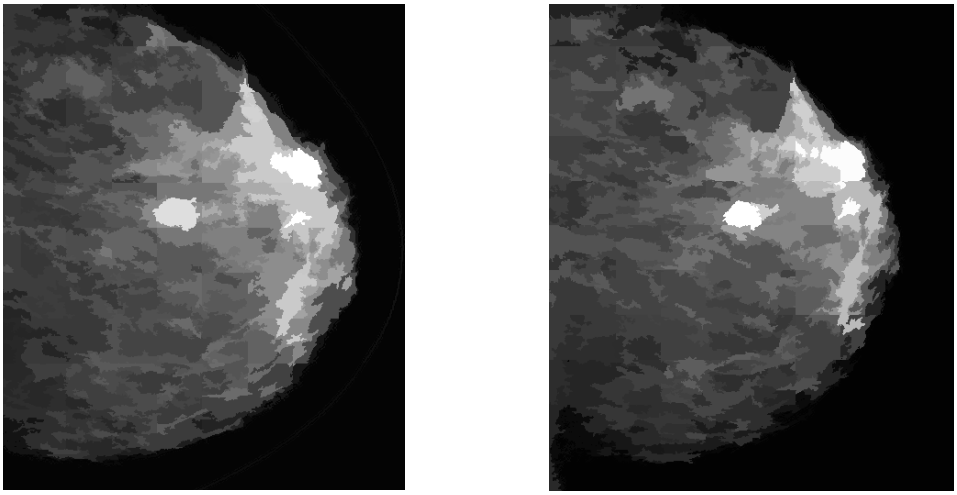

Figure 9.3: Mean density region map of Volpara®(left) and SAR (right) in Figure 9.1

SLIC clustering with various region sizes and regularization factors is illustrated in Figure 9.4. For mammograms, we have used a lower value for the regularization factor λ, which sets the trade-off between spatial regularization and cluster\region size, so that the SLIC segmented regions can adopt the true tissue shape based on local homogeneity.

$$\lambda = \frac{\text{regularizer}}{\text{regionSize}}$$

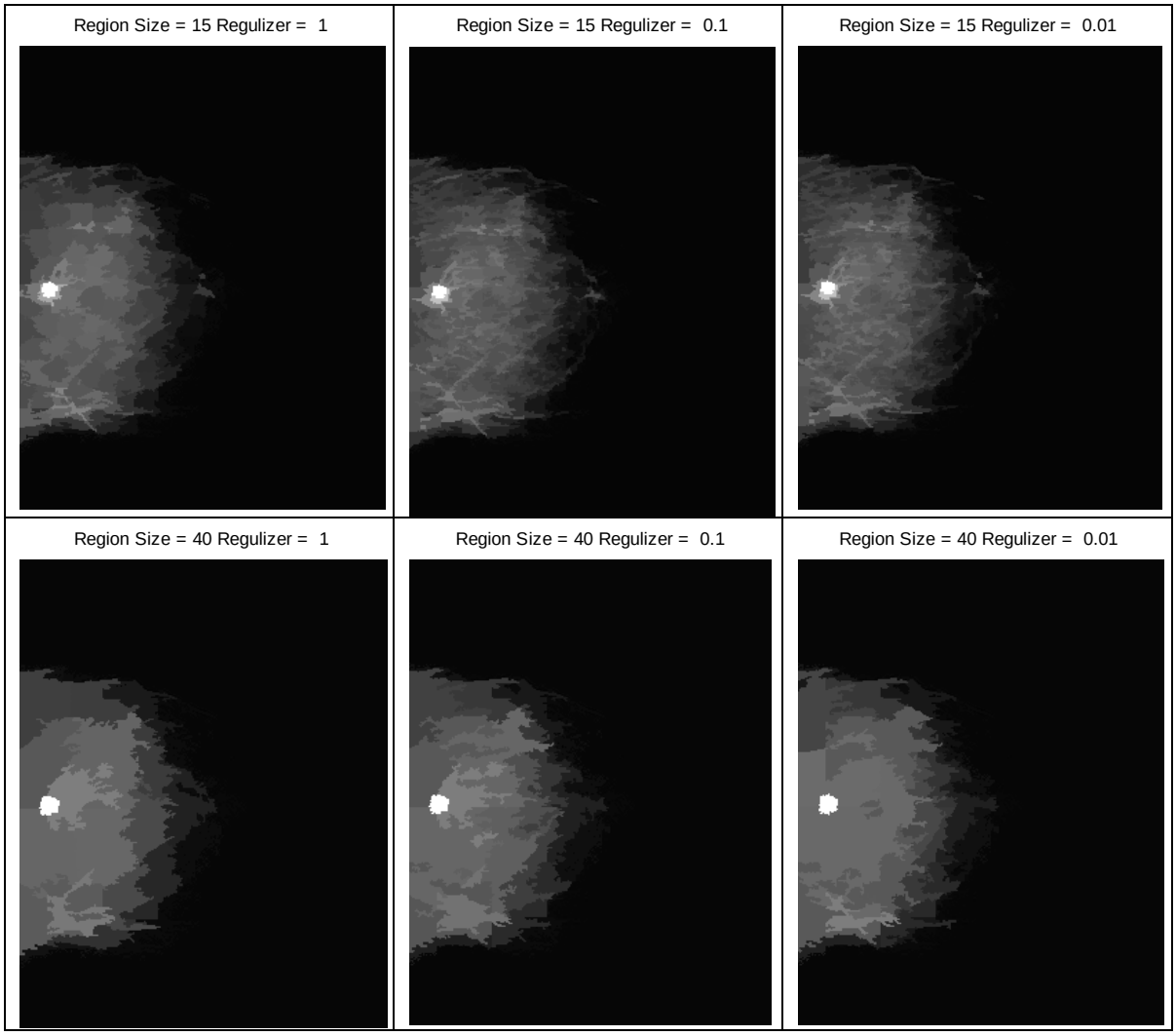

Figure 9.4: SLIC region clustering using various region sizes and regularization factors

We have applied SLIC to both Volpara® and SAR images, which gives basically the segmentation overlay while dividing the image into homogeneous regions or super-pixels. Then we computed the mean region density map, where each super-pixel now represents the mean density of that region, and then relating spatially corresponding super-pixel means that are comparable in size and shape. It is to be noted that Volpara® and SAR generate different SLIC segmentation regions because of the intrinsic variations in the images. Figure 9.5 gives a few examples of mean region density maps (MRDM) for Volpara® and SAR. A region of interest could also be extracted from MRDM; a couple of examples are given in Figure 9.6.

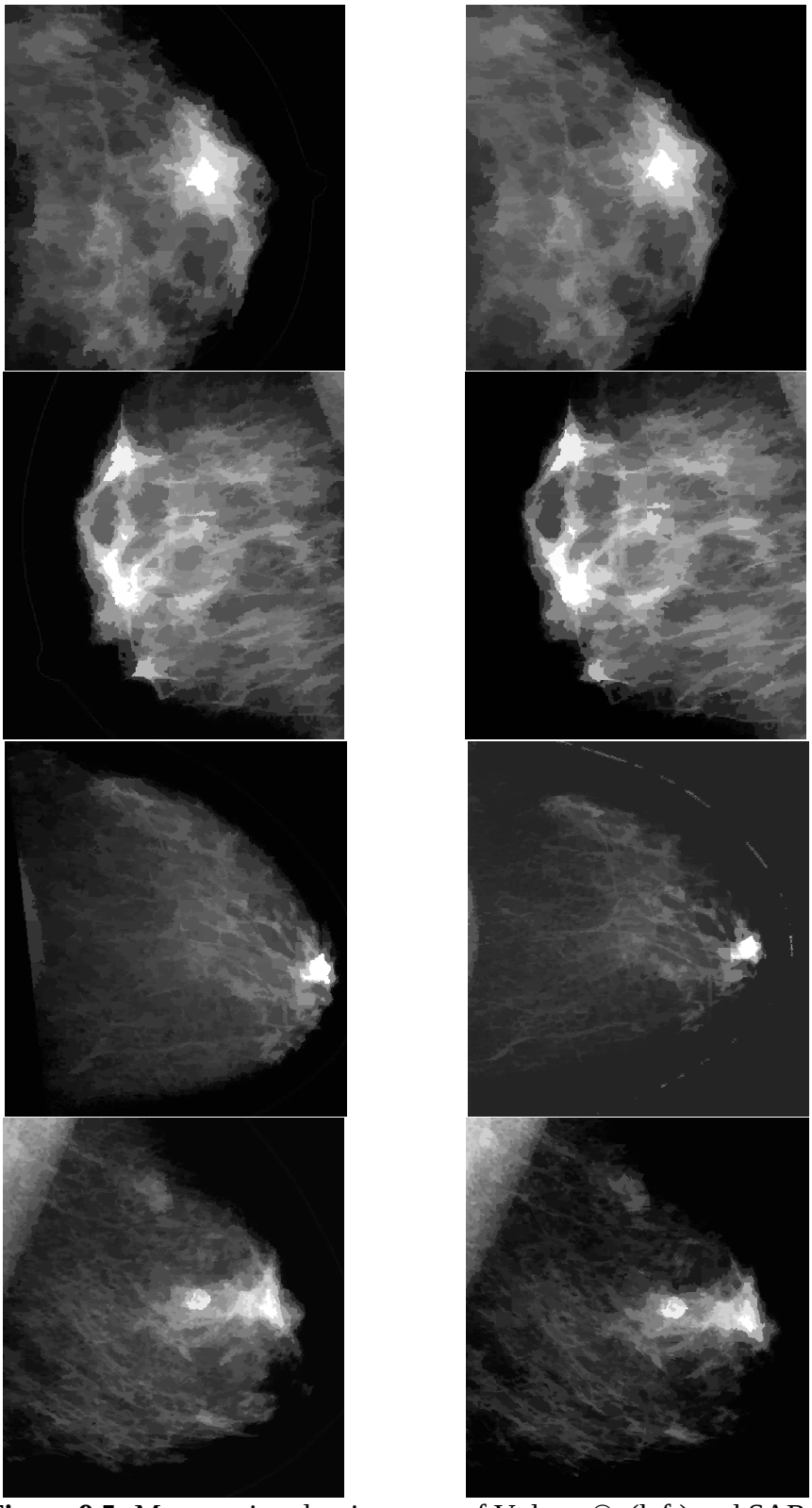

Figure 9.5: Mean region density maps of Volpara® (left) and SAR (right)

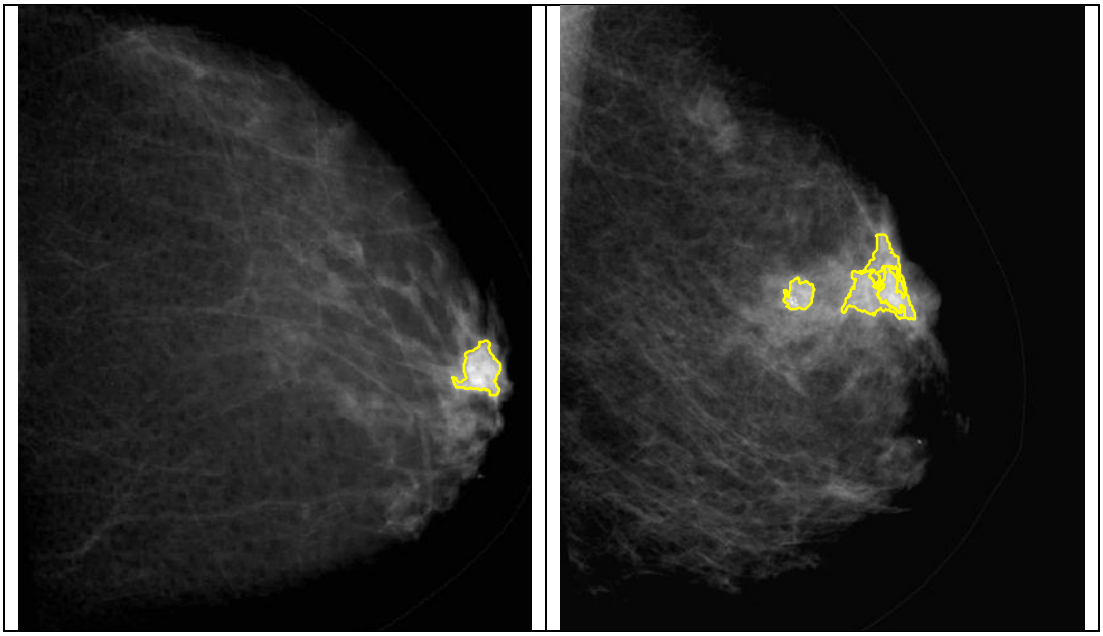

Figure 9.6: Automatic segmentation of ROI using mean density region maps in two Volpara® maps.

We applied SLIC to both Volpara® and SAR images, yielding the segmentation overlay while dividing the image into homogeneous regions or super-pixels. Then we computed a mean region density map, where each superpixel now represents the mean density of that region. The spatially corresponding Superpixels with similar sizes related manually for regression analysis. Figure 9.2 shows a Volpara® image segmented using SLIC, while the mean region density maps of a SAR\Volpara® image pair are given in Figure 9.3. Note that Volpara® and SAR generate different SLIC segmentations because of their intrinsic variations.

9. 3. SAR & Volpara® Relationship

Using the above procedure, 156 super-pixels from the 7 pairs of Volpara® and SAR mean regions density maps were manually corresponded and compared in order to establish a relationship between the two. A strong linear relationship was found for the complete population, with a regression coefficient R^2 = 0.9618. The mean SAR per Volpara® millimeter was calculated for a sample size of 1mm to 43mm, where an average for each complete mm was found, gives R^2 = 0.9875 (Figure 9.7 & 9.8). A SAR value of 0.78 is

approximately what Volpara® assumes is fat (SAR_{Fat}), and a SAR value of 1.116 is approximately what Volpara® considers to be fibroglandular (SAR_{FG}).

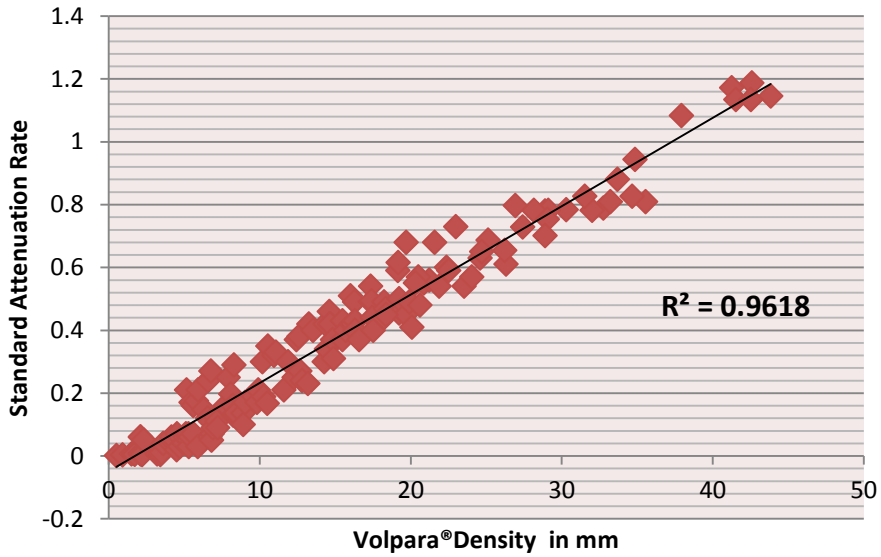

Figure 9.7: SAR-Volpara®- scatter graph for absolute sample values

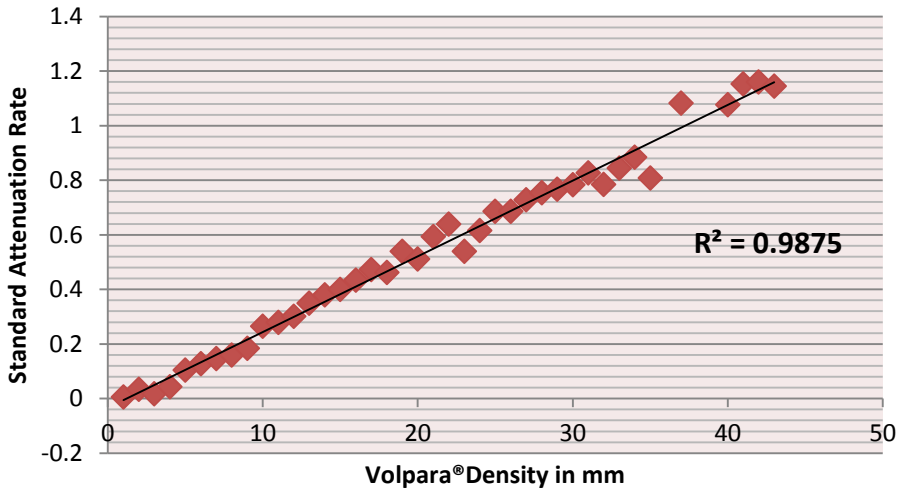

Figure 9.8: Mean SAR per millimetre of Volpara® density

Both SAR_{Fat} and SAR_{FG} are empirical estimates. However, SAR is calculated from an exact, carefully calibrated, physics model, whereas Volpara® is based on estimates from the image itself.

$$SAR_{Weighted} = \frac{(SAR - SAR_{Fat})}{(SAR_{FG} - SAR_{Fat})} = \ \% \text{ fibroglandular in Volpara®'s output} \qquad (9.1)$$

It is the percentage of fibroglandular that is of greater importance to clinicians and amounts to breast density. From the regression model,

$$Vol_{Estimated} = 35.608 * SAR_{Weighted} + 1.4251 \qquad (9.2)$$

$Vol_{Estimated}$ is an approximation of Volpara® image from linearly weighted SAR.

9. 4. Tissue to Background Density Ratio

Another important feature that not only reflects upon the contrast composition of Volpara® and SAR but also could be used potentially to reduce the number of false positives or to assess the saliency of regions is the tissue to background ratio (TBR). A mass that appears in a mammogram is virtually incompressible and dense relative to the rest of the breast tissue. This means that in a low or medium density breast, it will have a height with a difference from the background tissue. SAR and Volpara® density maps are generated for mammograms and segmented accordingly. Then each region is dilated using Integral Invariants diffusion and the surrounding layer is masked to get its mean density. To have a TBR comparison, a linearly weighted version of SAR is used here to make a relevance for analysis. Volpara® assumes two tissues, fat and fibroglandular. While some [108] argue that while these two broad classes clearly exist, significant variation exists in their composition from woman to woman (for example collagen density in stroma), lipid concentration in fat, and of course we have water in cysts, and mutated cells aggressively invading in malignancies. The SAR value therefore simply just measures x-ray absorption, and doesn't attempt to relate this to tissue type. A SAR value of 0.78 is approximately what Volpara® assumes to be fat, while 1.116 is approximately what

Volpara® considers fibroglandular. Please refer to Section 9.3 to see the SAR and Volpara® relationship.

We segmented a ribbon shaped structure around segmented regions of Volpara® and SAR and estimated its average density. It gives us an average density of a tissue to its background. It is achieved by taking the boundary of the Integral Invariant diffused version of segmented lesions. Figure 9.9 illustrates this. We observe a close pattern between SAR and Volpara® for TBR outcomes. A few examples of TBR comparison are presented in Figure 9.10 where the results are summarized in Figure 9.11.

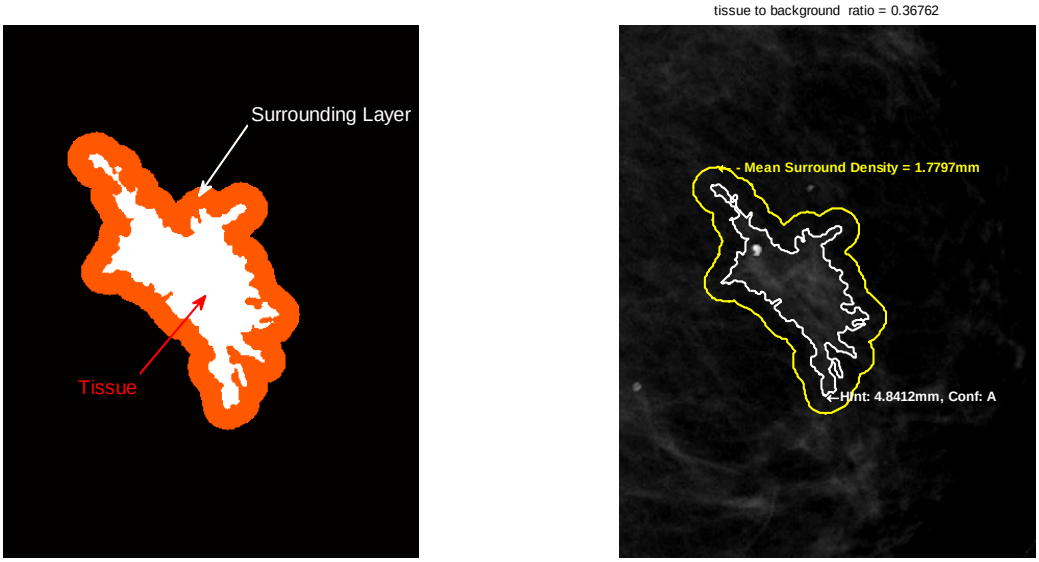

Figure 9.9: Two segmented regions and their TBR

Volpara	SAR
tissue to background ratio = 0.68456 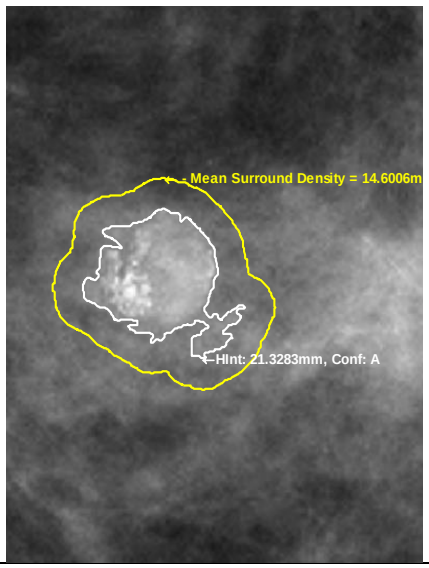	tissue to background ratio = 0.62199 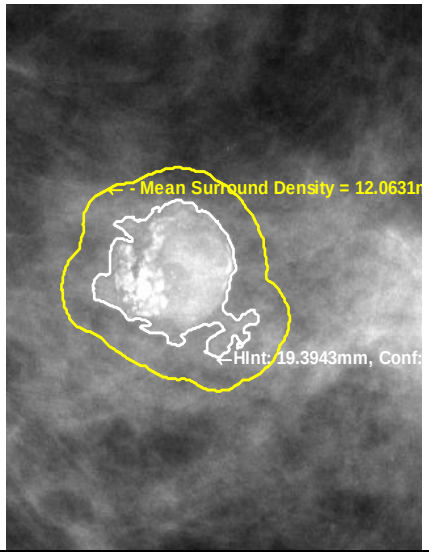
tissue to background ratio = 0.56989 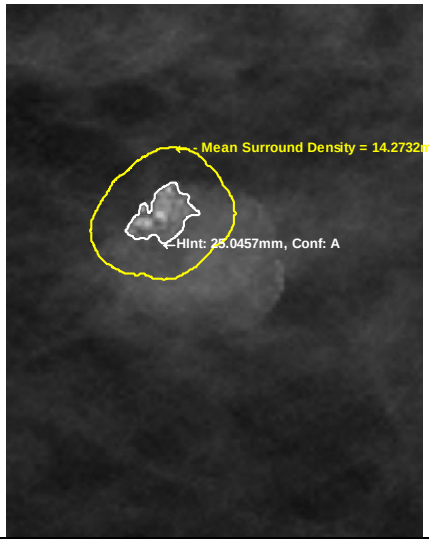	tissue to background ratio = 0.56843 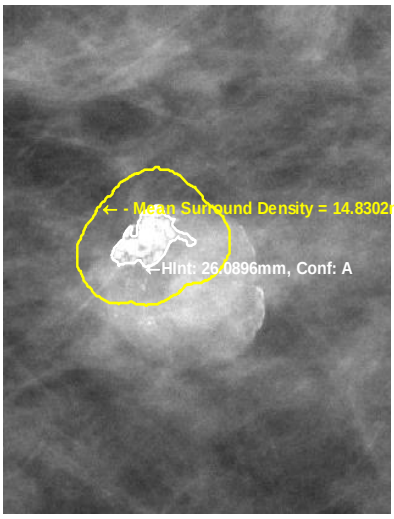
tissue to background ratio = 0.52439 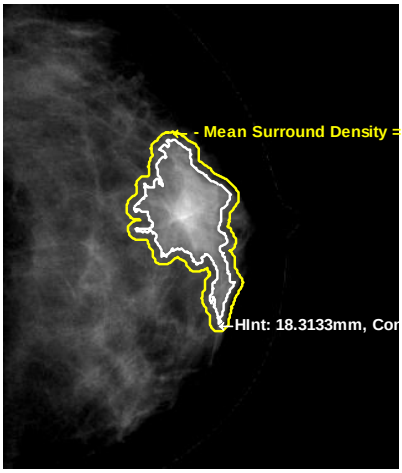	tissue to background ratio = 0.54828 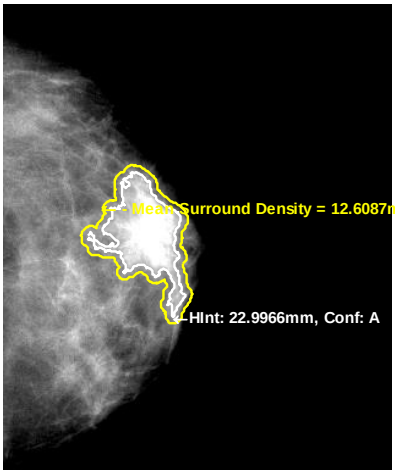

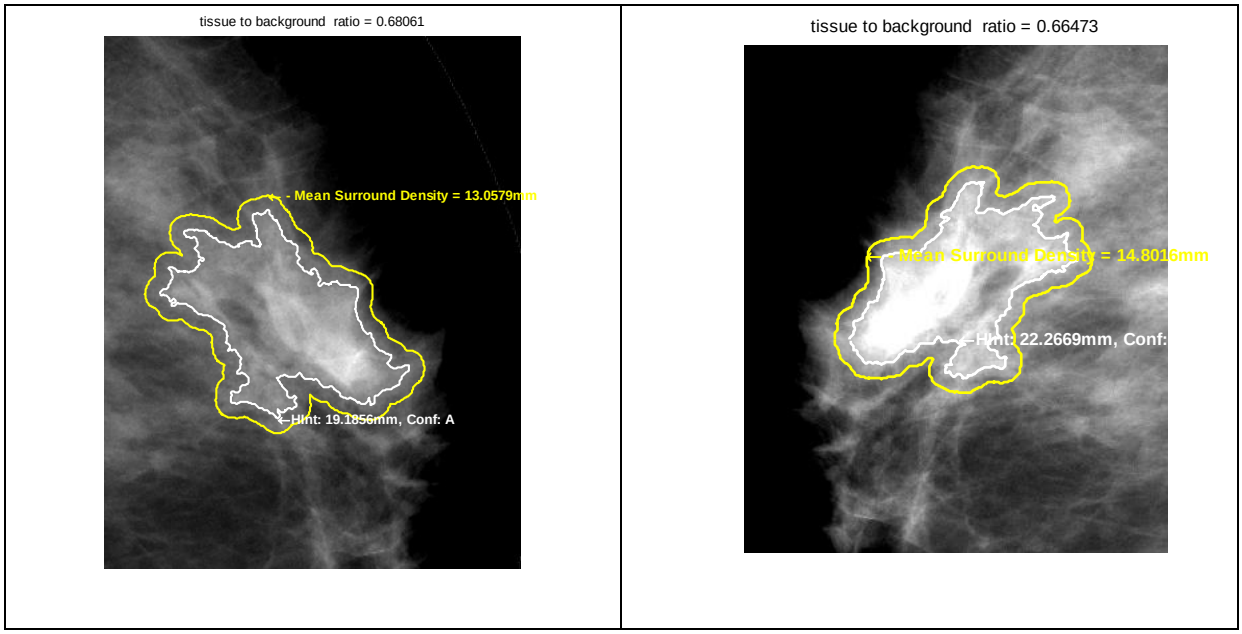

Figure 9.10: TBR of segmented regions from SAR and Volpara

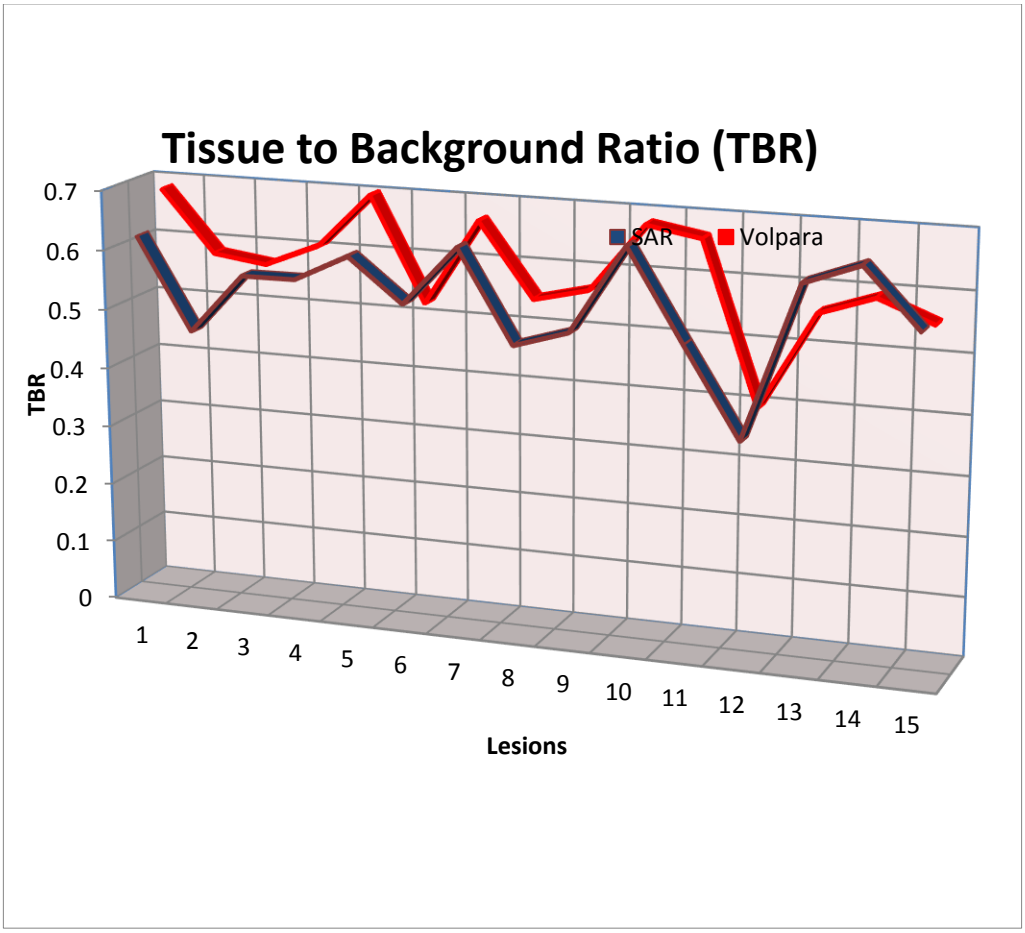

Figure 9.11: TBR of various lesions from Volpara® and SAR

9. 5. Conclusions

We have established a high correspondence between the FDA-approved fully-automated relative physics software Volpara® and the recently introduced absolute physics breast density metric SAR. We conclude that it is possible to compute volumetric estimates of breast density with high accuracy and reproducibility. However, as compared to SAR, Volpara® is in regular clinical practice at numerous hospitals around the word and is preferred for referring to breast density estimation in this thesis for this reason. Secondly, Volpara® gives a meaningful breast density measure as compared to its competitors, which is in mm and correlates closely to BIRADS breast density score for overall tissue density.

Both modalities yield a close tissue to background ratio for dense bright regions. There is a need now to further investigate this relationship and to fully understand the relation between the breast cancer risk and density estimating measures. The results indicate, despite the fact that the two models are based on different physics models, i.e. SAR has an absolute physics model and Volpara® has a relative physics model, both identify regions with nearly equal levels of significance, and this is an important finding.

`

Chapter 10

CONCLUSIONS AND FUTURE WORK

This chapter summarizes the main contributions of this thesis. It draws a number of conclusions and identifies the major limitations of this work. It also suggests some directions in which this research can be further advanced as well as applications where it may be applied.

10. 1. Conclusions

The primary objective of this thesis was to develop a robust and reliable shape analysis model that may be deployed in a CAD system to assist clinicians in the prognosis and diagnosis of tumours, which ultimately aims to reduce the mortality rates and enhance the quality of care. We have applied our shape analysis model to mammograms, with a particular interest in the identification and growth of suspicious or 'interesting' regions. We have also used temporal data to compare breast mammograms of a patient taken at different times. In addition, we applied our methods to Volpara® density maps, where available, which we believe are more robust for being invariant to imaging parameters. In this regard, we present a comprehensive review of breast density measures in Chapter 2, and of shape analysis with a focus on integral invariants in the Chapter 3. We consider the following to be the major contributions of this thesis:

1. Before we could apply our methods to mammograms, it was necessary to effectively characterise important mammographic regions and use them as closed contour shapes. We have developed a hybrid version of Hong's and Cerneaz' segmentation algorithms with some additional refinements and applied it to

mammograms from Mini-MIAS, the USF mammographic database, and density maps of SAR and Volpara. The hybrid algorithm is very efficient and results in good mammographic segmentations, certainly better than its predecessors. Chapter 4 provides a critical evaluation of, and the reasons for using, the particular segmentation method. The effectiveness of the method was assessed in a qualitative way; nevertheless, a quantitative method may be useful to evaluate the improvements in comparison to the original methods. One of the limitations of this method is the use of low-level image features such as intensity and homogeneity of regions, which may not be sufficient to achieve very precise segmentation boundaries. Though for the purpose of practicality to this point, it is a good compromise between the accuracy and computational cost.

2. We then explored the properties of Integral Invariants, which have already been used for shape matching in temporal mammograms. Multi-level integral invariants have been used in the past; however, they were not studied as an individual scale space before. Our shape analysis model based on Integral Invariant scale space is not only used for matching and decomposing shapes, but also for image filtering in terms of smoothing and feature enhancement for segmentation. In this latter regard, we compared the method to anisotropic filtering and to Gaussian diffusion as both are core to the scale space theory.
3. A novel local Region Matching Algorithm (RMA) was developed to decompose shapes into regions, to match regions in two shapes, and then to quantify the difference or articulations between shapes. Importantly, it is able to delineate complete occlusions and identify new growth, at least to a certain extent. The regions matching algorithm is based upon the linearity and causality of Integral

Invariants scale space. It has been applied to synthetic shapes from the Kimia database as well as to regions in mammograms.

4. We applied the Fast Marching Algorithm (FMA) along with Integral Invariants to matching breast regions in temporal mammograms. This reduced the correspondence error as compared to the previously used Dijkstra's method. This also improved the speed of matching in shape correspondence which results in a more regularized match and also found an accurate way for the initial alignment of two shapes.
5. Shape matching is a complex problem, where all known methods rely either on the boundary information describing a shape, such as curvature and the SUSAN edge detector, or on information from inside of a shape, such as bending invariants and the medial axis. We combined Eccentricity transforms and Integral Invariants, which improved the overall results by reducing the correspondence error and giving a more localized matching. Again, the method was applied to synthetic shapes and to match regions from inside the breast.
6. As noted earlier, we have used Volpara® density maps throughout our thesis. To assess their robustness, we have compared them to another breast density measure, the Standard Attenuation Rate (SAR). We found a linear relationship between the outcomes of the two modalities by comparing regions of breast using Super-pixel segmentation.
7. Finally, we developed a simple False Reduction method for mammographic regions using Integral Invariants scale space and the Fast Marching Algorithm.

10. 2. Future Work

The shape analysis model that we have developed is quite general and does not require any prior knowledge about the nature of the images or shapes enclosed in them. There are

many ways that this research can be extended. For instance, it could take the form of a CAD system that can be employed in a Clinical Decision Support System (CDSS). The Integral Invariants used here a circular ones applied on a 2D domain; however, medical images sometimes necessitate study of 3D images, such as 3D ultrasound or MRI for the study of breast cancer. Using Integral Invariants on 3D medical images may help in shape matching of reconstructed tissues or the whole organs. Furthermore, such a shape analysis model may be used on cytology images to analyse the behaviour of tumour cells. Here we discuss two of these very briefly.

10. 2. 1. Application in Clinical Decision Support Systems

Signal processing and knowledge representation for medical images (e.g. mammography, ultrasound, CT, MRI) is yielding many valuable clinical tools and is an established area of expertise around the world. Clinical decision support is a rapidly growing field with a substantial body of evidence showing its value in reducing medical error and providing personalization of patient care [328], [329]. At the moment, there is no established engineering framework for combining these technologies, so that image interpretation systems can automatically provide data for the use of clinical decision support systems. There is a need to develop a framework for integrating digital mammography and other imaging modalities into an existing decision support system for the breast cancer multidisciplinary meeting. Multi-disciplinary team (MDT) meetings [330], tumour boards, cancer conferences or commonly known as multidisciplinary meetings (MDM) are some of the terms given to a team of specialists that meet regularly to discuss a number of patient cases related to a certain disease.

10. 2. 1. 1. Clinical Decision Support Systems

Clinical decision support system (CDSS or CDS) an interactive decision support systems (DSS) are Computer Software, which is designed to assist physicians and other health professionals with decision making tasks including diagnosis of patient data, prognosis process and clinical workflow [329]. It is intended to provide a second opinion to the clinician with a number of choices based upon the analysis of patient's data and evidence base. The doctor is envisaged to use these systems at point of care.

10. 2. 1. 2. Types of CDSS

CDSS can be characterized in two following two ways on the basis of its structure [19],

1. Knowledge based CDSS
2. Non-knowledge based CDSS

A decision support system was developed for the use of General Practitioners (GP's) in their routine work called 'Oxford System of Medicine' (OSM) [331]. Since the research in knowledge based decision support systems headed towards professionalizing in a specific clinical domain and personalizing near individual patient care. Paul Taylor et al. proposed a prototype system CADMIUM_II that can incorporate image processing in a clinical decision support system for breast cancer using knowledge base PROforma language [332]. Two studies were carried out to analyse and understand how radiologists describe, interpret and make decisions about microcalcifications in mammograms. To this end 50 descriptors were designed in order to interpret the required data. In the second study, ten radiologists described 40 sets of calcifications in a scheme that was tested to differentiate between benign and malignant and assessed against the descriptors. The most discriminating descriptors were then included in the CADMIUM II knowledge base.

Another example of such a knowledge based system is MATE [333]. Fox et. al. conceived the structure of a knowledge-based clinical decision support system based on four pillars, that are decision theory, theories of knowledge representation, process design and organizational modelling [328] and attempted to incorporate image processing with CDSS [334], [335].Non-knowledge based CDSS uses machine learning algorithms to assess decisions based on the past experiences and estimated patterns in the clinical data. The most common types of these systems use Genetic Algorithms (GA) and Artificial Neural Networks (ANN) as a computational tool [336]. Some CDSS uses Bayesian networks, which are a graphical representation of the events and variables relationship based upon their conditional probabilities. Examples of Bayesian network based CDSS are Iliad and SimulConsult that covers more than 2400 diseases. B. Sesen recently modelled [337], [338] the English lung cancer database (LUCADA) for lung cancer ontology in OWL 2 [339], which is a web ontology language. It is a clinical decision support system, called Lung Cancer Assistant (LCA), which interprets existing patient data and analyses it in accordance to an evidence base (which has the data of over 115000 patients) to make meaningful predictions while facilitating the implementation of clinical guidelines in routine practice. LCA knowledge-base is implemented in SNOMED-CT [340]. LCA has two components: 1) a client that runs on an end user local computer, and 2) the server, which is remote and user accessible. LCA shows very promising results; however, like MATE, it has no imaging capabilities to read by itself.

Figure 10.1: A screenshot of LCA, where Bayesian recommendations and those that are guidelines-based are highlighted in the orange colour [341]

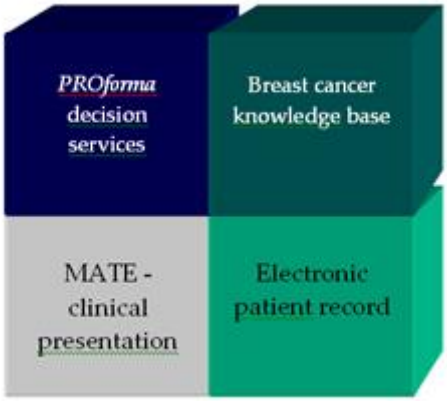

Figure 10.2: A computational framework of MATE CDSS [342]

10. 2. 1. 3. Role of Image Processing in Clinical Decision Support

There is a tremendous volume of research work available in image processing and analysis to determine diagnostic decisions for classification of breast tumour type, its size and staging information. However, the sad fact is that such information is hardly present at the point of care. It will be highly beneficial if the developed and proven research in image processing and shape analysis can be brought to the table for the patient's care. Image processing can play a vital role in the on-point decision making especially in the multidisciplinary meetings for breast cancer. There exists a limited study and not many platforms are known to provide explicit decision support for the differential diagnosis. For instant, micro-calcifications are of the most interest to radiologist while examining the breast mammograms of a certain patient. It will be of great value to link the properties that radiologist interpret in the screenings films to the knowledge base decision support engine for characterizing the calcifications in mammograms.

Presently there few systems known that integrate image processing with the differential decision support to help through the patient's treatment journey. Most such systems that use image processing for decision support are classifiers that are used to distinguish micro-calcifications or texture of lesions either circumscribed or speculated or to analyses the

speared and size of tumour. This information is then used to stage evaluate the level of suspicion (LOS). But all this is of little help if it is not used at the point of care. . In the case of cancer treatment, diagnosis and prognosis it is MDM's where the decisions are made for individual patient and can be regarded as the point of care.

10. 2. 1. 4. Scope of the Project

The image analysis model in this thesis may be used to incorporate image processing in a clinical decision support system for breast cancer (or any other cancer for that matter) using a knowledge base. The system will be aimed to help radiologist for differential diagnosis of mammographic abnormalities. This may involve identification of a set of terms that can represent knowledge required by the radiologist for decision making, identifying and extracting the image processing operators or features and providing links between the symbolic terms and image processing operators. It will identify to keep track of changes inside temporal mammograms to detect any abnormality as well as help in the prognosis of the disease. An image analysis framework in relation to CDSS is given in Figure 10.3. Our shape analysis model can detect abnormalities inside a breast, reduce the number of false positives, corresponds regions in temporal mammograms and quantify changes in it.

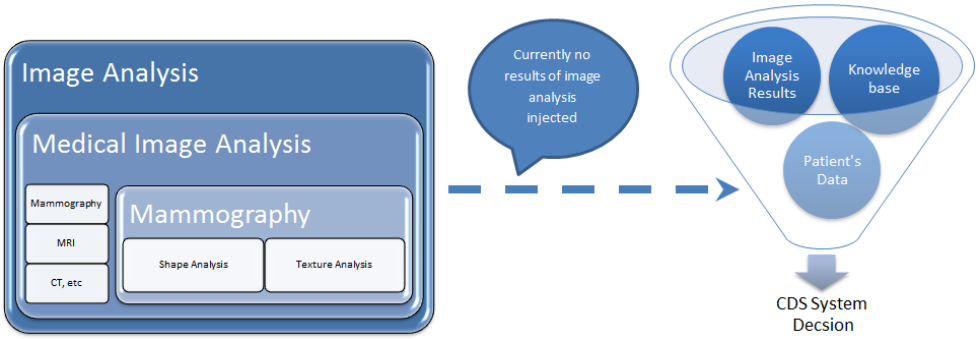

Figure 10.3: Working relationship of the proposed image analysis system for mammography in relation with a clinical decision support (CDS) system.

10. 2. 2. Application to Cytology Images

As stated earlier, the overall objective of this thesis is to develop and apply a shape analysis framework in a medical imaging environment. However, the medical environment is not restricted to screening images but also involves cytology. Cytology examinations using Fine Needle Biopsy (FNB) were an early step towards diagnosis of breast cancer though these have been supplanted by core biopsy under the control of stereo x-ray focussed imaging. Shape analysis of a tumour and other relevant cells for diagnostic and prognostic treatment procedures can be highly beneficial. This study can also be extended and generalized to detect new growth in any type of cells not just those from breast cancer.

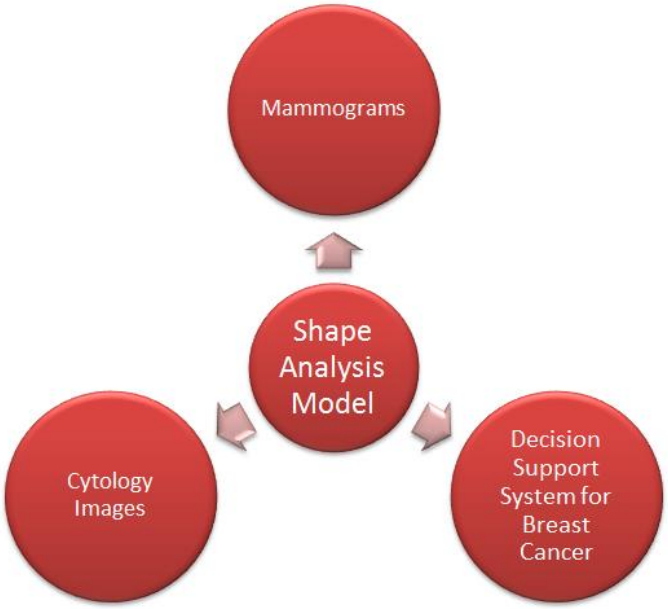

Figure 10.4: Overall project objective

There is a growing need for shape analysis in the field of cytology as well as in histology. Tumours are examples of complex shapes, and so this work can be extended to detect changes in tissue parenchyma at the cellular level. In this case, one of the cases of obvious interest is breast cancerous cells. This task aims to apply shape analysis to tumour cells and to analyse their growth both in terms of size and shape. Shape analyses of cancerous

cells can provide information about the level of aggressive behaviour that a particular cancer is expected to anticipate.

A model is given in the Figure 10.4, which propose to combine the two medical imaging modalities: mammograms and cytology images of tumour cells.

An image analysis system that can detect new growths in shapes could be very useful on cytology images, not least to analyse their behaviour in order to assess the aggressiveness of tumours. If the findings in mammography are found suspicious, the patient is recommended to a pathologist where FNA is performed. . Following readings are recommended to get an insight into the role of image processing and shape analysis in cytology images [343]–[352].

10. 2. 2. 1. Image Analysis of Cytology Images

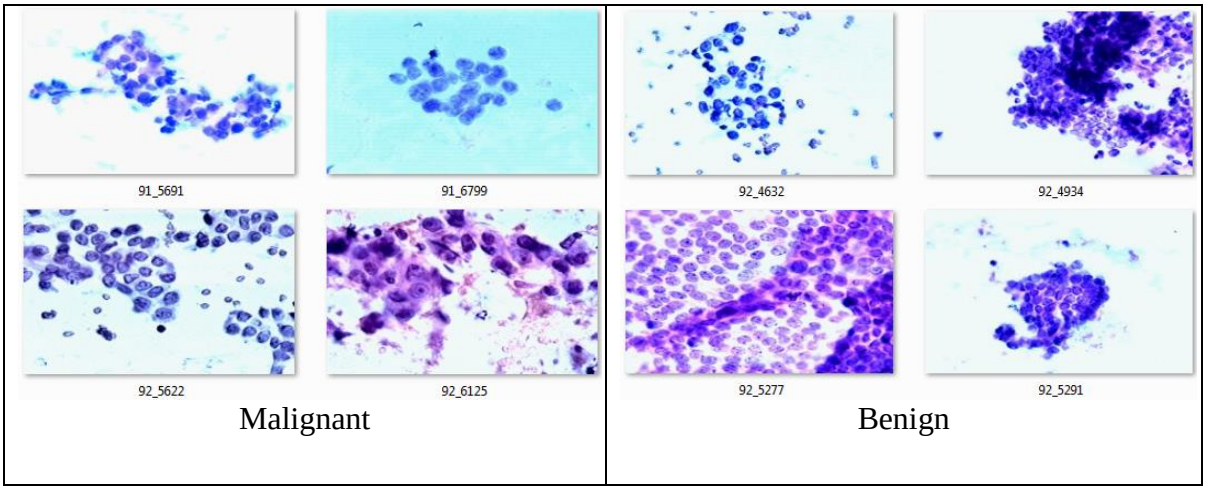

Figure 10.5: Examples of tumour cells from Wisconsin dataset [348]

There are two aims to look into cytology images of a tumour cell: either to differentiate between benign and malignant; or to grade the malignancy of a tumour in a histology slide.

10. 2. 2. 2. Classification between Benign and Malignant

The classification between benign and malignant tumours is usually done by the analysis of topological, texture and shape features of isolated nuclei. These features can be observed in three ways using our shape analysis model. Malignancy is suggested if the size

of the nuclei varies considerably in a group, and conversely, would be suggested benign for small nuclei variations. Our shape analysis model is highly invariant to articulations while matching shapes and retrieving them, and is sensitive to new growth in shapes. It could be used to analysis of area and parameter of a nucleus accurately, which are important in making such an observation. Secondly, the distribution and frequent occurrences of chromatin in the nuclei of healthy cells indicate cancer. This will require texture analysis, which may further be incorporated with the shape model. Finally, the structure of tissue with respect the distribution of nuclei is a decisive observation, represented by the distance of centroids of all nuclei and the distance to c-nearest nuclei [352]. The eccentricity transform used in our shape analysis model might be very useful to confirm this observation by finding if the tissue is a single layered structure or complex one.

10. 2. 2. 3. Grading Malignancy

Mostly, people referred for biopsy are diagnosed with malignancy. It would be more useful if the study of Cytology images is focused on grading malignancy and staging tumour for prognosis purposes.

The Bloom-Richardson grading scheme is a commonly used standard to grade cancer tissues [353], [354]. The system was originally introduced to grade histological images of breast cancer and is used to grade malignancy of cytological smears.

In the Bloom-Richardson grading system, three factors are taken into account and grades are assigned based on a three point system. The following are the factors of this system, summarized in Table 10.1.

SD	Cells in the images are grouped regularly	1
	Both grouped and single cells are found within the image	2
	Cells are spread irregularly	3
P	Nuclei have uniform size, shape and staining	1
	Moderate variations are found	2
	Very significant variations are found	3
HMF	Occasional figures per field are found	1
	Smears with two or three figures in most fields	2
	More than three figures per field are found	3

Table 10.1: Bloom-Richardson grading scheme summarized as in [347]

1) **Degree of structural differentiation (SD):** This is based on the classification of cell grouping within the cytological smears
2) **Pleomorphism (P):** This describes the difference in size, shape and staining of nuclei.
3) **Frequency of Hyperchromatic and mitosis figures (HMF):** This factor indicates cell growth as a result of cell division or mitosis.

Grades obtained for all three factors from a cytological image are added to attain a final grade, as given in Table 10.2. As the grade increases, the prognosis becomes worse.

It is proposed to start with the study of Pleomorphism and apply our shape analysis model to it in order to obtain the size and shape of the nuclei of tumour cells. Afterwards, a texture analysis framework may be developed in accordance with the shape analysis model to analyse textural changes for nuclei staining. Identifying the degree of the structural differentiation may be a challenging task and will require pattern classification methods to quantitatively grade degree of structural differentiation. Region Matching Algorithm may be employed to find the frequency of hyprochromatic and mitosis figures, which will be based on both of the techniques applied to SD and Pleomorphism

Score from Table 10.1	Tumour Grade	Level of Malignancy
3 – 5	Grade – I	Low malignancy
6 – 7	Grade – II	Intermediate Malignancy
8 – 9	Grade – III	High Malignancy

Table 10.2: Tumour grade and level of malignancy as per score from Table 10.1

References

[1] F. Janan, M. Brady, and R. Highnam, "False Positive Reduction in CADe Using Diffusing Scale Space," *Breast Imaging*. Springer, pp. 597–605, 2014.
[2] F. Janan, M. Brady, C. Tromans, and R. Highnam, "Standard Attenuation Rate and Volpara(R) Volumetric Density Maps," in *Second MICCAI International Workshop on Breast Image Analysis, BIA 2013, Nagoya, Japan*, 2013.
[3] F. Janan and M. Brady, "Shape matching by integral invariants on eccentricity transformed images," in *Engineering in Medicine and Biology Society (EMBC), 2013 35th Annual International Conference of the IEEE*, 2013, pp. 5099–5102.
[4] F. Janan and S. M. Brady, "Integral invariants for image enhancement," in *Engineering in Medicine and Biology Society (EMBC), 2013 35th Annual International Conference of the IEEE*, 2013, pp. 4018–4021.
[5] F. Janan and M. Brady, "Region matching in the temporal study of mammograms using integral invariant scale-space," in *Breast Imaging*, Springer, 2012, pp. 173–180.
[6] L. E. M. Duijm, J. H. Groenewoud, F. H. Jansen, J. Fracheboud, M. van Beek, and H. J. de Koning, "Mammography screening in the Netherlands: delay in the diagnosis of breast cancer after breast cancer screening," *Br. J. Cancer*, vol. 91, pp. 1795–1799, 2004.
[7] D. West, P. Mangiameli, R. Rampal, and V. West, "Ensemble strategies for a medical diagnostic decision support system: A breast cancer diagnosis application," *Eur. J. Oper. Res.*, vol. 162, pp. 532–551, 2005.
[8] K. Polat and S. Güne\cs, "Breast cancer diagnosis using least square support vector machine," *Digit. Signal Process.*, vol. 17, pp. 694–701, 2007.
[9] M. J. Homer and E. A. Sickles, *Mammographic interpretation: a practical approach*. McGraw-Hill New York, 1997.
[10] I. S. Fentiman, A. Fourquet, and G. N. Hortobagyi, "Male breast cancer," *Lancet*, vol. 367, pp. 595–604, 2006.
[11] W. H. Organization, "Cancer. 2009," *World Health Organ. Available from http://www. who. int/mediacentre/factsheets/fs297/en/index. html*, 2009.
[12] P. L. Porter, "Global trends in breast cancer incidence and mortality," *Salud pública de méxico*, vol. 51, 2009.
[13] D. Mankoff, "Imaging in breast cancer-breast cancer imaging revisited," *Breast Cancer Res.*, vol. 7, 2005.
[14] A. Oliver i Malagelada, "Automatic mass segmentation in mammographic images," 2007.
[15] J. Tang, R. M. Rangayyan, J. Xu, I. El Naqa, and Y. Yang, "Computer-aided detection and diagnosis of breast cancer with mammography: recent advances," *Inf. Technol. Biomed. IEEE Trans.*, vol. 13, pp. 236–251, 2009.
[16] R. Marti, R. Zwiggelaar, and C. M. Rubin, "Tracking Mammographic Structures Over Time.," in *BMVC*, 2001, pp. 1–10.
[17] M. P. Sampat, M. K. Markey, and A. C. Bovik, "Computer-aided detection and diagnosis in mammography," *Handb. Image Video Process.*, vol. 2, pp. 1195–1217, 2005.
[18] C. J. Vyborny, M. L. Giger, and R. M. Nishikawa, "Computer-aided detection and diagnosis of breast cancer," *Radiol. Clin. North Am.*, vol. 38, pp. 725–740, 2000.
[19] R. M. Rangayyan, F. J. Ayres, and J. E. Leo Desautels, "A review of computer-aided diagnosis of breast cancer: Toward the detection of subtle signs," *J. Frankl. Inst.*, vol. 344, pp. 312–348, 2007.

[20] J. J. Fenton, S. H. Taplin, P. A. Carney, L. Abraham, E. A. Sickles, C. D'Orsi, E. A. Berns, G. Cutter, R. E. Hendrick, and W. E. Barlow, "Influence of computer-aided detection on performance of screening mammography," *New Engl. J. Med.*, vol. 356, pp. 1399–1409, 2007.
[21] R. M. Rangayyan, *Biomedical image analysis*. CRC press, 2004.
[22] T. Square and B. Lane, "Find data," 2010.
[23] A. Jemal, F. Bray, M. M. Center, J. Ferlay, E. Ward, and D. Forman, "Global cancer statistics," *CA: Cancer J. Clin.*, vol. 61, pp. 69–90, 2011.
[24] C. Tromans and M. Brady, "An alternative approach to measuring volumetric mammographic breast density," in *Digital Mammography*, Springer, 2006, pp. 26–33.
[25] P. C. Stomper, D. J. D'souza, P. A. DiNitto, and M. A. Arredondo, "Analysis of parenchymal density on mammograms in 1353 women 25-79 years old.," *AJR. Am. J. Roentgenol.*, vol. 167, pp. 1261–1265, 1996.
[26] J. N. Wolfe, "Breast patterns as an index of risk for developing breast cancer," *Am. J. Roentgenol.*, vol. 126, pp. 1130–1137, 1976.
[27] J. N. Wolfe, "Risk for breast cancer development determined by mammographic parenchymal pattern," *Cancer*, vol. 37, pp. 2486–2492, 1976.
[28] N. F. Boyd, B. O'sullivan, J. E. Campbell, E. Fishell, I. Simor, G. Cooke, and T. Germanson, "Mammographic signs as risk factors for breast cancer.," *Br. J. Cancer*, vol. 45, 1982.
[29] J. Brisson, F. Merletti, N. L. Sadowsky, J. A. Twaddle, A. S. Morrison, and P. Cole, "Mammographic features of the breast and breast cancer risk," *Am. J. Epidemiol.*, vol. 115, pp. 428–437, 1982.
[30] G. Torres-Mejía, B. De Stavola, D. S. Allen, J. J. Pérez-Gavilán, J. M. Ferreira, I. S. Fentiman, and I. dos Santos Silva, "Mammographic features and subsequent risk of breast cancer: a comparison of qualitative and quantitative evaluations in the Guernsey prospective studies," *Cancer Epidemiol. Biomarkers & Prev.*, vol. 14, pp. 1052–1059, 2005.
[31] J. N. Wolfe, A. F. Saftlas, and M. Salane, "Mammographic parenchymal patterns and quantitative evaluation of mammographic densities: a case-control study," *Am. J. Roentgenol.*, vol. 148, pp. 1087–1092, 1987.
[32] I. Kato, C. Beinart, A. Bleich, S. Su, M. Kim, and P. G. Toniolo, "A nested case-control study of mammographic patterns, breast volume, and breast cancer (New York City, NY, United States)," *Cancer Causes & Control.*, vol. 6, pp. 431–438, 1995.
[33] A. F. Saftlas, R. N. Hoover, L. A. Brinton, M. Szklo, D. R. Olson, M. Salane, and J. N. Wolfe, "Mammographic densities and risk of breast cancer," *Cancer*, vol. 67, pp. 2833–2838, 1991.
[34] C. Byrne, C. Schairer, J. Wolfe, N. Parekh, M. Salane, L. A. Brinton, R. Hoover, and R. Haile, "Mammographic features and breast cancer risk: effects with time, age, and menopause status," *J. Natl. Cancer Inst.*, vol. 87, pp. 1622–1629, 1995.
[35] N. F. Boyd, J. W. Byng, R. A. Jong, E. K. Fishell, L. E. Little, A. B. Miller, G. A. Lockwood, D. L. Tritchler, and M. J. Yaffe, "Quantitative classification of mammographic densities and breast cancer risk: results from the Canadian National Breast Screening Study," *J. Natl. Cancer Inst.*, vol. 87, pp. 670–675, 1995.
[36] J. BRISSON, R. VERREAULT, A. S. MORRISON, S. TENNINA, and Fran. MEYER, "Diet, mammographic features of breast tissue, and breast cancer risk," *Am. J. Epidemiol.*, vol. 130, pp. 14–24, 1989.
[37] J. BRISSON, A. S. MORRISON, D. B. KOPANS, N. L. SADOWSKY, L. KALISHER, J. A. TWADDLE, J. E. MEYER, C. I. HENSCHKE, and P. COLE, "Height and weight, mammographic features of breast tissue, and breast cancer risk," *Am. J.*

Epidemiol., vol. 119, pp. 371–381, 1984.
[38] P. B. Lam, P. M. Vacek, B. M. Geller, and H. B. Muss, "The association of increased weight, body mass index, and tissue density with the risk of breast carcinoma in Vermont," *Cancer*, vol. 89, pp. 369–375, 2000.
[39] G. Maskarinec and L. Meng, "A case-control study of mammographic densities in Hawaii," *Breast Cancer Res. Treat.*, vol. 63, pp. 153–161, 2000.
[40] C. H. Van Gils, J. H. C. L. Hendriks, R. Holland, N. Karssemeijer, J. D. M. Otten, H. Straatman, and A. L. M. Verbeek, "Changes in mammographic breast density and concomitant changes in breast cancer risk," *Eur. J. Cancer Prev.*, vol. 8, pp. 509–516, 1999.
[41] T. Carlile, D. J. Thompson, K. J. Kopecky, F. I. Gilbert, P. M. Krook, A. J. Present, H. W. Russell, and B. A. Threatt, "Reproducibility and consistency in classification of breast parenchymal patterns," *Am. J. Roentgenol.*, vol. 140, pp. 1–7, 1983.
[42] L. Tabár and P. B. Dean, "Mammographic parenchymal patterns," *JAMA: J. Am. Med. Assoc.*, vol. 247, pp. 185–189, 1982.
[43] M. Y. R. O. N. Moskowitz, P. E. T. E. R. Gartside, and C. A. R. O. L. Y. N. McLaughlin, "Mammographic patterns as markers for high-risk benign breast disease and incident cancers.," *Radiology*, vol. 134, pp. 293–295, 1980.
[44] A. M. Oza and N. F. Boyd, "Mammographic parenchymal patterns: a marker of breast cancer risk.," *Epidemiol. Rev.*, vol. 15, pp. 196–208, 1992.
[45] A. F. Saftlas and M. SZKLO, "Mammographic parenchymal patterns and breast cancer risk," *Epidemiol. Rev.*, vol. 9, pp. 146–174, 1987.
[46] J. A. Harvey and V. E. Bovbjerg, "Quantitative Assessment of Mammographic Breast Density: Relationship with Breast Cancer Risk1," *Radiology*, vol. 230, pp. 29–41, 2004.
[47] N. F. Boyd, L. J. Martin, M. Bronskill, M. J. Yaffe, N. Duric, and S. Minkin, "Breast tissue composition and susceptibility to breast cancer," *J. Natl. Cancer Inst.*, vol. 102, pp. 1224–1237, 2010.
[48] B. T. Nicholson, A. P. LoRusso, M. Smolkin, V. E. Bovbjerg, G. R. Petroni, and J. A. Harvey, "Accuracy of assigned BI-RADS breast density category definitions," *Acad. Radiol.*, vol. 13, pp. 1143–1149, 2006.
[49] J. C. Boughey, L. C. Hartmann, S. S. Anderson, A. C. Degnim, R. A. Vierkant, C. A. Reynolds, M. H. Frost, and V. S. Pankratz, "Evaluation of the Tyrer-Cuzick (International Breast Cancer Intervention Study) model for breast cancer risk prediction in women with atypical hyperplasia," *J. Clin. Oncol.*, vol. 28, pp. 3591–3596, 2010.
[50] M. H. Gail, L. A. Brinton, D. P. Byar, D. K. Corle, S. B. Green, C. Schairer, and J. J. Mulvihill, "Projecting individualized probabilities of developing breast cancer for white females who are being examined annually," *J. Natl. Cancer Inst.*, vol. 81, pp. 1879–1886, 1989.
[51] J. Tyrer, S. W. Duffy, and J. Cuzick, "A breast cancer prediction model incorporating familial and personal risk factors," *Stat. Med.*, vol. 23, pp. 1111–1130, 2004.
[52] L. J. Martin and N. Boyd, "Potential mechanisms of breast cancer risk associated with mammographic density: hypotheses based on epidemiological evidence," *Breast Cancer Res*, vol. 10, pp. 1–14, 2008.
[53] Y.-P. Guo, L. J. Martin, W. Hanna, D. Banerjee, N. Miller, E. Fishell, R. Khokha, and N. F. Boyd, "Growth factors and stromal matrix proteins associated with mammographic densities," *Cancer Epidemiol. Biomarkers & Prev.*, vol. 10, pp. 243–248, 2001.
[54] C. M. Vachon, H. Sasano, K. Ghosh, K. R. Brandt, D. A. Watson, C. Reynolds, W.

L. Lingle, P. E. Goss, R. Li, and S. E. Aiyar, "Aromatase immunoreactivity is increased in mammographically dense regions of the breast," *Breast Cancer Res. Treat.*, vol. 125, pp. 243–252, 2011.
[55] S. Alowami, S. Troup, S. Al-Haddad, I. Kirkpatrick, and P. H. Watson, "Mammographic density is related to stroma and stromal proteoglycan expression," *Breast Cancer Res*, vol. 5, 2003.
[56] N. F. Boyd, H. M. Jensen, G. Cooke, and H. L. Han, "Relationship between mammographic and histological risk factors for breast cancer," *J. Natl. Cancer Inst.*, vol. 84, pp. 1170–1179, 1992.
[57] T. A. MacKenzie, L. Titus-Ernstoff, P. M. Vacek, B. Geller, J. E. Weiss, M. E. Goodrich, and P. A. Carney, "Breast density in relation to risk of ductal carcinoma in situ of the breast in women undergoing screening mammography," *Cancer Causes & Control.*, vol. 18, pp. 939–945, 2007.
[58] K. S. Reinier, P. M. Vacek, and B. M. Geller, "Risk factors for breast carcinoma in situ versus invasive breast cancer in a prospective study of pre-and post-menopausal women," *Breast Cancer Res. Treat.*, vol. 103, pp. 343–348, 2007.
[59] S. A. Bartow, F. A. Mettler Jr, and W. C. Black III, "Correlations between radiographic patterns and morphology of the female breast," *Rad Patterns Morph*, vol. 13, pp. 263–275, 1997.
[60] T. Li, L. Sun, N. Miller, T. Nicklee, J. Woo, L. Hulse-Smith, M.-S. Tsao, R. Khokha, L. Martin, and N. Boyd, "The association of measured breast tissue characteristics with mammographic density and other risk factors for breast cancer," *Cancer Epidemiol. Biomarkers & Prev.*, vol. 14, pp. 343–349, 2005.
[61] N. F. Boyd, J. M. Rommens, K. Vogt, V. Lee, J. L. Hopper, M. J. Yaffe, and A. D. Paterson, "Mammographic breast density as an intermediate phenotype for breast cancer," *Lancet Oncol.*, vol. 6, pp. 798–808, 2005.
[62] B. Newman, H. Mu, L. M. Butler, R. C. Millikan, P. G. Moorman, and M.-C. King, "Frequency of breast cancer attributable to BRCA1 in a population-based series of American women," *JAMA: J. Am. Med. Assoc.*, vol. 279, pp. 915–921, 1998.
[63] J. Peto, N. Collins, R. Barfoot, S. Seal, W. Warren, N. Rahman, D. F. Easton, C. Evans, J. Deacon, and M. R. Stratton, "Prevalence of BRCA1 and BRCA2 gene mutations in patients with early-onset breast cancer," *J. Natl. Cancer Inst.*, vol. 91, pp. 943–949, 1999.
[64] T. A. Sellers, C. M. Vachon, V. S. Pankratz, C. A. Janney, Z. Fredericksen, K. R. Brandt, Y. Huang, F. J. Couch, L. H. Kushi, and J. R. Cerhan, "Association of childhood and adolescent anthropometric factors, physical activity, and diet with adult mammographic breast density," *Am. J. Epidemiol.*, vol. 166, pp. 456–464, 2007.
[65] D. J. Hunter and W. C. Willett, "Diet, body size, and breast cancer," *Epidemiol. Rev.*, vol. 15, pp. 110–132, 1993.
[66] H. Lee-Han, G. Cooke, and N. F. Boyd, "Quantitative evaluation of mammographic densities: a comparison of methods of assessment," *Eur. J. Cancer Prev.*, vol. 4, pp. 285–292, 1995.
[67] J. S. Pankow, C. M. Vachon, C. C. Kuni, R. A. King, D. K. Arnett, D. M. Grabrick, S. S. Rich, V. E. Anderson, and T. A. Sellers, "Genetic analysis of mammographic breast density in adult women: evidence of a gene effect," *J. Natl. Cancer Inst.*, vol. 89, pp. 549–556, 1997.
[68] C. M. Vachon, R. A. King, L. D. Atwood, C. C. Kuni, and T. A. Sellers, "Preliminary sibpair linkage analysis of percent mammographic density," *J. Natl. Cancer Inst.*, vol. 91, pp. 1778–1779, 1999.
[69] A. C. of R. B.-R. Committee and A. C. of Radiology, *Breast imaging reporting and*

data system. American College of Radiology, 1998.
[70] B. I. Reporting, "Data System," *Breast Imaging Atlas. 4th ed. Reston: Am. Coll. Radiol.*, 2003.
[71] Z. Aitken, V. A. McCormack, R. P. Highnam, L. Martin, A. Gunasekara, O. Melnichouk, G. Mawdsley, C. Peressotti, M. Yaffe, and N. F. Boyd, "Screen-film mammographic density and breast cancer risk: a comparison of the volumetric standard mammogram form and the interactive threshold measurement methods," *Cancer Epidemiol. Biomarkers & Prev.*, vol. 19, pp. 418–428, 2010.
[72] N. Boyd, L. Martin, A. Gunasekara, O. Melnichouk, G. Maudsley, C. Peressotti, M. Yaffe, and S. Minkin, "Mammographic density and breast cancer risk: evaluation of a novel method of measuring breast tissue volumes," *Cancer Epidemiol. Biomarkers & Prev.*, vol. 18, pp. 1754–1762, 2009.
[73] J. A. Shepherd, K. Kerlikowske, L. Ma, F. Duewer, B. Fan, J. Wang, S. Malkov, E. Vittinghoff, and S. R. Cummings, "Volume of mammographic density and risk of breast cancer," *Cancer Epidemiol. Biomarkers & Prev.*, vol. 20, pp. 1473–1482, 2011.
[74] J. J. Heine, K. Cao, and D. E. Rollison, "Calibrated measures for breast density estimation," *Acad. Radiol.*, vol. 18, pp. 547–555, 2011.
[75] J. J. Heine, K. Cao, D. E. Rollison, G. Tiffenberg, and J. A. Thomas, "A quantitative description of the percentage of breast density measurement using full-field digital mammography," *Acad. Radiol.*, vol. 18, pp. 556–564, 2011.
[76] S. J. Graham, M. J. Bronskill, J. W. Byng, M. J. Yaffe, and N. F. Boyd, "Quantitative correlation of breast tissue parameters using magnetic resonance and X-ray mammography.," *Br. J. Cancer*, vol. 73, 1996.
[77] C. K. Glide-Hurst, N. Duric, and P. Littrup, "Volumetric breast density evaluation from ultrasound tomography images," *Med. Phys.*, vol. 35, 2008.
[78] S. Petroudi, K. Marias, R. English, R. Adams, and M. Brady, "Classification of mammogram patterns using area measurements and the standard mammogram form (SMF)," *Med. Imaging Underst. Anal.*, pp. 197–200, 2002.
[79] R. Highnam, X. Pan, R. Warren, M. Jeffreys, G. D. Smith, and M. Brady, "Breast composition measurements using retrospective standard mammogram form (SMF)," *Phys. Med. Biol.*, vol. 51, 2006.
[80] R. Highnam and J. M. Brady, *Mammographic image analysis*, vol. 14. Springer, 1999.
[81] R. P. Highnam, J. M. Brady, and B. J. Shepstone, "A representation for mammographic image processing," in *Digital Mammography, IEE Colloquium on*, 1996, pp. 4–1.
[82] J. W. Byng, N. F. Boyd, E. Fishell, R. A. Jong, and M. J. Yaffe, "Automated analysis of mammographic densities," *Phys. Med. Biol.*, vol. 41, 1996.
[83] J. W. Byng, M. J. Yaffe, G. A. Lockwood, L. E. Little, D. L. Tritchler, and N. F. Boyd, "Automated analysis of mammographic densities and breast carcinoma risk," *Cancer*, vol. 80, pp. 66–74, 1997.
[84] T. Matsubara, D. Yamazaki, M. Kato, T. Hara, H. Fujita, T. Iwase, and T. Endo, "An automated classification scheme for mammograms based on amount and distribution of fibroglandular breast tissue density," in *International Congress Series*, 2001, vol. 1230, pp. 545–552.
[85] R. Sivaramakrishna, N. A. Obuchowski, W. A. Chilcote, and K. A. Powell, "Automatic segmentation of mammographic density," *Acad. Radiol.*, vol. 8, pp. 250–256, 2001.
[86] C. H. Van Gils, J. H. C. L. Hendriks, J. D. M. Otten, R. Holland, and A. L. M.

Verbeek, “Parity and mammographic breast density in relation to breast cancer risk: indication of interaction,” *Eur. J. Cancer Prev.*, vol. 9, pp. 105–112, 2000.
[87] N. Karssemeijer, “Automated classification of parenchymal patterns in mammograms,” *Phys. Med. Biol.*, vol. 43, 1998.
[88] J. W. Byng, N. F. Boyd, E. Fishell, R. A. Jong, and M. J. Yaffe, “The quantitative analysis of mammographic densities,” *Phys. Med. Biol.*, vol. 39, 1994.
[89] A. Tagliafico, M. Calabrese, G. Tagliafico, E. Resmini, C. Martinoli, A. Rebora, A. Colao, R. Pivonello, and D. Ferone, “Increased mammographic breast density in acromegaly: quantitative and qualitative assessment.,” *Eur. J. Endocrinol. / Eur. Fed. Endocr. Soc.*, vol. 164, no. 3, pp. 335–340, 2011.
[90] A. Tagliafico, G. Tagliafico, S. Tosto, F. Chiesa, C. Martinoli, L. E. Derchi, and M. Calabrese, “Mammographic density estimation: comparison among BI-RADS categories, a semi-automated software and a fully automated one.,” *Breast* , vol. 18, no. 1, pp. 35–40, 2009.
[91] K. E. Martin, M. A. Helvie, C. Zhou, M. A. Roubidoux, J. E. Bailey, C. Paramagul, C. E. Blane, K. A. Klein, S. S. Sonnad, and H.-P. Chan, “Mammographic Density Measured with Quantitative Computer-aided Method: Comparison with Radiologists’ Estimates and BI-RADS Categories1,” *Radiology*, vol. 240, pp. 656–665, 2006.
[92] V. A. McCormack and I. dos Santos Silva, “Breast density and parenchymal patterns as markers of breast cancer risk: a meta-analysis,” *Cancer Epidemiol. Biomarkers & Prev.*, vol. 15, pp. 1159–1169, 2006.
[93] S. Prevrhal, J. A. Shepherd, R. Smith-Bindman, S. R. Cummings, and K. Kerlikowske, “Accuracy of mammographic breast density analysis: results of formal operator training,” *Cancer Epidemiol. Biomarkers & Prev.*, vol. 11, pp. 1389–1393, 2002.
[94] E. D. Pisano, C. A. Gatsonis, M. J. Yaffe, R. E. Hendrick, A. N. Tosteson, D. G. Fryback, L. W. Bassett, J. K. Baum, E. F. Conant, and R. A. Jong, “American College of Radiology Imaging Network Digital Mammographic Imaging Screening Trial: Objectives and Methodology1,” *Radiology*, vol. 236, pp. 404–412, 2005.
[95] M. Jeffreys, J. Harvey, and R. Highnam, “Comparing a new volumetric breast density method (VolparaTM) to cumulus,” in *Digital Mammography*, Springer, 2010, pp. 408–413.
[96] M. Jeffreys, R. Warren, R. Highnam, and G. D. Smith, “Initial experiences of using an automated volumetric measure of breast density: the standard mammogram form,” *Br. J. Radiol.*, vol. 79, pp. 378–382, 2006.
[97] J. Bozek, M. Kallenberg, M. Grgic, and N. Karssemeijer, “Comparison of lesion size using area and volume in full field digital mammograms,” in *Breast Imaging*, Springer, 2012, pp. 96–103.
[98] D. Kontos, P. R. Bakic, R. J. Acciavatti, E. F. Conant, and A. D. Maidment, “A comparative study of volumetric and area-based breast density estimation in digital mammography: results from a screening population,” in *Digital Mammography*, Springer, 2010, pp. 378–385.
[99] R. Highnam, M. Jeffreys, V. McCormack, R. Warren, G. D. Smith, and M. Brady, “Comparing measurements of breast density,” *Phys. Med. Biol.*, vol. 52, 2007.
[100] G. E. Mawdsley, A. H. Tyson, C. L. Peressotti, R. A. Jong, and M. J. Yaffe, “Accurate estimation of compressed breast thickness in mammography,” *Med. Phys.*, vol. 36, 2009.
[101] B. J. Augustine, M. J. Yaffe, D. Rico, J. Yang, G. E. Mawdsley, T. Li, J. Wu, and N. F. Boyd, “Volumetric breast density estimation on digitized mammograms—A preliminary clinical study,” in *Digital Mammography*, Springer, 2003, pp. 574–576.
[102] B. J. Augustine, M. J. Yaffe, D. Rico, J. Yang, G. E. Mawdsley, T. Li, J. Wu, and

N. F. Boyd, "Volumetric breast density estimation on digitized mammograms—A preliminary clinical study," in *Digital Mammography*, Springer, 2003, pp. 574–576.
[103] O. Pawluczyk, B. J. Augustine, M. J. Yaffe, D. Rico, J. Yang, G. E. Mawdsley, and N. F. Boyd, "A volumetric method for estimation of breast density on digitized screen-film mammograms," *Med. Phys.*, vol. 30, 2003.
[104] J. Diffey, A. Hufton, and S. Astley, "A new step-wedge for the volumetric measurement of mammographic density," in *Digital Mammography*, Springer, 2006, pp. 1–9.
[105] J. A. Shepherd, L. Herve, J. Landau, B. Fan, K. Kerlikowske, and S. R. Cummings, "Novel use of single X-ray absorptiometry for measuring breast density.," *Technol. Cancer Res. & Treat.*, vol. 4, pp. 173–182, 2005.
[106] O. Alonzo-Proulx, N. Packard, J. M. Boone, A. Al-Mayah, K. K. Brock, S. Z. Shen, and M. J. Yaffe, "Validation of a method for measuring the volumetric breast density from digital mammograms," *Phys. Med. Biol.*, vol. 55, 2010.
[107] C. E. Tromans, J. Diffey, and M. Brady, "Investigating the replacement of the physical anti-scatter grid with digital image processing," in *Digital Mammography*, Springer, 2010, pp. 205–212.
[108] C. E. Tromans, M. R. Cocker, and M. Brady, "A model of primary and scattered photon fluence for mammographic x-ray image quantification," *Phys. Med. Biol.*, vol. 57, 2012.
[109] C. Tromans, G. van Schie, N. Karssemeijer, and M. Brady, "A hypothesis-test framework for quantitative lesion detection and diagnosis," in *Breast Imaging*, Springer, 2012, pp. 458–465.
[110] C. Tromans and M. Brady, "Inferring the breast periphery from an image when measuring volumetric breast density," in *Breast Imaging*, Springer, 2012, pp. 252–259.
[111] C. E. Tromans, M. R. Cocker, and M. Brady, "Quantification and normalization of x-ray mammograms," *Phys. Med. Biol.*, vol. 57, 2012.
[112] S. van Engeland, P. R. Snoeren, H. Huisman, C. Boetes, and N. Karssemeijer, "Volumetric breast density estimation from full-field digital mammograms," *Med. Imaging, IEEE Trans.*, vol. 25, pp. 273–282, 2006.
[113] P. Kovesi, "Image features from phase congruency," *VIDERE: J. Comput. Vis. Res.*, vol. 1, pp. 1–26, 1999.
[114] R. Highnam, M. Brady, M. J. Yaffe, N. Karssemeijer, and J. Harvey, "Robust breast composition measurement-volparaTM," in *Digital Mammography*, Springer, 2010, pp. 342–349.
[115] R. Highnam, N. Sauber, S. Destounis, J. Harvey, and D. McDonald, "Breast density into clinical practice," in *Breast Imaging*, Springer, 2012, pp. 466–473.
[116] K. Hartman, R. Highnam, R. Warren, and V. Jackson, "Volumetric assessment of breast tissue composition from FFDM images," in *Digital Mammography*, Springer, 2008, pp. 33–39.
[117] P. L. Skippage, L. S. Wilkinson, S. D. Allen, N. Roche, M. Dowsett, and R. A'Hern, "Correlation of age and hormone replacement therapy with breast density as assessed by Quantra™," *Breast Cancer Res.*, vol. 11, 2009.
[118] P. L. Skippage, L. S. Wilkinson, S. D. Allen, N. Roche, M. Dowsett, and R. A'Hern, "Correlation of age and hormone replacement therapy with breast density as assessed by Quantra™," *Breast Cancer Res.*, vol. 11, 2009.
[119] J. Wang, A. Aziz, D. Newitt, B. N. Joe, N. Hylton, and J. A. Shepherd, "Comparison of Hologic' s Quantra Volumetric Assessment to MRI Breast Density," in *Breast Imaging*, Springer, 2012, pp. 619–626.

[120] S. Ciatto, D. Bernardi, M. Calabrese, M. Durando, M. A. Gentilini, G. Mariscotti, F. Monetti, E. Moriconi, B. Pesce, and A. Roselli, "A first evaluation of breast radiological density assessment by QUANTRA software as compared to visual classification," *Breast*, vol. 21, pp. 503–506, 2012.
[121] N. Tuncbilek, A. Sezer, and U. U\ugr, "Qualitative and quantitative analysis of fibroglandular tissue in the digital environment," in *Proffered paper at 10th National Congress of Breast Diseases, Izmir, Turkey*, 2009.
[122] E. Rafferty, A. Smith, and L. Niklason, "Comparison of three methods of estimating breast density: BI-RADS density scores using full field digital mammography, breast tomosynthesis, and volumetric breast density," *Proffered Pap. at Rad Soc North Am, Chicago, USA: ssM01*, 2009.
[123] P. R. Bakic, A.-K. Carton, D. Kontos, C. Zhang, A. B. Troxel, and A. D. Maidment, "Breast Percent Density: Estimation on Digital Mammograms and Central Tomosynthesis Projections1," *Radiology*, vol. 252, pp. 40–49, 2009.
[124] J. Xu, "Shape matching using morphological structural shape components," in *Image Processing, 2008. ICIP 2008. 15th IEEE International Conference on*, 2008, pp. 2596–2599.
[125] D. Mumford, "Mathematical theories of shape: Do they model perception?," in *San Diego,'91, San Diego, CA*, 1991, pp. 2–10.
[126] K. V. Mardia and I. L. Dryden, "Shape distributions for landmark data," *Adv. Appl. Probab.*, pp. 742–755, 1989.
[127] A. Duci, A. J. Yezzi, S. K. Mitter, and S. Soatto, "Shape representation via harmonic embedding," in *Computer Vision, 2003. Proceedings. Ninth IEEE International Conference on*, 2003, pp. 656–662.
[128] E. Sharon and D. Mumford, "2d-shape analysis using conformal mapping," *Int. J. Comput. Vis.*, vol. 70, pp. 55–75, 2006.
[129] D. G. Kendall, "Shape manifolds, procrustean metrics, and complex projective spaces," *Bull. Lond. Math. Soc.*, vol. 16, pp. 81–121, 1984.
[130] D. Zhang and G. Lu, "Review of shape representation and description techniques," *Pattern Recognit.*, vol. 37, pp. 1–19, 2004.
[131] A. Amanatiadis, V. G. Kaburlasos, A. Gasteratos, and S. E. Papadakis, "Evaluation of shape descriptors for shape-based image retrieval," *Image Process. IET*, vol. 5, pp. 493–499, 2011.
[132] Y. Gdalyahu and D. Weinshall, "Flexible syntactic matching of curves and its application to automatic hierarchical classification of silhouettes," *Pattern Anal. Mach. Intell. IEEE Trans.*, vol. 21, pp. 1312–1328, 1999.
[133] E. G. M. Petrakis, A. Diplaros, and E. Milios, "Matching and retrieval of distorted and occluded shapes using dynamic programming," *Pattern Anal. Mach. Intell. IEEE Trans.*, vol. 24, pp. 1501–1516, 2002.
[134] Y.-H. Gu and T. Tjahjadi, "Coarse-to-fine planar object identification using invariant curve features and B-spline modeling," *Pattern Recognit.*, vol. 33, pp. 1411–1422, 2000.
[135] F. S. Cohen and J.-Y. Wang, "Part I: Modeling image curves using invariant 3-D object curve models-a path to 3-D recognition and shape estimation from image contours," *Pattern Anal. Mach. Intell. IEEE Trans.*, vol. 16, pp. 1–12, 1994.
[136] Z. Huang and F. S. Cohen, "Affine-invariant B-spline moments for curve matching," *Image Process. IEEE Trans.*, vol. 5, pp. 1473–1480, 1996.
[137] Y. Wang, E. K. Teoh, and D. Shen, "Structure-adaptive B-snake for segmenting complex objects," in *Image Processing, 2001. Proceedings. 2001 International Conference on*, 2001, vol. 2, pp. 769–772.

[138] Y. Wang, E. K. Teoh, and D. Shen, "Lane detection and tracking using B-Snake," *Image Vis. Comput.*, vol. 22, pp. 269–280, 2004.
[139] Y. Wang and E. K. Teoh, "A novel 2D shape matching algorithm based on B-spline modeling," in *Image Processing, 2004. ICIP'04. 2004 International Conference on*, 2004, vol. 1, pp. 409–412.
[140] S. Zhang and K.-K. Ma, "A novel shape matching method using biological sequence Dynamic alignment," in *Multimedia and Expo, 2000. ICME 2000. 2000 IEEE International Conference on*, 2000, vol. 1, pp. 343–346.
[141] B. Yu, L. Guo, T. Zhao, and X. Qian, "A curve matching algorithm based on Freeman Chain Code," in *Intelligent Computing and Intelligent Systems (ICIS), 2010 IEEE International Conference on*, 2010, vol. 3, pp. 669–672.
[142] F. Arrebola and F. Sandoval, "Corner detection and curve segmentation by multiresolution chain-code linking," *Pattern Recognit.*, vol. 38, pp. 1596–1614, 2005.
[143] F. Mokhtarian and A. Mackworth, "Scale-based description and recognition of planar curves and two-dimensional shapes," *Pattern Anal. Mach. Intell. IEEE Trans.*, pp. 34–43, 1986.
[144] F. Mokhtarian, S. Abbasi, and J. Kittler, "Efficient and robust retrieval by shape content through curvature scale space," *Ser. Softw. Eng. Knowl. Eng.*, vol. 8, pp. 51–58, 1997.
[145] T. Y. Thomas, *The differential invariants of generalized spaces*, vol. 75. Cambridge, 1934.
[146] P. J. Olver, *Equivalence, invariants and symmetry*. Cambridge University Press, 1995.
[147] S. Manay, B.-W. Hong, A. J. Yezzi, and S. Soatto, *Integral invariant signatures*. Springer, 2004.
[148] Q.-X. Huang, S. Flöry, N. Gelfand, M. Hofer, and H. Pottmann, "Reassembling fractured objects by geometric matching," in *ACM Transactions on Graphics (TOG)*, 2006, vol. 25, pp. 569–578.
[149] Y.-L. Yang, Y.-K. Lai, S.-M. Hu, and H. Pottmann, "Robust principal curvatures on multiple scales," in *Symposium on Geometry Processing*, 2006, pp. 223–226.
[150] S. Manay, D. Cremers, B.-W. Hong, A. J. Yezzi, and S. Soatto, "Integral invariants for shape matching," *Pattern Anal. Mach. Intell. IEEE Trans.*, vol. 28, pp. 1602–1618, 2006.
[151] J. Sato and R. Cipolla, "Affine integral invariants for extracting symmetry axes," *Image Vis. Comput.*, vol. 15, pp. 627–635, 1997.
[152] J. Sato and R. Cipolla, "Affine integral invariants and matching of curves," in *Pattern Recognition, 1996., Proceedings of the 13th International Conference on*, 1996, vol. 1, pp. 915–919.
[153] M. Bauer, T. Fidler, and M. Grasmair, "Local uniqueness of the circular integral invariant," *arXiv Prepr. arXiv:1107.4257*, 2011.
[154] M. Sonka, V. Hlavac, and R. Boyle, "Image processing, analysis, and machine vision," 1999.
[155] S. Z. Li, "Shape matching based on invariants," 1998.
[156] D. Mumford, A. Latto, and J. Shah, "The representation of shape," in *Proc. IEEE Workshop Computer Vision*, 1984, pp. 183–191.
[157] T. H. Reiss, *Recognizing planar objects using invariant image features*. Springer-Verlag New York, Inc., 1993.
[158] D. Chetverikov and Y. Khenokh, "Matching for shape defect detection," in *Computer Analysis of Images and Patterns*, 1999, pp. 367–374.

[159] R. Alferez and Y.-F. Wang, "Geometric and illumination invariants for object recognition," *Pattern Anal. Mach. Intell. IEEE Trans.*, vol. 21, pp. 505–536, 1999.
[160] S. Belongie, J. Malik, and J. Puzicha, "Shape matching and object recognition using shape contexts," *Pattern Anal. Mach. Intell. IEEE Trans.*, vol. 24, pp. 509–522, 2002.
[161] A. Bengtsson and J.-O. Eklundh, "Shape representation by multiscale contour approximation," *IEEE Trans. Pattern Anal. Mach. Intell.*, vol. 13, pp. 85–93, 1991.
[162] R. D. Brandt and F. Lin, "Representations that uniquely characterize images modulo translation, rotation, and scaling," *Pattern Recognit. Lett.*, vol. 17, pp. 1001–1015, 1996.
[163] A. M. Bruckstein, E. Rivlin, and I. Weiss, "Scale space semi-local invariants," *Image Vis. Comput.*, vol. 15, pp. 335–344, 1997.
[164] T. Cohignac, C. Lopez, and J. M. Morel, "Integral and local affine invariant parameter and application to shape recognition," in *Pattern Recognition, 1994. Vol. 1-Conference A: Computer Vision & Image Processing., Proceedings of the 12th IAPR International Conference on*, 1994, vol. 1, pp. 164–168.
[165] S. Helgason, *Groups & Geometric Analysis: Radon Transforms, Invariant Differential Operators and Spherical Functions*, vol. 1. Access Online via Elsevier, 1984.
[166] D. M. Squire and T. M. Caelli, "Invariance Signatures: Characterizing contours by their departures from invariance," *Comput. Vis. Image Underst.*, vol. 77, pp. 284–316, 2000.
[167] D. Forsyth, J. L. Mundy, A. Zisserman, and C. M. Brown, *Projectively invariant representations using implicit algebraic curves*. Springer, 1990.
[168] L. Nielsen and G. Sparr, "Projective area-invariants as an extension of the cross-ratio," *CVGIP: Image Underst.*, vol. 54, pp. 145–159, 1991.
[169] C.-L. Huang and D.-H. Huang, "A content-based image retrieval system," *Image Vis. Comput.*, vol. 16, pp. 149–163, 1998.
[170] C. A. Rothwell, A. Zisserman, D. A. Forsyth, and J. L. Mundy, "Canonical frames for planar object recognition," in *Computer Vision—ECCV'92*, 1992, pp. 757–772.
[171] C. A. Rothwell, A. Zisserman, D. A. Forsyth, and J. L. Mundy, "Planar object recognition using projective shape representation," *Int. J. Comput. Vis.*, vol. 16, pp. 57–99, 1995.
[172] A. Shashua and N. Navab, "Relative affine structure: Canonical model for 3D from 2D geometry and applications," *Pattern Anal. Mach. Intell. IEEE Trans.*, vol. 18, pp. 873–883, 1996.
[173] A. Zisserman, D. Forsyth, J. Mundy, C. Rothwell, J. Liu, and N. Pillow, "3D object recognition using invariance," *Artif. Intell.*, vol. 78, pp. 239–288, 1995.
[174] L. Van Gool, T. Moons, and D. Ungureanu, "Affine/photometric invariants for planar intensity patterns," in *Computer Vision—ECCV'96*, Springer, 1996, pp. 642–651.
[175] D. Forsyth, J. L. Mundy, A. Zisserman, C. Coelho, A. Heller, and C. Rothwell, "Invariant descriptors for 3 d object recognition and pose," *IEEE Trans. Pattern Anal. Mach. Intell.*, vol. 13, pp. 971–991, 1991.
[176] J. Lasenby, E. Bayro-Corrochano, A. N. Lasenby, and G. Sommer, "A new framework for the formation of invariants and multiple-view constraints in computer vision," in *Image Processing, 1996. Proceedings., International Conference on*, 1996, vol. 1, pp. 313–316.
[177] J. B. Cole, H. Murase, and S. Naito, "A Lie group theoretic approach to the invariance problem in feature extraction and object recognition," *Pattern Recognit. Lett.*, vol. 12, pp. 519–523, 1991.
[178] E. Calabi, P. J. Olver, C. Shakiban, A. Tannenbaum, and S. Haker, "Differential

and numerically invariant signature curves applied to object recognition," *Int. J. Comput. Vis.*, vol. 26, pp. 107–135, 1998.
[179] K. Kanatani, *Group-theoretical methods in image understanding*, vol. 2. springer-Verlag Berlin, 1990.
[180] R. Lenz, *Group theoretical methods in image processing*. Springer-Verlag New York, Inc., 1990.
[181] E. Trucco, "Geometric Invariance in Computer Vision," *AI Commun.*, vol. 8, pp. 193–194, 1995.
[182] W. Cao, P. Hu, Y. Liu, M. Gong, and H. Li, "Gaussian-curvature-derived invariants for isometry," *Sci. China Inf. Sci.*, pp. 1–12, 2011.
[183] R. White, C. Kamath, and S. Newsam, *Matching Shapes Using Local Descriptors*. United States. Department of Energy, 2004.
[184] G. Taubin and D. B. Cooper, *Object recognition based on moment (or algebraic) invariants*. IBM TJ Watson Research Center, 1991.
[185] T. Fidler, M. Grasmair, H. Pottmann, and O. Scherzer, "Inverse problems of integral invariants and shape signatures," *Preprint*, 2007.
[186] S. M. Smith and J. M. Brady, "SUSAN—A new approach to low level image processing," *Int. J. Comput. Vis.*, vol. 23, pp. 45–78, 1997.
[187] M. S. Mansoory, M. Ashtiyani, and H. Sarabadani, "Automatic Crack Detection in Eggshell Based on SUSAN Edge Detector Using Fuzzy Thresholding," *Mod. Appl. Sci.*, vol. 5, 2011.
[188] K. S. Arun and K. S. Sarath, "Evaluation of SUSAN Filter for the Identification of Micro Calcification," *Int. J. Comput. Appl.*, vol. 15, pp. 41–44, 2011.
[189] Y. LI, Y. GAO, L. LU, P. WANG, Z. ZHANG, and J. ZHANG, "Hybrid corner detection algorithm for brain magnetic resonance image registration," *Chin. J. Med. Imaging Technol.*, vol. 2, 2012.
[190] H. Si-ming, L. Bing-han, and W. Wei-zhi, "Moving shadow detection based on Susan algorithm," in *Computer Science and Automation Engineering (CSAE), 2011 IEEE International Conference on*, 2011, vol. 3, pp. 16–20.
[191] S. Xu, L. Han, and L. Zhang, "An Algorithm to Edge Detection Based on SUSAN Filter and Embedded Confidence," in *Intelligent Systems Design and Applications, 2006. ISDA'06. Sixth International Conference on*, 2006, vol. 2, pp. 720–723.
[192] G. Rezai-Rad and M. Aghababaie, "Comparison of SUSAN and sobel edge detection in MRI images for feature extraction," in *Information and Communication Technologies, 2006. ICTTA'06. 2nd*, 2006, vol. 1, pp. 1103–1107.
[193] J. Zeng and D. Li, "SUSAN edge detection method for color image," *Jisuanji Gongcheng yu Yingyong*, vol. 47, pp. 194–196, 2011.
[194] Z.-G. Qu, P. Wang, Y.-H. Gao, and P. Wang, "Randomized SUSAN edge detector," *Opt. Eng.*, vol. 50, pp. 110502–110502, 2011.
[195] E. Rafajlowicz, "SUSAN edge detector reinterpreted, simplified and modified," in *Multidimensional (nD) Systems, 2007 International Workshop on*, 2007, pp. 69–74.
[196] Y. Xingfang, H. Yumei, and L. Yan, "An improved SUSAN corner detection algorithm based on adaptive threshold," in *Signal Processing Systems (ICSPS), 2010 2nd International Conference on*, 2010, vol. 2.
[197] S. Z. Li, "Matching: invariant to translations, rotations and scale changes," *Pattern Recognit.*, vol. 25, pp. 583–594, 1992.
[198] M. Kliot and E. Rivlin, "Invariant-based shape retrieval in pictorial databases," in *Computer Vision—ECCV'98*, Springer, 1998, pp. 491–507.
[199] E. R. Davies, *Machine vision: theory, algorithms, practicalities*. Access Online via

Elsevier, 2004.
[200] L. Zalcman, “Offbeat integral geometry,” *Am. Math. Mon.*, vol. 87, pp. 161–175, 1980.
[201] H. Cramér and H. Wold, “Some theorems on distribution functions,” *J. Lond. Math. Soc.*, vol. 1, pp. 290–294, 1936.
[202] B. W. Hong, *Image Segmentation, Shape, and Registration: Application to Mammography*. University of Oxford, 2004.
[203] C. a. Hann and M. S. Hickman, “Projective curvature and integral invariants,” *Acta Appl. Math.*, vol. 74, pp. 177–193, 2002.
[204] H. Pottmann, J. Wallner, Q.-X. Huang, and Y.-L. Yang, “Integral invariants for robust geometry processing,” *Comput. Aided Geom. Des.*, vol. 26, pp. 37–60, 2009.
[205] F. Mokhtarian and A. K. Mackworth, “A theory of multiscale, curvature-based shape representation for planar curves,” *IEEE Trans. Pattern Anal. Mach. Intell.*, vol. 14, pp. 789–805, 1992.
[206] I. Weiss, “Noise-resistant invariants of curves,” *Pattern Anal. Mach. Intell. IEEE Trans.*, vol. 15, pp. 943–948, 1993.
[207] L. S. Davis, “Understanding shape: Angles and sides,” *Comput. IEEE Trans.*, vol. 100, pp. 236–242, 1977.
[208] R. C. Veltkamp, “Shape matching: Similarity measures and algorithms,” in *Shape Modeling and Applications, SMI 2001 International Conference on.*, 2001, pp. 188–197.
[209] M. Rusinol, P. Dosch, and J. Lladós, “Boundary shape recognition using accumulated length and angle information,” in *Pattern Recognition and Image Analysis*, Springer, 2007, pp. 210–217.
[210] A. Ion, G. Peyré, Y. Haxhimusa, S. Peltier, W. G. Kropatsch, and L. D. Cohen, “Shape matching using the geodesic eccentricity transform-a study,” in *Proceedings of the 31st annual workshop of the Austrian Association for Pattern (OAGM/AAPR)*, 2007, pp. 97–104.
[211] E. Ozcan and C. K. Mohan, “Partial shape matching using genetic algorithms,” *Pattern Recognit. Lett.*, vol. 18, pp. 987–992, 1997.
[212] C. T. Zahn and R. Z. Roskies, “Fourier descriptors for plane closed curves,” *Comput. IEEE Trans.*, vol. 100, pp. 269–281, 1972.
[213] A. Sharma and R. Horaud, “Shape matching based on diffusion embedding and on mutual isometric consistency,” in *Computer Vision and Pattern Recognition Workshops (CVPRW), 2010 IEEE Computer Society Conference on*, 2010, pp. 29–36.
[214] A. M. Bronstein, M. M. Bronstein, and R. Kimmel, “Generalized multidimensional scaling: a framework for isometry-invariant partial surface matching,” *Proc. Natl. Acad. Sci. United States Am.*, vol. 103, pp. 1168–1172, 2006.
[215] D. Mateus, R. Horaud, D. Knossow, F. Cuzzolin, and E. Boyer, “Articulated shape matching using Laplacian eigenfunctions and unsupervised point registration,” in *Computer Vision and Pattern Recognition, 2008. CVPR 2008. IEEE Conference on*, 2008, pp. 1–8.
[216] M. R. Ruggeri, G. Patanè, M. Spagnuolo, and D. Saupe, “Spectral-driven isometry-invariant matching of 3D shapes,” *Int. J. Comput. Vis.*, vol. 89, pp. 248–265, 2010.
[217] S. Wang, Y. Wang, M. Jin, X. D. Gu, and D. Samaras, “Conformal geometry and its applications on 3d shape matching, recognition, and stitching,” *Pattern Anal. Mach. Intell. IEEE Trans.*, vol. 29, pp. 1209–1220, 2007.
[218] A. M. Bronstein, M. M. Bronstein, A. M. Bruckstein, and R. Kimmel, “Analysis of two-dimensional non-rigid shapes,” *Int. J. Comput. Vis.*, vol. 78, pp. 67–88, 2008.
[219] A. B. Hamza and H. Krim, “Geodesic matching of triangulated surfaces,” *Image Process. IEEE Trans.*, vol. 15, pp. 2249–2258, 2006.

[220] R. Osada, T. Funkhouser, B. Chazelle, and D. Dobkin, "Shape distributions," *ACM Trans. Graph.*, vol. 21, pp. 807–832, 2002.
[221] H. Ling and D. W. Jacobs, "Shape classification using the inner-distance," *Pattern Anal. Mach. Intell. IEEE Trans.*, vol. 29, pp. 286–299, 2007.
[222] K. Nasreddine, A. Benzinou, and R. Fablet, "Shape geodesics for boundary-based object recognition and retrieval," in *Image Processing (ICIP), 2009 16th IEEE International Conference on*, 2009, pp. 405–408.
[223] M. Leordeanu and M. Hebert, "A spectral technique for correspondence problems using pairwise constraints," in *Computer Vision, 2005. ICCV 2005. Tenth IEEE International Conference on*, 2005, vol. 2, pp. 1482–1489.
[224] O. Duchenne, F. Bach, I.-S. Kweon, and J. Ponce, "A tensor-based algorithm for high-order graph matching," *Pattern Anal. Mach. Intell. IEEE Trans.*, vol. 33, pp. 2383–2395, 2011.
[225] L. Torresani, V. Kolmogorov, and C. Rother, "Feature correspondence via graph matching: Models and global optimization," in *Computer Vision–ECCV 2008*, Springer, 2008, pp. 596–609.
[226] J. Maciel and J. P. Costeira, "A global solution to sparse correspondence problems," *Pattern Anal. Mach. Intell. IEEE Trans.*, vol. 25, pp. 187–199, 2003.
[227] M. Reuter, F.-E. Wolter, and N. Peinecke, "Laplace-spectra as fingerprints for shape matching," in *Proceedings of the 2005 ACM symposium on Solid and physical modeling*, 2005, pp. 101–106.
[228] C. Xu, J. Liu, and X. Tang, "2D shape matching by contour flexibility," *Pattern Anal. Mach. Intell. IEEE Trans.*, vol. 31, pp. 180–186, 2009.
[229] K. Siddiqi, A. Shokoufandeh, S. J. Dickinson, and S. W. Zucker, "Shock graphs and shape matching," *Int. J. Comput. Vis.*, vol. 35, pp. 13–32, 1999.
[230] Y. W. Chen and C. L. Xu, "Rolling penetrate descriptor for shape-based image retrieval and object recognition," *Pattern Recognit. Lett.*, vol. 30, pp. 799–804, 2009.
[231] L. Gorelick, M. Galun, E. Sharon, R. Basri, and A. Brandt, "Shape representation and classification using the poisson equation," *Pattern Anal. Mach. Intell. IEEE Trans.*, vol. 28, pp. 1991–2005, 2006.
[232] O. Van Kaick, G. Hamarneh, H. Zhang, and P. Wighton, "Contour correspondence via ant colony optimization," in *Computer Graphics and Applications, 2007. PG'07. 15th Pacific Conference on*, 2007, pp. 271–280.
[233] J. Tian, L. Ma, and W. Yu, "Ant colony optimization for wavelet-based image interpolation using a three-component exponential mixture model," *Expert Syst. with Appl.*, vol. 38, pp. 12514–12520, 2011.
[234] J. Tian, W. Yu, L. Chen, and L. Ma, "Image edge detection using variation-adaptive ant colony optimization," in *Transactions on computational collective intelligence V*, Springer, 2011, pp. 27–40.
[235] T. Davidovic, D. Ramljak, M. Selmic, and D. Teodorovic, "Parallel bee colony optimization for scheduling independent tasks on identical machines," in *Proceedings of the International Symposium on Operational Research*, 2010, pp. 389–392.
[236] D. U. Š. A. N. Teodorovic, T. Davidovic, and M. Selmic, "Bee colony optimization: the applications survey," *ACM Trans. Comput. Log.*, vol. 1529, 2011.
[237] J. Shi, F. Chen, J. Lu, and G. Chen, "An evolutionary image matching approach," *Appl. Soft Comput.*, vol. 13, pp. 3060–3065, 2013.
[238] C. Xu and H. Duan, "Artificial bee colony (ABC) optimized edge potential function (EPF) approach to target recognition for low-altitude aircraft," *Pattern Recognit. Lett.*, vol. 31, pp. 1759–1772, 2010.

[239] R. C. Veltkamp and M. Hagedoorn, *State of the art in shape matching*. Springer, 2001.
[240] K. Mikolajczyk and C. Schmid, "A performance evaluation of local descriptors," *Pattern Anal. Mach. Intell. IEEE Trans.*, vol. 27, pp. 1615–1630, 2005.
[241] O. Van Kaick, H. Zhang, G. Hamarneh, and D. Cohen-Or, "A survey on shape correspondence," in *Computer Graphics Forum*, 2011, vol. 30, pp. 1681–1707.
[242] T. B. Sebastian, P. N. Klein, and B. B. Kimia, "On aligning curves," *Pattern Anal. Mach. Intell. IEEE Trans.*, vol. 25, pp. 116–125, 2003.
[243] E. W. Dijkstra, "A note on two problems in connexion with graphs," *Numer. Math.*, vol. 1, pp. 269–271, 1959.
[244] L. J. Latecki, R. Lakamper, and T. Eckhardt, "Shape descriptors for non-rigid shapes with a single closed contour," in *Computer Vision and Pattern Recognition, 2000. Proceedings. IEEE Conference on*, 2000, vol. 1, pp. 424–429.
[245] S. Belongie, J. Malik, and J. Puzicha, "Matching shapes," in *Computer Vision, 2001. ICCV 2001. Proceedings. Eighth IEEE International Conference on*, 2001, vol. 1, pp. 454–461.
[246] T. B. Sebastian, P. N. Klein, and B. B. Kimia, "Alignment-based recognition of shape outlines," in *Visual Form 2001*, Springer, 2001, pp. 606–618.
[247] M. Frenkel and R. Basri, "Curve matching using the fast marching method," in *Energy Minimization Methods in Computer Vision and Pattern Recognition*, 2003, pp. 35–51.
[248] J. Suckling, J. Parker, D. R. Dance, S. Astley, I. Hutt, C. Boggis, I. Ricketts, E. Stamatakis, N. Cerneaz, and S.-L. Kok, "The mammographic image analysis society digital mammogram database," 1994.
[249] C. Rose, D. Turi, A. Williams, K. Wolstencroft, and C. Taylor, "Web services for the DDSM and digital mammography research," in *Digital Mammography*, Springer, 2006, pp. 376–383.
[250] M. Heath, K. Bowyer, D. Kopans, R. Moore, and P. Kegelmeyer, "The digital database for screening mammography," in *Proceedings of the 5th international workshop on digital mammography*, 2000, pp. 212–218.
[251] B.-W. Hong and M. Brady, "Segmentation of mammograms in topographic approach," 2003.
[252] N. R. Mudigonda, R. M. Rangayyan, and J. E. Leo Desautels, "Detection of breast masses in mammograms by density slicing and texture flow-field analysis," *Med. Imaging, IEEE Trans.*, vol. 20, pp. 1215–1227, 2001.
[253] R. C. Gonzalez, R. E. Woods, and S. L. Eddins, *Digital image processing using MATLAB*, vol. 2. Gatesmark Publishing Knoxville, 2009.
[254] M. U. Guide, "The mathworks," *Inc., Natick, MA*, vol. 5, 1998.
[255] N. J. Cerneaz, "Model based analysis of mammograms.," University of Oxford, 1994.
[256] Y. Zhang, N. Tomuro, J. Furst, and D. S. Raicu, "A Contour-based Mass Segmentation in Mammograms," in *Proc. of the Soc. Res. Symp*, 2009.
[257] D. O. N. A. T. O. Cascio, F. Fauci, R. Magro, G. Raso, R. Bellotti, F. De Carlo, S. Tangaro, G. De Nunzio, M. Quarta, and G. Forni, "Mammogram segmentation by contour searching and mass lesions classification with neural network," *Nucl. Sci. IEEE Trans.*, vol. 53, pp. 2827–2833, 2006.
[258] S. Singh and R. Al-Mansoori, "Identification of Regions of Interest in Digital Mammograms," *J. Intell. Syst.*, vol. 10, no. 2, pp. 1–41, 2000.
[259] G. S. Muralidhar, M. K. Markey, and A. C. Bovik, "Snakules for automatic classification of candidate spiculated mass locations on mammography," in *Image Analysis*

& Interpretation (SSIAI), 2010 IEEE Southwest Symposium on, 2010, pp. 197–200.
[260] T. Ojala, J. Näppi, and O. Nevalainen, "Accurate segmentation of the breast region from digitized mammograms.," *Comput. Med. Imaging Graph. : Off. J. Comput. Med. Imaging Soc.*, vol. 25, no. 1, pp. 47–59, 2001.
[261] B. M. Shahedi, R. Amirfattahi, F. T. Azar, and S. Sadri, "Accurate breast region detection in digital mammograms using a local adaptive thresholding method," in *Image Analysis for Multimedia Interactive Services, 2007. WIAMIS'07. Eighth International Workshop on*, 2007, pp. 26–26.
[262] K. Wang, H. Qin, P. R. Fisher, and W. Zhao, "Automatic registration of mammograms using texture-based anisotropic features," in *Biomedical Imaging: Nano to Macro, 2006. 3rd IEEE International Symposium on*, 2006, pp. 864–867.
[263] H. Schiabel, V. T. Santos, and M. F. Angelo, "Segmentation technique for detecting suspect masses in dense breast digitized images as a tool for mammography CAD schemes," in *Proceedings of the 2008 ACM symposium on Applied computing*, 2008, pp. 1333–1337.
[264] T. C. Wang and N. B. Karayiannis, "Detection of microcalcifications in digital mammograms using wavelets.," *IEEE Trans. Med. Imaging*, vol. 17, no. 4, pp. 498–509, 1998.
[265] M. M. Anguh and A. C. Silva, "Multiscale segmentation and enhancement in mammograms," in *Computer Graphics and Image Processing, 1997. Proceedings., X Brazilian Symposium on*, 1997, pp. 136–139.
[266] M. Bajger, F. Ma, and M. J. Bottema, "Automatic tuning of MST segmentation of mammograms for registration and mass detection algorithms," in *Digital Image Computing: Techniques and Applications, 2009. DICTA'09.*, 2009, pp. 400–407.
[267] F. Ma, M. Bajger, and M. J. Bottema, "Robustness of two methods for segmenting salient features in screening mammograms," in *Digital Image Computing Techniques and Applications, 9th Biennial Conference of the Australian Pattern Recognition Society on*, 2007, pp. 112–117.
[268] C. D'Elia, G. Poggi, and G. Scarpa, "A tree-structured Markov random field model for Bayesian image segmentation," *Image Process. IEEE Trans.*, vol. 12, pp. 1259–1273, 2003.
[269] S. Zhu, H. Shi, L. Liu, and D. Ye, "Sampling Method Based on Scale Space with Gaussian Kernel," *Jisuanji Kexue yu Tansuo*, vol. 6, pp. 644–653, 2012.
[270] T. Lindeberg, "Scale selection properties of generalized scale-space interest point detectors," *J. Math. Imaging Vis.*, pp. 1–34, 2013.
[271] L. Shapiro, "Stockman G: Computer Vision." Prentice Hall, 2002.
[272] B. M. ter Haar Romeny, "Scale-space theory for multiscale geometric image analysis."
[273] T. Lindeberg, *Scale-space theory in computer vision*. Springer, 1993.
[274] E. Reinhard, W. Heidrich, P. Debevec, S. Pattanaik, G. Ward, and K. Myszkowski, *High dynamic range imaging: acquisition, display, and image-based lighting*. Morgan Kaufmann, 2010.
[275] R. Fisher, S. Perkins, A. Walker, and E. Wolfart, "Spatial filters-Laplacian/Laplacian of Gaussian." 2003.
[276] B. M. ter Haar Romeny, *Geometry-driven diffusion in computer vision*. Kluwer academic Dordrecht, 1994.
[277] B. M. T. H. Romeny, "Introduction to scale-space theory: Multiscale geometric image analysis," in *Verlag. First International Conference on Scale-Space theory*, 1996.
[278] J. Babaud, A. P. Witkin, M. Baudin, and R. O. Duda, "Uniqueness of the Gaussian

kernel for scale-space filtering," *Pattern Anal. Mach. Intell. IEEE Trans.*, pp. 26–33, 1986.
[279] A. Witkin, "Scale-space filtering: A new approach to multi-scale description," in *Acoustics, Speech, and Signal Processing, IEEE International Conference on ICASSP'84.*, 1984, vol. 9, pp. 150–153.
[280] J. J. Koenderink, "The structure of images," *Biol. Cybern.*, vol. 50, pp. 363–370, 1984.
[281] Y. Yu and S. T. Acton, "Speckle reducing anisotropic diffusion," *Image Process. IEEE Trans.*, vol. 11, pp. 1260–1270, 2002.
[282] P. Perona and J. Malik, "Scale-space and edge detection using anisotropic diffusion," *Pattern Anal. Mach. Intell. IEEE Trans.*, vol. 12, pp. 629–639, 1990.
[283] J. Weickert, *Anisotropic diffusion in image processing*, vol. 1. Teubner Stuttgart, 1998.
[284] L. M. J. Florack, B. M. ter Haar Romeny, J. J. Koenderink, and M. A. Viergever, "Linear scale-space," *J. Math. Imaging Vis.*, vol. 4, pp. 325–351, 1994.
[285] L. M. J. Florack, B. M. ter Haar Romeny, J. J. Koenderink, and M. A. Viergever, "Families of tuned scale-space kernels," in *Computer Vision—ECCV'92*, 1992, pp. 19–23.
[286] L. M. Florack, B. M. ter Haar Romeny, J. J. Koenderink, and M. A. Viergever, "Images: Regular tempered distributions," in *Shape in Picture*, Springer, 1994, pp. 651–659.
[287] L. M. J. Florack, B. T. H. Romeny, J. J. Koenderink, and M. A. Viergever, "Cartesian differential invariants in scale-space," *J. Math. Imaging Vis.*, vol. 3, pp. 327–348, 1993.
[288] B. M. ter Haar Romeny, L. M. Florack, A. H. Salden, and M. A. Viergever, "Higher order differential structure of images," *Image Vis. Comput.*, vol. 12, pp. 317–325, 1994.
[289] M. Nielsen, L. Florack, and R. Deriche, "Regularization, scale-space, and edge detection filters," *J. Math. Imaging Vis.*, vol. 7, pp. 291–307, 1997.
[290] J. J. Koenderink, "Scale-time," *Biol. Cybern.*, vol. 58, pp. 159–162, 1988.
[291] T. Lindeberg, "Linear spatio-temporal scale-space," in *Scale-Space Theory in Computer Vision*, Springer, 1997, pp. 113–127.
[292] T. Lindeberg, "Scale-space theory: A basic tool for analyzing structures at different scales," *J. Appl. Stat.*, vol. 21, pp. 225–270, 1994.
[293] A. L. Yuille and T. A. Poggio, "Scaling theorems for zero crossings," *Pattern Anal. Mach. Intell. IEEE Trans.*, pp. 15–25, 1986.
[294] R. Kimmel, "Fast Marching Methods," in *Numerical Geometry of Images*, Springer, 2004, pp. 87–108.
[295] R. A. Hummel, "The Scale-Space Formulation of Pyramid Data Structures.," DTIC Document, 1986.
[296] R. A. Hummel, "Representations Based on Zero-Crossings in Scale-Space.," DTIC Document, 1986.
[297] M. Jagersand, "Saliency maps and attention selection in scale and spatial coordinates: An information theoretic approach," in *Computer Vision, 1995. Proceedings., Fifth International Conference on*, 1995, pp. 195–202.
[298] R. P. Feynman, R. B. Leighton, and M. L. Sands, *The Feynman lectures on physics: Mainly mechanics, radiation, and heat*, vol. 1. Basic Books, 2011.
[299] M. Felsberg and G. Sommer, "The monogenic scale-space: A unifying approach to phase-based image processing in scale-space," *J. Math. Imaging Vis.*, vol. 21, pp. 5–26, 2004.
[300] A. Oliver, J. Marti, R. Marti, A. Bosch, and J. Freixenet, "A new approach to the classification of mammographic masses and normal breast tissue," in *Pattern Recognition,*

2006. ICPR 2006. 18th International Conference on, 2006, vol. 4, pp. 707–710.
[301] X. Lladó, A. Oliver, J. Freixenet, R. Martí, and J. Martí, "A textural approach for mass false positive reduction in mammography," *Comput. Med. Imaging Graph.*, vol. 33, pp. 415–422, 2009.
[302] A. Oliver, X. Lladó, J. Martí, R. Martí, and J. Freixenet, "False positive reduction in breast mass detection using two-dimensional PCA," in *Pattern Recognition and Image Analysis*, Springer, 2007, pp. 154–161.
[303] A. Oliver, X. Lladó, J. Freixenet, and J. Martí, "False positive reduction in mammographic mass detection using local binary patterns.," *Med. Image Comput. Comput. Interv. : MICCAI ... Int. Conf. Med. Image Comput. Comput. Interv.*, vol. 10, no. Pt 1, pp. 286–293, 2007.
[304] L. Li, Y. Zheng, L. Zhang, and R. A. Clark, "False-positive reduction in CAD mass detection using a competitive classification strategy," *Med. Phys.*, vol. 28, pp. 250–258, 2001.
[305] Q. D. Truong, M. P. Nguyen, V. T. Hoang, H. T. Nguyen, D. T. Nguyen, T. D. Nguyen, and V. D. Nguyen, "Feature Extraction and Support Vector Machine Based Classification for False Positive Reduction in Mammographic Images," in *Frontier and Future Development of Information Technology in Medicine and Education*, Springer, 2014, pp. 921–929.
[306] L. I. Rudin, S. Osher, and E. Fatemi, "Nonlinear total variation based noise removal algorithms," *Phys. D: Nonlinear Phenom.*, vol. 60, pp. 259–268, 1992.
[307] G. Peyré, "The Numerical Tours of Signal Processing Part 2: Multiscale Processings," *Comput. Sci. & Eng.*, pp. 68–71, 2011.
[308] J. A. Sethian, *Level set methods and fast marching methods: evolving interfaces in computational geometry, fluid mechanics, computer vision, and materials science*, vol. 3. Cambridge university press, 1999.
[309] R. Kimmel and J. A. Sethian, "Fast marching methods for robotic navigation with constraints," *Cent. Pure Appl. Math. Report, Univ. California, Berkeley*, 1996.
[310] G. Peyré, M. Péchaud, R. Keriven, and L. D. Cohen, "Geodesic methods in computer vision and graphics," *Found. Trends¯ Comput. Graph. Vis.*, vol. 5, pp. 197–397, 2010.
[311] A. Dubrovina, "Fast Marching Methods - Tutorial 9@ONLINE," Jun. 2012.
[312] J. N. Tsitsiklis, "Efficient algorithms for globally optimal trajectories," *Autom. Control. IEEE Trans.*, vol. 40, pp. 1528–1538, 1995.
[313] J. Helmsen, E. Puckett, P. Colella, and M. Dorr, "Two new methods for simulating photolithography development in 3D," in *Proc. SPIE*, 1996, vol. 2726, pp. 253–261.
[314] M. Boué and P. Dupuis, "Markov chain approximations for deterministic control problems with affine dynamics and quadratic cost in the control," *SIAM J. Numer. Anal.*, vol. 36, pp. 667–695, 1999.
[315] Y.-H. R. Tsai, L.-T. Cheng, S. Osher, and H.-K. Zhao, "Fast sweeping algorithms for a class of Hamilton–Jacobi equations," *SIAM J. Numer. Anal.*, vol. 41, pp. 673–694, 2003.
[316] H. Zhao, "A fast sweeping method for eikonal equations," *Math. Comput.*, vol. 74, pp. 603–627, 2005.
[317] G. Hadley, "NONLINEAR AND DYNAMIC PROGRAMMING,.," 1964.
[318] D. P. Bertsekas, *Dynamic programming and optimal control*, vol. 1. Athena Scientific Belmont, 1995.
[319] M. Sniedovich, *Dynamic programming: Foundations and principles*. CRC press, 2010.

[320] L. D. Cohen and R. Kimmel, "Global minimum for active contour models: A minimal path approach," *Int. J. Comput. Vis.*, vol. 24, pp. 57–78, 1997.
[321] R. Kimmel and J. A. Sethian, "Optimal algorithm for shape from shading and path planning," *J. Math. Imaging Vis.*, vol. 14, pp. 237–244, 2001.
[322] A. Duci, A. J. Yezzi, S. Mitter, and S. Soatto, "Region matching with missing parts," in *Computer Vision—ECCV 2002*, Springer, 2002, pp. 48–62.
[323] A. Ion, N. M. Artner, G. Peyré, W. G. Kropatsch, and L. D. Cohen, "Matching 2D and 3D articulated shapes using the eccentricity transform," *Comput. Vis. Image Underst.*, vol. 115, pp. 817–834, 2011.
[324] A. Ion, N. M. Artner, G. Peyré, S. B. L. Mármol, W. G. Kropatsch, and L. Cohen, "3D shape matching by geodesic eccentricity," in *Computer Vision and Pattern Recognition Workshops, 2008. CVPRW'08. IEEE Computer Society Conference on*, 2008, pp. 1–8.
[325] R. Achanta, A. Shaji, K. Smith, A. Lucchi, P. Fua, and S. Süsstrunk, "Slic superpixels," *École Polytech. Fédéral de Lausssanne*, vol. 149300, 2010.
[326] A. Vedaldi and B. Fulkerson, "VLFeat: An open and portable library of computer vision algorithms," in *Proceedings of the international conference on Multimedia*, 2010, pp. 1469–1472.
[327] S. Lloyd, "Least squares quantization in PCM," *Inf. Theory, IEEE Trans.*, vol. 28, pp. 129–137, 1982.
[328] J. Fox, D. Glasspool, V. Patkar, M. Austin, L. Black, M. South, D. Robertson, and C. Vincent, "Delivering clinical decision support services: there is nothing as practical as a good theory," *J. Biomed. informatics*, vol. 43, pp. 831–843, 2010.
[329] E. S. Berner, *Clinical Decision Support Systems*. Springer Science+ Business Media, LLC, 2007.
[330] F. C. Wright, C. De Vito, B. Langer, and A. Hunter, "Multidisciplinary cancer conferences: a systematic review and development of practice standards," *Eur. J. Cancer*, vol. 43, pp. 1002–1010, 2007.
[331] J. Fox, A. Glowinski, C. Gordon, S. Hajnal, and M. O'Neil, "Logic engineering for knowledge engineering: design and implementation of the Oxford System of Medicine," *Artif. Intell. Med.*, vol. 2, pp. 323–339, 1990.
[332] E. Alberdi, P. Taylor, R. Lee, J. Fox, M. Sordo, and A. Todd-Pokropek, "CADMIUM II: acquisition and representation of radiological knowledge for computerized decision support in mammography.," in *Proceedings of the AMIA Symposium*, 2000.
[333] D. Acosta, V. Patkar, M. Keshtgar, and J. Fox, "Challenges in delivering decision support systems: the MATE experience," in *Knowledge Representation for Health-Care. Data, Processes and Guidelines*, Springer, 2010, pp. 124–140.
[334] P. Taylor, J. Fox, and A. Todd-Pokropek, "A model for integrating image processing into decision aids for diagnostic radiology," *Artif. Intell. Med.*, vol. 9, pp. 205–225, 1997.
[335] P. Taylor, E. Alberdi, R. Lee, J. Fox, and A. Todd-Pokropek, "Incorporating image processing in a clinical decision support system," in *Information Processing in Medical Imaging*, 2001, pp. 134–140.
[336] P. J. Lisboa and A. F. Taktak, "The use of artificial neural networks in decision support in cancer: a systematic review," *Neural networks*, vol. 19, pp. 408–415, 2006.
[337] M. B. Sesen, R. Banares-Alcantara, J. Fox, T. Kadir, and J. M. Brady, "Lung Cancer Assistant: An ontology-driven, online decision support prototype for lung cancer treatment selection." OWL-ED, 2012.
[338] M. B. Sesen, E. Jiménez-Ruiz, R. Banares-Alcántara, and J. M. Brady, "Evaluating

OWL 2 Reasoners in the context of Clinical Decision Support in Lung Cancer Treatment Selection," in *OWL Reasoner Evaluation (ORE) Workshop*, 2013.
[339] B. Motik, P. F. Patel-Schneider, B. Parsia, C. Bock, A. Fokoue, P. Haase, R. Hoekstra, I. Horrocks, A. Ruttenberg, and U. Sattler, "OWL 2 web ontology language: Structural specification and functional-style syntax," *W3C Recomm.*, vol. 27, 2009.
[340] P. L. Elkin, S. H. Brown, C. S. Husser, B. A. Bauer, D. Wahner-Roedler, S. T. Rosenbloom, and T. Speroff, "Evaluation of the content coverage of SNOMED CT: ability of SNOMED clinical terms to represent clinical problem lists," in *Mayo Clinic Proceedings*, 2006, vol. 81, pp. 741–748.
[341] B. Sesen, "This is a screenshot of LCA @ONLINE," Apr. 2013.
[342] V. Patkar, D. Acosta, T. Davidson, A. Jones, J. Fox, and M. Keshtgar, "Using computerised decision support to improve compliance of cancer multidisciplinary meetings with evidence-based guidance," *BMJ open*, vol. 2, 2012.
[343] K. Preston Jr, "Digital picture analysis in cytology," in *Digital Picture Analysis*, Springer, 1976, pp. 209–294.
[344] W. H. Wolberg, W. N. Street, and O. L. Mangasarian, "Breast cytology diagnosis via digital image analysis," *Anal. Quant. Cytol. Histol.*, vol. 15, pp. 396–404, 1993.
[345] F. Meyer, "Automatic screening of cytological specimens," *Comput. Vision, Graph. Image Process.*, vol. 35, pp. 356–369, 1986.
[346] L. da Fontoura Costa and R. M. Cesar Jr, *Shape analysis and classification: theory and practice*. CRC press, 2010.
[347] \Lukasz Jele´n, T. Fevens, and A. Krzy\.zak, "Classification of breast cancer malignancy using cytological images of fine needle aspiration biopsies," *Int. J. Appl. Math. Comput. Sci.*, vol. 18, pp. 75–83, 2008.
[348] W. N. Street, W. H. Wolberg, and O. L. Mangasarian, "Nuclear feature extraction for breast tumor diagnosis," in *IS&T/SPIE's Symposium on Electronic Imaging: Science and Technology*, 1993, pp. 861–870.
[349] W. H. Wolberg and O. L. Mangasarian, "Computer-aided diagnosis of breast aspirates via expert systems.," *Anal. Quant. Cytol. Histol. Int. Acad. Cytol. [and] Am. Soc. Cytol.*, vol. 12, pp. 314–320, 1990.
[350] W. H. Wolberg, W. N. Street, and O. L. Mangasarian, "Image analysis and machine learning applied to breast cancer diagnosis and prognosis," *Anal. Quant. Cytol. Histol.*, vol. 17, pp. 77–87, 1995.
[351] W. H. Wolberg, W. N. Street, and O. L. Mangasarian, "Machine learning techniques to diagnose breast cancer from image-processed nuclear features of fine needle aspirates," *Cancer Lett.*, vol. 77, pp. 163–171, 1994.
[352] P. Filipczuk, T. Fevens, A. Krzyzak, and R. Monczak, "Computer-Aided Breast Cancer Diagnosis Based on the Analysis of Cytological Images of Fine Needle Biopsies," 2013.
[353] C. W. Elston and I. O. Ellis, "Assessment of histological grade," *Breast*, vol. 13, pp. 356–384, 1998.
[354] V. L. Doussal, M. Tubiana-Hulin, S. Friedman, K. Hacene, F. Spyratos, and M. Brunet, "Prognostic value of histologic grade nuclear components of Scarff-Bloom-Richardson (SBR)," *Cancer*, vol. 64, pp. 1914–1921, 1989.

Appendix 1

Examples of segmented density maps after applying false positive reduction method. These density mammograms are expected to be normal.

Segmented Density Maps	After Applying FPR
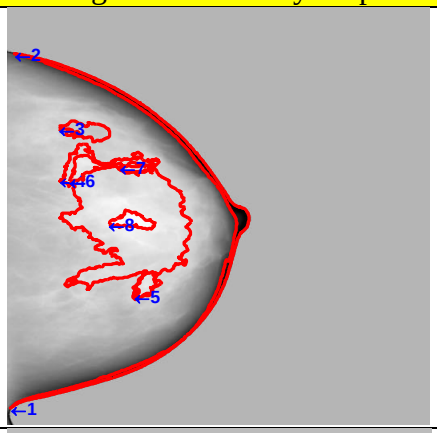	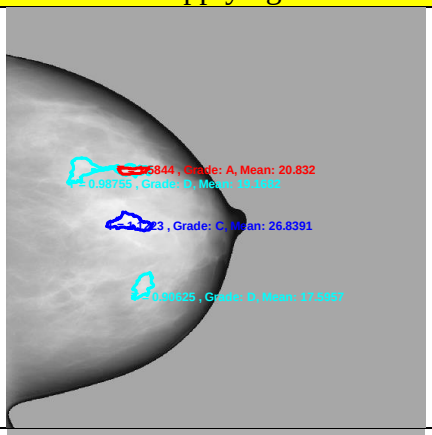
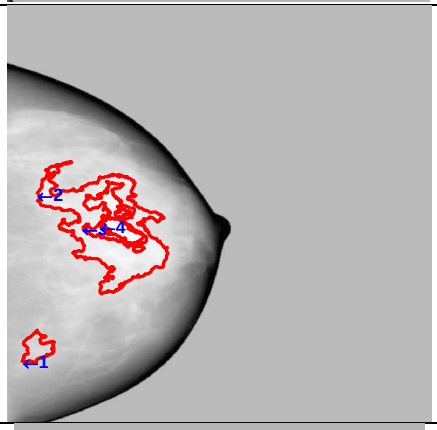	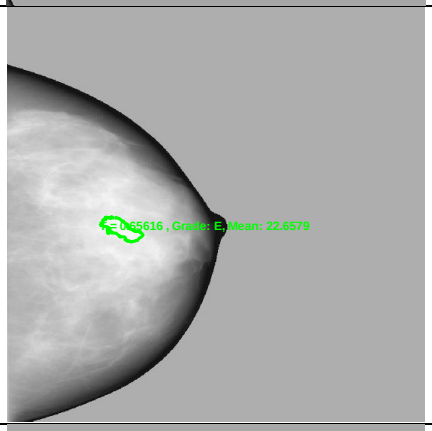
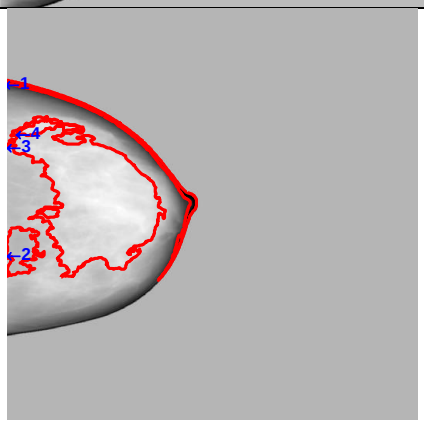	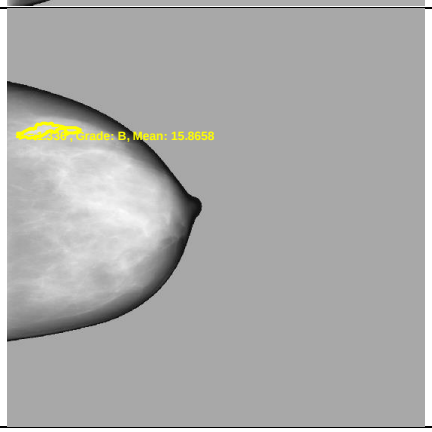

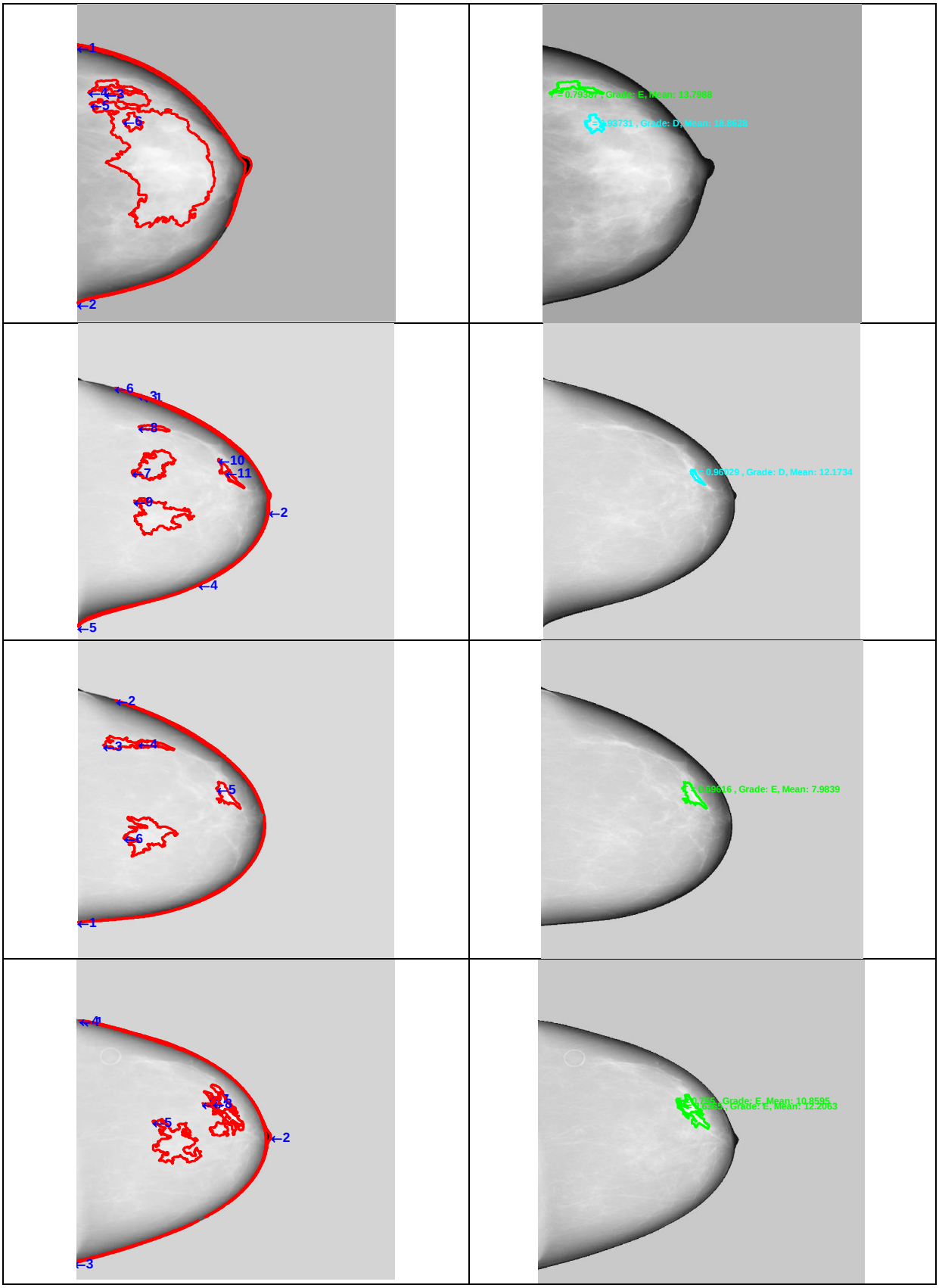
1
4
3
5
6
2
0.79387 , Grade: E, Mean: 13.7988
0.93731 , Grade: D, Mean: 10.8628
6
3
8
7
10
11
9
2
4
5
0.96029 , Grade: D, Mean: 12.1734
2
3
4
5
6
1
0.89616 , Grade: E, Mean: 7.9839
4
5
2
3
0.97... Grade: E, Mean: 10.8595
0.96... Grade: E, Mean: 12.2083

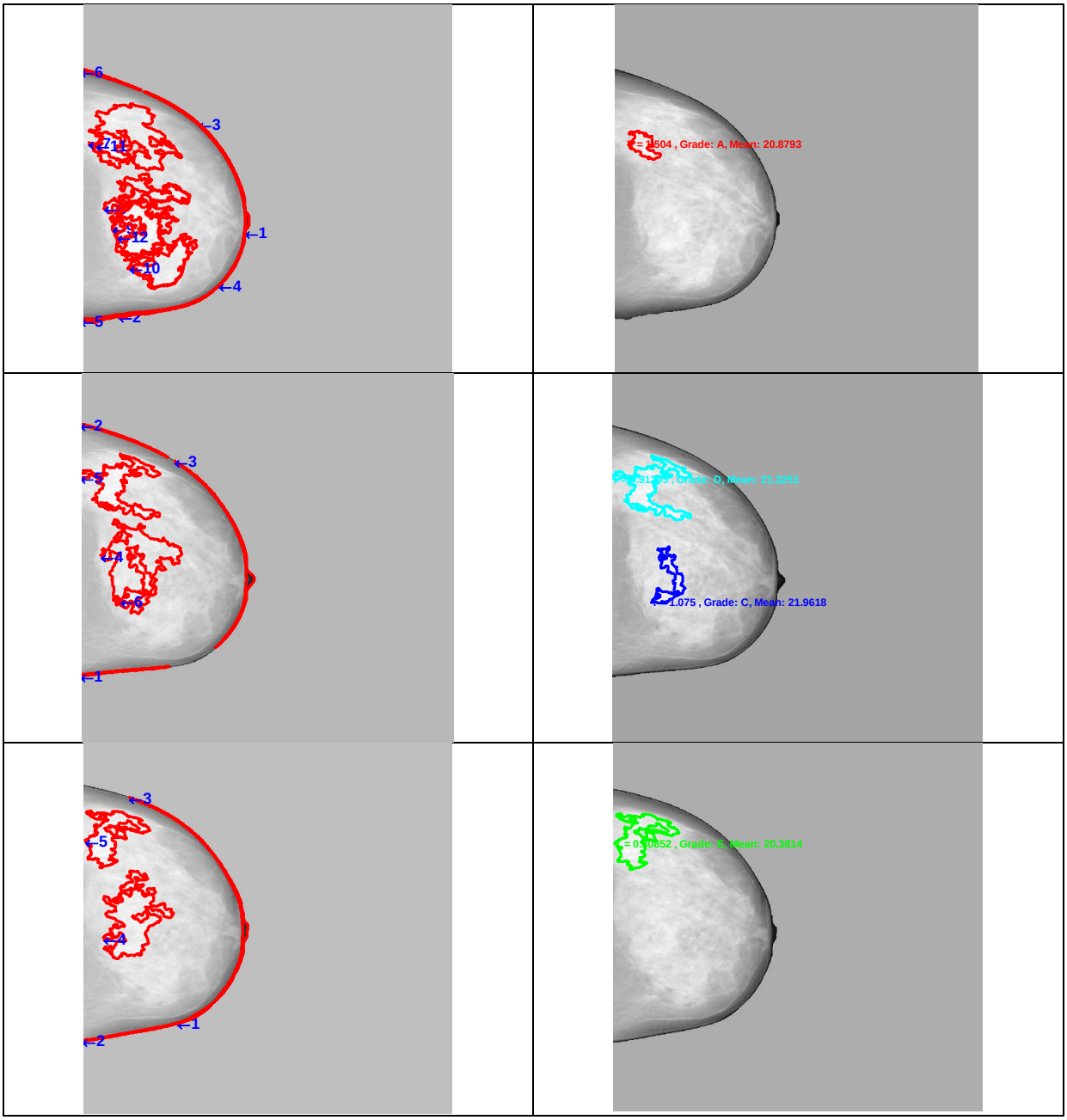
6
3
1
12
10
4
5
2
= 1.504 , Grade: A, Mean: 20.8793
2
3
4
6
1
= 1.075 , Grade: C, Mean: 21.9618
3
5
4
1
2

Appendix II

Examples of RMA application on 2D plannar shapes

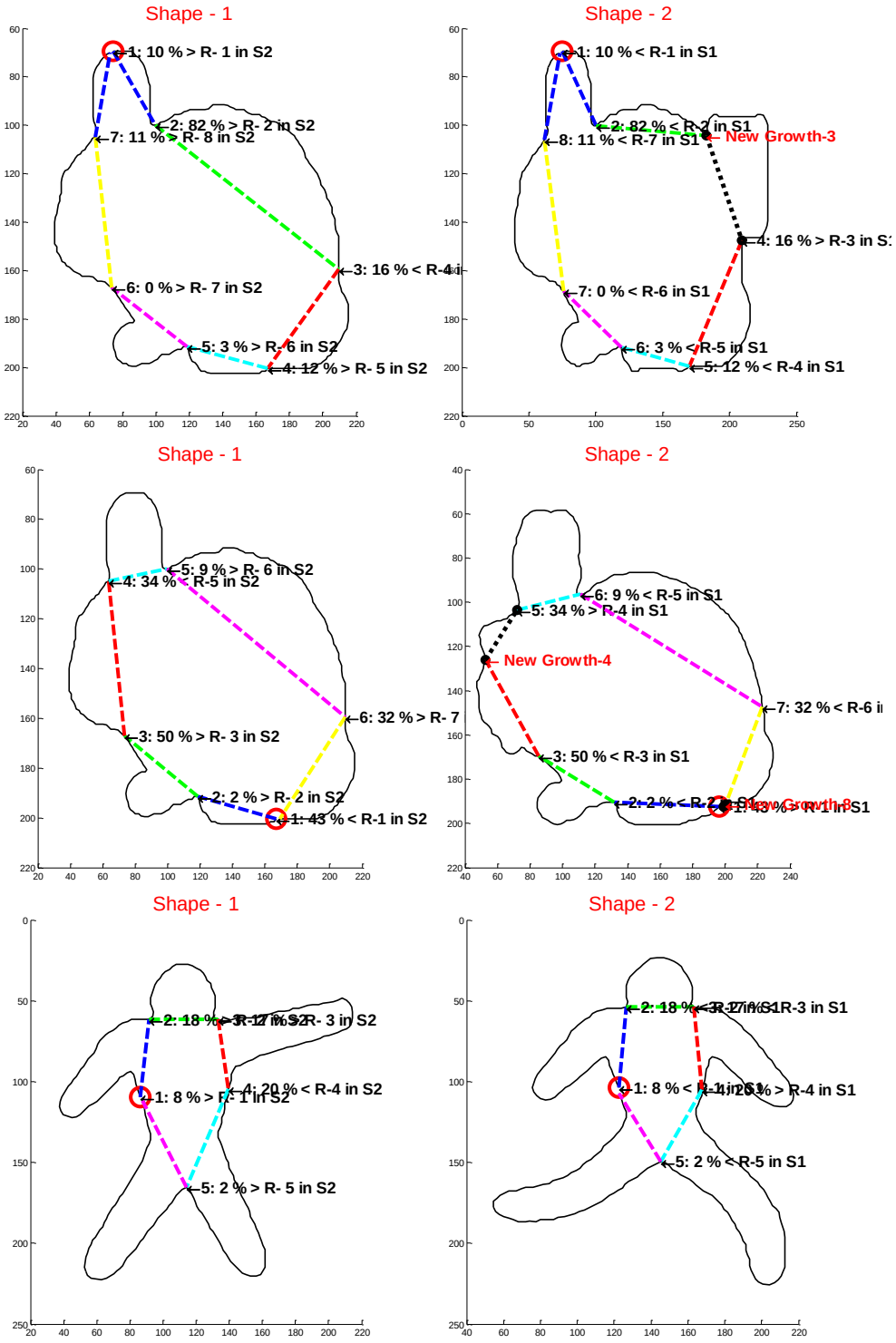

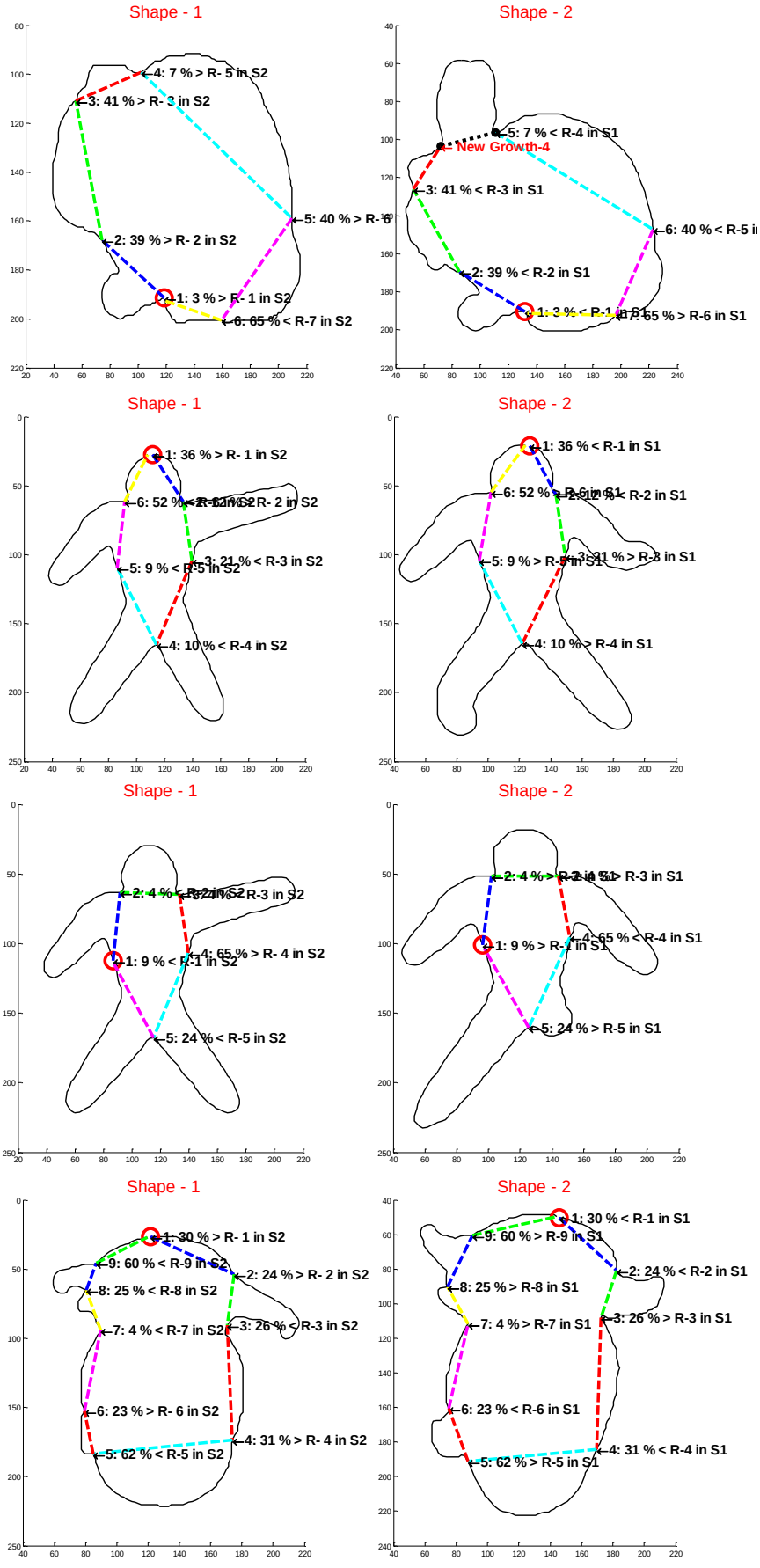
Shape - 1
4: 7 % > R- 5 in S2
3: 41 % > R- 3 in S2
5: 40 % > R- 6
2: 39 % > R- 2 in S2
1: 3 % > R- 1 in S2
6: 65 % < R-7 in S2
Shape - 2
5: 7 % < R-4 in S1
4: New Growth-4
3: 41 % < R-3 in S1
6: 40 % < R-5 i
2: 39 % < R-2 in S1
1: 3 % < R-1 in S1
7: 65 % > R-6 in S1
Shape - 1
1: 36 % > R- 1 in S2
6: 52 % > R- 6 in S2
2: 39 % > R- 2 in S2
3: 21 % < R-3 in S2
5: 9 % < R-5 in S2
4: 10 % < R-4 in S2
Shape - 2
1: 36 % < R-1 in S1
6: 52 % > R-6 in S1
2: 39 % < R-2 in S1
3: 21 % > R-3 in S1
5: 9 % > R-5 in S1
4: 10 % > R-4 in S1
Shape - 1
2: 4 % < R-2 in S2
3: 21 % < R-3 in S2
4: 65 % > R- 4 in S2
1: 9 % < R-1 in S2
5: 24 % < R-5 in S2
Shape - 2
2: 4 % < R-2 in S1
3: 21 % > R-3 in S1
4: 65 % < R-4 in S1
1: 9 % > R-1 in S1
5: 24 % > R-5 in S1
Shape - 1
1: 30 % > R- 1 in S2
9: 60 % < R-9 in S2
2: 24 % > R- 2 in S2
8: 25 % < R-8 in S2
7: 4 % < R-7 in S2
3: 26 % < R-3 in S2
6: 23 % > R- 6 in S2
4: 31 % > R- 4 in S2
5: 62 % < R-5 in S2
Shape - 2
1: 30 % < R-1 in S1
9: 60 % > R-9 in S1
2: 24 % < R-2 in S1
8: 25 % > R-8 in S1
7: 4 % > R-7 in S1
3: 26 % > R-3 in S1
6: 23 % < R-6 in S1
4: 31 % < R-4 in S1
5: 62 % > R-5 in S1

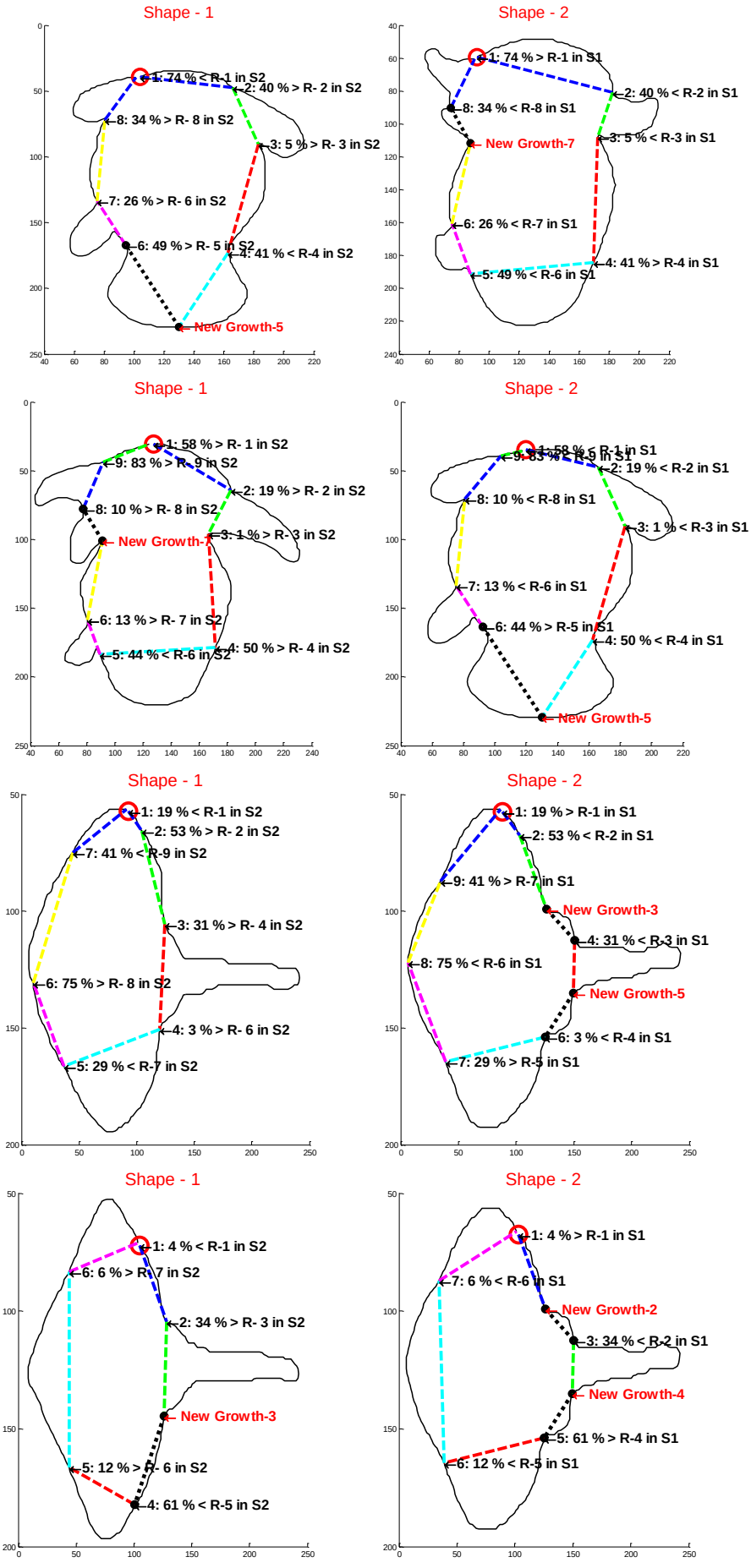
Shape - 1
1: 74 % < R-1 in S2
2: 40 % > R- 2 in S2
8: 34 % > R- 8 in S2
3: 5 % > R- 3 in S2
7: 26 % > R- 6 in S2
6: 49 % > R- 5 in S2
4: 41 % < R-4 in S2
New Growth-5
Shape - 2
1: 74 % > R-1 in S1
2: 40 % < R-2 in S1
8: 34 % < R-8 in S1
New Growth-7
3: 5 % < R-3 in S1
6: 26 % < R-7 in S1
4: 41 % > R-4 in S1
5: 49 % < R-6 in S1
Shape - 1
1: 58 % > R- 1 in S2
9: 83 % > R- 9 in S2
2: 19 % > R- 2 in S2
8: 10 % > R- 8 in S2
New Growth-7
3: 1 % > R- 3 in S2
6: 13 % > R- 7 in S2
4: 50 % > R- 4 in S2
5: 44 % < R-6 in S2
Shape - 2
1: 58 % < R-1 in S1
9: 83 % < R-9 in S1
2: 19 % < R-2 in S1
8: 10 % < R-8 in S1
3: 1 % < R-3 in S1
7: 13 % < R-6 in S1
6: 44 % > R-5 in S1
4: 50 % < R-4 in S1
New Growth-5
Shape - 1
1: 19 % < R-1 in S2
2: 53 % > R- 2 in S2
7: 41 % < R-9 in S2
3: 31 % > R- 4 in S2
6: 75 % > R- 8 in S2
4: 3 % > R- 6 in S2
5: 29 % < R-7 in S2
Shape - 2
1: 19 % > R-1 in S1
2: 53 % < R-2 in S1
9: 41 % > R-7 in S1
New Growth-3
4: 31 % < R-3 in S1
8: 75 % < R-6 in S1
New Growth-5
6: 3 % < R-4 in S1
7: 29 % > R-5 in S1
Shape - 1
1: 4 % < R-1 in S2
6: 6 % > R- 7 in S2
2: 34 % > R- 3 in S2
New Growth-3
5: 12 % > R- 6 in S2
4: 61 % < R-5 in S2
Shape - 2
1: 4 % > R-1 in S1
7: 6 % < R-6 in S1
New Growth-2
3: 34 % < R-2 in S1
New Growth-4
5: 61 % > R-4 in S1
6: 12 % < R-5 in S1

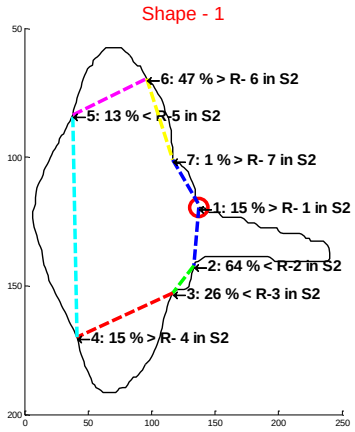
Shape - 1
6: 47 % > R- 6 in S2
5: 13 % < R-5 in S2
7: 1 % > R- 7 in S2
1: 15 % > R- 1 in S2
2: 64 % < R-2 in S2
3: 26 % < R-3 in S2
4: 15 % > R- 4 in S2

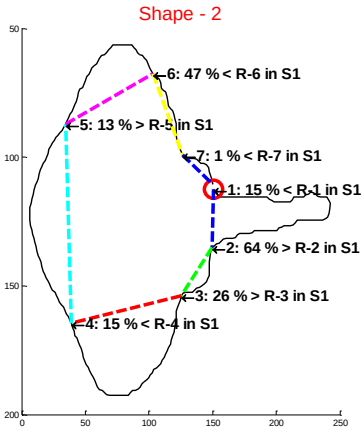
Shape - 2
6: 47 % < R-6 in S1
5: 13 % > R-5 in S1
7: 1 % < R-7 in S1
1: 15 % < R-1 in S1
2: 64 % > R-2 in S1
3: 26 % > R-3 in S1
4: 15 % < R-4 in S1

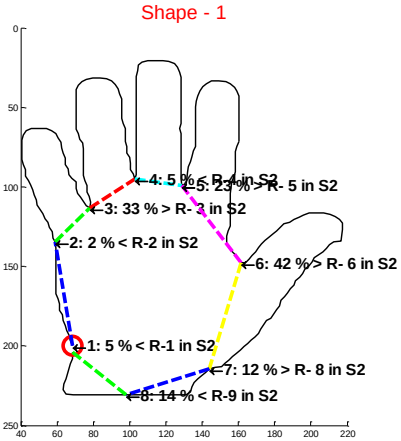
Shape - 1
4: 5 % < R-4 in S2
5: 23 % > R- 5 in S2
3: 33 % > R- 3 in S2
2: 2 % < R-2 in S2
6: 42 % > R- 6 in S2
1: 5 % < R-1 in S2
7: 12 % > R- 8 in S2
8: 14 % < R-9 in S2

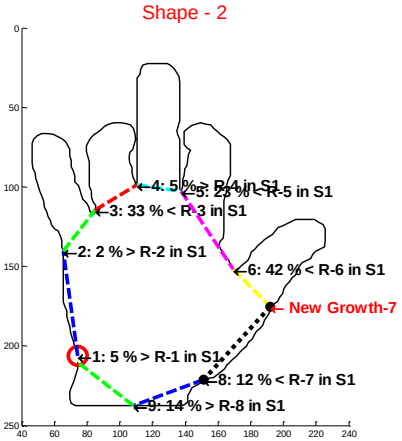
Shape - 2
4: 5 % > R-4 in S1
5: 23 % < R-5 in S1
3: 33 % < R-3 in S1
2: 2 % > R-2 in S1
6: 42 % < R-6 in S1
New Growth-7
1: 5 % > R-1 in S1
8: 12 % < R-7 in S1
9: 14 % > R-8 in S1

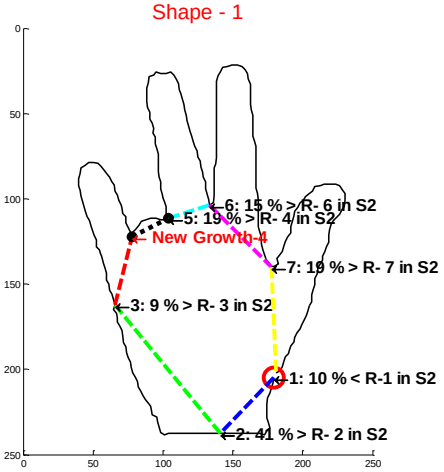
Shape - 1
6: 15 % > R- 6 in S2
5: 19 % > R- 4 in S2
New Growth-4
7: 19 % > R- 7 in S2
3: 9 % > R- 3 in S2
1: 10 % < R-1 in S2
2: 41 % > R- 2 in S2

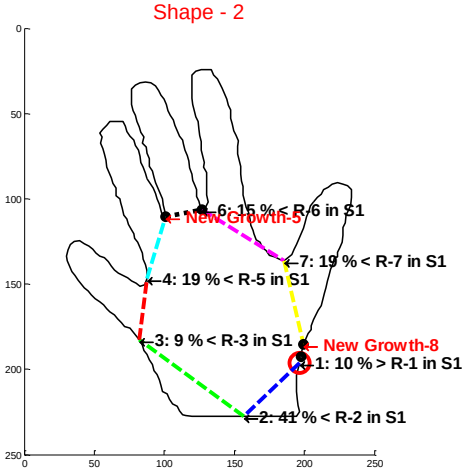
Shape - 2
6: 15 % < R-6 in S1
New Growth-5
7: 19 % < R-7 in S1
4: 19 % < R-5 in S1
3: 9 % < R-3 in S1
New Growth-8
1: 10 % > R-1 in S1
2: 41 % < R-2 in S1

Appendix III

Examples of shape description using eccentricity transform while using mean distance value from the feature set

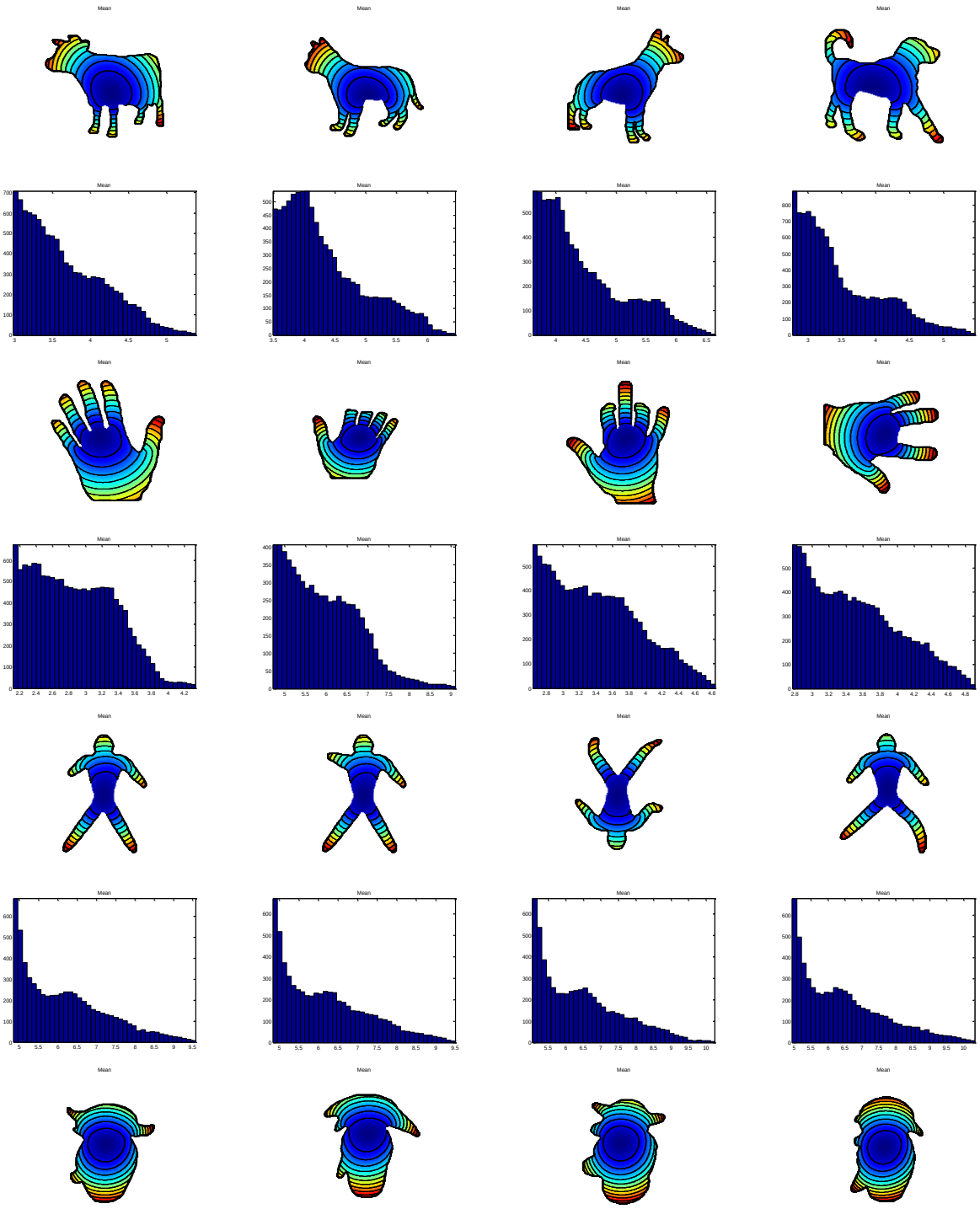

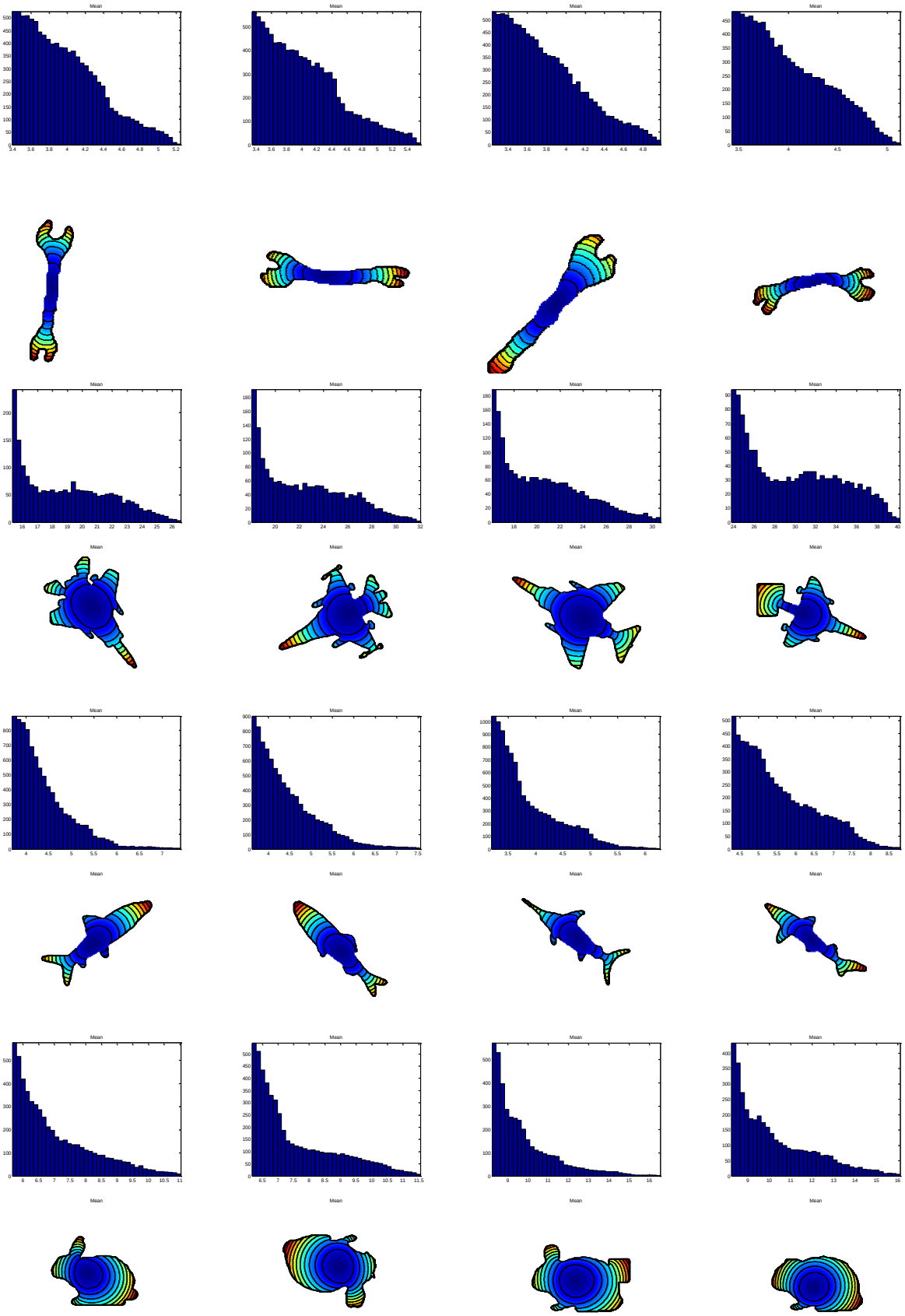
Mean

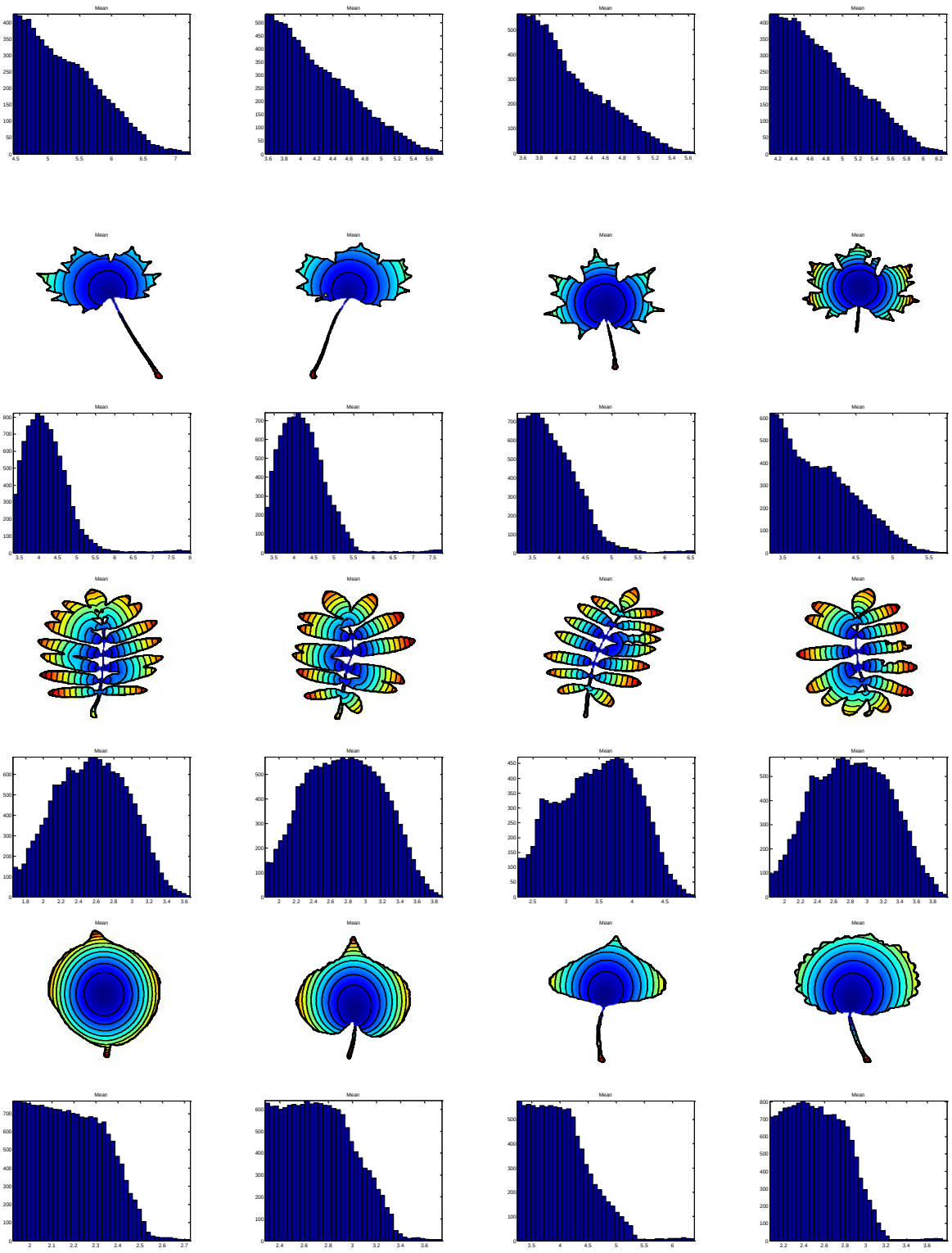
Mean